HIGH-THROUGHPUT METHODS

FOR CHARACTERIZING THE MECHANICAL PROPERTIES OF COATINGS

A Dissertation
Submitted to the Graduate Faculty
of the
North Dakota State University
of Agriculture and Applied Science

By

Chavanin Siripirom

In Partial Fulfillment
for the Degree of
DOCTOR OF PHILOSOPHY

Major Department:
Coatings and Polymeric Materials

March 2012

Fargo, North Dakota

North Dakota State University
Graduate School

Title

High-throughput Methods for Characterizing the Mechanical Properties of Coatings

By

Chavanin Siripirom

The Supervisory Committee certifies that this ***disquisition*** complies with North Dakota State University's regulations and meets the accepted standards for the degree of

DOCTOR OF PHILOSOPHY

SUPERVISORY COMMITTEE:

Dr. Dean C. Webster
Chair

Dr. Stuart Croll

Dr. Victoria Gelling

Dr. Ghodrat Karami

Approved by Department Chair:

Nov 11, 2012
Date

Dr. Dean C. Webster
Signature

ABSTRACT

The characterization of mechanical properties in a combinatorial and high-throughput workflow has been a bottleneck that reduced the speed of the materials development process. High-throughput characterization of the mechanical properties was applied in this research in order to reduce the amount of sample handling and to accelerate the output. A puncture tester was designed and built to evaluate the toughness of materials using an innovative template design coupled with automation. The test is in the form of a circular free-film indentation. A single template contains 12 samples which are tested in a rapid serial approach. Next, the operational principles of a novel parallel dynamic mechanical-thermal analysis instrument were analyzed in detail for potential sources of errors. The test uses a model of a circular bilayer fixed-edge plate deformation. A total of 96 samples can be analyzed simultaneously which provides a tremendous increase in efficiency compared with a conventional dynamic test. The modulus values determined by the system had considerable variation. The errors were observed and improvements to the system were made. A finite element analysis was used to analyze the accuracy given by the closed-form solution with respect to testing geometries, such as thicknesses of the samples. A good control of the thickness of the sample was proven to be crucial to the accuracy and precision of the output. Then, the attempt to correlate the high-throughput experiments and conventional coating testing methods was made. Automated nanoindentation in dynamic mode was found to provide information on the near-surface modulus and could potentially correlate with the pendulum hardness test using the loss tangent component. Lastly, surface characterization of stratified siloxane-polyurethane coatings was carried out with X-ray photoelectron spectroscopy, Rutherford backscattering spectroscopy, transmission electron

microscopy, and nanoindentation. The siloxane component segregates to the surface during curing. The distribution of siloxane as a function of thickness into the sample showed differences depending on the formulation parameters. The coatings which had higher siloxane content near the surface were those coatings found to perform well in field tests.

ACKNOWLEDGMENTS

I would like express my deepest gratitude to my advisor, Dr. Dean Webster, for his guidance, advice, and support during my study at NDSU. Without him this work would not be accomplished. My gratitude is also extended to Dr. Brian Hinderliter for his valuable suggestions. I would like to thank Dr. Stuart Croll, Dr. Ghodrat Karami, and Dr. Victoria J. Gelling for their comments and suggestions and serving on my research committee.

I would like to thank the Department of Coatings and Polymeric Materials and Center for Nanoscale Science and Engineering at North Dakota State University for my stipend support. The Department of Coatings and Polymeric Materials has given me tremendous opportunity to grow as a researcher and as a person. I cannot imagine a nicer workplace. I am very grateful for the discussions with the colleagues in my research group. I would like to acknowledge Erik Jarabek, Jared Risan, Heidi Docktor, Brad Halverson, and Christy Gallagher for their help with instrumentations.

I am most thankful to the support and encouragement from my family and friends. I am fortunate to have met many wonderful people throughout my time in graduate school. I will always be grateful for this experience and opportunity.

TABLE OF CONTENTS

LIST OF TABLES

LIST OF FIGURES

LIST OF APPENDIX FIGURES

CHAPTER 1. INTRODUCTION

Combinatorial and high-throughput methods have been utilized in the pharmaceutical industry for more than a decade.[1, 2] The combinatorial and high-throughput methods refer to screening through multiple combinations of compounds in parallel and in an accelerated fashion. Thousands of samples of drug formulations can be synthesized and screened through for their activity in a single day. In a complex system, such as in drug discovery and materials research, they contain a mixture of ingredients which can influence the overall desired properties. In coatings, a formulation consists of a combination of resins, crosslinkers, solvents, catalysts, and etc. Each component can have an effect on the properties. The mixture can be synthesized or formulated one at a time, until the right combination that meets the criteria is found. But then an understanding of an impact of specific components will be hindered; such as the sensitivity of each component to a certain property. Thus, the most important factor in a combinatorial study is the design of experiments to investigate multiple variables at the same time. The full factorial and fractional factorial designs have been utilized. The goal of the design of experiments is to define a minimum number of experiments, using probability and statistics, in order to determine the main effects and interactions between variables.[3] Figure 1.1 shows the combinatorial and high-throughput workflow. Multiples samples are made, tested and analyzed in the workflow. The process is highly automated in order to achieve the acceleration. Each step requires a similar amount of time; otherwise the slow part of the process is identified as bottleneck.

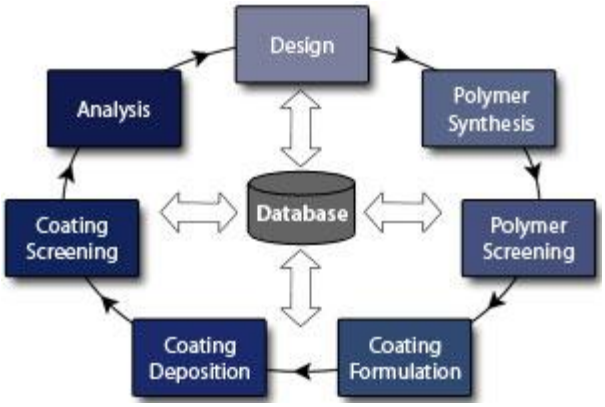

Figure 1.1. Coatings research and development workflow (Reproduced from ref.[4])

The initial development of the combinatorial materials research laboratory (CMRL) at NDSU was sponsored by the Office of Naval Research. The researchers at CMRL have utilized combinatorial and high-throughput tools for marine coatings research. The focus has been on the development of fouling-release coatings based on silicone chemistry. Silicone elastomers have been studied and tested as fouling-release coatings.[5, 6] However, they can easily tear and thus are not durable in service. They are toughened by using reinforcing fillers, but the fillers can alter the surface and bulk properties and affect the fouling-release property. Thus, one of the most important parameters for marine coating design becomes the toughness of the coating. It is of interest to apply the high-throughput concept throughout characterization technique, including the toughness measurement. The emphasis of this thesis is on high-throughput mechanical characterization methods that are available and are developed at the combinatorial materials research laboratory, NDSU. One of the focuses of our research group has been the development of siloxane-polyurethane coatings.[7-10] An effort is made to create a tough coating based on polyurethane chemistry and incorporating a silicone component to obtain fouling-release performance. The following sections contain a review of existing high-throughput

characterization methods of mechanical properties of polymers and a brief outline of each chapter.

1.1. High-throughput Characterization Methods for the Mechanical Properties of Polymers

The existing high-throughput characterization methods for the mechanical properties are presented here. Tweedie et al. used high-throughput nanomechanical screening on a discrete polymer library containing 576 samples from pairwise combinations of 24 monomers as shown in Figure 1.2.[11] Polymer samples were deposited on the glass slides with a sample diameter of 300 μm. Thus, including two replicates, there are a total of 1,728 spots on a single glass slide. Most nanoindentation instruments are computerized with an X-Y translation stage; thus they can be automated and become a high-throughput instrument. A pendulum-based nanoindenter with a scanning stage, NanoTest 600 NT1 from Micro Material Ltd., Wrexham, UK, was used with a diamond Berkovich indenter. Elastic modulus values were extracted from the unloading portion of the indentation data.

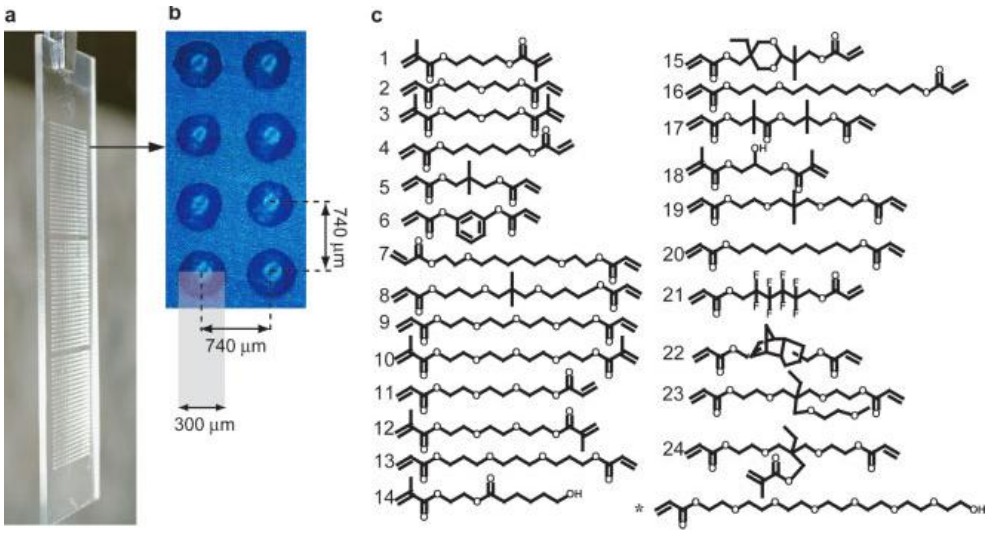

Figure 1.2. A glass slide containing spots of polymer (Reproduced from ref.[11])

Lin-Gibson et al. created a gradient sample on the dental resin blend by varying the co-monomer composition and the irradiation time as shown in Figure 1.3.[12] They performed nanoindentation using an MTS Nanoinstruments NanoXP instrument (Oak Ridge, TN). A continuous stiffness method was used at 45 Hz and 5 nm dynamic oscillations. The elastic modulus values were recorded between the depth ranges of 1 to 4 µm and the averages were taken. Potyrailo et al. developed a high-throughput instrument for abrasion resistance of coatings.[13] The air blast abrasive test and oscillating sand test were used on a 48-element library of coatings. The degree of abrasion was determined by the induced haze. A coating was illuminated at a normal angle to the surface, and the transmitted and scattered lights were measured. Figure 1.4 shows the high-throughput spectroscopic analysis system.

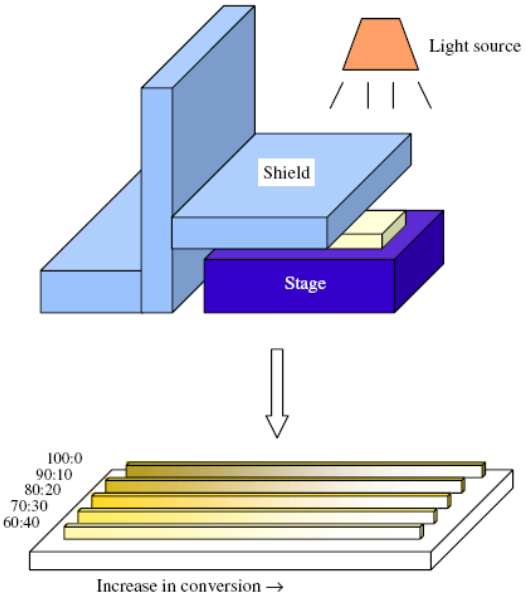

Figure 1.3. Gradient sample with each strip correspond to a discrete composition and the degree of conversion is varied by the irradiation time (Reproduced from ref.[12])

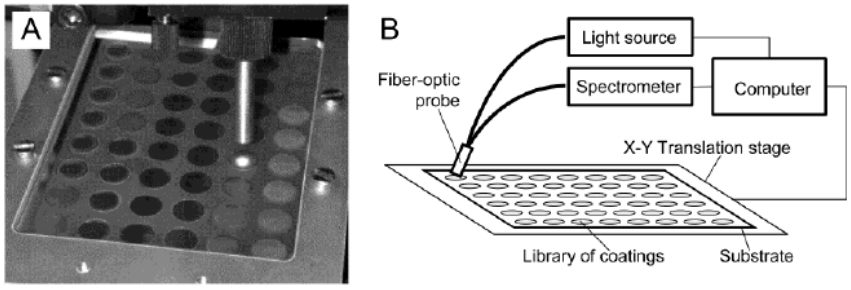

Figure 1.4. High-throughput abrasion resistance measurement (Reproduced from ref.[13])

Schneider et al. measured stress and strain at break on thermally treated isotactic polypropylene.[14] The polypropylene sample was sandwiched between two steel plates as shown in Figure 1.5. The press at one end was at elevated temperature and the other end was at ambient temperature. Tensile testing was performed for mechanical characterization. Small dumbbell specimens (downsized by a factor of 4 from the ISO 527 type 5A standard) were used with two specimens at each location.

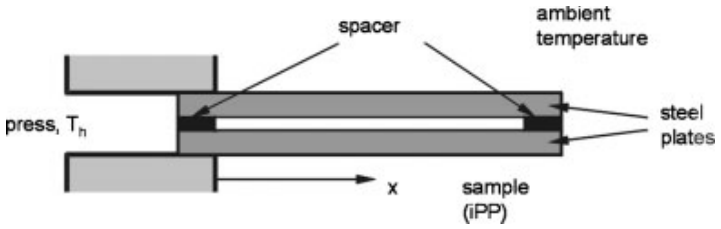

Figure 1.5. Schematic of temperature gradient plate (Reproduced from ref.[14])

Stafford et al. induced a compressive stress to a substrate/film laminate, as shown in Figure 1.6, which caused a laminate buckling.[15] The film had a gradient of composition and the wavelength of buckling instability was measured using a small angle light scattering (SALS) apparatus in order to calculate the elastic modulus.

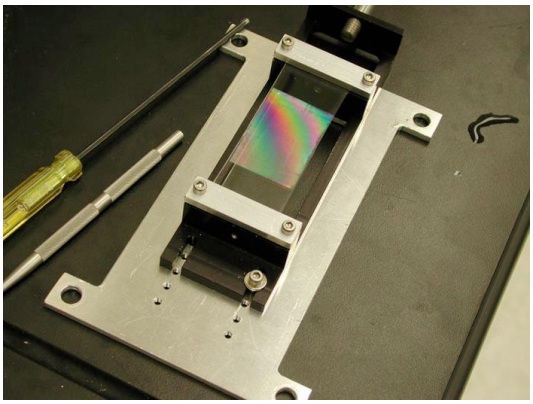

Figure 1.6. Laminate buckling under compressive stress (Reproduced from ref.[15])

Sormana et al. performed a circular free-film indentation on a gradient library.[16, 17] The instrument could operate in a quasi-static mode and a dynamic impact mode, which the sample holder dropped on to an indenter with a force sensor at the translation stage. The instrument described in Chapter 2 has a similar concept to the studies from Sormana et al.[16-19]

Kossuth et al. introduced a parallel dynamic mechanical-thermal analysis (pDMTA) instrument.[20] The polymer samples were deposited on a polyimide film supported on a perforated aluminum plate. The schematic of the test is shown in Figure 1.7. There are 96 spots on the sample plate and 96 samples can be measured simultaneously using 96 force-measuring sensors. The details are in Chapter 3.

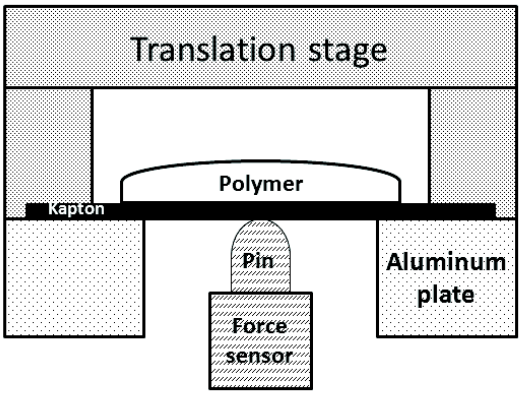

Figure 1.7. Schematic of pDMTA testing

1.2. Overview of Chapters

1.2.1. High-throughput characterization of mechanical properties at NDSU

A combinatorial study consisting of more than 200 samples needs mechanical characterization for toughness. In this study, tensile properties are of importance, particularly the elastic modulus, the strain to break and the energy to break. In a standard test method, Teflon® or Tedlar® substrates, which act as the release films, are prepared for each of the coatings. Each coating is cut into 3-5 individual pieces of ASTM specified dumbbell-shape specimen using a cutting die. The thickness is measured and the tensile test is performed with replicates. The coatings are very flexible due to low glass transition temperatures compared with the ambient temperature (testing at a room temperature). In order to persist with a particular strain rate specified by an ASTM method, each test lasts 5-10 minutes since a 100% elongation or more is observed. Even though the engineering stress-strain description already does not apply because of the high extension, and the strain gauge for thin film and video imaging are not used. Hence, the sample preparation and tensile testing processes take roughly two weeks to complete with only 3 replicates. An alternative method is needed to accelerate the time needed to characterize the toughness of coatings libraries.

Chapter 2 presents an automated toughness measurement. The instrument is also call a puncture tester because the test is in the form of puncturing a circular free film. The energy to break is measured from the test and the result is compared with conventional tensile and tear tests. The relative stiffness can also be extracted if needed. The goal is to minimize sample handling and replace rather tedious and time-consuming tensile testing for a large combinatorial study.

Chapter 3 presents a finite element analysis for the parallel DMTA instrument from Symyx Technologies, Inc. The glass transition temperature results have been satisfactory, but the modulus output has had large variability. The geometry and property of samples which may affect the accuracy of the output are investigated. The goal is to understand the sources of variance/error and to improve the modulus output using the correction factor based on the finite element model.

Chapter 4 attempts to correlate conventional coating tests to existing high-throughput characterization methods. A slight trend can be observed, because coating tests, such as impact resistance, pencil hardness and pendulum hardness, characterize a combination of fundamental properties. Thus, the high-throughput characterization techniques need to be adapted to simulate coating tests, if the trend to conventional coating testing is what we are after.

Figure 1.8 summarizes the motivation of our research. The times to run tests on ~200 samples are estimated based on experiences using current tools at the NDSU facility. The total times to run the tests include the entire process from the preparation of substrates to testing time. The man hours in the chart represents the amount of time a worker needs to spend to execute the entire process. The automation is aimed to reduce the hours needed to operate from the worker. Each block on the blue bar represents the worker's time consumed in each step.

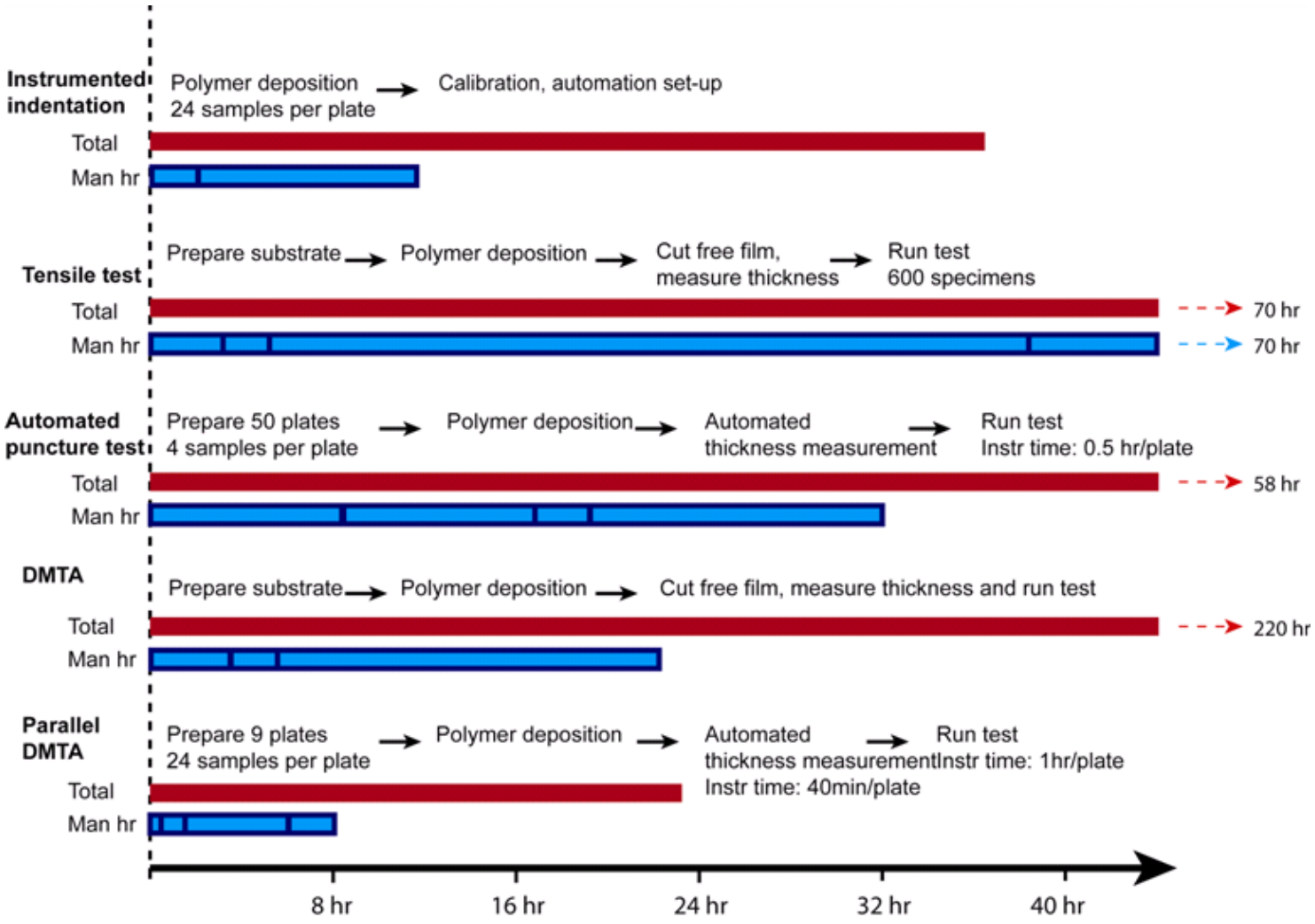

Figure 1.8. Estimated times for different methods for characterizing 200 samples are shown. The total is the total time it takes to complete the test.

1.2.2. Surface characterization of siloxane-polyurethane fouling-release coating

The siloxane-polyurethane coating is a unique crosslink system with the bulk containing polyurethane and self-stratified siloxane towards the air interface. The surface of the coatings has low surface energy which allows for easy removal of fouling organisms. Several series of coatings have been explored using high throughput screening and screening with biological assays have shown differences in fouling-release performance as a function of composition.[7,9,10] To further understand the morphology of these stratified coatings, surface characterization using X-ray photoelectron spectroscopy, Rutherford backscattering spectroscopy, transmission electron microscopy, are performed. The goal is to look for the distributions of siloxane components with respect to formulation parameters and how they transfer to the performance in the field test.

1.3. Conclusions

High-throughput instrumentation increases our productivity and effectively reduces cost. With the aid of high-throughput methods, mechanical characterization, which previously were bottlenecks, were accelerated. This was accomplished by intuitive designs from sample handling to testing technique. The testing technique can be performed in a rapid serial set-up or in a parallel manner. The most important element is a solid scientific background to support and validate the new designs. Here, the parallel DMTA deviates from a simple analysis by using a bilayer geometry coupling with parallel testing. The automated puncture tester uses a rapid serial method, but the states of stresses are complex. An automated nanoindentation instrument characterizes near surface properties with certain assumptions of the material behavior. The instruments should be robust and easy to use. The miniaturization of the geometry may be unavoidable for high-throughput testing,

which, combining with the more complex testing scheme, could result in lower accuracy. However, the relative ranking of materials is the sole goal for doing the combinatorial study in the first place, hence sufficiency becomes an operational word in our context. Consequently, there may always be a case for further improvement as this will be apparent in each of the high-throughput characterization chapters.

1.4. References

1. Webster, D. C., Radical change in research and development: The shift from conventional methods to high throughput methods. *JCT CoatingsTech* **2005,** *2* (15), 24-29.

2. Webster, D. C.; Bennett, J.; Kuebler, S.; Kossuth, M. B.; Jonasdottir, S., High throughput workflow for the development of coatings. *JCT CoatingsTech* **2004,** *1* (6), 34-39.

3. Bonitz, V. S. Development of a novel high-throughput screening method for the evaluation of barrier properties of corrosion protective coatings. Ph.D. Thesis, North Dakota State University, Fargo, 2007.

4. Combi Science. http://www.ndsu.edu/cnse/facilities_equipment/combi_science.html(accessed 03/17/2012).

5. Brady Jr, R. F., Properties which influence marine fouling resistance in polymers containing silicon and fluorine. *Progress in Organic Coatings* **1999,** *35* (1-4), 31-35.

6. Brady Jr, R. F.; Singer, I. L., Mechanical factors favoring release from fouling release coatings. *Biofouling* **2000,** *15* (1-3), 73-81.

7. Ekin, A.; Webster, D. C., Combinatorial and high-throughput screening of the effect of siloxane composition on the surface properties of crosslinked siloxane-polyurethane coatings. *Journal of Combinatorial Chemistry* **2007,** *9*, 178-188.

8. Majumdar, P.; Ekin, A.; Webster, D. C., Thermoset siloxane-urethane fouling release coatings. *ACS Symposium Series 957 (Smart Coatings)* **2007**, 178-188.

9. Sommer, S.; Ekin, A.; Webster, D. C.; Stafslien, S. J.; Daniels, J.; VanderWal, L. J.; Thompson, S. E. M.; Callow, M. E.; Callow, J. A., A preliminary study on the properties and fouling-release performance of siloxane-polyurethane coatings prepared from poly(dimethylsiloxane) (PDMS) macromers. *Biofouling* **2010,** *26* (8), 961-972.

10. Sommer, S.; Stafslien, S. J.; Webster, D. C.; Bodkhe, R.; Pieper, R.; Daniels, J.; VanderWal, L. J.; David, R.; Callow, M. E.; Callow, J. A.; Ralston, E.; Swain, G.; Brewer, L.; Wendt, D.; Dickinson, G.; Teo, S., Comparison of laboratory analysis with field testing of siloxane-polyurethane fouling-release coatings. **2011**.

11. Tweedie, C. A.; Anderson, D. G.; Langer, R.; Van Vliet, K. J., Combinatorial material mechanics: high-throughput polymer synthesis and nanomechanical screening. *Advanced Materials* **2005,** *17*, 2599-2604.

12. Lin-Gibson, S.; Landis, F. A.; Drzal, P. L., Combinatorial investigation of the structure-properties characterization of photopolymerized dimethacrylate networks. *Biomaterials* **2006,** *27*, 1711-1717.

13. Potyrailo, R.; Chisholm, B. J.; Olson, D. R.; Brennan, M. J.; Molaison, C. A., Development of combinatorial chemistry methods for coatings: high-throughput screening of abrasion resistance of coatings libraries. *Analytical Chemistry* **2002,** *74* (19), 5105-5111.

14. Schneider, K.; Zafeiropoulos, N. E.; Haubler, L.; Stamm, M., High-throughput screening of the influence of thermal treatment on the mechanical properties of semicrystalline polymers: a case study for iPP. *Macromolecular Rapid Communications* **2004,** *25*, 355-359.

15. Stafford, C. M.; Guo, S.; Harrison, C.; Chiang, M. Y. M., Combinatorial and high-throughput measurements of the modulus of thin polymer films. *Review of Scientific Instruments* **2005,** *76*, 062207.

16. Sormana, J.-L.; Chattopadhyay, S.; Meredith, J. C., High-throughput mechanical characterization of free-standing polymer films. *Review of Scientific Instruments* **2005,** *76*, 062214.

17. Sormana, J.-L.; Meredith, J. C., High-throughput dynamic impact characterization of polymer films. *Materials Research Innovations* **2003,** *7*, 295-301.

18. Sormana, J.-L.; Meredith, J. C., High-throughput screening of mechanical properties on temperature-gradient polyurethaneurea libraries. *Macromolecular Rapid Communications* **2003,** *24*, 118-122.

19. Sormana, J.-L.; Meredith, J. C., High-throughput discovery of structure-mechanical property relationships for segmented poly(urethane-urea)s. *Macromolecules* **2004,** *37*, 2186-2195.

20. Kossuth, M. B.; Hajduk, D. A.; Freitag, C.; Varni, J., Parallel dynamic thermomechanical measurements of polymer libraries. *Macromolecular Rapid Communications* **2004,** *25*, 243-248.

CHAPTER 2. HIGH-THROUGHPUT TOUGHNESS MEASUREMENT OF POLYMERIC COATINGS

2.1. Introduction and Rationale

2.1.1. Introduction to toughness

In materials science, by definition, toughness is the energy-absorbing capacity of a material prior to fracture.[1] Both the loads and deflections relate to the imposing energy on the material, thus a stress-strain curve is relevant in describing toughness. Figure 2.1 shows a stress-strain curve and the represented resilience and toughness.

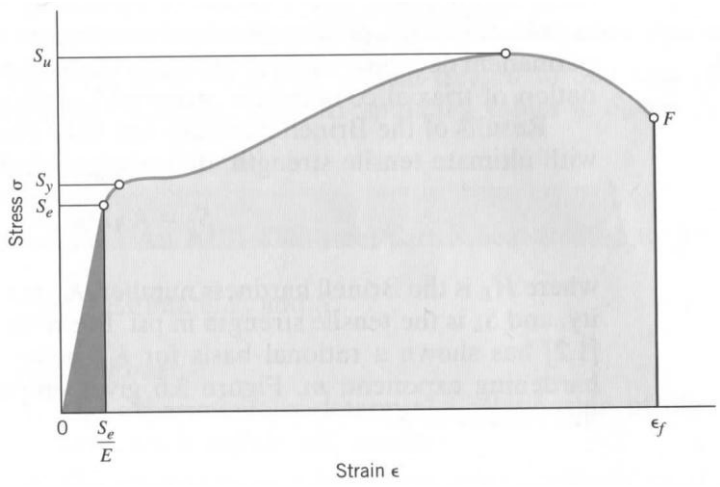

Figure 2.1. S_e represents the elastic limit. (Reproduced from ref.[1])

Resilience is the capacity of a material to absorb energy within the elastic region as shown in Figure 2.1 as a darker gray shaded area. S_e in Figure 2.1 represents the elastic limit where no plastic deformation has taken place and the material will return to the original state when loaded within the elastic range. A parameter called the modulus of resilience, R_m, is a measure of the absorbed energy per unit volume of material in tensile

loading to its elastic limit. The resilience can be represented by the triangular area under the elastic region of the stress-strain curve, as seen in the following equation.

$$R_m = \frac{1}{2}(S_e)\left(\frac{S_e}{E}\right) = \frac{S_e^2}{2E} \tag{2.1}$$

Toughness is the total capacity of a material to absorb energy before fracture. This is represented by the total shaded area in Figure 2.1. Equation 2.2 shows the modulus of toughness, T_m, which is the energy absorbed per unit volume when loaded in tension.

$$T_m = \int_0^{\epsilon_f} \sigma d\epsilon \tag{2.2}$$

Integration is performed to calculate the area under the stress-strain curve. A rough estimate of the integral is sometimes used depending on the material behavior as shown in Equation 2.3.

$$T_m \approx \frac{S_y + S_u}{2}\epsilon_f \tag{2.3}$$

The area under the engineering stress-strain curve approximates the energy density to fracture a sample. This slow absorption of energy of a material is referred to as toughness. In metallurgy, toughness comes from high strength and high ductility. Ductility is plastic deformation before failure. The material needs to have a decent combination of strength and ductility to achieve good toughness. In polymeric materials, high strength and flexibility are important. Polymers with high strength and significant inelastic deformation will appear the toughest from the total area under the stress-strain curve. Toughness can be affected by the rate of loading time and temperature. Faster rate of loading and lower temperature normally reduce the toughness of the material. Most components that are designed to absorb energy are generally characterized using impact loading. Since in real applications, the material is selected according to the design specification to carry the load within the elastic limit to maintain its shape and functioning purpose. However, in many

cases, the materials can experience impact loading and cyclic loading such that failure analysis becomes important. Thus, toughness is also commonly defined as the ability of a material to withstand impact blow and the cyclic loading is associated with the fatigue characterization of a material through a fracture mechanics approach.[2]

2.1.2. Impact toughness

Toughness is commonly defined as the ability of a material to withstand impact. There are two main types of impact tests used: pendulum tests and falling weight tests. Pendulum tests are common among plastics and metals. A pendulum apparatus with a notched Charpy specimen is shown in Figure 2.2. The Charpy specimen is supported as a horizontal beam.[3] The specimen can be either notched or unnotched.

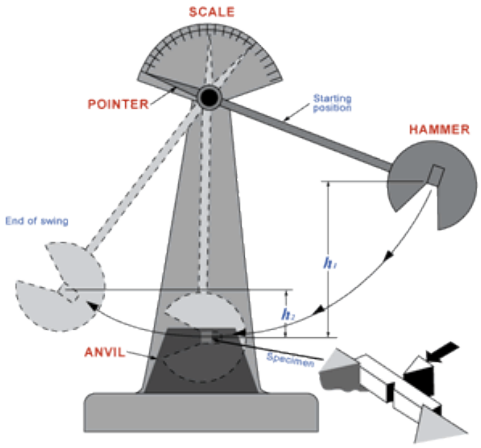

Figure 2.2. Charpy test (Reproduced from ref.[4])

The hammer is lifted and strikes the specimen. The impact strength is calculated by using the energy removed from the pendulum after impact divided by the cross-sectional area of the specimen in the swing direction. Another common pendulum test is the Izod test. Charpy is similar to a three-point bending test whereas Izod is a cantilever bending test. For both tests, however, specimens with different sizes cannot be compared because

bending is involved during impact resulting in deformation volume. The results from different sizes then do not give results that are proportional to the cross-sectional area.[3]

For thin section materials, there are ASTM D1822 (standard test method for tensile-impact energy to break plastics and electrical insulating materials) and ASTM D3420 (standard test method for pendulum impact resistance of plastic film). In tensile impact, the pendulum strikes one of the clamping bases at one end and the specimen extends and ruptures. Falling dart methods are used with films and sheeting. ASTM D5420 (standard test method for impact resistance of flat, rigid plastic specimen by means of a striker impacted by a falling weight) is also called the Gardner impact test. Other methods that use a falling dart are ASTM D1709 for plastic film and ASTM D5628 for flat, rigid plastic. These are non-instrumented tests where the impact energy through mass and height of the falling weight are adjusted to determine the point of failure. Instrumented impact tests are also used. ASTM D4272 is the standard test method for total energy impact of plastic films by dart drop. A sensor is used to detect the time of flight to determine the change in kinetic energy from calculating the velocity after impact. ASTM D3763 (standard test method for high speed puncture properties of plastics using load and displacement sensors) monitors force and displacement during impact, thus additional information, such as peak force, displacement at peak force and the shape of the force-displacement curve, can be characterized. Figure 2.3 shows the dart containing built-in load-sensing transducer. The load cell is placed close to the impact point to reduce interference from the force wave (ringing effect).

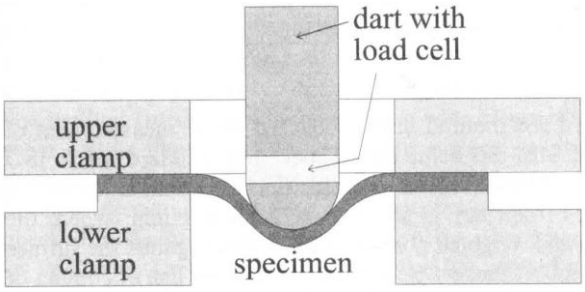

Figure 2.3. Instrumented falling dart method (Reproduced from ref.[3])

Toughness generally decreases as the rate of loading increases. Impact strength of a material and toughness are also dependent on the temperature. Figure 2.4 shows a drastic change in toughness around the transition temperature between brittle and ductile behavior. Impact tests can be used to measure the energy-absorbing capacity at different temperatures to observe the transition; this is important for the selection of components in the design to avoid failure.

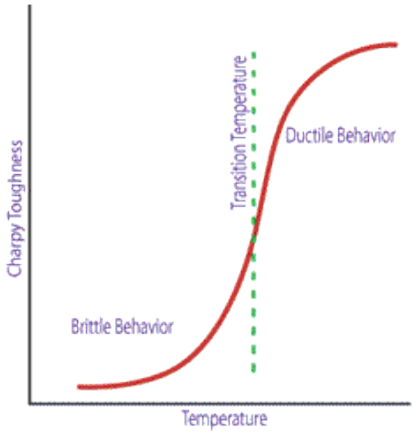

Figure 2.4. Impact toughness of a material as a function of temperature

2.1.3. Fracture toughness

Materials can fail in a yielding-dominant or a fracture-dominant type. In fracture-dominant type of failures, there is a highly localized plasticity as a result of microscopic flaws and cracks. The basics of fracture mechanics can be explained with an energy balance approach as shown below by considering a loaded infinitely thick plate.[5]

$$U = U_o + U_a + U_\gamma - F \tag{2.4}$$

where U = total plate energy when crack is present

U_o = total plate energy without crack

U_a = change in elastic strain energy as a result of a crack with length $2a$

U_γ = change in surface energy due to the introduction of a crack

F = work applied to the system

According to Griffith, a certain amount of energy is required for a crack to initiate and grow. This relates to the surface energy of the material, strain energy and crack size.[5]

Under a fixed grip condition, F=0, we have

$$U = U_o - \frac{\pi\sigma^2 a^2}{E} + 4a\gamma_e \tag{2.5}$$

where γ_e is surface energy per unit area, E is Young's modulus, and σ is stress.

A crack will occur when U decreases,

$$\frac{dU}{d(2a)} = \frac{d}{d(2a)}\left(-\frac{\pi\sigma^2 a^2}{E} + 4a\gamma_e\right) < 0 \tag{2.6}$$

Thus, for crack extension to occur,

$$\frac{\pi\sigma^2 a}{E} > \gamma_e \tag{2.7}$$

Strain energy release rate, G, is defined by Irwin as

$$G = \frac{\pi\sigma^2 a}{E} \tag{2.8}$$

Critical strain energy release rate, G_c, is then equal to $2\gamma_e$. Critical stress intensity factor, K_c is defined as

$$G_c = \frac{K_c^2}{E} \tag{2.9}$$

Figure 2.5 shows the critical stress intensity as a function of thickness for high strength steel. K_{Ic} is called the plane strain fracture toughness.

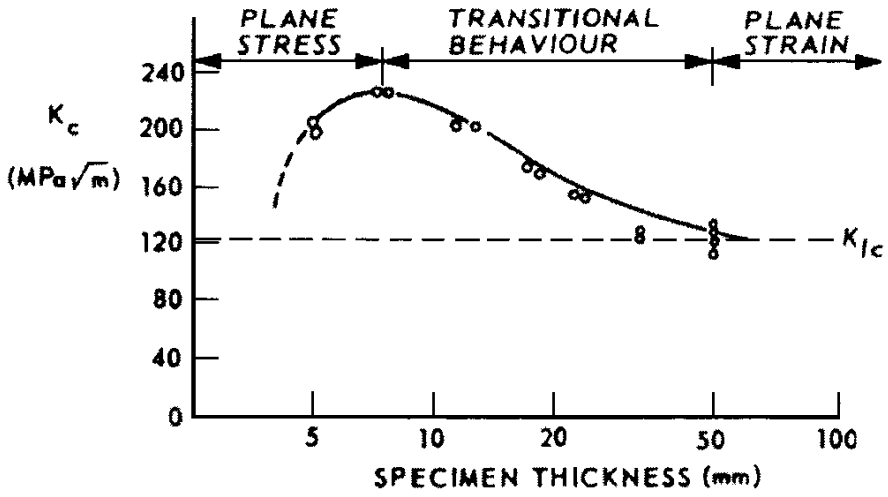

Figure 2.5. Critical stress intensity as a function of specimen thickness for a high strength maraging steel (Reproduced from ref. [5])

K_{Ic} can be considered a material property; however, it is still dependent on temperature and loading rate. Unlike the impact test, the fracture toughness test provides an ability to separate the geometry from the material response. ASTM D5045 is the standard test method for plane-strain fracture toughness and strain energy release rate of plastics materials. Two common specimens are compact tension and single edge notched as shown in Figure 2.6.

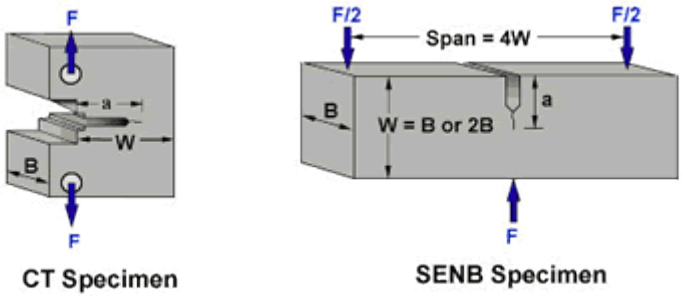

Figure 2.6. Compact tension specimen and single edge notched bend specimen (Reproduced from ref.[4])

ASTM D5045 is based on ASTM E399 which is fracture toughness test for metals. The method includes the detailed procedure for G_c for plastic. It specifies specimen

preparation and correction for the penetration of loading pin/supports into the specimen. A razor blade or tapping is used to produce a crack tip radius of approximately 10-15 μm. Fracture toughness can be calculated based on the load at the onset of crack growth. If the specimen dimensions satisfy plane strain conditions, K_{IC} is obtained. The presented method assumes elastic conditions where there is limited plasticity in the crack tip region. For more ductile materials, the J-Integral concept in elastic-plastic fracture mechanic is used.[5]However, there has not been a J-testing standard for plastics at the present time.

2.1.4. Fracture behavior of polymer

When a polymer is strained, the strain energy is stored in the polymer by chain extension, bond bending and bond stretching. This strain energy is required to create the new surface which includes the orientation of the chains near the surface and the breaking of chains that span the cracking region. Heat is also generated and dissipated at the crack tip and the new surface could be different than the normal surface. Failure behavior in a polymer depends on whether it is in the ductile or brittle state. In ductile state, there is a shear flow of polymer molecules sliding past one another, whereas, in the brittle state, there are bond bending and stretching. Crazing will form at the right angles to the applied stress. If the polymer experiences crazing, failure usually occurs after 1% to 2% extension which results in a brittle failure. On the other hand, a ductile material will experience shear yielding which involves molecular slip at 45 degrees to the applied stress. A polymer can be stretched at least 10% to 20% extension as it undergoes yielding. Figure 2.7 shows images of crazing and shear yielding which are the two modes of polymer failure upon loading.

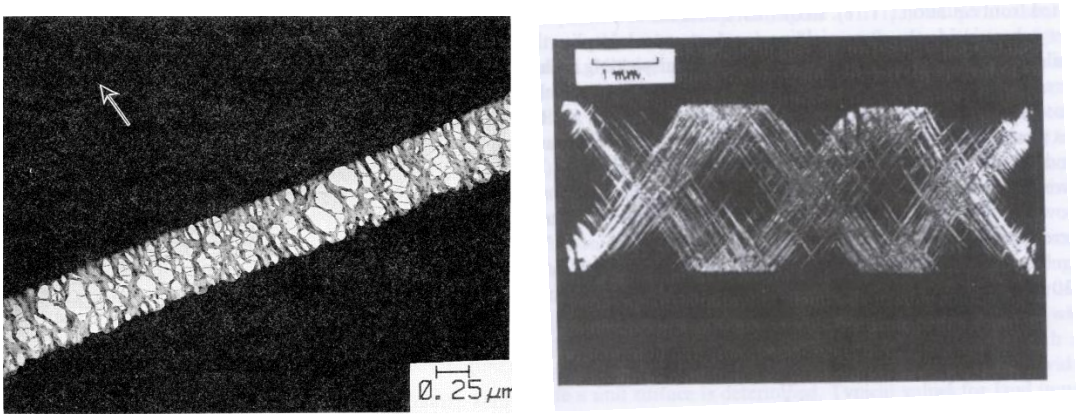

Figure 2.7. Crazing with the pointed arrow representing the direction of axial stress (left) and shear yielding (right) (Reproduced from ref.[6, 7])

Under compression loading or hydrostatic pressure, a polymer will tend to fail by shear yielding as shown in Figure 2.8 which shows the failure envelope for PMMA under biaxial stress.

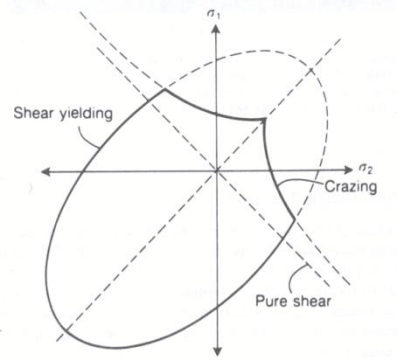

Figure 2.8. failure envelope for PMMA under biaxial stress (Reproduced from ref.[7])

The fracture resistance of a polymer is then determined by the ability to develop a yield zone in the region of a crack tip which is normally in the state of triaxial stress. In the molecular aspects of fracture for polymers, chain scission and chain pullout occurs.[7] Chain scission normally consumes only a small fraction of the fracture energy. Viscoelastic energy dissipation is the major energy consuming factor. In tougher polymers, chain scission is delayed in favor of molecular relaxation. Chain scission of a C-C bond

consumes 83 kcal/mol with most of the energy being consumed to open the bond angle from 109° to 180°. The original length of C-C bond of 1.54Å is elongated to the breaking length threshold which is 2.54Å. The frictional value in Equation 2.4 considers the energy expended in pulling one chain with respect to its neighbor in the bulk:

$$\mu_0 = \frac{2E_v}{vnL^2} \tag{2.10}$$

where μ_0 is the molecular frictional coefficient per unit length of mer, E_v is the energy for chain pullout, v is the velocity of the chain being pulled out, n is the total number of chains subtracted by the chain scissions per unit volume, and L is the length segment of the chain being pulled out.

For polystyrene with a molecular weight of 151,000 g/mol, E_v is roughly 260×10^6 J/m^3. As a result of frictional forces, the temperature for polystyrene chain pullout was found to be as high as 150° to 250° C. Furthermore, the molecular weight of a polymer governs the amount of entanglements. A polymer with a molecular weight below the critical molecular weight for entanglements has a very low strength and is brittle.[8]

2.1.5. Toughness in polymeric film and sheeting

A polymer thin film has been characterized with the J-integral concept using video imaging to detect crack initiation and to measure crack extension.[9] A simpler fracture toughness testing for when the plane strain condition is not possible is the essential work of fracture (EWF) method.[10, 11] The basis of EWF is as follows:

$$W_f = W_e + W_p \tag{2.11}$$

where W_f is total work of fracture, W_e is the essential work of fracture characterizing the fracture process zone and W_P is the nonessential work of fracture characterizing the plastic zone.

The film specimen is notched and the crack is called the ligament in this context of a thin film. Both single-edged-notched-tension and double-edged-notched-tension specimens are commonly used.[12] Figure 2.9 shows the double-edged-notched-tension specimen. The essential work term and the plastic zone term can be resolved into smaller terms as seen in Equation 2.12.

$$W_f = w_e lB + w_p \beta\, l^2 \tag{2.12}$$

where w_e and w_f are specific essential work and specific plastic work, l is the ligament length, β is the shape factor of yield zone and B is the thickness of the specimen.

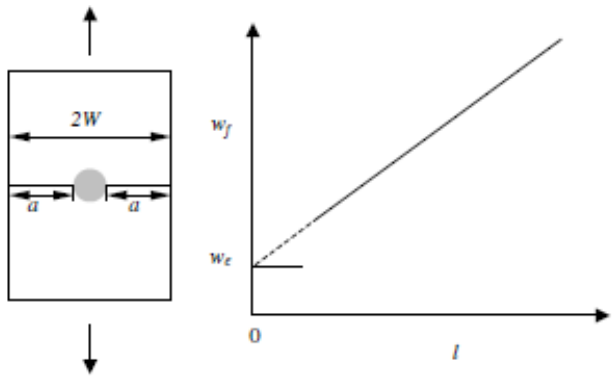

Figure 2.9. Essential work of fracture specimen (left) and the expected linear relationship between fracture energy and ligament length (right) (Reproduced from ref. [13])

The first term on the right side of Equation 2.12 ($w_e lB$) represents the energy required to fracture and is linearly proportional to ligament length whereas the second term ($w_P \beta l^2$) is proportional to the second power of ligament length. $w_p\beta$ is the non-essential work of fracture and is thought of as a measure of resistance against stable crack propagation. The specific work of fracture, w, can be written as:

$$w = \frac{W_f}{lB} = w_e + w_p \beta l \tag{2.13}$$

The specific work of fracture as a function of ligament length ($w = f(l)$) is non-linear when it is under plane strain or in the plane stress/strain transition.[14] Equation 2.13 is in the form of a linear equation with w_e as the y-intercept and $w_p\beta$ as the slope. Fracture specimens with different ligament lengths are used to create data points along the fracture energy as a function of ligament length. Then, w_e is found using curve fitting, thus extrapolating and locating the intersection. This EWF concept has been applied to highly ductile materials, films and plates. Plane stress exists when the flow stress is independent of the ligament length.[15] Plane strain occurs when $l/B \leq 1$ and plane stress occurs when $l/B >> 1$. In most literature, plane stress was ensured using $l/B > 3$-5.

Elastomers are another type of material for which linear elastic fracture mechanics does not work. Previously, ductility and a large plastic zone were the reasons for adopting the J-integral and EWF. Here, a change in entropy is involved for rubber-like materials.[16] Elastomers have an extremely high extensibility generated by low mechanical stress. The deformation induces changes in entropy whereas internal energy does not change. Thus, the tearing energy concept was developed for rubber materials by Rivlin and Thomas which is based on the theoretical analysis of crack growth behavior.[16] The equation for tearing energy (T) is shown in Equation 2.14:

$$T = -\left(\frac{\partial U}{\partial A}\right)_a \tag{2.14}$$

where U is the total elastic strain energy (potential energy), a is crack length and A is the crack area.

Tearing energy is the energy required per unit thickness of a specimen to create a unit increase in crack length. The tearing energy is proportional to an increase in crack

length. The calculation is also independent of the geometry and manner of loading, but the stored energy density has to be measured. A trouser tear specimen is shown in Figure 2.10.

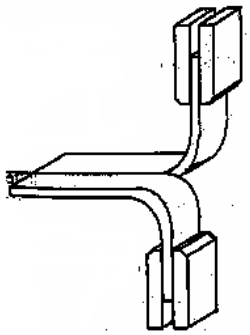

Figure 2.10. Trouser tear test (Reproduced from ASTM D624-00)

Equation 2.14 can be extended to the following equations:

$$-\left(\frac{dU}{da}\right) = TB \tag{2.15}$$

where B is the sample thickness.

The change in energy (dU) is equal to the work input (dW).

$$T = \frac{dW}{Bda} \tag{2.16}$$

The work done to the specimen on trouser specimen can be written as:

$$dW = F(2da) \tag{2.17}$$

Thus, we have, for trouser tear,

$$T = \frac{2F}{B} \tag{2.18}$$

Equation 2.18 assumes that the work input is entirely consumed by crack propagation. Equation 2.19 takes into account the stretching in the legs of the trouser tear specimen:

$$T = \frac{2\lambda F}{B} - wE \tag{2.19}$$

where λ is the extension ratio in the legs, w is the total width of specimen, and E is strain energy density in the legs.

For some elastomers, if w can be large enough, λ and E would approach 1 and 0, respectively. Therefore, Equation 2.19 can be approximated by Equation 2.18. Excessive leg extension can occur on highly extensible materials, thus the legs can be reinforced with a textile to minimize the extension.

2.1.6. Toughness in polymeric coatings

As stated, toughness is the ability of a material to absorb energy via static or impact loadings. Fracture toughness methods characterize the energy required to create new surfaces. K_c is used for linear elastic materials. The J-integral concept and EWF are used for elastic-plastic materials. For rubbery materials, J-integral and tear energy are used. In polymeric coating application, toughness implies strength and resilience, and the ability to withstand impact or wear and tear.[8] Toughness of a polymeric coating is a desired property in most cases. Coatings must possess flexibility and toughness which allow the coatings to withstand stresses from shrinking and swelling, forming, mechanical load and weathering. In actuality, coatings and substrates work together. The previously presented tests only characterize the polymeric material itself. Coatings are unique in this regard. Flexibility of a coating on the substrate depends on its extensibility, the coating thickness and the adhesion of the coating to the substrate. Good adhesion will bring better apparent flexibility than a coating with poor adhesion. In order to evaluate flexibility and toughness, common tests for coatings adhered to substrates are bending and impact tests. Figure 2.11 shows the conical mandrel bend tester.

Figure 2.11. Conical mandrel bend tester (Reproduced from ref.[17])

Figure 2.12 shows coating test panels subjected to conical mandrel and reverse impact tests.

Figure 2.12. Coatings on metal panels subjected to conical mandrel bending (left) and reverse impact test (right)

These tests are more severe than in actual service conditions because they are normally performed on a fresh, unaged sample. Coatings tend to become more brittle with time due to the loss of plasticizing components and structural changes due to degradation or crosslinking, thus severe tests are useful indicators of long-term serviceability. Flexibility and toughness of coatings depends on humidity, temperature and strain rate.

Flexibility of coatings, such as latexes, can be sensitive to even a slight change in humidity. Generally, tests should be conducted at a relative humidity of 50 ± 5%. Coatings need to be conditioned in a controlled humidity atmosphere for a day or more before testing. Test temperature is an important parameter which determines the behavior of coatings around the glass transition temperature. Flexibility and toughness of coatings are normally tested at 25 ± 1 °C after specimens are equilibrated at the testing temperature. In some instances, tests are performed at lower temperature as the coatings may need to withstand stresses in cold climates. ASTM D522 describes a test method for the elongation of attached organic coatings with a conical mandrel apparatus. Mandrel bend tests give useful flexibility ratings. However, they are operated manually and, thus, strain rate is not precisely controlled. They are considered to be high strain rate tests for measuring crack resistance rating with approximately 1 second bending motion. In a conical mandrel bend test, the coated panel is bent 135° around the cone. The large end and small end of the cone will produce 3% and 30% elongation, respectively. The bend time is 15 seconds if the percent elongation is to be measured. Other flexibility tests are cylindrical mandrel bend tests, T-bend tests, cupping tests, and forming tests. Then, there are the impact resistance tests. A hemispherical indenter strikes the coated panel creating a dimple as shown in Figure 2.12. Tests can be performed either with coating facing the impact surface or with impact from the backside of the panel (reverse impact). Cracking of the coating around the dimple area determines the point of failure. ASTM D2794 describes the test method for resistance of organic coatings to the effects of rapid deformation (impact). For tensile tests, ASTM D2370 describes a test method for tensile properties of organic coatings. The sample is cut into a rectangular specimen. 10 replicates are used for each sample and the strain rate is 5-

100%/min. To minimize the grip effect, the dumbbell-shaped cutting dies for tensile tests from ASTM D412 (Vulcanized rubber and thermoplastic elastomer – Tension) and from ASTM D638 (Tensile properties of plastics) are used. For dumbbell specimens, a bench marker or a contact extensometer is used to monitor the strain on the straight narrow section.

2.2. Circular Free-film Indentation

It is crucial that we understand the definition of toughness in order to design a high-throughput measurement which can qualitatively rank toughness in coatings. The weight drop impact test has been used to characterize the toughness of polymer films on substrates. Tensile tests can also give toughness values which is the area under the stress-strain curve. It should be realized that these energy-absorbed methods give values that are geometry and size dependent and, thus, are not truly intrinsic material properties. The toughness concept has been reviewed from a fracture mechanics perspective, but the tests are time-consuming and involve high resource experimentation. An automated, high-throughput toughness evaluation instrument is developed based on the work done by Sormana.[18-22] The test apparatus is in the form of circular free-film indentation that deforms the film until rupture. Toughness and elastic modulus are important parameters in the design of coatings. Current methods used are conventional tensile test and impact test. These tests require a significant amount of time in specimen preparation (die cutting), sample handling, and testing time. Thus, the high-throughput instrument is being implemented in the combinatorial workflow in our laboratory that allows us to rank toughness and elasticity. Circular free-film puncturing can be easily automated because the film only needs to be clamped in the circular area and by not having to cut the specimen

into a specific shape. A specially designed 8 × 4 in. template was used to obtain free films. The instrumentation process included the design of components, programming and testing. Experiments were carried out to validate the use of the instrument with silicone elastomer and polyurethane libraries. Tear and tensile experiments are used for correlations.

2.2.1. High-throughput mechanical characterization of free-standing polymer films

The high-throughput mechanical characterization of free-standing polymer films was applied to gradient libraries by Sormana et al.[20, 22] There was a need to miniaturize the instrumentation to allow for rapid-serial mechanical testing since the size of their sample regions was a few millimeters in diameter on a continuous gradient library. It would be tedious and difficult to cut an individual sample to perform a tensile test. Thus, they chose to work with a falling-dart impact test where sample preparation can be much simpler. Figure 2.13 shows different techniques to introduce biaxial stresses on circular polymeric free-film.

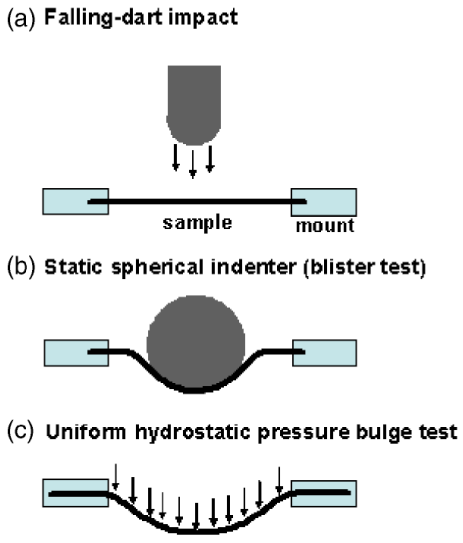

Figure 2.13. Different deformation methods on polymeric free-film (Reproduced from ref.[19])

The transverse loading normal to the film surface produces biaxial stresses. As shown in Figure 2.14, three components of biaxial stresses are radial, tangential and bending. There is also shear stress between indenter and film at large deformation.

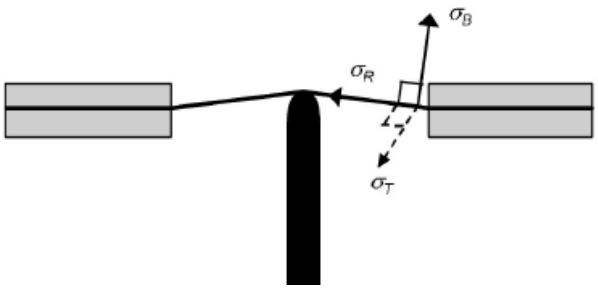

Figure 2.14. Three principle stresses as a result of indenting on free film (Reproduced from ref. [19])

The states of stresses are obviously more complicated than that in a simple tensile test. The instrument from Sormana et al. is shown in Figure 2.15. It can operate in two modes; impact and static. In the impact mode, the sample holder is dropped on to the indenter connected to the force sensor. The indenter and force sensor are rested on the x-y positioning stage in order to move to the free-film locations. Figure 2.16 shows the sample holder from Sormana's instrument. The polymer film was cured on a silicon wafer and they were immersed in water to release the gradient film from the silicon substrate. The holder consists of a 10×10 circular-hole grid with 3-mm diameter and 1-mm spacing between each hole. The indenters they used were 500 μm and 1.4 mm in diameter.

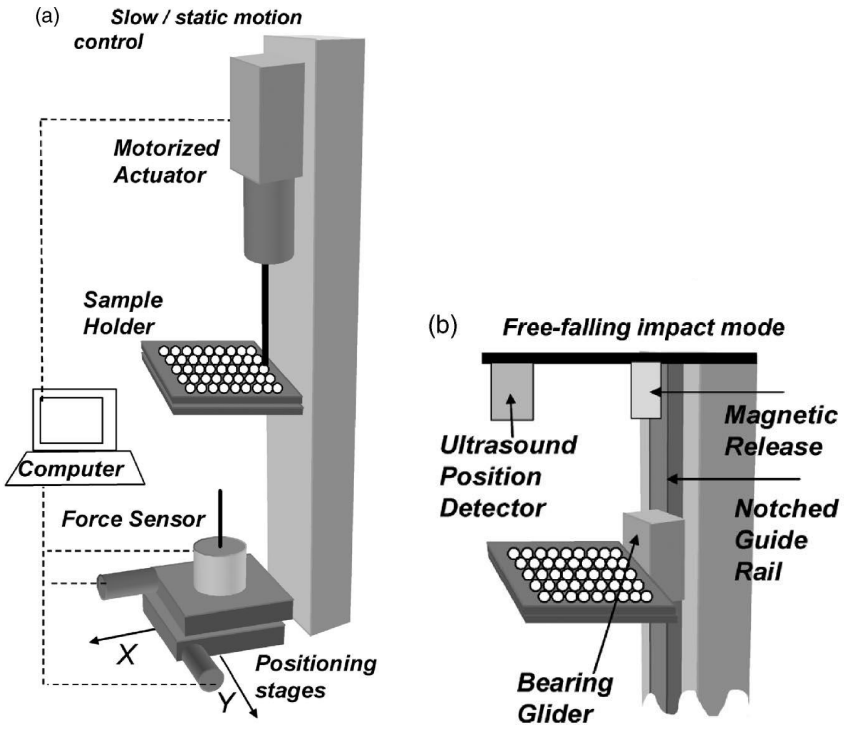

Figure 2.15. Quasi-static and impact modes of the instrument from Sormana (Reproduced from ref. [19])

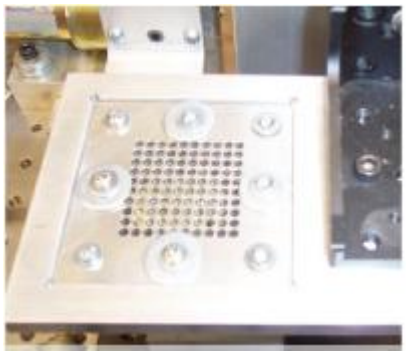

Figure 2.16. Sample grid isolating continuous gradient film into individual testing circular area (Reproduced from ref. [19])

Our combinatorial laboratory uses arrays of discrete samples. They are typically in either a 4×6 sample grid or a 4×3 sample grid, as shown in Figure 2.17. The 4×3 sample grid is on an 8 in. × 4 in. panel and has 1.5 in × 1.0 in. sample area for each of the 12 individual samples. The 4×6 grid plate is usually in the form of a stamped aluminum plate creating 24 wells for polymer samples to be dispensed using pipets. For the 4×3 grid plate,

polymer samples are either applied to metal panel with drawdown method or dispensed into a stamped aluminum plate with 12 wells.

Figure 2.17. 24-well aluminum panel (left) and an automated deposition of coatings with doctor blade on 8 in. × 4 in. panel (right) (Reproduced from ref.[23])

2.2.2. Obtaining free films

Polymeric coatings can be carefully removed from its substrate to obtain free film. Glass has lower surface energy and is also smoother than a metal panel, thus it is relatively easy to peel a coating off of glass. Care must be taken in handling the sample, so that no damage and plastic deformation can occur. Tedlar™ and Teflon™ substrates (Dupont) may also provide excellent release films, but the wetting of their surfaces by the coating can be an issue for some systems. After the film is released from the substrate, mounting and clamping the sample can induce stresses. Scott et al. obtain a circular free film by casting into a mold with a thick circular edge to eliminate the clamping effect. However, most coating formulations contain volatile components and mold casting method is also difficult to apply to the existing template size.

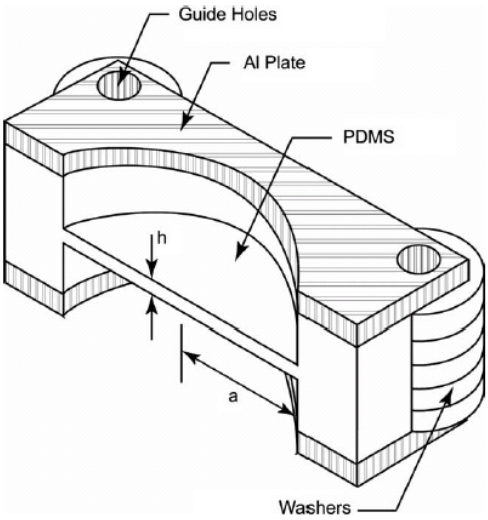

Figure 2.18. Silicone is casted in a mold into a circular thin film with thick edge to eliminate clamping stress on the film (Reproduced from ref.[24])

Maner et al. performed free-film indentation on a very thin film as shown in Figure 2.19.[25] The embedded fibers on the glass plate are etched away with a weak acid to create a circular film area with a supported edge.

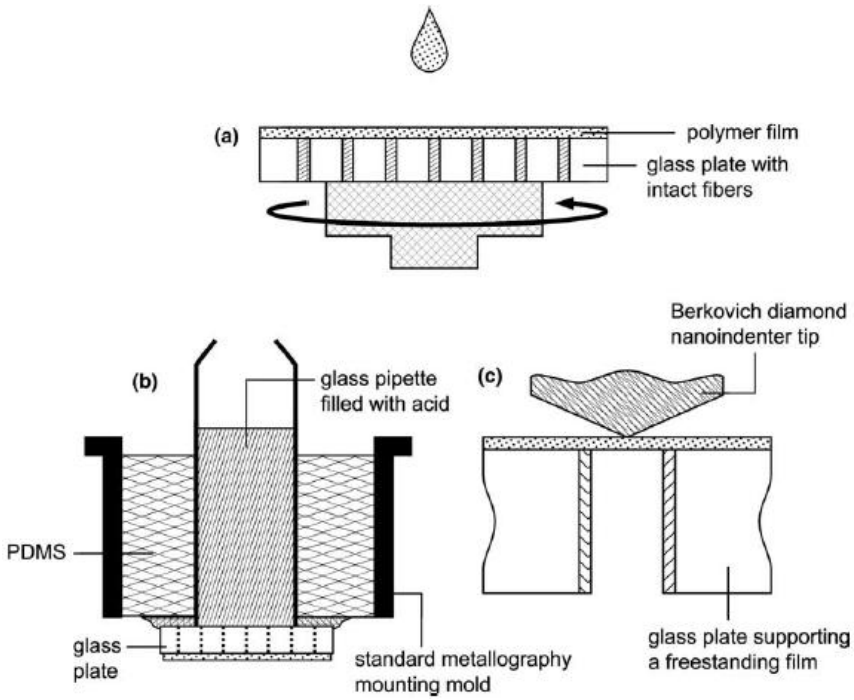

Figure 2.19. Free-film indentation on the etched plate; a) film deposition by spin coating, b) etching fibers with acid, and c) indentation (Reproduced from ref.[25])

Several concepts were tested to create a free-film discrete array. These experiments were performed in collaboration with James Bahr. One of the techniques was using a low melting point alloy as a metal template and, upon heating, the alloy was melted away and a free-film could be obtained. However, the residue of melted alloy adhered to the polymer surface and created a thin metallic film when cooled. Finally, a method was proposed using a cut polymer mesh as a support when the films were peeled off a Teflon substrate. The prepared meshing template and Teflon substrate are shown in Figure 2.20.

Figure 2.20. Free-film array template; Teflon substrate (left) and the circular-cut mesh on each of the 12 wells

The substrate consists of an adhesive backed Teflon film and aluminum panel. The backing is removed, attached to the aluminum and pressed to minimize areas of trapped air. A 5-mil, 10-mil, or 15-mil polyethylene film would is cut into the 8 in. × 4 in. and the inner film is removed creating 12 wells using a custom-made stamping blade. 3M Photo Mount™ spray adhesive is applied on to the cut polyethylene film and the 8 in. × 4 in. polypropylene mesh with thickness of 0.26 mm is attached. Another custom-design

stamping die is used to cut 0.5 in. diameter circular holes on the mesh. Then, 3M Photo Mount™ spray adhesive is applied on the mesh side where there is a polyethylene film underneath. A custom-made device is made to block the spray adhesive getting on the mesh where the coating would be applied. Figure 2.21 shows cross-sectional schematic layers of the free-film array template. The red colored layers represent the adhesive.

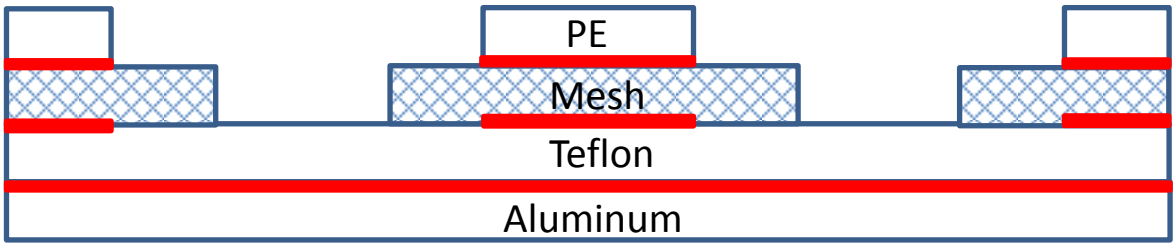

Figure 2.21. Schematic of the layers of free-film array template; the solid red colored layers represent thin adhesive layers.

The coating formulations are deposited in each well and when they are cured, the mesh with the PE template is peeled off from the Teflon substrate. The mesh provides the support for the film to be peeled off and 12 circular free-film regions are then obtained. This free-film template is relatively easy to make due to its simplicity. All 12 coatings can be peeled off at once which accelerates the film preparation process. Nonetheless, the template has a few issues regarding the film uniformity over the well area. There could be trapped air underneath the mesh when the polymer is dispensed into the well. Thus, the edges of the free-film area are prone to defects, especially if the bubbles are present at the edges. Also, thickness of the films is a function of wet film thickness, solids content and shrinkage, this implies that different thicknesses are to be expected among different formulations of coatings.

2.2.3. Prototype instrumentation

The measurements of load and displacement are required to perform the indentation test. A force transducer/load cell can be attached at the end of the indenter. For keeping track of the displacement, the actuator that drives the indenter itself can be recorded or a linear voltage displacement transducer can be used. The free film from Figure 2.18 from Scott et al. was fixed in place with the indenter shaft floating in an air bearing.[24] The positioning stage with a load cell pushes the end of the indenter shaft into the specimen.

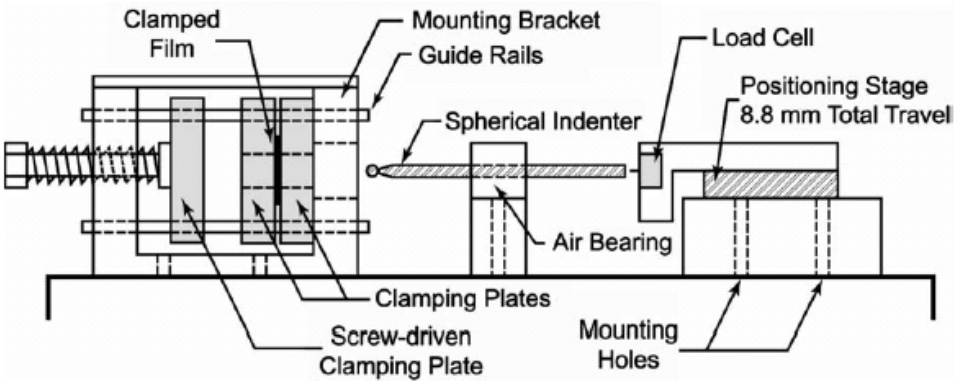

Figure 2.22. Schematic of testing system using air bearing (Reproduced from ref.[24])

The air bearing automatically aids in the centering and aligning of the indenter. The positioning stage is used to monitor the displacement. Figure 2.23 shows a similar system. The video camera can be used to match the displacement from the actuator and to monitor the adhesive force and the shape of film deformation.

It was desired to build a similar system to be used with the custom-designed free-film template. The task was simply to assemble two motorized linear stages and an actuator into a system capable of sweeping through the 6 in. × 4 in. free film array and performing indentation on each sample.

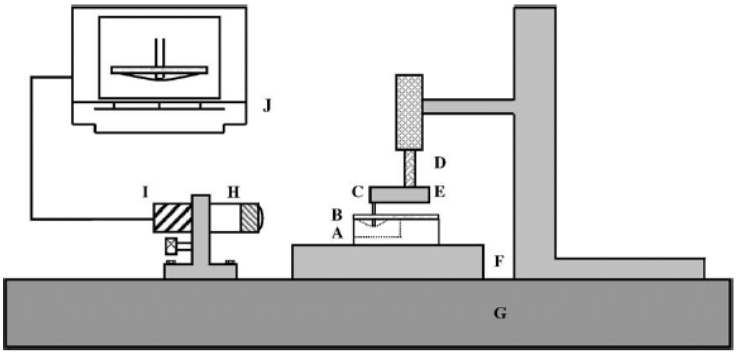

Figure 2.23. Schematic of free-film indentation from Ju et al.; The system consists of silicone sample (A), sample holder (B), cylindrical graphite indenter (C), actuator (D), force transducer (E), X-Y translation stage (F), isolator bench (G), camera system and acquisition (H, I, J). (Reproduced from ref.[26])

The moving stages, actuator and controller were purchased from Newport Corporation. The motorized linear stage was the ILS series high-performance mid-range travel linear stage with the resolution of 0.5 μm. For actuator, the LTA-HS Precision motorized actuator with 50-mm travel and the resolution of 0.035 μm was selected. The stages and actuator were connected to a ESP300 3-Axis motion controller/driver. Load cells were Model 31 miniature load cells from Honeywell International Inc. with various load capacities such as 10 lb, 50 lb, and 100 lb. An in-line amplifier, also from Honeywell, was used to amplify the voltage signal from the load sensor. The data acquisition was done was done using a NI PCI-6221 data acquisition card with LABVIEW software from National Instruments Corporation. The coordinate-measuring machine (CMM) probes distributed by McMaster-Carr were used as the indenters. They were made of steel balls glued to steel shafts with thread mounts. Custom-made parts were made to accommodate all the components. To connect the probe and the load cell, a cylindrical aluminum shaft was made as shown in Figure 2.24. The flatness of the top and bottom, and the perpendicularity of the thread hole were crucial because the steel ball needed to be at the center of the circular indentation hole as it is indenting the film. Another cylindrical shaft

was machined to link the actuator and the load cell with a male thread for the actuator and a female thread to connect the load cell. The diameter of this shaft needed to be small enough for when the actuator was retracted. The tolerances of top shaft were also very tight to allow reasonable centering of the probe during the test. The aluminum L-shape bracket was made to mount the actuator to the stand on the moving stages.

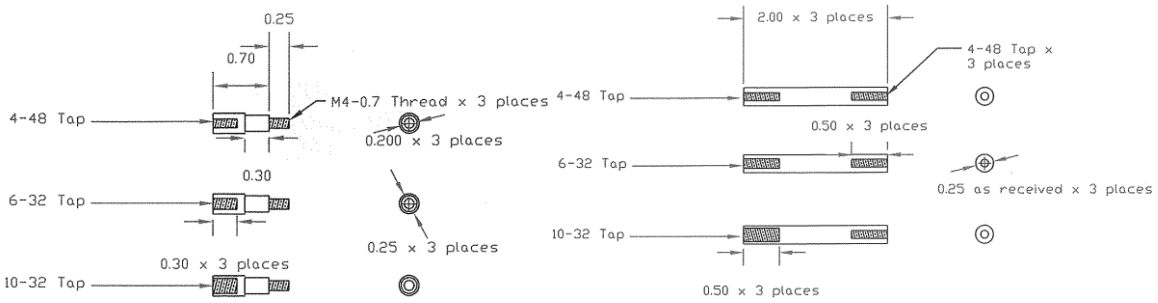

Figure 2.24. CNC machine parts providing connection between actuator, load cell and indenter. (Courtesy of James Bahr)

Figure 2.25 and Figure 2.26 show two of the designs that we could employ with the development tools we had. The first one has the indentation in vertical direction and the other one has the indentation in horizontal direction. The vertical set-up design was chosen based on the ease of implementation. Both of the designs are fundamentally the same. One of the differences is the anticipated machine compliances. In the vertical design, we need sufficient clearance for the indenter to reach the farthest column on the sample array. The horizontal design likely has lower machine compliance due to a much shorter beam used to mount the actuator. In the horizontal design, the film takes on its own weight which is assumed negligible. An air bearing, as in Figure 2.22, can also be implemented in the horizontal design. The free-film template is clamped between aluminum plates exposing the circular free-film areas as shown in Figure 2.27. Flat rubber washers are glued on the inside of the top plate to secure the template.

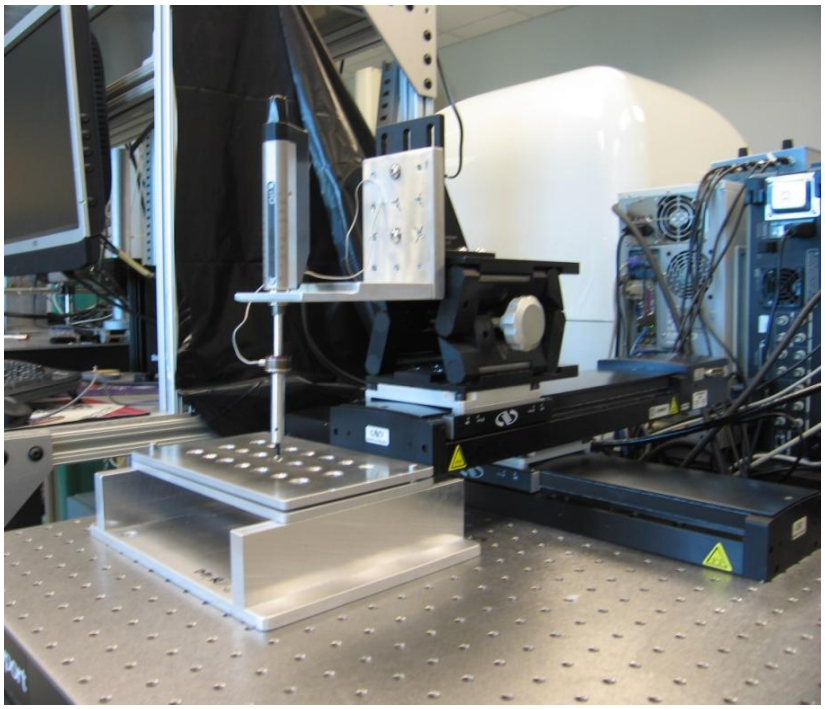

Figure 2.25. Vertical set-up indentation

Figure 2.26. Horizontal set-up indentation

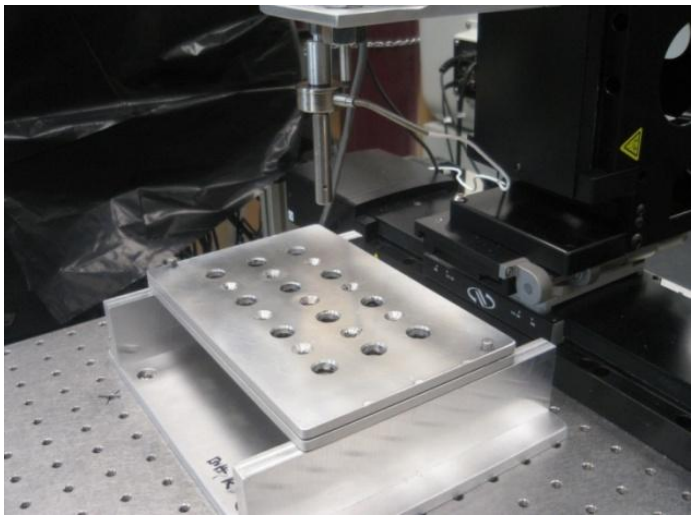

Figure 2.27. Sample holder with guided columns and screw holes

The load cells were calibrated with standard weights. Weights were placed on the load cell in compression. The output voltages were measured in LabVIEW™ by taking mean average of 1000 Hz sampling rate for 1 second. First, a shunt calibration on an amplifier was done in order to make the maximum load corresponds to the maximum voltage. For example, for the 10-lb load cell, the maximum load of +/-44.48 N (10 lbs.) was adjusted to +/-10 V; thus the expected factor was 4.448 N/V. Second, with standard weights, the calibration curves as in Figure 2.28 could be obtained yielding the slopes of -0.2253 V/N and -0.2249 V/N (or 4.438 N/V and 4.446 N/V) from the first and second runs, respectively. If the fit was done on data points with less than 0.2 N load, the result was 4.466 N/V. This only showed a slight non-linearity of the load cell.

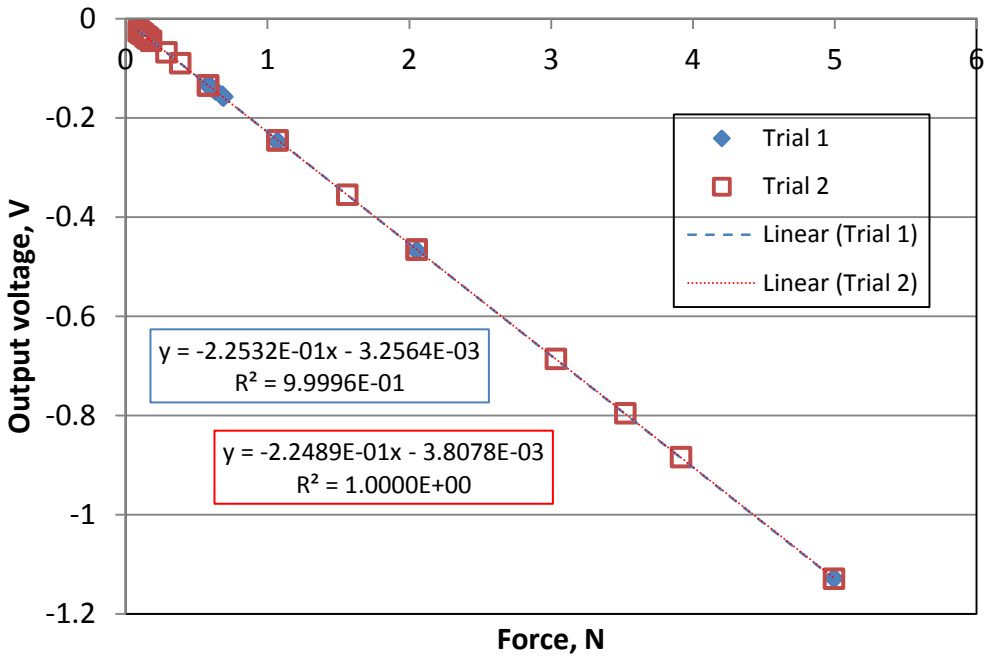

Figure 2.28. Calibration of a 10-lb load cell in compression loading

The calibration factor was then used in LabVIEW™ for load output calculation. In order to smooth the signal in the acquisition, a finite impulse response (FIR) filter (specifically, 4th order Butterworth) with a low-pass frequency of 4 Hz was used. The low-pass filter of 4 Hz would remove the 50 or 60 Hz AC noise when the signals were sampled at low rates. Figure 2.29 shows the filtered and unfiltered voltage signals as a function of indentation time on a silicone film with constant velocity. As the indenter approached the sample, the signal was being recorded as shown in the plateau on the left side of Figure 2.29. Then, the contact was made and the voltage changed drastically. The voltage kept decreasing as higher compressive load was being measured until the film broke and there was a sudden change in voltage. The low-pass filter greatly reduces noise in the signal. Nevertheless, care must be taken using the filter because the signal can be dampened to the point where the signal response behaves slowly to changes. Due to the weight of the

indenter and the shaft, an off-set voltage was measured for each of the specific configurations.

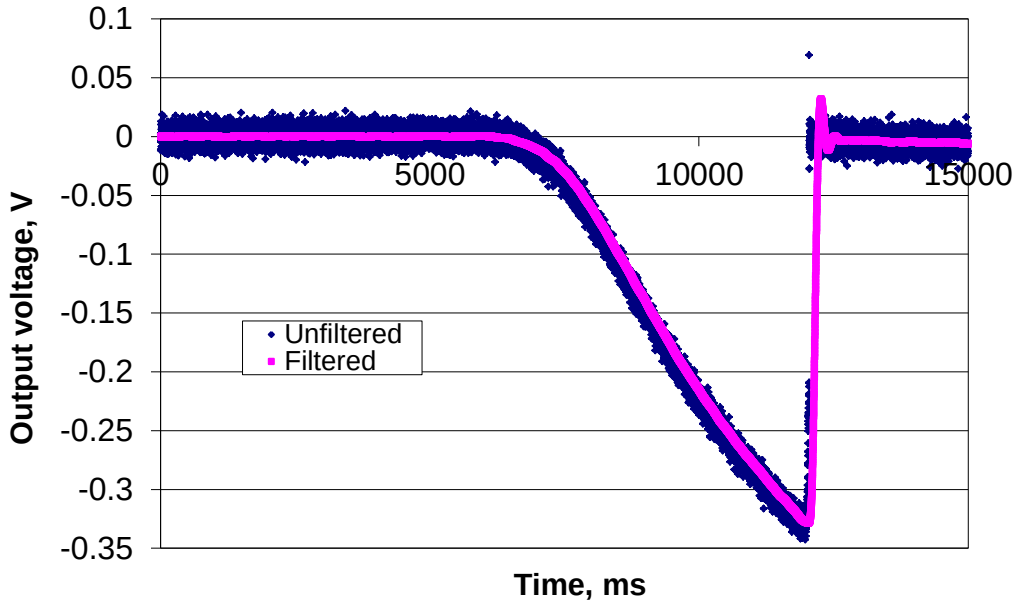

Figure 2.29. Test run with filtered and unfiltered signals

The final goal was to automate the instrument so that 12 samples could be run with one execution. A state logic diagram, in Figure 2.30, was written to specify the automatic control needed to run the test. It simply states the positioning and working in loops until the test is finished. Firstly, the required test parameters are needed. These are the scaling factors for different load cells, coating thicknesses, speed of the indenter, and offset voltage due to the weight of the indenter and fixture. Then, the actuator moves to the center of the circular hole and the indentation begins. It is important to the instrument to realize the situation during indentation to save computational and operational time, and to prevent damage to itself. Three conditions are specified as criteria for proceeding to the next state. Once the voltage limit is reached, the indenter needs to stop and withdraw. The actuator also has a traveling range limit. The instrument should also realize when the film ruptures. This is approximated by monitoring a significant and sudden load decrease.

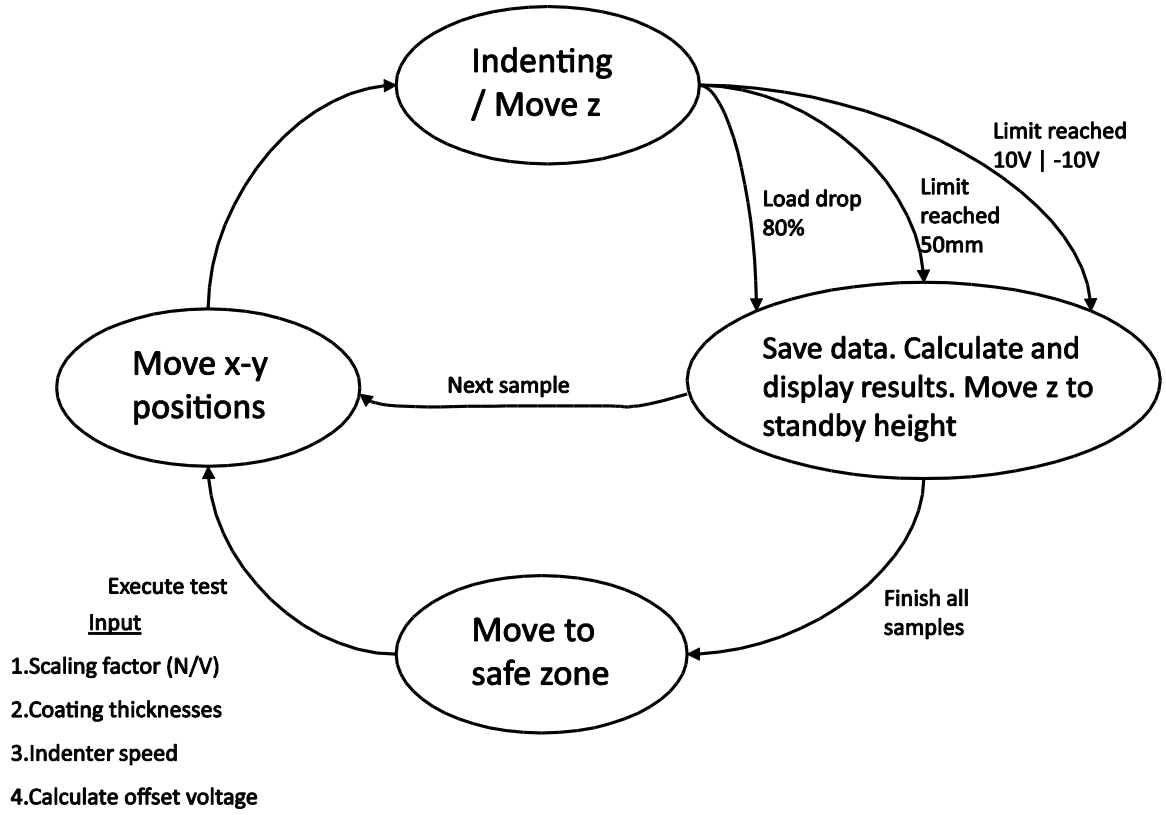

Figure 2.30. State logic diagram for high-throughput toughness measurement

2.3. Experimental and Results

2.3.1. Preliminary testing

In a preliminary experiment, silicone films were tested using the free-film indentation system and the conventional tensile and tear tests. Six different coatings were tested. Three of them were unfilled silicone rubber with different vinyl terminated PDMS (DMS-V05, DMS-V21 and DMS-V35) from Gelest, Inc. The crosslink densities were varied by using different molecular weight of PDMS and thus physical properties such as modulus and toughness were varied. These were relatively weak coatings and could be torn quite easily. The composition DMS-V05 was extremely brittle. The other three coatings were commercial products: Intersleek 425, RTV-11, and Silastic T2. Intersleek 425 is a commercial marine coating from International Paint. RTV-11, silicone rubber

compound is a general purpose two part silicone elastomer from GE Silicones. Silastic T2 is a translucent high strength silicone moldmaking rubber from Dow Corning. Each formulation was mixed and cast on to two circular free-film templates and two Teflon plates (to obtain free film for tensile and tear tests).

In the tensile test, a dumbbell-shape specimen was cut using ASTM D412 Die D cutting tool. The strain rate of 0.1/s (or 10%/s) was chosen. The effective gauge length is used because neither strain gauge nor image acquisition technique was used to observe the changes in length in the straight section of the dumbbell. The appendix shows the effective gauge length calculation. The effective gauge length was calculated to be 45.9 mm, thus the clamping jaws were separated at 4.59 mm/s to obtain the specified strain rate. Young's modulus was calculated by linear regression of the data between strains of 0% to 10%. Toughness from tensile test was calculated from the area under the stress-strain curve.

In free-film indentation, the stress-strain calculation followed the approximation from Sormana et al.[19] Basically, a Pythagorean theorem is used to calculate the amount of radial elongation with respect to the indenter displacement assuming it is a point load and the film is linear (straight). Figure 2.31 shows the schematic of the deformation when the force F_z is applied to film with radius a. The indenter displaces by an amount of z.

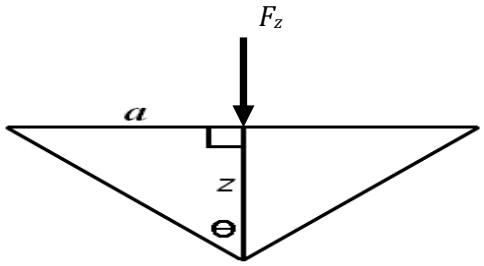

Figure 2.31. Approximation of linear film stretching under point load at low strain

The force in the radial direction is represented by F_r. θ represents the angle shown in Figure 2.31. h is the thickness of the film. Here, stress and strain calculations are stated to be operational definitions of stress-strain which imply that they only are for comparison purposes because of their extreme simplicity in the assumptions. They can be calculated as follows:

$$F_r = \frac{F_Z}{\cos\theta}$$

$$\cos\theta = \frac{z}{\sqrt{z^2 + a^2}}$$

$$\sigma = \frac{F_r}{2\pi a h} = \frac{F_Z}{2\pi a h}\frac{\sqrt{z^2 + a^2}}{z} \tag{2.20}$$

$$\varepsilon = \frac{\sqrt{z^2 + a^2} - a}{a} \tag{2.21}$$

The area under the stress-strain can then be defined as:

$$\int \sigma \, d\varepsilon = \int \frac{F_Z}{2\pi a h}\frac{\sqrt{z^2 + a^2}}{z} d\left(\frac{\sqrt{z^2 + a^2} - a}{a}\right) \tag{2.22}$$

$$= \frac{1}{2\pi a^2 h}\int F_Z dz$$

From this approximation, it shows in eq. (2.22) that the stress-strain integral is equal to the force-displacement integral divided by $2\pi a^2 h$. The only changing variable is the thickness, *h*, and the rest is constant. Thus, comparing the breaking energy among the films requires integration of force-displacement curve divided by the thickness and there would be no need for stress-strain calculation. Keeping in mind that stress-strain calculation shown here is a crude approximation and will only work at low strain because the non-linearity of the film geometry as the test progresses, this approximation was

performed assuming point load and only pure stretching in the radial direction. Then, the strain rate of 0.1/s of tensile test can be matched to the indenter speed for free-film indentation. This gives the indenter speed of 2.546 mm/s. In reality with better strain description, the strain rate will change as a function of displacement when the indentation speed is held constant.

With constant speed, the indenter displacement is easily calculated from the indentation time. The indenter diameter was 1.57 mm in this preliminary work. Figure 2.32 shows the force versus time indentation data on Intersleek 425. The force rapidly rises as the contact is made and breaks very quickly, after only less than 10 mm indenter displacement. Using Eq. 2.20 and 2.21, the stress-strain curve is shown in Figure 2.33.

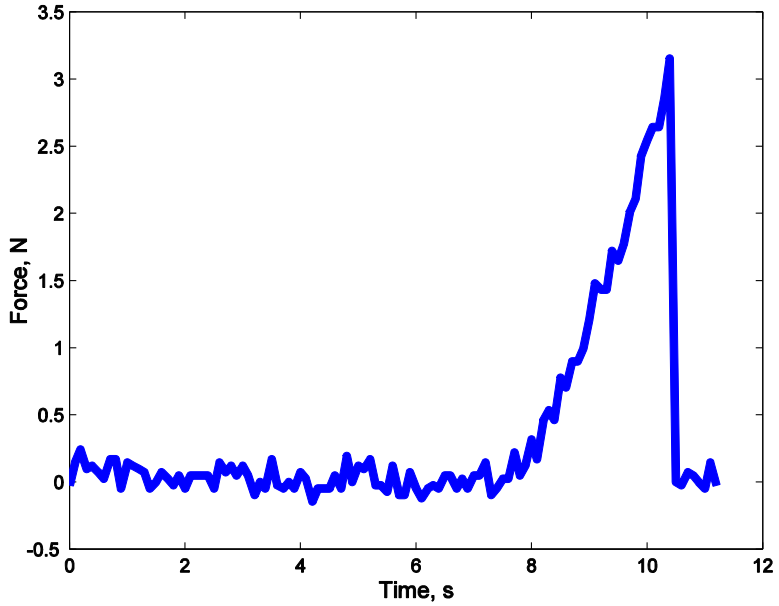

Figure 2.32. Force vs time/displacement (without digital filter) from free-film indentation on Intersleek 425

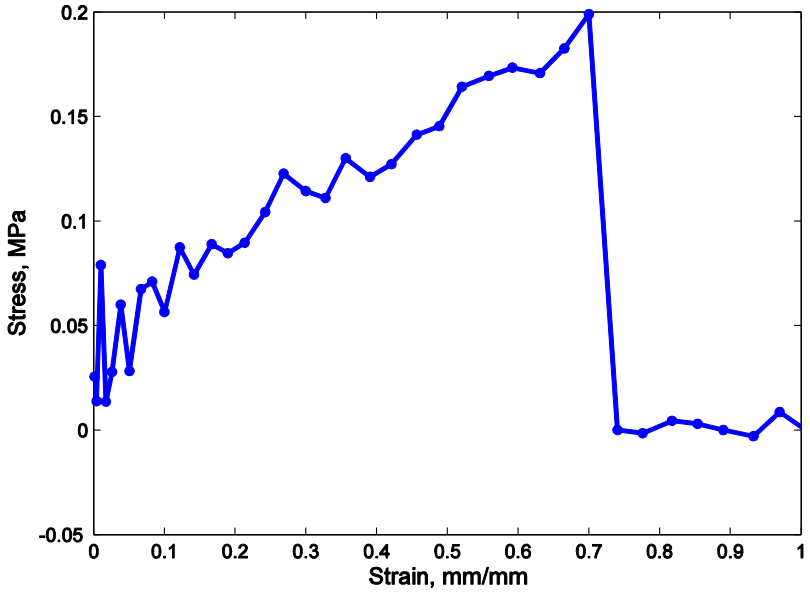

Figure 2.33. Stress-strain curve from free-film indentation on Intersleek 425

The trouser sample was used for this tearing experiment. Tear strength was calculated from the load that causes catastrophic tear divided by the thickness of a specimen. ASTM D624, a standard test method for tear strength of conventional vulcanized rubber and thermoplastic elastomers, was used as a guideline. Each sample had five replicates.

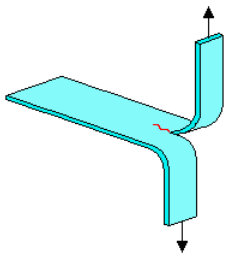

Figure 2.34. Trouser tear specimen (Reproduced from ref.[27])

Table 2.1 shows the results of six coatings. All three tests showed the same monotonic increase. The monotonic behavior is shown in Figure 2.35 and 2.36. It was an acceptable result and showed that our high-throughput toughness measurement set-up can potentially be a success as a screening tool.

Table 2.1. Comparison of energy to break from different methods

Sample	Puncture energy (kJ/m^3)	Tear Strength (N/m)	Toughness from tensile test (kJ/m^3)	Modulus from tensile test (MPa)
Unfilled V05	34.5 +/- 3.3	55.2 +/- 5.55	51.5 +/- 6.58	2.49 +/- 0.11
Unfilled V21	56.2 +/- 37.7	120 +/- 26.1	156 +/- 64.0	1.05 +/- 0.06
Unfilled V35	99.8 +/- 20.5	175 +/- 21.8	865 +/- 92.0	0.546 +/- 0.060
Intersleek 425	227 +/- 45.6	524 +/- 4.97	1510 +/- 488	1.13 +/- 0.12
RTV11	486 +/- 101	609 +/- 6.35	3050 +/- 335	1.10 +/- 0.04
T2 Silastic	1960 +/- 294	13300 +/- 3050	10500 +/- 470	1.60 +/- 0.06

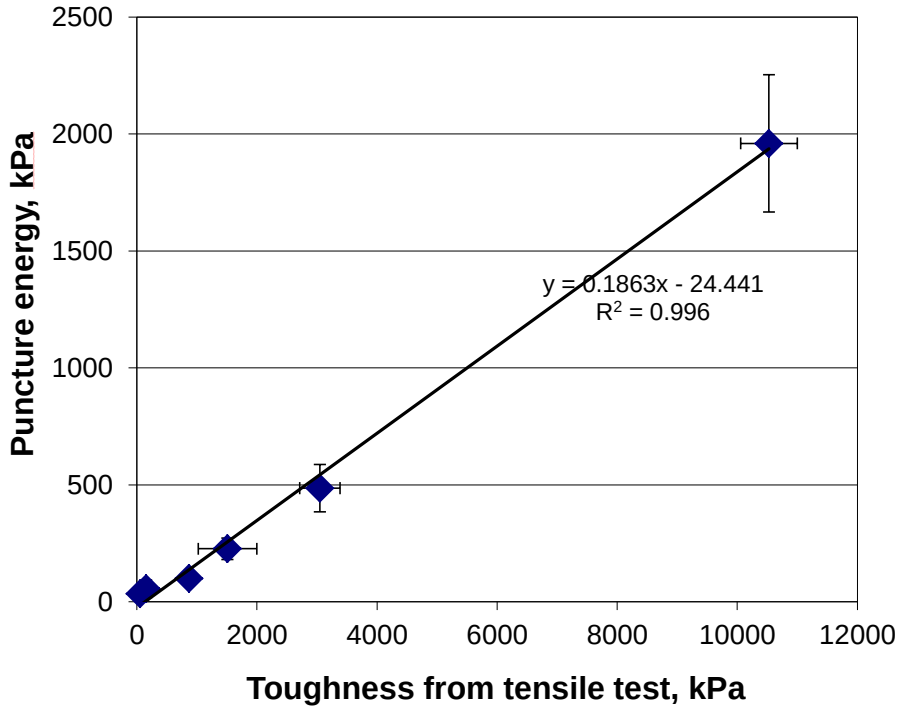

Figure 2.35. Puncture energy vs. toughness from tensile test

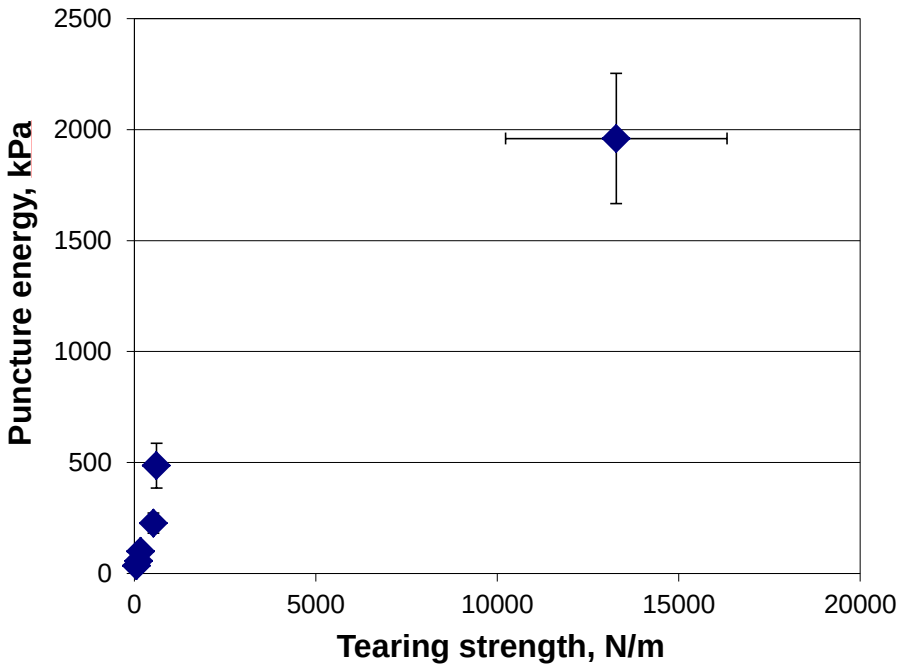

Figure 2.36. Puncture energy vs. tearing strength

2.3.2. Issues and possible improvements

It can be concluded that the puncture energy and toughness from tensile test are linearly correlated with the presented experimental procedure, according to the previous section. The spherical indenter diameter of 1.57 mm was used. It raised an interesting question whether with the smaller indenter, it could be more of a piercing action instead of largely stretching and thus it would correlate with the tearing test better due to areas of stress concentration. The selection of indenter size was limited by the range of actuator travel that would be enough to break the film. Also, the edges of the circular mesh are stress concentration areas. When the polymer solution is dispensed on the free-film template, a dried film normally takes the shape shown in Figure 2.37. The mesh has a thickness of 0.26 mm and when the dried film is thinner, the edge is raised and the mesh

fiber can be protruding from the polymer. Thus, the film can be uneven, and it can contain weak and stress concentration regions due to how it is made.

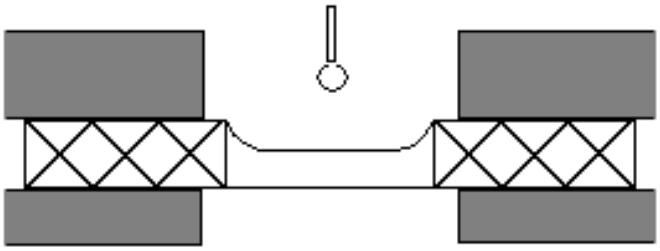

Figure 2.37. Schematic of a cross-sectional view of a clamped circular free-film suspended on a mesh

In Figure 2.37, the sample is clamped with the clamp resting on the film area supported by the mesh. Figure 2.38 shows a dried film thicker than the mesh being clamped.

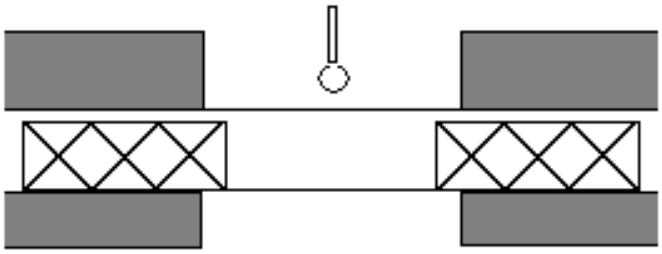

Figure 2.38. Schematic of a cross-sectional view of a clamped circular free-film suspended on a mesh when the film is thicker than the mesh

Figure 2.38 shows a seemingly more uniform film when the dried film is thicker than the 0.26-mm mesh support. Thus, care must be taken so that the thicknesses of dried films in the study have consistency. Clamping pressure is another parameter which needs to be consistent among samples. The mesh naturally acts as the clamping edges as the material is stiffer because of the reinforcement from the mesh. Excess clamping pressure will squeeze the material underneath the clamp and flex the free film. The clamping plates are two aluminum plates with the top plate containing flat rubber O-rings to press over the

mesh area. Thus, the clamping pressure on each well could be slightly different if the films on the wells are at different thicknesses. Thus, film uniformity, clamping pressure, centering of the indenter, and locating the point of contact can contribute to some errors in the measurements.

Figure 2.39 shows the raw data of puncture test using different indenter speeds (0.1 mm/sec and 1 mm/sec). They are the same coatings with similar thicknesses, the responses were quite different. It shows that the slope of the force-displacement curve may not directly relate to the Young's modulus .

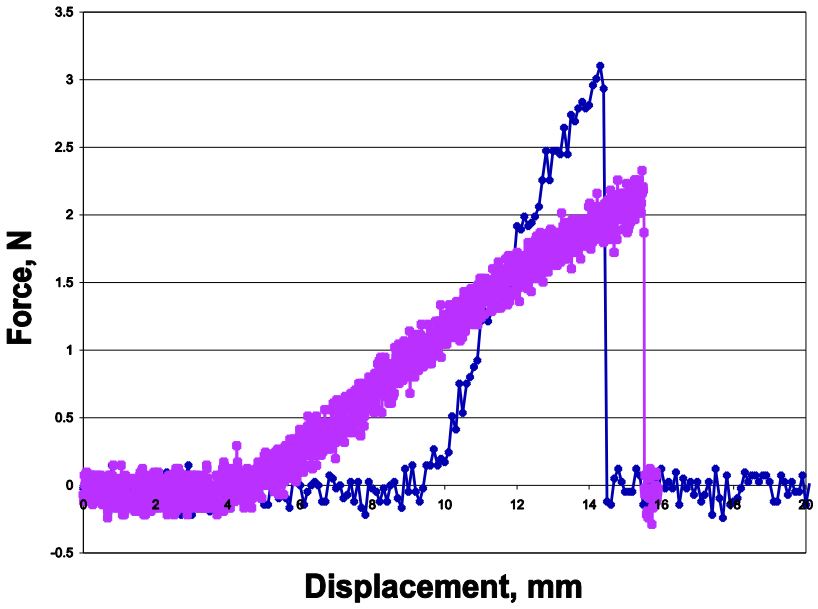

Figure 2.39. The effect of puncturing speed

Lubrication between the indenter and the film has a great effect. The maximum load usually reached is higher without lubrication than with lubricant. It means that the location of failure can be different and we should ensure that failure occurs at the vicinity of the tip of the indenter. For highly stretchable films, failure usually occurs at the circular edge between contact and non-contact parts of the film. As a result, a tiny circular piece of film popped out due to higher stresses near the edge of contact and not at the tip of the

blunt hemispherical indenter. A silicone fluid, trimethylsiloxy-terminated PDMS with MW of 3,780 and viscosity of 50 cSt was used in the previous experiment. Care must be taken so that the lubricant would not plasticize the coatings when they were tested. Also, the selection of load cells dictates the resolution the data, thus load cell should be changed depending on the expected load of the coatings in the study.

2.3.3. Combinatorial study on antifouling/fouling release coatings containing quaternary ammonium salt groups

Polysiloxane antimicrobial coatings having tethered quaternary ammonium salt (QAS) groups were studied at CNSE.[28-30] Coatings were tailored to have low surface energy and antimicrobial properties, but they were macroscopically weak. The reason was because the quaternary ammonium compound does not mix well with the polysiloxane which resulted in inhomogeneity. Nevertheless, the studies were performed to assess the degree of differentiation from free-film indentation experiments. Fouling release properties and contact angles were measured to study surface properties. One of the studies performed by Majumdar et al. was to enhance mechanical properties of coatings using silica filler.[30] Another study was done to observe effect of the molecular weight of the oil. The library consisted of 36 coatings with varying oil type, crosslinking type, oil amount and filler amount. This library was then used for high-throughput toughness analysis as it represented an actual research problem. The crosslinking reaction scheme is shown in Figure 2.40. The silanol-terminated PDMS had a molecular weight of 49,000 g/mol. Quaternary ammonium salt compound was octadecyldimethyl (3-trimethoxysilylpropyl) ammoniumchloride. n-octadecyltrimethoxysilane was used as a control crosslinker (C18 crosslinker) to compare to those with QAS. Different kinds and amounts of oil were variables, as shown in Figure

2.41, and two different loadings of filler were 10wt% and 20wt%. Thus, there were 24 coatings plus 2 controls without any oil. The other ten formulations used C18 crosslinker instead of QAS. The formulations are shown in Table 2.2.

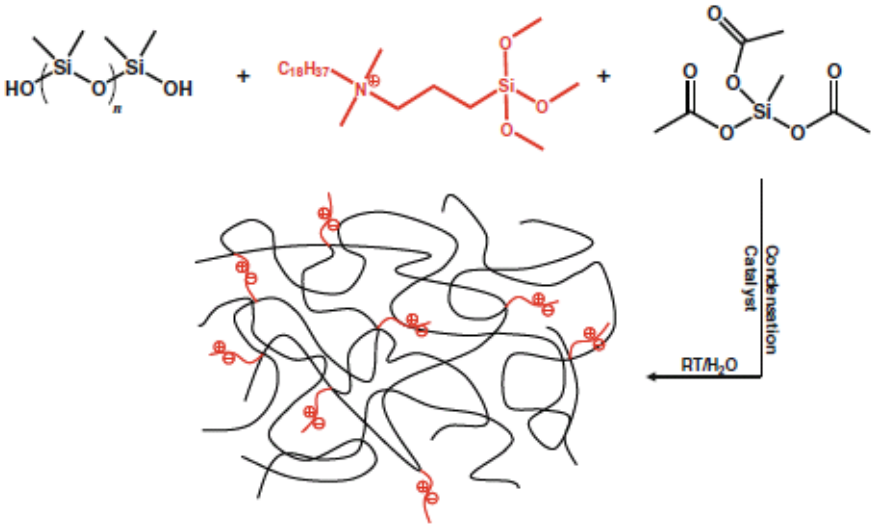

Figure 2.40. Crosslink network formed by condensation of silanol groups (Reproduced from ref.[30])

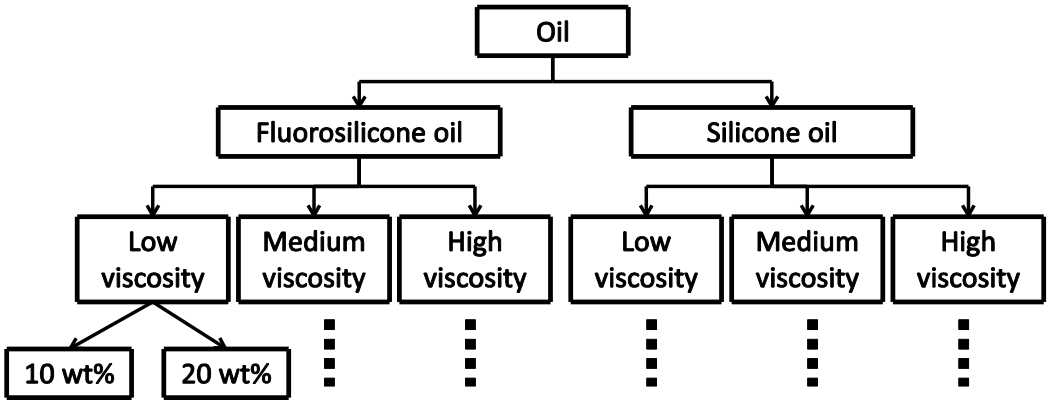

Figure 2.41. Diagram showing variables in the formulations

All silicone compounds were supplied by Gelest Inc. Fluorosilicone oils were FMS-123, FMS-131, and FMS-141 with the following viscosity and molecular weight; 300-350 cSt. (MW=2400), 1000 cSt. (MW=4600), and 10000 cSt. (MW=14,000), respectively. Silicone oils were DMS-T23, DMS-T31, and DMS-T41 with the following viscosity and

molecular weight; 350 cSt. (MW=13650), 1000 cSt. (MW=28000), and 10000 cSt. (MW=62700), respectively.

Here, the focus was on the mechanical properties of the coatings, particularly to test the high-throughput toughness analysis system. Majumdar et al. compared 4 PDMS coatings.[30] The first two have QAS with no filler and 20% silica filler. The other two have C18 with no filler and 20% silica filler. The result from tensile test is shown in Figure 2.42. It was concluded that PDMS-QAS has lower strength and toughness than PDMS-C18 which is inconsistent with results from others for elastomeric ionomers. The strength and toughness normally increase because ionic aggregates inhibit polymer chains sliding and increase entanglement during deformation.

The addition of silica to PDMS-QAS significantly increases the modulus, strength, and toughness, as compared to PDMS-C18 where the toughness actually decreases with the addition of silica. Thus, it is an indication that the QAS groups provide "an enhancement in interfacial adhesion between the polymer matrix and silica particles."[30] The PDMS-QAS library presented here would further examine the QAS effect on polysiloxane and the effect of oil on mechanical properties. Tensile test, tear test, and puncture test were used because it was, again, desirable to validate the puncture test high-throughput method. Accordingly, the puncture results were compared against other conventional tests for elastomers. For the tear test, the specimens were cut using an ASTM D624 Die C, as shown in Figure 2.43. Previously, the trouser tear specimens were cut manually with a razor blade in the preliminary study, thus this cutting die for tear test should provide better consistency. A 68 mm grip separation was chosen with a grip separation speed of 500 mm/min.

Table 2.2. Polysiloxane containing QAS formulations

Coating	Description	PDMS (g)	C18 Crosslinker (g)	Quat Salt (g)	Catalyst (g)	Crosslinker (g)	Silica Filler (g)	Oil Type	Oil Amount (g)	Toluene
323-171-1	PDMS-QAS-20% Filler (control)	30	x	4.965	9	7.5	6	x	x	30
323-171-2	PDMS-QAS-20% Filler-non fluoro-low vis 20%	30	x	4.965	9	7.5	6	DMS T23	6	30
323-171-3	PDMS-QAS-20% Filler-non fluoro-low vis 10%	30	x	4.965	9	7.5	6	DMS T23	3	30
323-171-4	PDMS-QAS-20% Filler-non fluoro-mid vis 20%	30	x	4.965	9	7.5	6	DMS T31	6	30
323-171-5	PDMS-QAS-20% Filler-non fluoro-mid vis 10%	30	x	4.965	9	7.5	6	DMS T31	3	30
323-171-6	PDMS-QAS-20% Filler-non fluoro-high vis 20%	30	x	4.965	9	7.5	6	DMS T41	6	30
323-171-7	PDMS-QAS-20% Filler-non fluoro-high vis 10%	30	x	4.965	9	7.5	6	DMS T41	3	30
323-171-8	PDMS-QAS-20% Filler- fluoro-low vis 20%	30	x	4.965	9	7.5	6	FMS-123	6	30
323-171-9	PDMS-QAS-20% Filler- fluoro-low vis 10%	30	x	4.965	9	7.5	6	FMS-123	3	30
323-171-10	PDMS-QAS-20% Filler- fluoro-mid vis 20%	30	x	4.965	9	7.5	6	FMS-131	6	30
323-171-11	PDMS-QAS-20% Filler- fluoro-mid vis 10%	30	x	4.965	9	7.5	6	FMS-131	3	30
323-171-12	PDMS-QAS-20% Filler- fluoro-high vis 20%	30	x	4.965	9	7.5	6	FMS-141	6	30
323-171-13	PDMS-QAS-20% Filler- fluoro-high vis 10%	30	x	4.965	9	7.5	6	FMS-141	3	30
323-171-14	PDMS-QAS-10% Filler (control)	30	x	4.965	9	7.5	3	x	x	15
323-171-15	PDMS-QAS-10% Filler-non fluoro-low vis 20%	30	x	4.965	9	7.5	3	DMS T23	6	15
323-171-16	PDMS-QAS-10% Filler-non fluoro-low vis 10%	30	x	4.965	9	7.5	3	DMS T23	3	15
323-171-17	PDMS-QAS-10% Filler-non fluoro-mid vis 20%	30	x	4.965	9	7.5	3	DMS T31	6	15
323-171-18	PDMS-QAS-10% Filler-non fluoro-mid vis 10%	30	x	4.965	9	7.5	3	DMS T31	3	15
323-171-19	PDMS-QAS-10% Filler-non fluoro-high vis 20%	30	x	4.965	9	7.5	3	DMS T41	6	15
323-171-20	PDMS-QAS-10% Filler-non fluoro-high vis 10%	30	x	4.965	9	7.5	3	DMS T41	3	15
323-171-21	PDMS-QAS-10% Filler- fluoro-low vis 20%	30	x	4.965	9	7.5	3	FMS-123	6	15
323-171-22	PDMS-QAS-10% Filler- fluoro-low vis 10%	30	x	4.965	9	7.5	3	FMS-123	3	15
323-171-23	PDMS-QAS-10% Filler- fluoro-mid vis 20%	30	x	4.965	9	7.5	3	FMS-131	6	15
323-171-24	PDMS-QAS-10% Filler- fluoro-mid vis 10%	30	x	4.965	9	7.5	3	FMS-131	3	15
323-171-25	PDMS-QAS-10% Filler- fluoro-high vis 20%	30	x	4.965	9	7.5	3	FMS-141	6	15
323-171-26	PDMS-QAS-10% Filler- fluoro-high vis 10%	30	x	4.965	9	7.5	3	FMS-141	3	15
323-171-27	PDMS-No QAS-20% Filler-non fluoro-high vis 20%	30	2.248	x	9	7.5	6	DMS T31	6	30
323-171-28	PDMS-No QAS-20% Filler-non fluoro-low vis 20%	30	2.248	x	9	7.5	6	DMS T23	6	30
323-171-29	PDMS-No QAS-20% Filler- fluoro-high vis 20%	30	2.248	x	9	7.5	6	FMS 141	6	30
323-171-30	PDMS-No QAS-20% Filler- fluoro-low vis 20%	30	2.248	x	9	7.5	6	FMS 123	6	30
323-171-31	PDMS-No QAS-10% Filler-non fluoro-high vis 20%	30	2.248	x	9	7.5	3	DMS T31	6	15
323-171-32	PDMS-No QAS-10% Filler-non fluoro-low vis 20%	30	2.248	x	9	7.5	3	DMS T23	6	15
323-171-33	PDMS-No QAS-10% Filler- fluoro-high vis 20%	30	2.248	x	9	7.5	3	FMS 141	6	15
323-171-34	PDMS-No QAS-10% Filler- fluoro-low vis 20%	30	2.248	x	9	7.5	3	FMS 123	6	15
323-171-35	PDMS-No QAS- 10% Filler-no oil	30	2.248	x	9	7.5	3	x	x	15
323-171-36	PDMS No QAS-20% Filler-no oil	30	2.248	x	9	7.5	6	x	x	30

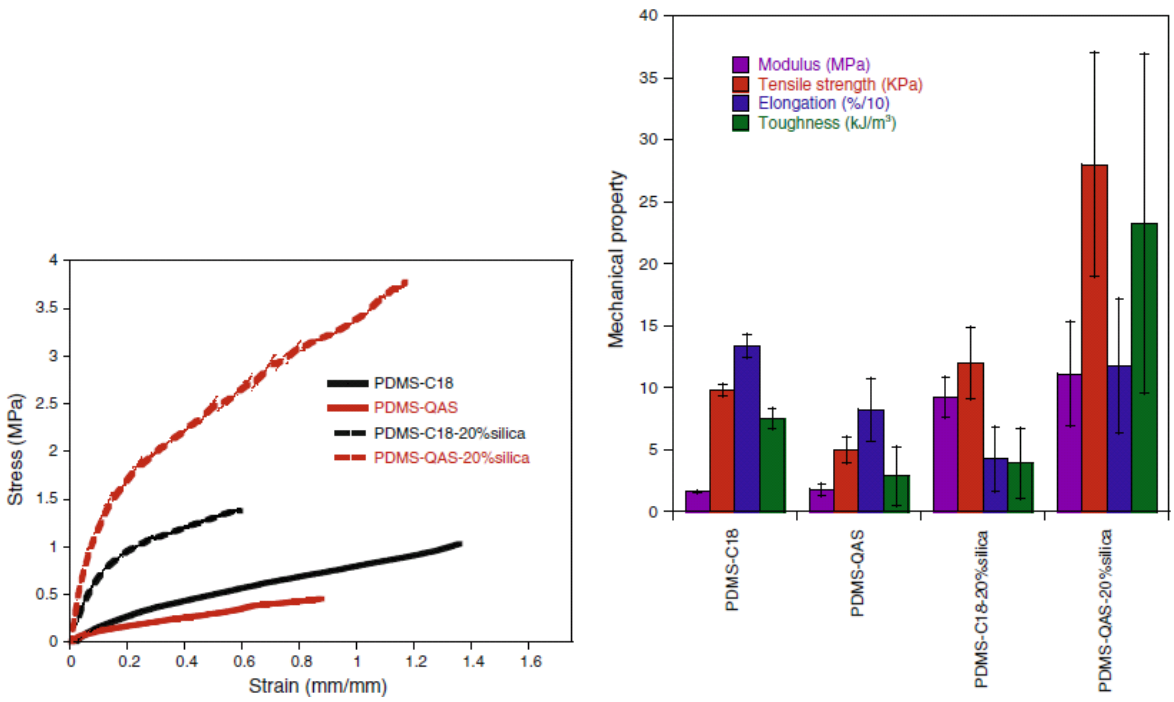

Figure 2.42. Results from tensile test; stress-strain curves (left) and the associated measurements (right) (Reproduced from ref.[30])

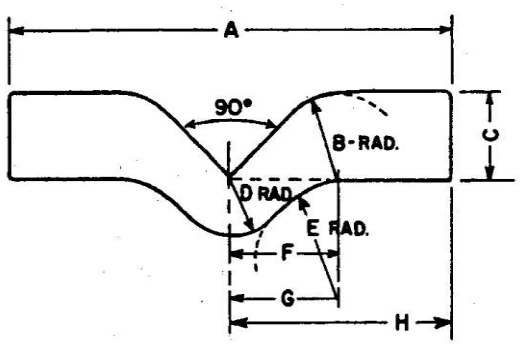

Figure 2.43. ASTM D624-00 Die C tensile test

Thickness was measured in the center where the tear will initiate (at the sharp notch). Tear strength was calculated by dividing maximum force to break the specimen with thickness. ASTM D624 called for ~2 mm thick sample, but thicknesses of coatings were in the 100 µm range. They asked for reporting the median from 3 or 5 replicates. Median average was used because the specimen possibly could be sensitive to nicks and imperfections from cutting and material itself. For all experiments, 5 replicates on each

formulation were made. From the results of the tear test, the median and the mean average were similar, thus mean average and standard deviation (1σ) was used for comparison purposes. Toughness from the puncture test was calculated using the area under the force-displacement divided by the thickness. From Table 2.2, the puncture data for sample# 22, 27, 29 and 36 could not be obtained because the coatings were sticking to the Teflon substrate and cracked when being peeled off. There was no tensile data for sample #27 through #30 and sample #34 because of the same problem. All samples were available for the tear test. Sample #27 through #36, which used C18 crosslinker instead of QAS, became very brittle, thus the samples could crack during free-film preparation.

Comparison between toughness from the puncture test and conventional tests are shown in Figure 2.44 and 2.45.

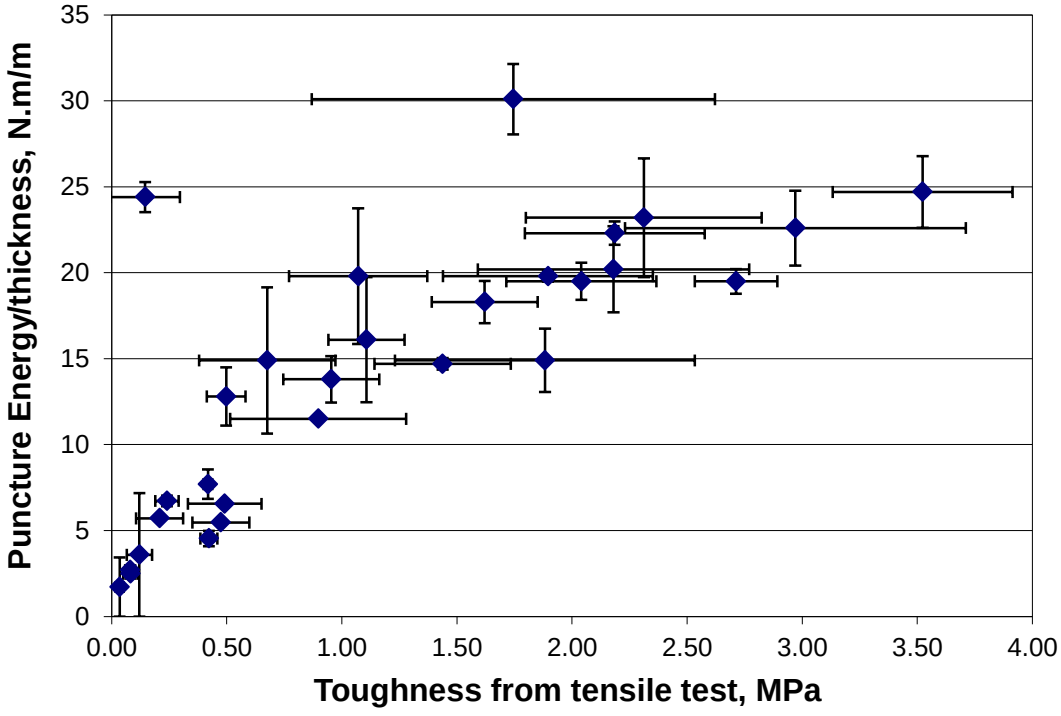

Figure 2.44. Puncture energy vs. toughness from tensile test: a linear regression gives R^2 = 0.60.

A linear correlation can be observed as expected in both figures. These samples had a lot of imperfections which could contribute to a scattered nature of the correlation. Some samples did not have good cohesive strength and they also showed phase separations which the top layer was brittle and cracked as it cured, but the bottom layer was flexible and tacky. Another observation from Figure 2.44 is that, within the ranges of measurement, the standard deviations from the puncture results were lower than the standard deviations from tensile results. This could be a consequence of selective failure area underneath the indenter whereas the failures in tensile tests were more random depending on the location of imperfections.

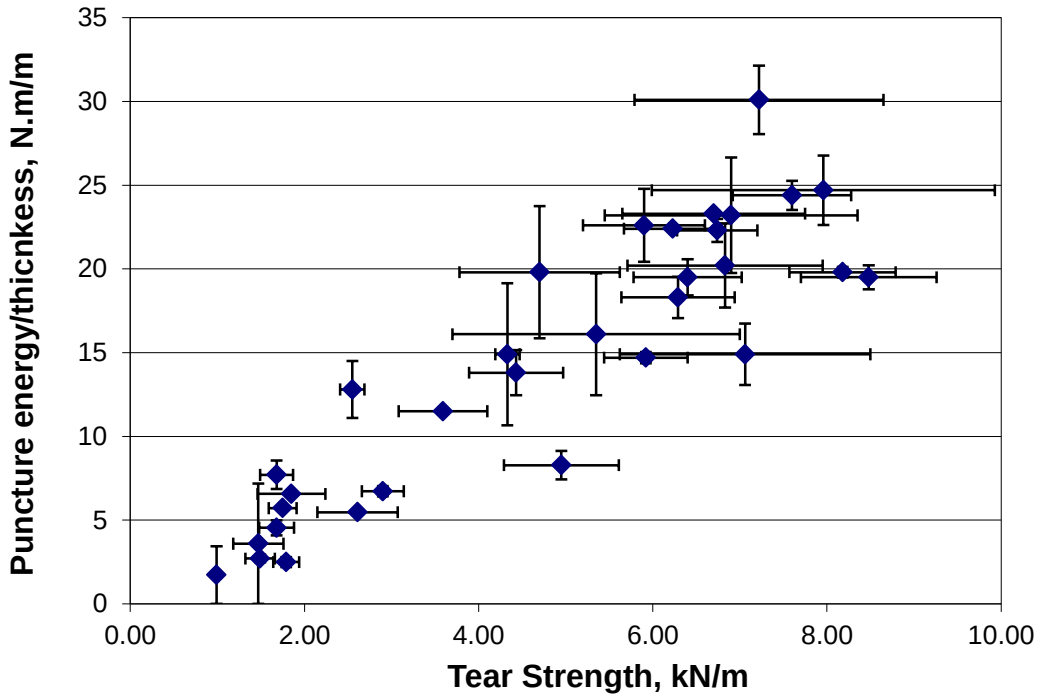

Figure 2.45. Puncture energy vs. tear strength: a linear regression gives $R^2 = 0.81$.

The results implied that the puncture test can give similar toughness trend as compared to tensile and tear tests. The trend illustrates that the presented high-throughput toughness test can be a valid ranking tool for combinatorial study.

Next, the effect of oil, filler amount, and QAS on mechanical properties can be observed using the following scatter plots. Figure 2.46 shows the effect of oil viscosity, oil type, oil wt% and filler wt% on toughness measured from puncture test. The data points on scatter plots with zero value imply that the data are not available on particular coatings.

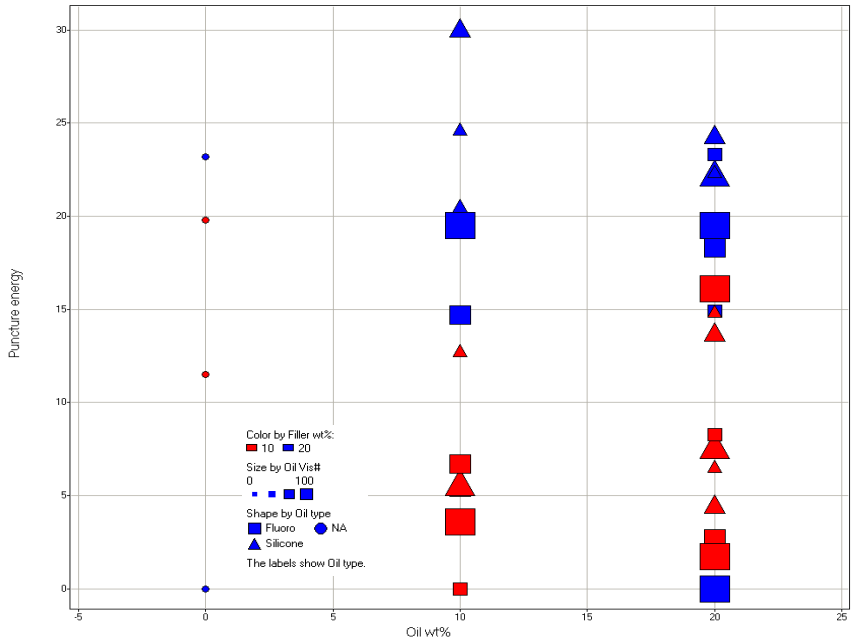

Figure 2.46. Effect of oil viscosity, oil type, oil wt% and filler wt% on toughness from puncture test results

Coatings with 20 wt% silica are noticeably tougher than coatings with 10 wt% silica. Other trends are difficult to extract which implies that oil has a minimal effect on toughness since their utilization was to improve surface properties and was not aimed at mechanical properties. However, it can be observed that coatings with 10 wt% oil have the best toughness performance. From both Figure 2.46 and 2.47, coatings with silicone oils usually outperform coatings with fluorosilicone oils. Figure 2.47 compares the toughness from the puncture test and tensile test. It also helps differentiating how coatings with silicone oils are likely to group together and vice versa for the fluorosilicone oils.

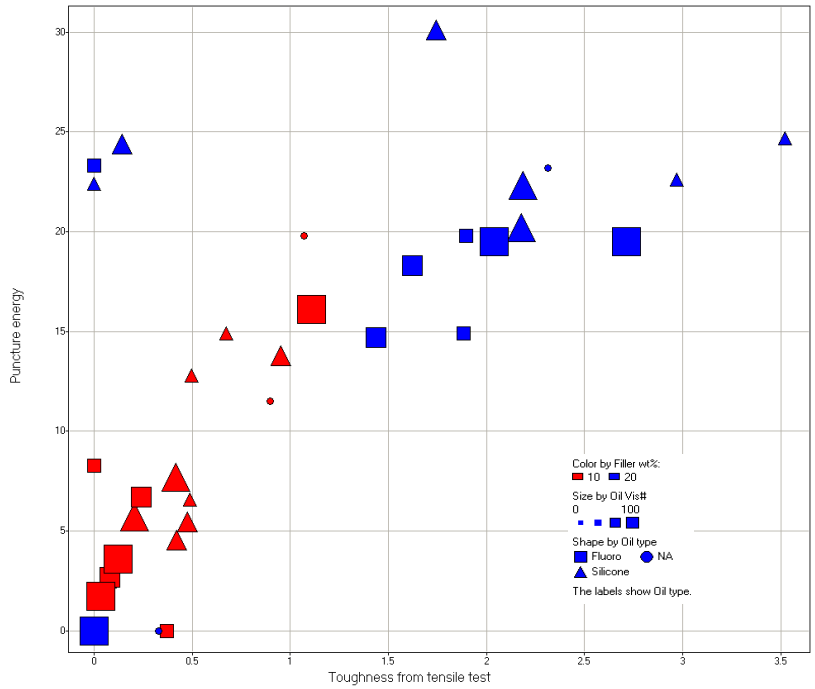

Figure 2.47. Effect of oil viscosity, oil type, filler wt%, and crosslinker type on toughness from puncture test versus tensile test

Coatings with lower viscosity from the silicone oil groups are relatively tougher than coatings with high viscosity silicone. Figure 2.48 and Figure 2.49 show the effect of C18 crosslinker and QAS on toughness from puncture test and tear strength, respectively. With 20 wt% filler, coatings with QAS generally are tougher than coatings without QAS, but the opposite is true for 10%wt filler.

It was stated that QAS enhances adhesion between the binder and silica filler.[30] With better adhesion of binder and filler, the coatings should have good toughness. It seems to be the case at 20wt% silica, but the results for 10wt% silica would suggest otherwise. The high-throughput toughness test was able to observe the trends as well as the other more labor-intensive conventional tests.

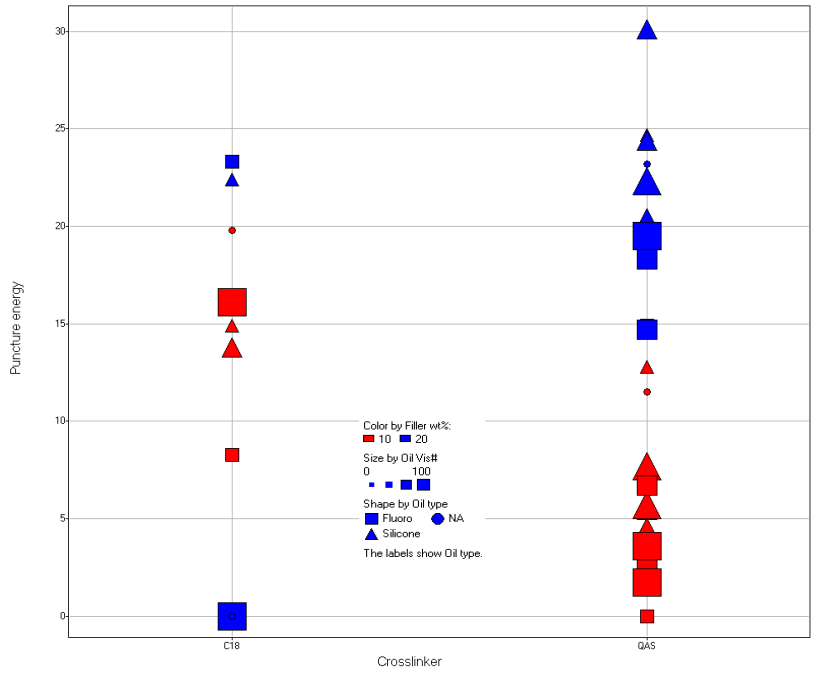

Figure 2.48. Effect of oil viscosity, oil type, filler wt%, and crosslinker type on toughness from puncture test results

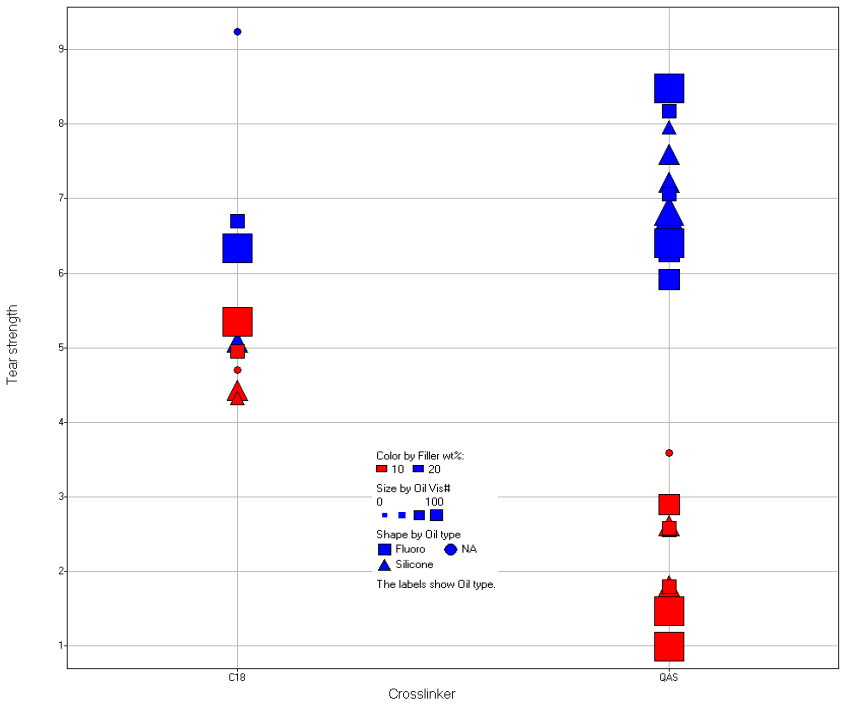

Figure 2.49. Effect of oil viscosity, oil type, filler wt%, and crosslinker on tear strength

2.4. Further Development of High-throughput Puncture Tester

A robust high-throughput puncture tester was later built by CNSE engineers after successful results were observed. Previously, the prototype was put together using high accuracy, high precision control and development tools which could be used for future problems and developing new solutions. A new design was made with new components selected by the engineers using the same basic principles of the prototype. An outside contractor was hired to program an automation, data acquisition and graphical user interface. The drawbacks were that the accuracy and the ability to customize testing scenario were sacrificed, but new features were made and it was more user-friendly to operate and extract the results. The new features include pneumatic plate clamping and a temperature controlled plate underneath the sample holder. The puncture test station is shown in Figure 2.50. As seen in Figure 2.50, there are two load cells; one at 5lb capacity and another at 50lb capacity. Both were included to cover ranges of measured loads. Lubricant fluid can be dispensed into the reservoir. The indenter will dip itself on the sponge in the reservoir before moving to the sample and indent. Sample preparation is done the same way as was done with the prototype. The free-film template is clamped between the sample holder plates as seen in Figure 2.51.

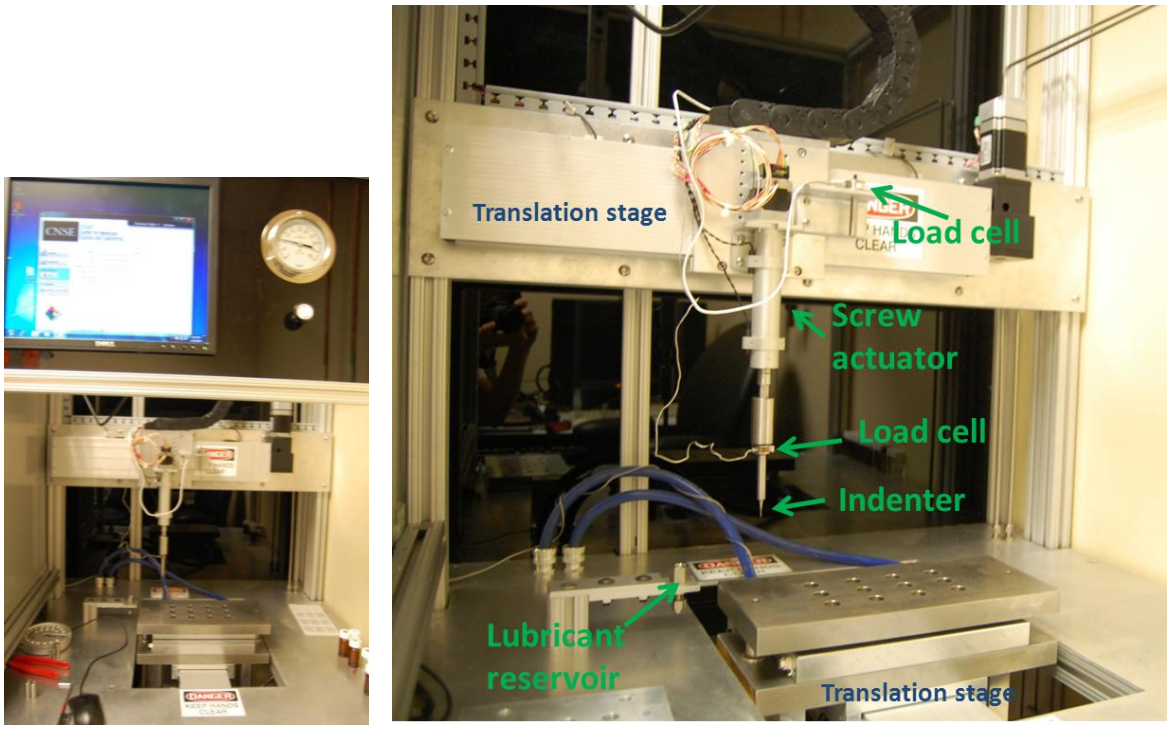

Figure 2.50. Puncture tester bench

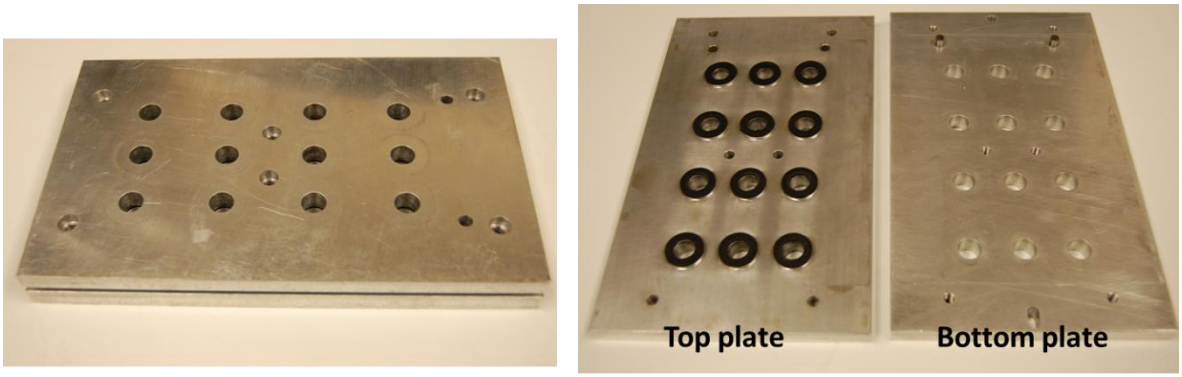

Figure 2.51. The sample holder plates where the free-film template is held. The plate has flat O-rings to enhance grip on the free-film template.

The sample holder plates fit into the guiding column on the plate attached to the moving stage. This plate can accommodate fluid circulating for temperature control as seen in Figure 2.52. Figure 2.52 (right) shows the clamping jaws opened and sample plates inserted.

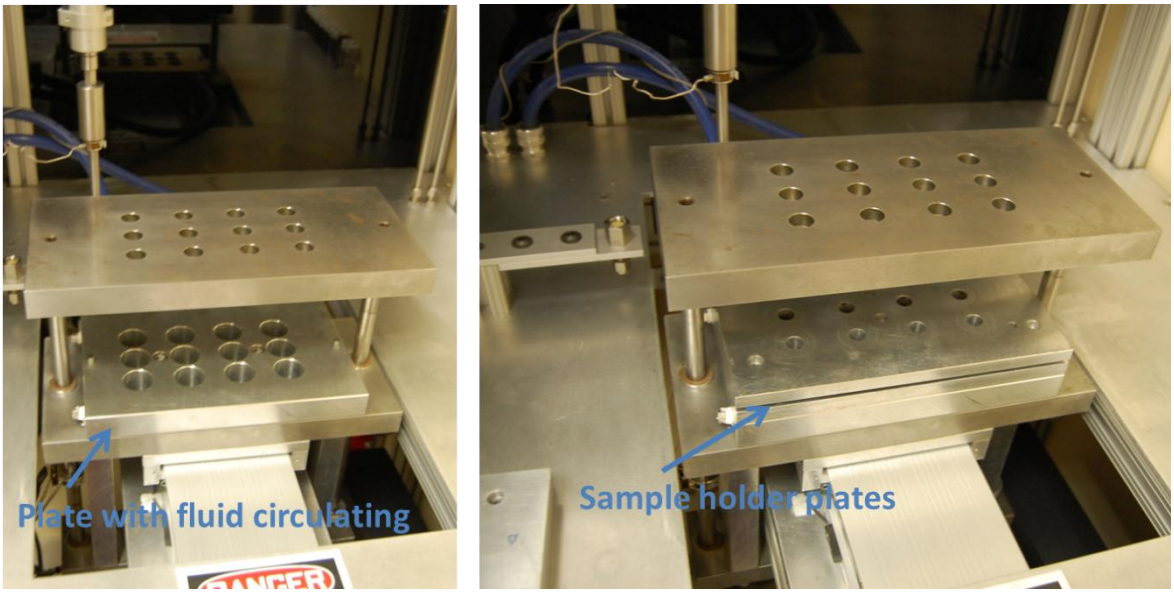

Figure 2.52. The pictures show opened pneumatic clamp with bottom plate containing temperature controlled circulating fluid. The picture on the right shows the sample holder plates being inserted before pneumatic clamping.

The polystat® closed system circulator from Cole-Parmer® is used to circulate the fluid. The operating temperature range is -10°C to 80°C. Figure 2.53 shows the pneumatic clamping pressure gauge and the control knob.

Figure 2.53. Clamping pressure gauge and control knob

The operational indenter speed is stated to be between 0.25 in/min to 30 in/min. After the test is executed, a report is generated with graph for each well and a result table. Figure 2.54 shows an example of plot on one of the wells. The unit on x-axis is lbs. and the unit on y-axis is in inches.

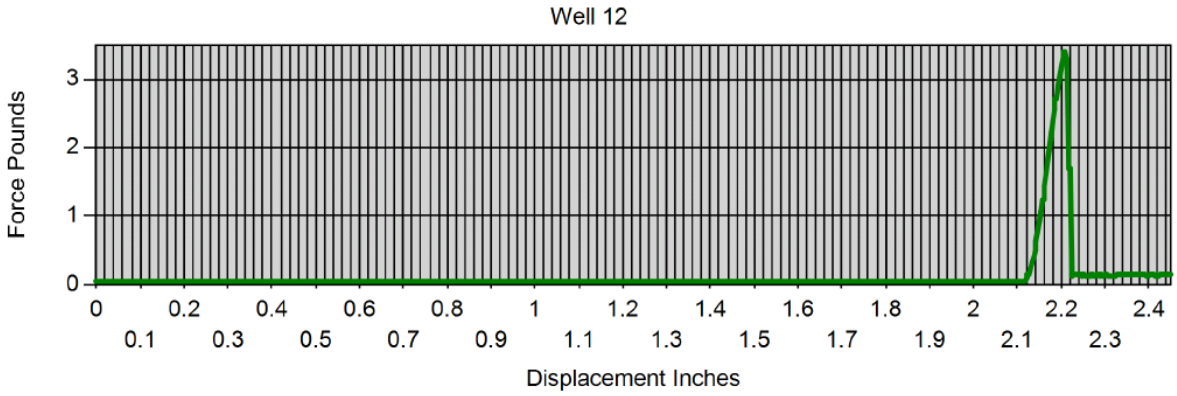

Figure 2.54. Output report from puncture tester showing plot of force-displacement curve

Table 2.3 shows the result table showing measurements on each of the 12 wells and only 3-4 significant figures should be used from the output report.

Table 2.3. Output report from puncture tester

Well	Max Displacement, in.	Max Force, lbs	Toughness, lb-in.
1	2.8597	3.1320	0.2675
2	2.4464	3.2210	0.2729
3	2.4498	3.2310	0.2631
4	2.4498	3.2965	0.2842
5	2.4498	3.3280	0.2779
6	2.4498	3.3000	0.2802
7	2.4498	3.3450	0.2928
8	2.4498	3.3660	0.2819
9	2.4498	3.3865	0.2765
10	2.4498	3.3370	0.2807
11	2.4498	3.3690	0.2717
12	2.4498	3.3980	0.2803

The maximum displacement is the traveling distance of the indenter, thus it is not useful in the analysis. The instrument does not utilize an algorithm to find contact point or

film breakage. Maximum force is valid. However, the elongation of film in the indenter direction is also important to determine the energy to break. The instrument calculates 'toughness' by finding area-under-the-curve during the entire distance the indenter travels. Thus, it represents the energy exerted on the film (whether the film breaks or not). The unit is then in lbs.-in. It can be noted that thickness is not an input for this calculation. The instrument does not know if the film breaks. The indenter will travel until the end of the range of the actuator. Thus, after the film breaks, the load can still be measured as the indenter shaft rubs against the film as seen in Figure 2.54. In some cases, the indenter shaft can create significant load due to a much larger shaft as seen in Figure 2.55.

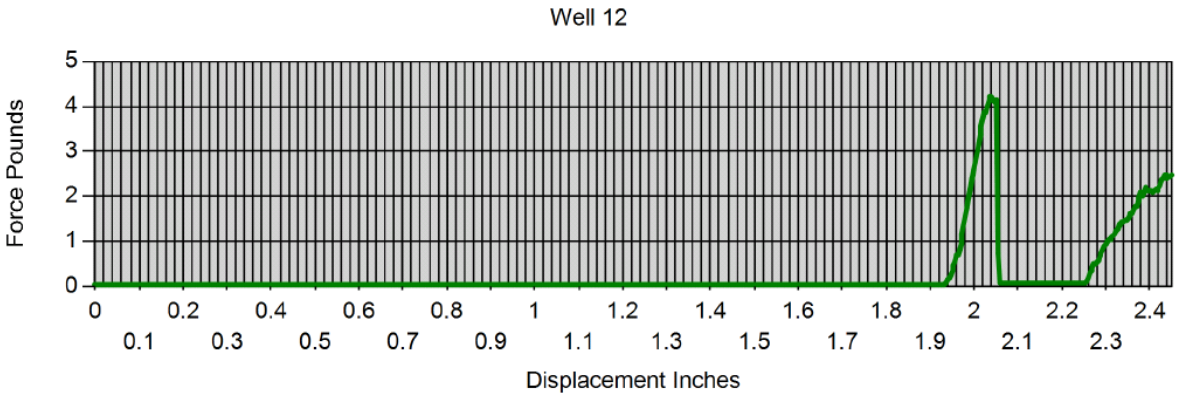

Figure 2.55. Second peak resulting from probe shaft sliding along an already torn film.

The instrument allows us to obtain raw data in load-displacement data points. The beginning and ending for force curve can be manually selected. Nevertheless, a simple program was written using MATLAB to manipulate and extract the necessary data in a single execution. An Excel file generated from puncture tester was input into MATLAB. Once the program is executed, the program locates and separates data from each well. The contact points are located by checking algebraic criteria along data points. Then, the breaking points are located by checking for a specified amount of sudden decrease in load. Figure 2.56 shows one of the program output plots which is a plot of force-displacement on

12 wells and shows a slight variation among each well. This is the indentation result on a 10-mil thick polyethylene sheet.

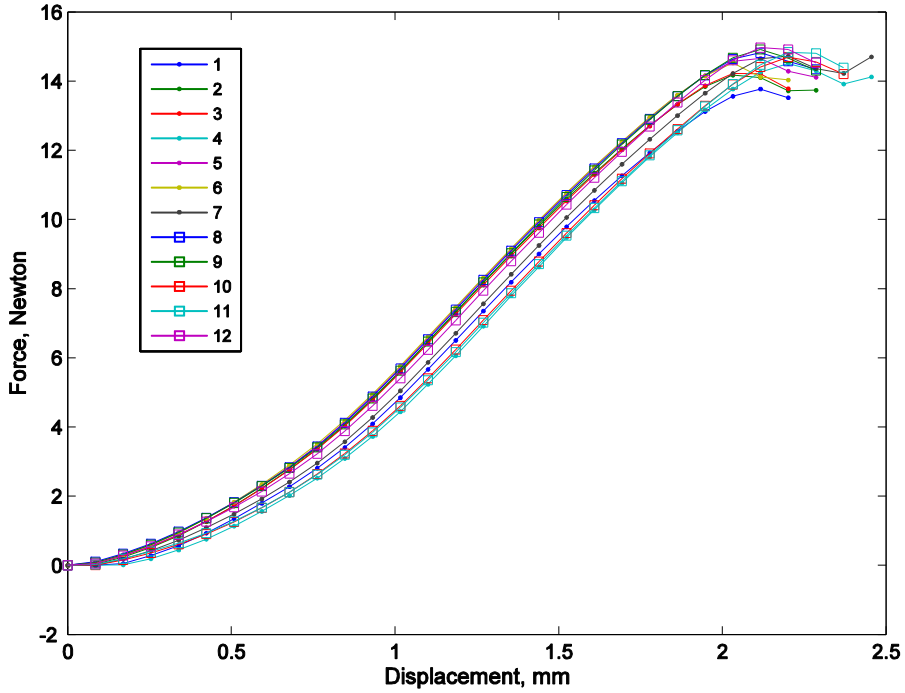

Figure 2.56. Puncture test data from indenting on 10-mil thick polyethylene sheet

The thicknesses can be specified to calculate toughness, stress-strain curve and estimated modulus based on the slope of the stress-strain curve at a specific strain. The details and codes of the program can be found in the appendix. The new automated puncture tester has been tested with commercial silicone rubbers and 102 formulations of quaternary ammonium salt siloxane coatings with different filler treatments and loadings. Figure 2.57 shows the outputs from one of the quaternary ammonium salt siloxane libraries containing 4 coating formulations with 3 replicates and the plots generated by MATLAB algorithm.

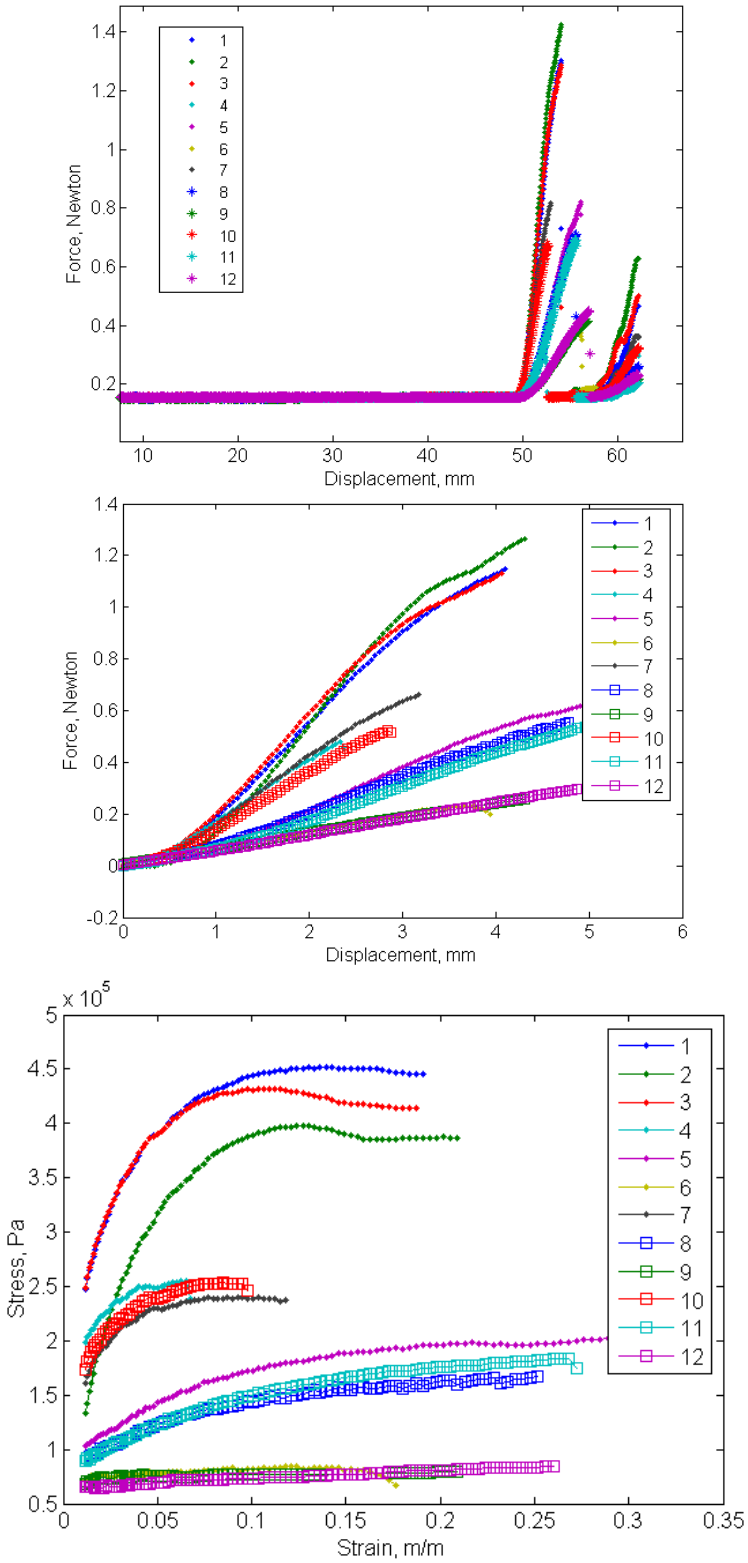

Figure 2.57. Raw data (top) was processed to generate force-displacement data (center) and operational stress-strain curves (bottom).

The commercial rubbers consist of Dow Corning 3140, Intersleek 757, Intersleek 970 and T2 Silastic. Figure 2.58 shows the results from automated puncture tester on the commercial rubbers showing noticeable differences within the group.

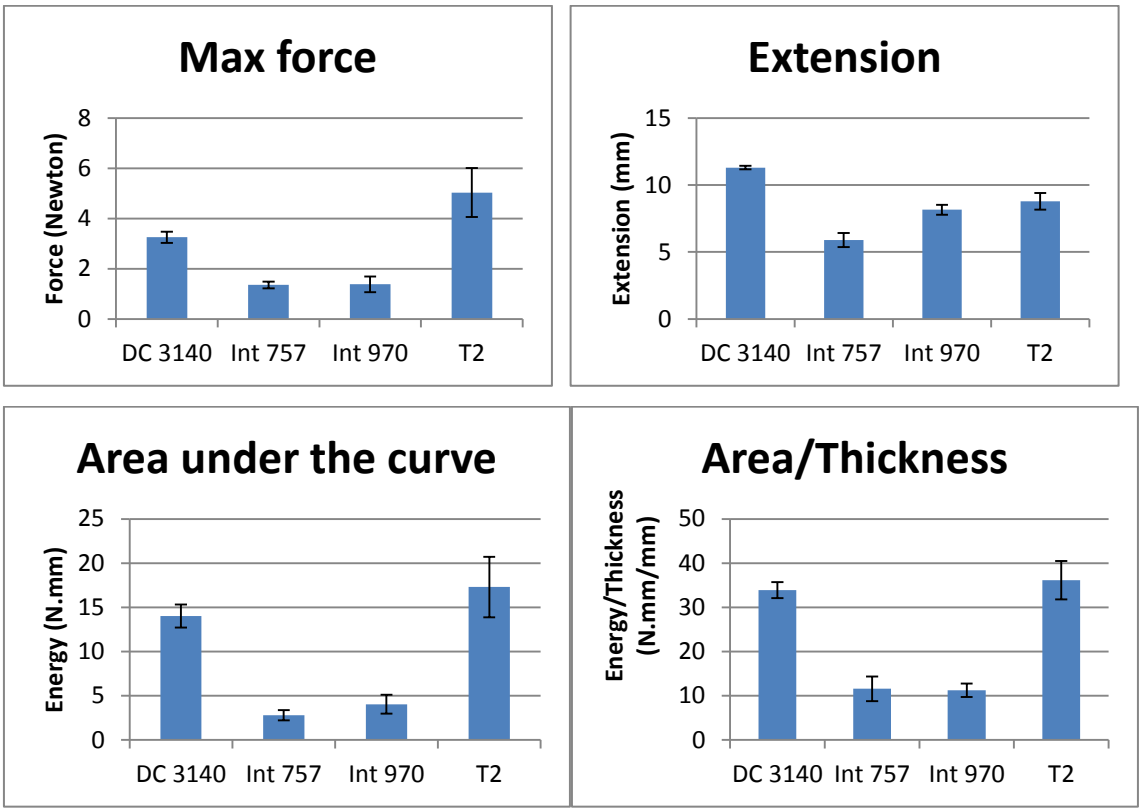

Figure 2.58. Results on four commercial rubbers after manipulation of raw data

2.5. Modulus Determination

A high-throughput toughness instrument was built and examined. Toughness was measured based the energy required to break a polymer film. During the experiment, the circular free-film is loaded normal to the surface and at the center. As the indenter pushes in, the load and displacement are recorded simultaneously. It is easily recognized that the slope of the curve depends on the stiffness of the material. The ability to rank elastic moduli from the instrument is intriguing and enhances its usefulness. However, elastic modulus is not the only parameter governing the load-displacement response. The geometry of the circular free-film and its stiffness indicate the expected behavior of the

material under transverse loading. This shell deformation phenomenon can be largely divided into two models: plate and membrane.[31] In general case, there are radial, tangential and bending stresses as shown in Figure 2.14, and the solution for indentation involving three stresses could only be solved numerically. Analytical solutions exist using the assumptions of plate and membrane models. Plate model is applicable to relatively stiff and thick materials that the radial and tensile stresses can be negligible and only bending stress is assumed. On the other hand, the membrane model neglects bending stress due to relatively low modulus and thin materials. A membrane material undergoes purely elastic and tension conditions. Plate and membrane models can be solved using analytical closed-form solutions under certain assumptions. Komaragiri et al. created the map that can be used to identify test parameters which eliminate the need for numerical solution to extract properties with closed-form solutions.[32] The solutions provide overall descriptions of freestanding circular elastic film under point and pressure loads. Figure 2.59 shows a schematic of a point-load free-film indentation and associated variables. The point load, P, is applied resulting in a max displacement, w at $r = 0$.

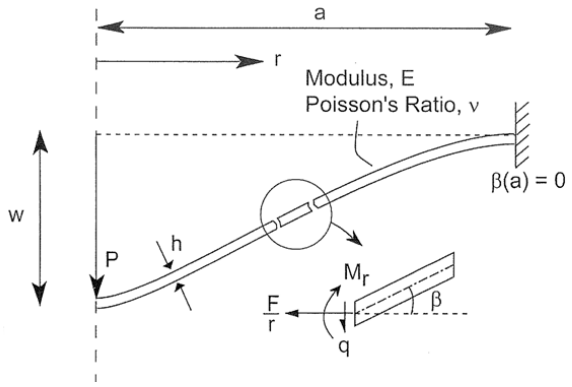

Figure 2.59. Indentation under a point load. (Reproduced from ref.[32])

Figure 2.60 shows a map with normalized parameters, γ and α. Equations 2.23 and 2.24 show the equations for both the normalized parameters:

$$\gamma = \frac{log\left[\frac{P}{2\pi Eah}\right]}{log\left[\frac{h}{a\sqrt{12(1-\nu^2)}}\right]} \tag{2.23}$$

where ν is the Poisson's ratio, E is Young's modulus, a is span length (radius), h is thickness and P is load.

$$\alpha = \frac{log\ \epsilon_0}{\log\left[\frac{h}{a\sqrt{12(1-\nu^2)}}\right]} \tag{2.24}$$

where $\epsilon_0$is pre-strain.

These γ and α predict the behavior of the mechanical response. Regions 1, 2 and 3 (Figure 2.60) specify plate behavior, linear (pre-stretched) membrane behavior and non-linear membrane behavior, respectively.

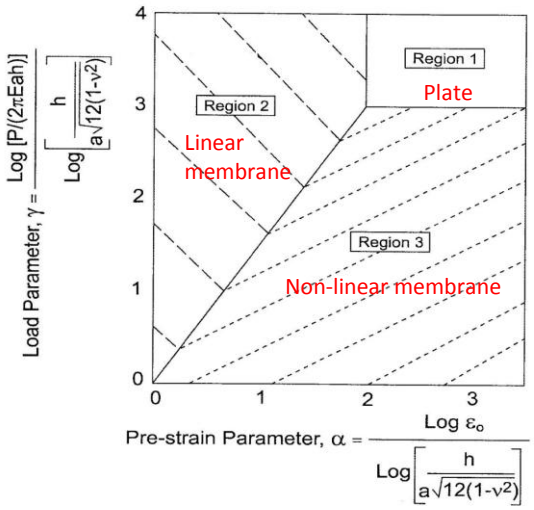

Figure 2.60. Behavioral map of circular free-film (Reproduced from ref.[32])

When the load and pre-strain increase, γ and α, respectively, decrease. We can see that the load, elastic modulus, span radius, film thickness, Poisson's ratio and pre-strain are the parameters governing the behavior between plate and membrane. The difference lies in the resulting mode of deformation. Plate behavior indicates that there is significant bending and negligible stretching and membrane behavior is the opposite. Under region 1 and 3,

plate and non-linear membrane, closed-form analytical solutions exist. $w(r)$ represents displacement as a function of radial location, r. When $r = 0$, $w(0)$ is the displacement w at the center. In Equation 2.25, the closed-form equation for linear plate with no pre-strain is shown. Plate region is defined with normalized parameters where $\alpha > 2$ and $\gamma > 3$.

$$\frac{w(0)}{a} = \frac{Pa}{16\pi D} \tag{2.25}$$

where $D$is the bending stiffness (or flexural rigidity) and is written as:

$$D = \frac{Eh^3}{12(1-\nu^2)} \tag{2.26}$$

The non-linear membrane solution with small rotation is shown in eq. 2.27 for Poisson's ratio of 1/3.

$$\frac{w(0)}{a} = \left(\frac{3P}{\pi Eah}\right)^{1/3} \tag{2.27}$$

The non-linear membrane region is specified by the inequalities of $2\gamma/3 < \alpha$ and $\gamma < 3$. For different Poisson's ratio, Komaragiri gives an approximate function from numerical evaluation,

$$\frac{w(0)}{a} = f(\nu)\left(\frac{P}{Eah}\right)^{1/3} \tag{2.28}$$

where $f(\nu) \approx 1.0491 - 0.1462\nu - 0.15827\nu^2$

The solutions are for zero pre-strain with a point load. There are approximate solutions for finite contact of spherical indenter.[24, 33] In case of a plate, the finite contact solution also takes into account the Hertzian contact.[34] Thus, the total displacement (w_{total}) is the combination of deformation from Hertzian contact (w_{Hertz}) and deformation from plate bending from point load solution (w_{plate}).

$$w_{total} = w_{Hertz} + w_{plate} \tag{2.29}$$

$$w_{total} = \left(\frac{9P^2}{16RE_r^2}\right)^{1/3} + \left(\frac{3Pa^2(1-\nu^2)}{4\pi Eh^3}\right)$$

where R is the radius of spherical indenter. To account for deformation from the indenter,[34]

$$\frac{1}{E_r} = \frac{1-\nu_s^2}{E_s} + \frac{1-\nu_i^2}{E_i} \tag{2.30}$$

For membrane model with finite contact, assuming Poisson's ratio of 0.5 and zero pre-strain,

$$\frac{w}{R} = \left(\frac{16}{9\pi}\right)^{1/3}\left(\frac{a}{R}\right)^{3/4}\left(\frac{P}{EhR}\right)^{1/3} \tag{2.31}$$

Liu and Ju created a novel technique to characterize thin elastomeric membrane.[35] A sphere with known dimension and weight was placed on the circular free-film. Obviously, the sphere rolls to the center by itself. A camera was set up to capture the deformation allowing them to solve characterize a Mooney-Rivlin material based on non-linear membrane theory. Sormana and Meredith compared stress-strain curves between free-film indentation using operational stress-strain equations (eq. (2.20) and eq. (2.21)) and traditional uniaxial tensile test.[22] In Figure 2.61, the secant modulus at 100% strain was used for comparison on the segmented poly(urethane-urea)s.

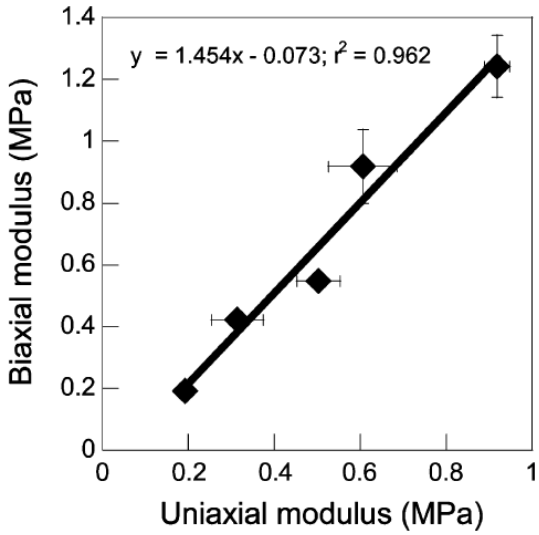

Figure 2.61. Comparison of modulus results on segmented poly(urethane-urea)s from free-film indentation and tensile test using "effective" secant modulus at 100% strain (Reproduced from ref.[22])

The materials characterized by Sormana and Meredith were soft elastomers which underwent significant extension. The operational stress equation (Equation 2.20) becomes meaningless once the cosine approaches zero. The ability to rank stiffness will work for elastomers, but, keeping in mind that, an arbitrary secant modulus is obtained, not the Young's modulus. Another algebraically simple and direct way to approximate the membrane problem was shown by Kyle Maner and Matthew Begley as shown in the following calculation. It basically has the same stress-strain definition from Equation 2.20 and Equation 2.21. Figure 2.62 shows the schematic of a two dimensional test with associated parameters.

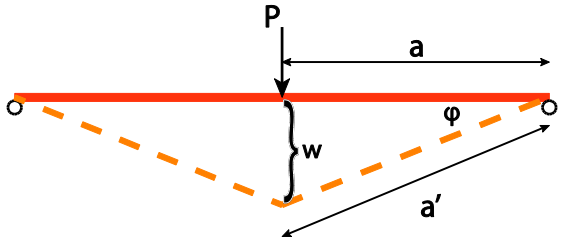

Figure 2.62. Schematic of two-dimensional indentation

Strain-displacement relationship can be written as

$$\varepsilon = \sqrt{\widehat{w}^2 + 1} - 1 + \varepsilon_0 \tag{2.32}$$

where $\widehat{w} = w/a$ and ε_0 is pre-strain. Stress-strain relationship from Hooke's law is well known as $\sigma = E\varepsilon$. Then, from equilibrium of forces, we have

$$\sum F_y = 0 = -P + 2(F \sin \varphi)$$

$$F = \frac{P}{2 \sin \varphi} \tag{2.33}$$

Combining Equation 2.32, Equation 2.33, and stress-strain relationship, we have

$$P = 2EA \frac{\sqrt{\widehat{w}^2+1}-1+\varepsilon_0}{\sqrt{\widehat{w}^2+1}} \tag{2.34}$$

where A is the area. For small displacements,$\widehat{w} \ll 1$, then the term $\sqrt{\widehat{w}^2 + 1}$ approaches one; $\sqrt{\widehat{w}^2 + 1} \approx 1 + \frac{1}{2}\widehat{w}^2 + 0(\widehat{w}^3) + \cdots$

$$P = \frac{EA\widehat{w}^3+2EA\varepsilon_0\widehat{w}}{1+\frac{1}{2}\widehat{w}^2} \tag{2.35}$$

Load as a function of deflection can be written as

$$P(\widehat{w}) = (\widehat{w}^3 + 2\widehat{w}\varepsilon_0)EA \tag{2.36}$$

Equation 2.36 can be used to fit the load-deflection at low strain with material that undergoes pure tension.

However, going back to the behavioral map study, there is a transition region in which the analytical plate and membrane models above cannot be represented. The transition region can occur between plate and membrane regions as the applied load increases during indentation. The behavior of our testing material depends on the parameters stated above. Also, the load and displacement resolution of the measurement system will govern whether the simple plate model is possible. It is more likely that the

measurement system will capture material in transition region from the beginning because of the size of the geometry and the resolution. Figure 2.63 shows the behavioral map with linear and non-linear responses in the shaded areas for h/a=0.005. The white area in the middle of the graph is the transition region. The bottom white area is the large rotation regime and outside the range for non-linear membrane ($w \sim P^{1/3}$) response.

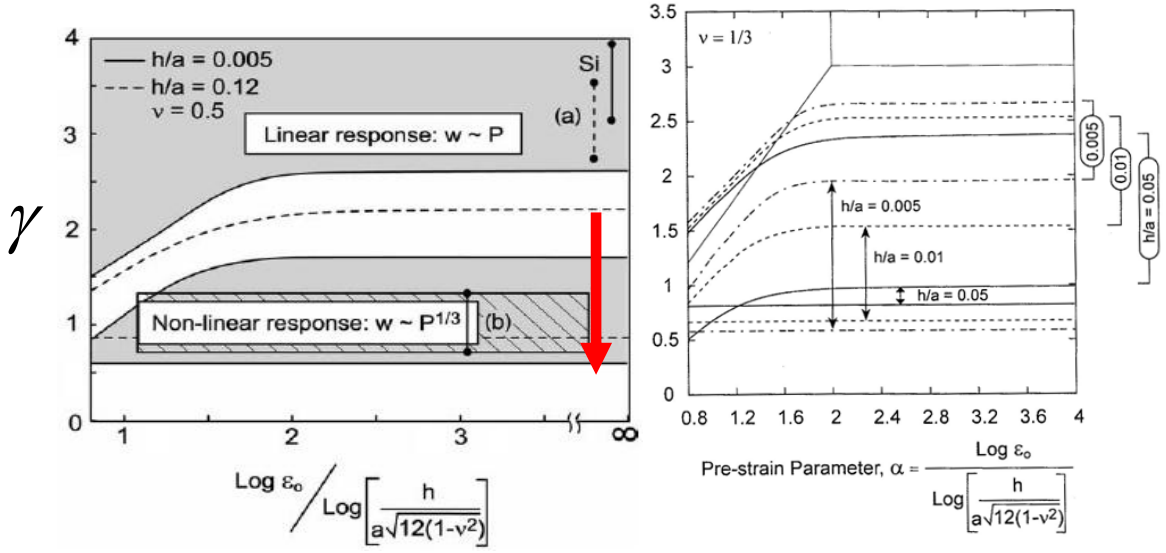

Figure 2.63. The figure on the left side shows the transition region (white area in the center) depends on the geometric parameter, h/a. The figure on the right shows the transition region at different geometric parameters(Reproduced from ref.[24, 36])

The transition region moves with the geometry parameter (h/a). The dotted lines in Figure 2.63 (left) show the transition region with h/a = 0.12. In Figure 2.63 (left), lines of the graph specified by a) and b) are the locations where Scott et al. performed experiments with silicon plate and polydimethysiloxane (PDMS) elastomer. For our test geometry, the parameter, 'a', is fixed by the hole radius of our fixture at 0.25 in (6.35 mm). Thickness of the film, h, can range from 100-400 μm, thus h/a can approximately vary from 0.016 to 0.063. Assuming the pre-strain is small or negligible, the red arrow in Figure 2.63 represents an indentation testing of a 460 μm thick film with E=1.1 MPa. The starting point

of γ (tail of the red arrow) depends on the resolution of the measurements. As the load increases, the γ position decreases (moves downward), moving from transition into non-linear membrane. Figure 2.64 shows a decrease in γ as the load increases.

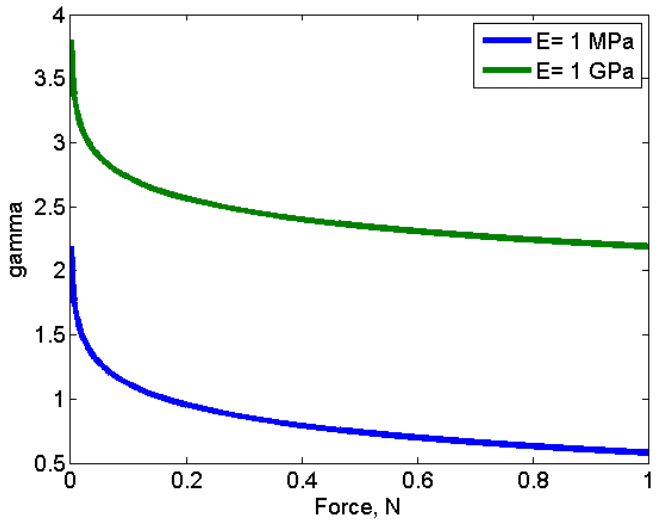

Figure 2.64. A change in γ as a function of load for a=6.35mm and h=300μm; h/a=0.047

With a large value of h/a, the transition region gets larger and membrane region gets smaller. For example at h/a=0.12, the behavior of film goes directly from transition region into large rotation regime because the membrane regime cannot be satisfied.[37]

Our free-film template controls the thickness and diameter of free film. The load behavior may not fall under either plate or membrane theory, but a transition region with point-load assumption can be solved numerically following Komaragiri.[36] Komaragiri numerically solved the simplified Reissner equations, which describe film deformation of axisymmetric shells for small static strain, using finite difference and relaxation methods.[31, 36, 38] The general equations are in the form of two second-order non-linear differential equations. The procedure from Komaragiri, written in FORTRAN, was followed and Figure 2.65 showed our result of the numerical simulation using MATLAB. MATLAB code is shown in the appendix.

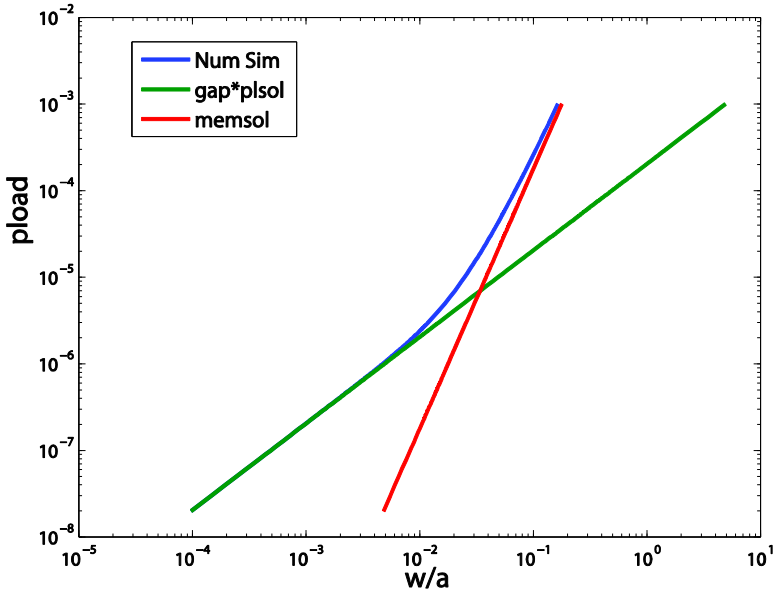

Figure 2.65. Numerical simulation result; green, red and blue lines represent plate, membrane and numerical solutions for $h/a = 0.016$, $\nu = 0.33$, and zero pre-strain

The parameters in the simulation are normalized. *pload* is represented by the following equation.

$$pload = \frac{12P(1-\nu^2)}{Ea^2} \tag{2.37}$$

The simulation result can be used to match the experimental data to obtain the elastic modulus. However, pre-strain (residual stress or pre-stretch) is one of the inputs and may require an arbitrary guess to fit the data. There are three required inputs for the simulation; Poisson's ratio, film thickness, and pre-strain. The final task is to find the best combination of pre-strain and elastic modulus that closely fits the experimental data as shown in Figure 2.66.[36]

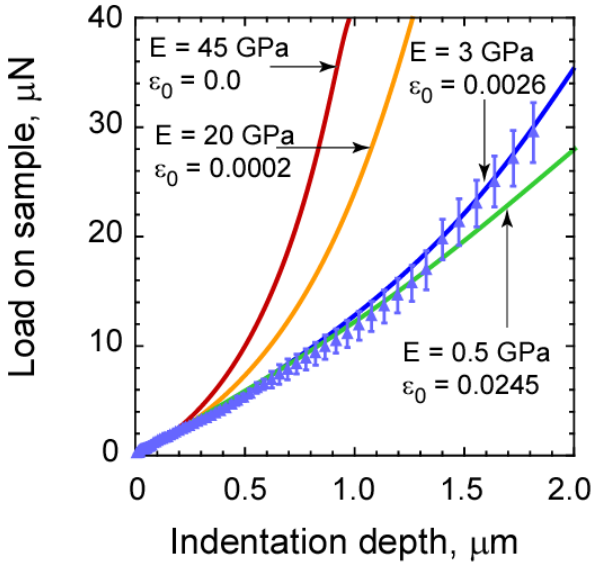

Figure 2.66. Experimental data plotted against numerical simulation results with different combination of modulus and pre-strain. (Reproduced from ref.[36])

The automated puncture tester can be useful for both stiffness and toughness ranking of materials. If the analytical and numerical solutions for the shell problem are employed, the machine compliance needs to be measured. The apparatus will flex, especially under a stiff plate, thus the displacement of the indenter into the film can be corrected. For hard coatings, the plate theory can be used provided that the resolution of the load and displacement is small enough. For soft coatings, it is more likely to operate in the transition region with our instrument. The numerical simulation result is a general solution that covers all point-load small-strain behavior. An algorithm can be created to calculate the modulus from each curve using numerical simulation and optimization. A linear interpolation is applied to the experimental data points (for example, with MATLAB's function, yi=interp1q(x,Y,xi)) in order to approximate the load data at the same depth with numerical result. Then, optimization is used to find best combinations of parameters that give the minimum goodness of fit between the experimental data and the simulated result (for example, Chi-squared: $\chi^2 = \sum \frac{[P_{numerical}(w) - P_{experiment}(w)]^2}{P_{experiment}}$).

2.6. Conclusion

The high-throughput puncture instrument was incorporated into the combinatorial workflow at NDSU. Mechanical property testing is one of the bottlenecks in the characterization process. The free-film template is specially made to work with our existing system and the instrument is built and tested. The results show that the puncture instrument in the form of circular free-film indentation can be used to rank toughness in polymeric coatings.

2.7. References

1. Juvinall, R. C.; Marshek, K. M., *Fundametals of Machine Component Design*. 3rd ed.; John Wiley & Sons, Inc.: 2000.

2. Askeland, D. R., *The Science and Engineering of Materials*. 3rd ed.; PWS Publishing Company: 1994.

3. Brown, R., *Handbook of Polymer Testing: Physical Methods*. Marcel Dekker, Inc.: 1999.

4. Toughness. http://www.ndt-ed.org/EducationResources/CommunityCollege/ Materials/Mechanical/Toughness.htm (accessed 10/22/2011).

5. Janssen, M.; Zuidema, J.; Wanhill, R., *Fracture Mechanics*. 2nd ed.; Spon Press: Oxfordshire, 2004.

6. McCrum, N. G.; Buckley, C. P.; Bucknall, C. B., *Principles of Polymer Engineering*. 2nd ed.; Oxford University Press, Inc.: New York, 1997.

7. Sperling, L. H., *Introduction to Physical Polymer Science*. 4th ed.; John Wiley & Sons, Inc.: Hoboken, 2006.

8. Koleske, J. V., *Paint and coating testing manual: fourteenth edition of the Gardner-Sward handbook*. American Society for Testing and Materials: Ann Arbor, MI, 1995.

9. Tielking, J. T., A fracture toughness test for polymer film. *Polymer Testing* **1993,** *12*, 207-220.

10. Casellas, J. J.; Frontini, P. M.; Carella, J. M., Fracture characterization of low-density polyethylenes by the essential work of fracture: changes induced by thermal treatments and testing temperature. *Journal of Applied Polymer Science* **1999,** *74*, 781-796.

11. Lievana, E.; Bernal, C.; Frontini, P., Essential work of fracture of rubber-modified polyamide 6 in impact. *Polymer engineering and science* **2004,** *44* (9), 1707-1715.

12. Ching, E. C. Y.; Poon, W. K. Y.; Li, R. K. Y.; Mai, Y.-w., Effect of strain rate on the fracture toughness of some ductile polymers using the essential work of fracture (EWF) approach. *Polymer Engineering and Science* **2000,** *40* (12), 2558-2568.

13. Duan, K.; Hu, X.; Stachowiak, G., Modified essential work of fracture model for polymer fracture. *Composites Science and Technology* **2006,** *66* (16), 3172-3178.

14. Grellmann, W.; Seidler, S., *Deformation and Fracture Behaviour of Polymers*. Springer: 2001.

15. Lach, R.; Schneider, K.; Weidisch, R.; Janke, A.; Knoll, K., Application of the essential work of fracture concept to nanostructured polymer materials. *European Polymer Journal* **2005,** *41*, 383-392.

16. Rivlin, R. S.; Thomas, A. G., Rupture of rubber. I. Characteristic energy for tearing. *Journal of Polymer Science* **1953,** *10* (3), 291-318.

17. Gardco:: Conical Mandrel Test BD3000. http://www.gardco.com/pages/impact_flex/mn/bd3000.cfm (accessed 02/14/2012).

18. Sormana, J.-L. High-throughput impact characterization of mechanical properties in combinatorially prepared segmented polyurethaneurea elastomers Master thesis, Georgia Institute of Technology, 2002.

19. Sormana, J.-L.; Chattopadhyay, S.; Meredith, J. C., High-throughput mechanical characterization of free-standing polymer films. *Review of Scientific Instruments* **2005,** *76*, 062214.

20. Sormana, J.-L.; Meredith, J. C., High-throughput dynamic impact characterization of polymer films. *Materials Research Innovations* **2003,** *7*, 295-301.

21. Sormana, J.-L.; Meredith, J. C., High-throughput screening of mechanical properties on temperature-gradient polyurethaneurea libraries. *Macromolecular Rapid Communications* **2003,** *24*, 118-122.

22. Sormana, J.-L.; Meredith, J. C., High-throughput discovery of structure-mechanical property relationships for segmented poly(urethane-urea)s. *Macromolecules* **2004,** *37*, 2186-2195.

23. COMBINATORIAL SCIENCE - COATING DEPOSITION. http://www.ndsu.edu/cnse/facilities_equipment/combi_deposition.html (accessed 02/12/2012).

24. Scott, O. N.; Begley, M. R.; Komaragiri, U.; Mackin, T. J., Indentation of freestanding circular elastomer films using spherical indenters. *Acta Materialia* **2004,** *52*, 4877-4885.

25. Maner, K. C.; Begley, M. R.; Oliver, W. C., Nanomechanical testing circular freestanding polymer films with sub-micron thickness. *Acta Materialia* **2004,** *52*, 5451-5460.

26. Ju, B.-F.; Ju, Y.; Saka, M.; Liu, K.-K.; Wan, K.-T., A systematic method for characterizing the elastic properties and adhesion of a thin polymer membrane. *International Journal of Mechanical Sciences* **2005,** *47*, 319-332.

27. Trouser Tear Resistance - ISO 6383-1. http://www.ides.com/property_descriptions/ISO6383-1.asp (accessed 02/14/2012).

28. Majumdar, P.; Lee, E.; Gubbins, N.; Christianson, D. A.; Stafslien, S. J.; Daniels, J.; VanderWal, L.; Bahr, J.; Chisholm, B. J., Combinatorial materials research applied to the development of new surface coatings XIII: an investigation of polysiloxane antimicrobial coatings containing tethered quarternary ammonium salt groups *Journal of Combinatorial Chemistry* **2009,** *11* (6), 1115-1127.

29. Majumdar, P.; Lee, E.; Patel, N.; Ward, K.; Stafslien, S. J.; Daniels, J.; Chisholm, B. J.; Boudjouk, P.; Callow, M. E.; Callow, J. A.; Thompson, S. E. M., Combinatorial materials research applied to the development of new surface coatings IX: an investigation of novel antifouling/fouling-release coatings containing quaternary ammonium salt groups. *Biofouling* **2008,** *24* (3), 185-200.

30. Majumdar, P.; Mayo, B.; Kim, J.; Gallagher-Lein, C.; Lee, E.; Gubbins, N.; Chisholm, B. J., The utilization of specific interactions to enhance the mechanical properties of polysiloxane coatings. *Journal of Coatings Technology and Research* **2010,** *7* (2), 239-252.

31. Libai, A.; Simmonds, J. G., *The Nonlinear Theory of Elastic Shells*. Cambridge University Press: New York, 1998.

32. Komaragiri, U.; Begley, M. R.; Simmonds, J. G., The mechanical response of freestanding circular elastic films under point and pressure loads. *Journal of Applied Mechanics* **2005,** *72,* 203-212.

33. Begley, M. R.; Mackin, T. J., Spherical indentation of freestanding circular thin films in the membrane regime. *Journal of the Mechanics and Physics of Solids* **2004,** *52,* 2005-2023.

34. Johnson, K. L., *Contact Mechanics*. Cambridge University Press: 1987.

35. Liu, K.-K.; Ju, B.-F., A novel technique for mechanical characterization of thin elastomeric membrane. *Journal of Physics D: Applied Physics* **2001,** *34,* L91-L94.

36. Komaragiri, U. Mechanics of freestanding circular thin films subjected to point and pressure loads. Master thesis, University of Virginia, 2004.

37. Scott, O. N. Indentation Experiments to Characterize Freestanding Films. Master thesis, University of Virginia, 2004.

38. Press, W. H.; Flannery, B. P.; Teukolsky, S. A.; Vetterling, W. T., *Numerical recipes in Fortran: the art of scientific computing*. 2nd ed.; Cambridge University Press: 1992.

CHAPTER 3. A STUDY OF MODULUS DETERMINATION USING PARALLEL DYNAMIC MECHANICAL-THERMAL ANALYSIS INSTRUMENT

3.1. Introduction and Rationale

3.1.1. Introduction to a dynamic mechanical-thermal analysis instrument

Dynamic mechanical-thermal analysis (DMTA), also known as dynamic mechanical analysis (DMA), is a technique used to measure viscoelastic properties of materials as they are deformed under periodic strain under varying temperature.[1, 2] The analysis involves a very small strain deformation wherein the stresses are below yield strength and tensile strength, thus the test is non-destructive. In dynamic testing, either oscillating stress or strain is applied and the resulting oscillating strain or stress response is measured. There are different modes of deformation are shown in Figure 3.1. Common DMTA modes consist of tension, three-point bending, compression, shear, or dual-cantilever bending. One of the requirements in dynamic mechanical test for coatings is the requirement for the use of a free film because it allows for a simple calculation of properties. Performance of coatings is influenced by the coating-substrate interactions, thus this presents a limitation of DMTA. The most commonly used mode of deformation for coating films is the film tensile mode as seen in Figure 3.1 e). Shear test using rotating plates is also possible for coating films. Other modes, such as 3-point bending, would not accommodate the rigidity and geometry of the coating film.

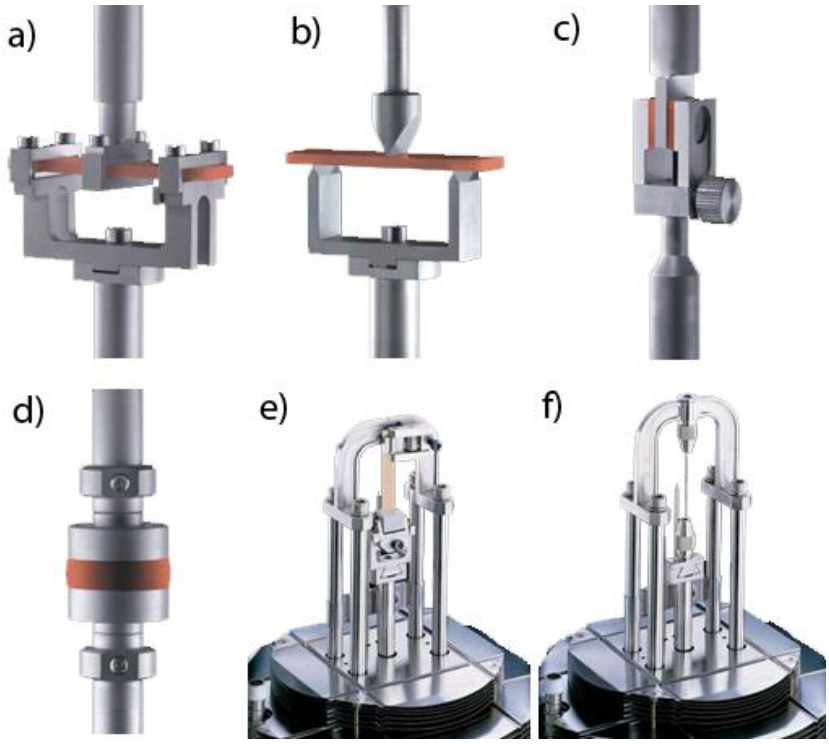

Figure 3.1. Different modes of deformation: a) dual cantilever, b) 3-point bend, c) shear sandwich, d) compression, e) tension (film), and f) tension (fiber) (Courtesy of TA Instruments)

Figure 3.2 shows the oscillating stress and strain and the phase lag, δ, of the response. The oscillating stress and strain do not coincide due to the viscoelastic nature of polymer materials. The phase lag, δ, represents the degree which the two waves are out of phase. The phase lag is zero if the material is perfectly elastic and it lies between 0 and 90° for viscoelastic materials.

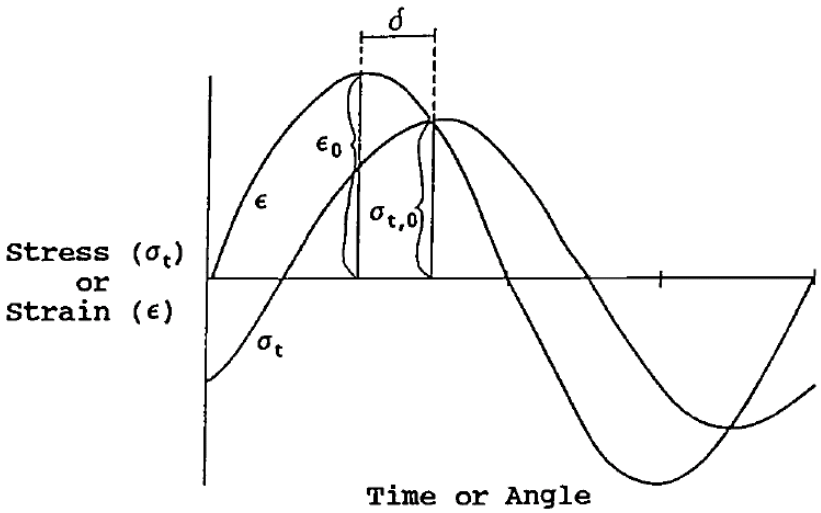

Figure 3.2. Viscoelastic nature under periodic stress and strain; applied strain (ε) and resulting stress (σ_t) in tensile DMA experiment. Phase lag (δ), maximum strain (ε_0) and maximum stress (σ_0) are shown. (Reproduced from ref.[2])

The tensile storage modulus and tensile loss modulus can be calculated as shown in equation 3.1 using the maximum stress and strain values at a specific frequency:

$$E^* = \frac{stress}{strain}$$

$$E' = E^* \cos\delta \qquad (3.1)$$

$$E'' = E^* \sin\delta$$

$$\tan\delta = \frac{E'}{E''}$$

It can be represented geometrically as in Figure 3.3.

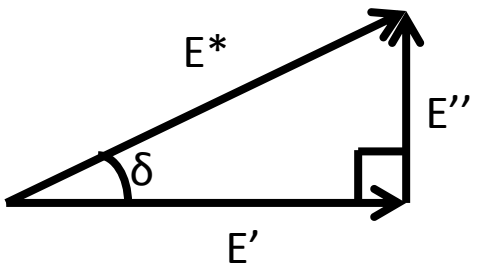

Figure 3.3. Viscoelastic nature under periodic stress: E' is tensile storage modulus, E'' is tensile loss modulus and δ is the phase lag.

Depending on the application, the dynamic mechanical properties are measured as a function of frequency or temperature. Figure 3.4 represent typical DMTA data.

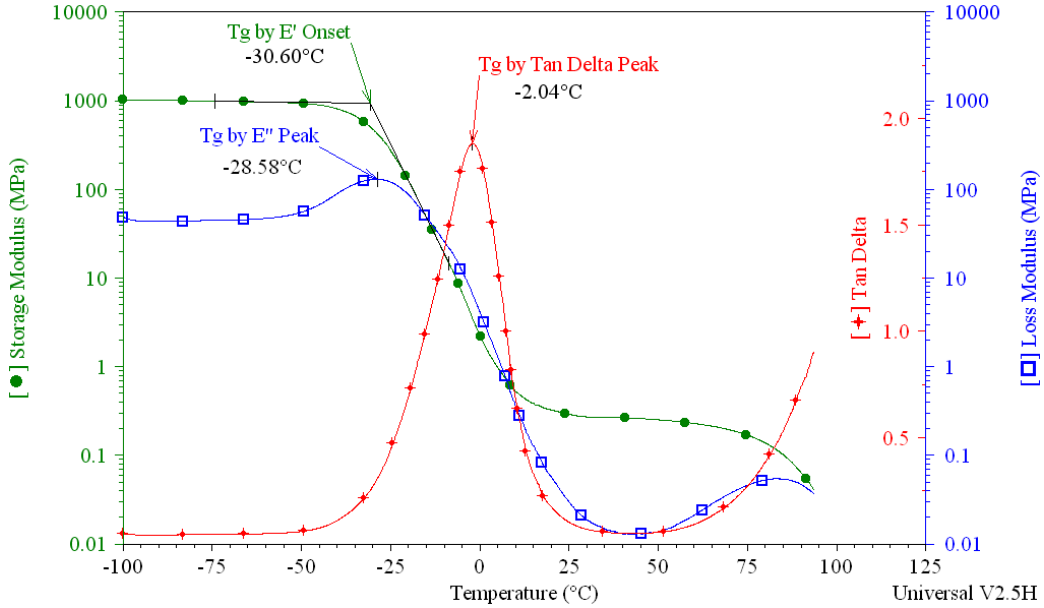

Figure 3.4. Example of DMA result (Courtesy of TA Instruments)

DMTA results can provide the storage and loss moduli with respect to temperature. The transition region can observed and T_g can be calculated with a few different methods as shown in Figure 3.4. At the rubbery plateau, there is a minimal viscous part, and we can apply rubber elasticity theory to calculate the crosslink density for a crosslinked polymer.

3.1.2. Parallel dynamic mechanical-thermal analysis instrument

The parallel dynamic mechanical-thermal analysis (pDMTA) instrument from Symyx Inc. is a high-throughput DMTA that allows ninety-six samples to be simultaneously characterized. If we observe the different clamps in Figure 3.2, the samples need to be cut or molded individually and must be carefully mounted onto the fixtures. The pDMTA approach accelerates the sample preparation and testing processes by using a 114mm×78mm perforated aluminum plate for 96 samples and having 96 load sensors to measure the properties of all samples simultaneously inside an environmental chamber.

The pDMTA plate with polymer deposited is shown in Figure 3.5 c). The diameter of the perforated circular hole is approximately 5 mm. Figure 3.5 a) shows the measuring pin at the bottom location and the vertical-travel translation stage above the pins where the pDMTA plate will be attached during the experiment.

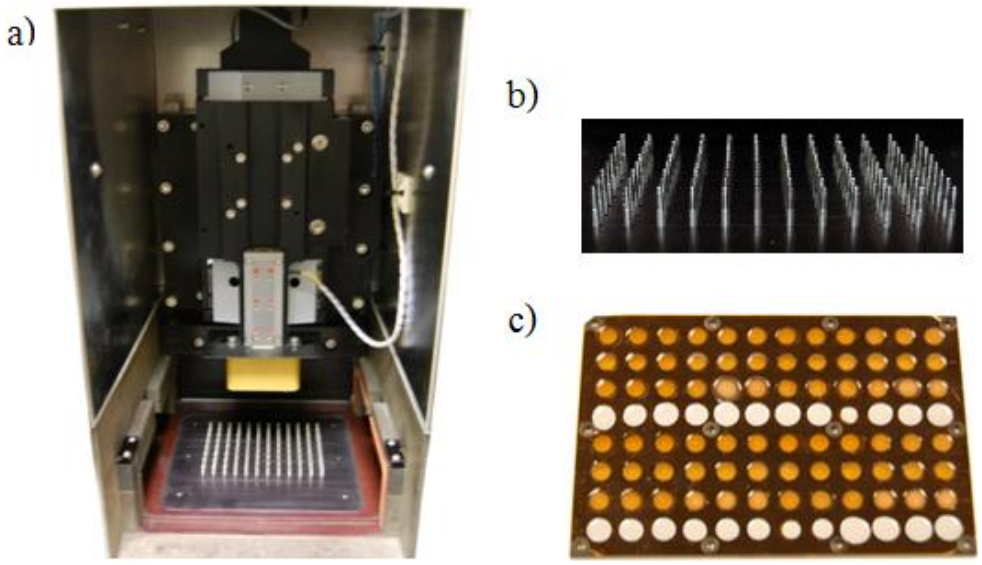

Figure 3.5. Components of pDMTA: a) a translation stage, b) 96 pins for independent and simultaneous measurement, c) 8 × 12 array samples

Dupont™ Kapton VN, a polyimide film, with 2 mil (50.8 μm) thickness is used as a substrate due to its dimensional stability at elevated temperatures. It has a low coefficient of thermal expansion and has a glass transition temperature quoted at around 360°C to 410°C.[3] The pDMTA plate is fixed to the stage and gradually moves down until the pins make contact with the Kapton substrate from the backside of the perforated pDMTA plate. Figure 3.6 shows the schematic of the pDMTA set-up on a single measured location.

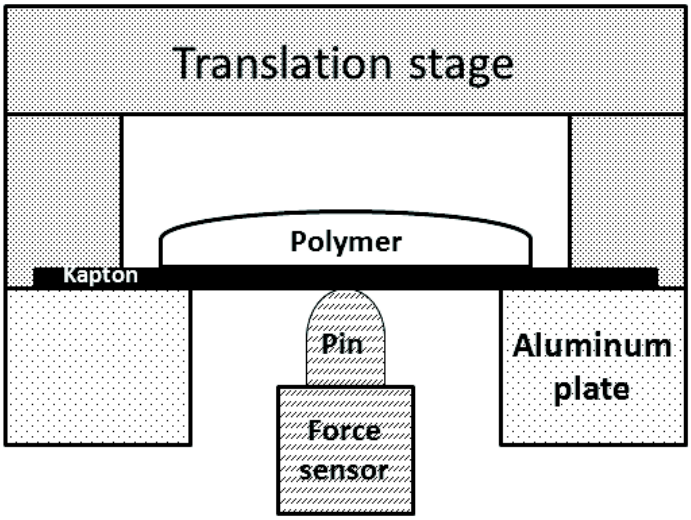

Figure 3.6. Schematic of pDMTA testing

The pin (or, in other words, an indenter) makes contact with the Kapton in the center of the circular hole. The polymer film or droplet adheres on top of the Kapton. The pDMTA plate carrying Kapton film and polymer samples sinusoidally moves while the force sensors underneath the pins record the load being applied to the Kapton film.

The overall experimental workflow is shown in Figure 3.7.

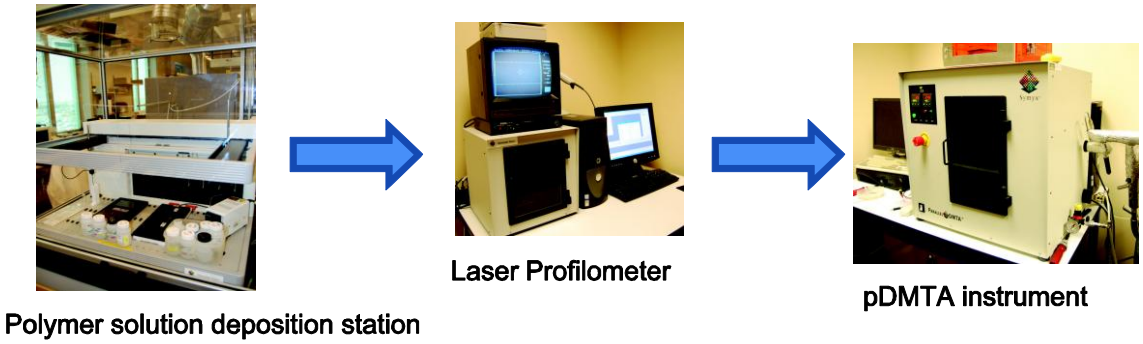

Figure 3.7. Instrumentation workflow for pDMTA experiment

Firstly, the polymer solution is applied on to a prepared pDMTA substrate using an automated solution dispensing instrument. The volume of the dispensing solution is controlled, so that the cured polymer is around 100 µm thick. When the polymer is cured, the thickness is measured with an automated laser profilometer specifically modified for

pDMTA samples and then the modulus measurements are made using the pDMTA instrument.

Pieper et al. studied the effect of polyol composition on properties of siloxane-polyurethane coatings.[4] For pDMTA experiment, the samples were cooled down to -110°C and ramped up to 100°C with a heating rate of 1°C per minute. The glass transition temperature was determined using the peak of the tan delta curve. Figure 3.8 shows T_g results using differential scanning calorimetry (DSC) and pDMTA, both of which give a similar trend.

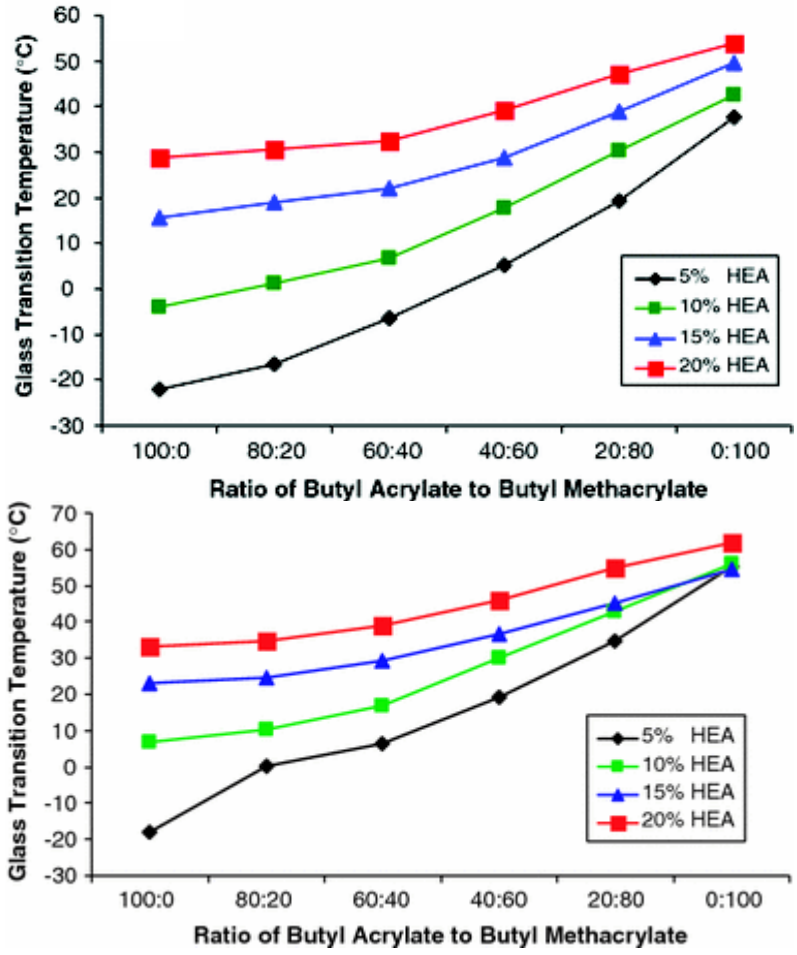

Figure 3.8. Glass transition temperature results from DSC (top) and from pDMTA (bottom) (Reproduced from ref.[4])

Uhl et al. compared T_g values from DSC, conventional DMTA and pDMTA on UV-curable cycloaliphatic epoxies.[5] Both samples behaved similarly, as shown in Figure 3.9, which demonstrated that pDMTA could be an effective rapid screening tool. The paper noted the variability in four replicates as a result of height and shape variations of the sample on Kapton substrate. The result of the four replicates is shown in Figure 3.10. The figure displays the storage modulus measurement at 25°C and at 120°C. At both temperatures, significant variations can be observed.

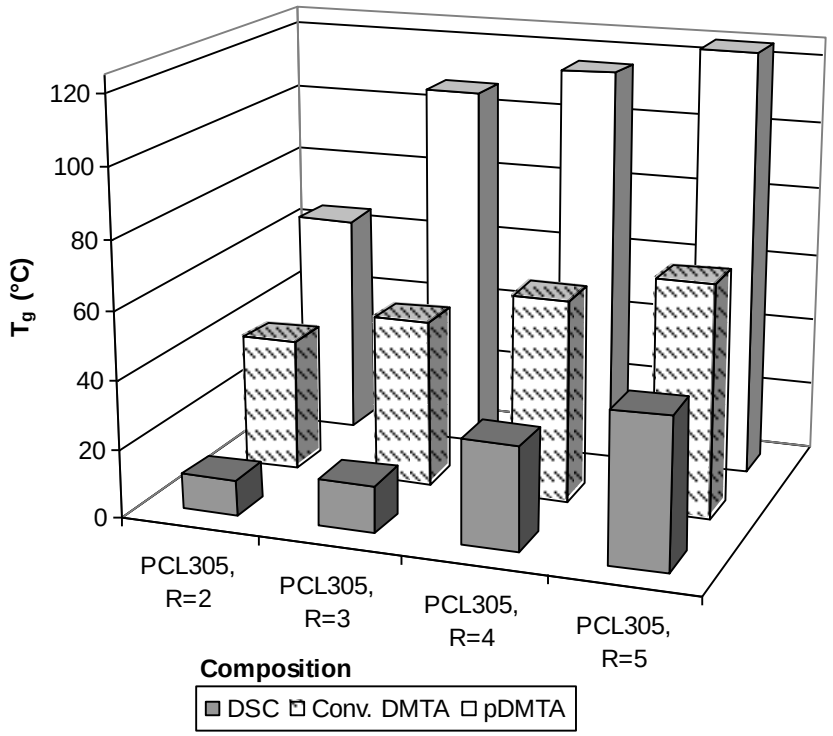

Figure 3.9. Comparison of T_g by DSC, conventional DMTA and pDMTA (Reproduced from ref.[5])

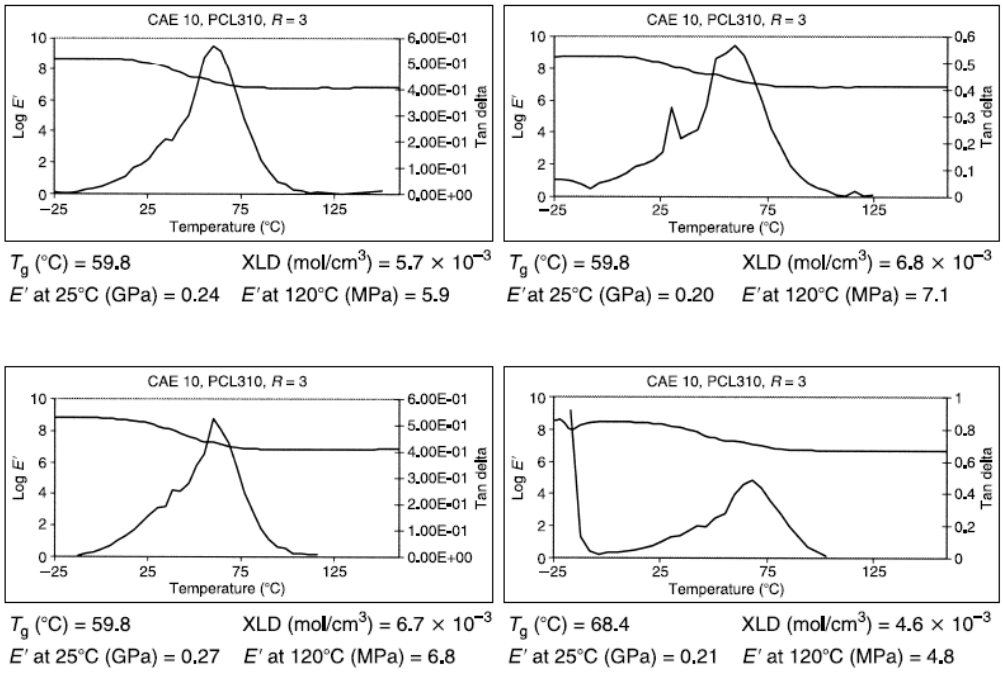

Figure 3.10. pDMTA results on four replicates on the same plate (Reproduced from ref.[5])

3.1.3. Modulus determination in a parallel dynamic mechanical-thermal analysis

Comparing between Figure 3.2 and 3.6, similarities and differences of the test geometries from conventional testing could be observed. First of all, the pDMTA experiment is that of an axisymmetric bi-layer system. The upper part of Kapton and measured polymer is free to move which is similar to that of a three-point bending test, however the bottom part of Kapton is constricted and cannot rotate. Due to the design of the pDMTA, the boundary condition of the test is neither clamped nor simply supported. Circular plate deformation with simply supported and fixed edge modes can be described with closed-form solutions. Symyx uses an analytical closed-form equation to solve the problem shown in Figure 3.6 which inherently contains assumptions and simplifications. The circular plate bending problems with a very small central circular area load are shown in Figure 3.11.

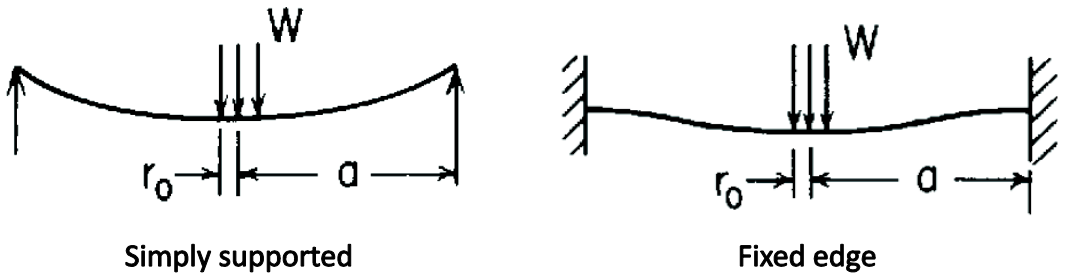

Figure 3.11. Modes of circular plate deformation: a, r_0, and W represents radius, circular area where pressure is uniformly applied, and a total force on r_0, respectively. (reproduced from ref.[6])

The two modes are different at the boundaries. For the clamped geometry, there are reaction forces in both x- and y-directions and fixed displacement whereas the simply supported problem has only a reaction force in the y-direction and there can be a rotation. Their respective bending behaviors can be described with the following equations.[6]

1) Simply supported circular plate with a uniform load over a very small central circular area (represented by r_0)

For $r>r_0$, $$y = \frac{-W}{16\pi D}\left[\frac{3+\nu}{1+\nu}(a^2 - r^2) - 2r^2 \ln\frac{a}{r}\right] \quad (3.2)$$

where r represents the distance from the center, ν is the Poisson's ratio, and D is the flexural rigidity. Flexural rigidity is a measure of resistance to bending deformation and is defined as: $$D = \frac{Et^3}{12(1-\nu^2)} \quad (3.3)$$

where E is the Young's modulus and t is the plate thickness.

At $r=0$, $$y_{max} = \frac{-Wa^2}{16\pi D}\frac{3+\nu}{1+\nu} \quad (3.4)$$

2) Fixed-edge circular plate with a uniform load over a very small central circular area (represented by r_0),

For $r>r_o'$, $$y = \frac{-W}{16\pi D}\left[(a^2 - r^2) - 2r^2 \ln\frac{a}{r}\right] \quad (3.5)$$

where $r_0' = \sqrt{1.6r_0^2 + t^2} - 0.675t$, if $r_0 < 0.5t$, or $r_0' = r_0$, if $r_0 \geq 0.5t$

At r = 0, $$y_{max} = \frac{-Wa^2}{16\pi D} \quad (3.6)$$

The composite (in this case, a bilayer) circular plate closed-form solution is derived from using a bilayer stiffness equation and the fixed-edge plate solution. The stiffness is a measure of the transverse load, *W*, as a function of displacement, y_{max}. For the fixed-edge problem, equation (3.7) shows the relationship of stiffness with other parameters.

$$k = \frac{W}{y_{max}} = 16\pi \frac{D}{a^2} \quad (3.7)$$

Next, the equation for bimetallic circular plates is used. The equivalent flexural rigidity, D_e, is the flexural rigidity of the bimetallic plates and can be written as:

$$D_e = \frac{E_a t_a^3}{12(1-\nu_a^2)} K_{2p} \quad (3.8)$$

where $$K_{2p} = 1 + \frac{E_b t_b^3 (1-\nu_a^2)}{E_a t_a^3 (1-\nu_b^2)} + \frac{3(1-\nu_a^2)^2 \left(1+\frac{t_b}{t_a}\right)^2 \left(1+\frac{E_a t_a}{E_b t_b}\right)}{\left(1+\frac{E_a t_a}{E_b t_b}\right)^2 - \left(\nu_a + \nu_b \frac{E_a t_a}{E_b t_b}\right)^2} \quad (3.9)$$

where the subscript *a* and *b* represent the polymer sample and Kapton, respectively, for our case as shown in Figure 3.12.

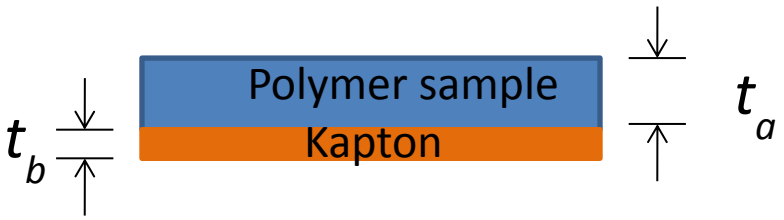

Figure 3.12. A bilayer of polymer sample and Kapton

Then, Symyx applies the equivalent flexural rigidity to the fixed-edge circular plate equation (Equation 3.7), assumes that the Poisson's ratios of polymer sample and Kapton are the same, and divides k_c by the stiffness of Kapton, k_b.

Dimensionless parameters are introduced.

$$\varepsilon = \frac{E_a}{E_b}, \tau = \frac{t_a}{t_b} \quad (3.10)$$

Substituting and arranging terms with bilayer stiffness divided by bottom layer stiffness, we have

$$K = \frac{k_c}{k_b} = 1 + \varepsilon\tau^3 + \frac{3(1+\tau)^2\left(1+\frac{1}{\varepsilon\tau}\right)}{\left(1+\frac{1}{\varepsilon\tau}\right)^2} \tag{3.11}$$

where *K* is bilayer (composite) stiffness divided by the Kapton stiffness.

Further algebraic manipulation and substitution of $\varepsilon\tau$ with μ give us a quadratic equation.

$$\tau^2\mu^2 + (4 + 6\tau + 4\tau^2 - K)\mu + (1 - K) = 0 \tag{3.12}$$

The equation is applicable for the deflection up to half of the composite thickness ($y_{max} < (t_a+t_b)/2$) and the composite thickness has to be less than a quarter of the diameter ($t_a+t_b < 2a$). The quadratic equation can be easily solved for roots and the positive is selected because the modulus cannot be a negative number. Figure 3.13 illustrates the modulus determination method in Symyx's algorithm. The required inputs are the known and measured values. The thickness of the Kapton is fixed and the sample's thickness is measured with the laser profilometer. The frequency is always set at 10 Hz, but it is a user defined parameter which can be varied. Uncoated Kapton plate stiffness is measured before polymer application. The stiffness values are input into the formula as complex numbers. Thus, $E_{coating}$, E_{Kapton}, and μ are normally complex numbers. Symyx noted that the elastic modulus of Kapton is approximately 2.4 GPa with a phase angle of approximately five degrees at room temperature. At other temperatures, the Kapton stiffness, k_b, is adjusted based on empirical corrections that have been determined through conventional DMTA measurements by Symyx. The corrected bare plate stiffness is then used twice as a part of dimensionless parameter, *K*, to calculate μ and as a stiffness value in a single layer fixed-edge circular plate equation to calculate E_{Kapton}. E_{Kapton} can also directly be obtained with a conventional DMTA experiment, thus a given choice to the user with regards to the

modulus of Kapton. In a perfect scenario, bending from fixed-edge circular plate and tensile loading from DMTA should correspond to the same elastic modulus of Kapton. The appendix to this chapter shows a step-by-step modulus calculation from an actual experimental data set.

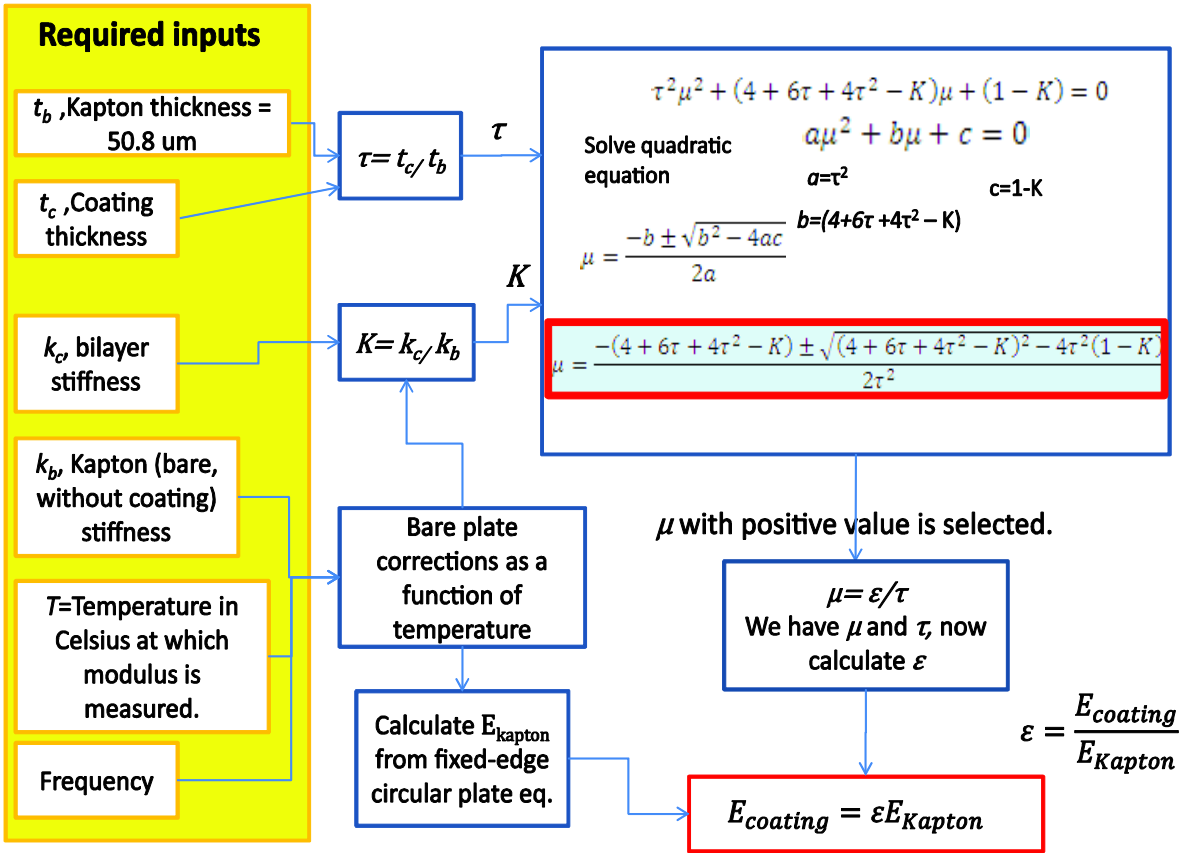

Figure 3.13. Flowchart of modulus calculation in pDMTA

The modulus results obtained from pDMTA experiments were not satisfactory, even at room temperature. A control study was done where polystyrene, poly(methyl methacrylate) and a poly(styrene-co-maleic anhydride) copolymer were each deposited on two pDMTA arrays (96×2=192 spots for each polymer). Storage moduli at room temperature for polystyrene, poly(methyl methacrylate) and poly(styrene-co-maleic anhydride) were measured to be 2.20+/-4.81 GPa, 0.65+/-1.96 GPa and 2.73+/-4.59,

respectively, which represent the coefficients of variation of 219%, 302% and 168%, respectively. Thus, it was of interest to understand the sources of errors and to improve the accuracy of the modulus output.

3.2. Investigation into Source of Errors

As with many high-throughput instruments, the accuracy may be sacrificed, but the ability to rapidly screen a library of materials has merit in the initial stages of material development. However, an error of 200% is, perhaps, too high to be a dependable high-throughput tool for mechanical property studies of materials.

3.2.1. Identify the objective and potential sources of error

From the background of Symyx's calculation method in previous section, each parameter that contributes to the modulus calculation can be clearly observed. It is noticed that the thickness parameter is to the power of three as a result of the flexural rigidity equation (equation 3.7) and its error potentially has great effect to the plate bending scheme. Thus, the profile measurement from laser profilometer and thickness calculation is examined. The method that the instrument uses to measure the stiffness is also inspected. Then, finite element analysis is used to assess the accuracy of the closed-form solution (equation 3.12). Figure 3.14 illustrates the potential source of errors that are considered. The objective is to understand the process and reduce the errors as much as possible.

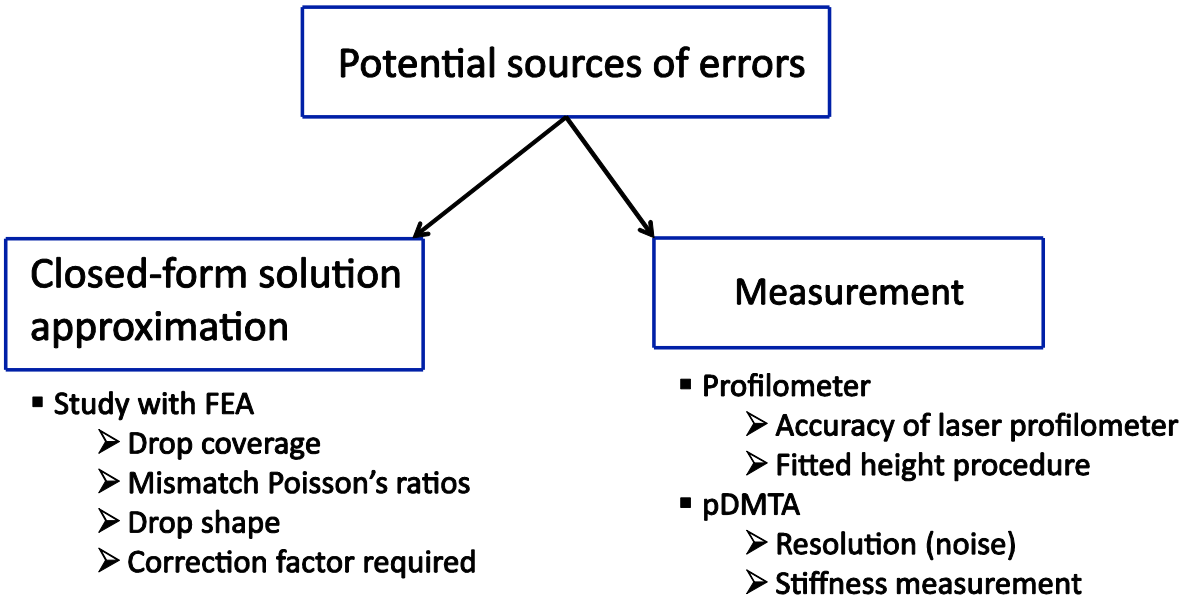

Figure 3.14. An outline of potential source of errors

3.2.2. Sources of errors

3.2.2.1. pDMTA sample array preparation

Kapton film is supplied with an adhesive backing except on the perforated spots. The film with adhesive is attached on to the perforated aluminum plate. Weights are used to compress the Kapton, with a rubber sheet in between, to the aluminum plate for a tight bond. The pDMTA plate is baked in a vacuum oven overnight at 140°C. Sand blasting can also be used to roughen the Kapton surface to improve the adhesion of the polymer sample. It can be observed that after the plate preparation, the Kapton film over the hole appears to have been deformed from stretching due to baking with a rubber sheet or with the sand blasting procedure. Symyx uses a Keyence LT-8110 Laser confocal displacement meter and mounts it on top of an x-y translation stage for the thickness measurement. Here, the laser profilometer is used to observe the curvature of the Kapton film on a prepared pDMTA plate. The laser is adjusted to approximately move through the center line of the

perforated plate location in one direction creating a single 2-D profile. The 2-D traces on ninety-six locations for the pDMTA plate with Kapton are shown in Figure 3.15.

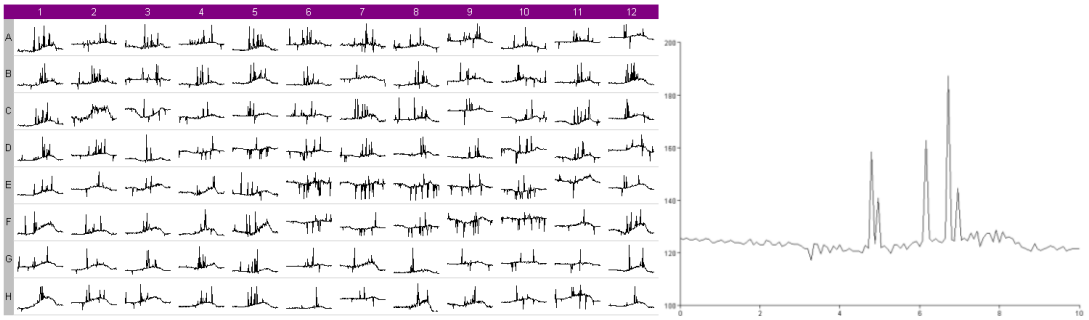

Figure 3.15. A screen shot of Kapton profiles: 96 profiles (left) and an individual profile showing a flat substrate and noise spikes (right)

Figure 3.15 shows that the as-received Kapton sheet is relatively smooth within 10 µm. It also shows the random noise of the profilometer. Figure 3.16 confirms that the Kapton film has changed its shape and that curvature is created over the circular free-film area. Both the baking method and sand blasting have been examined independently and both contribute to the permanent deformation.

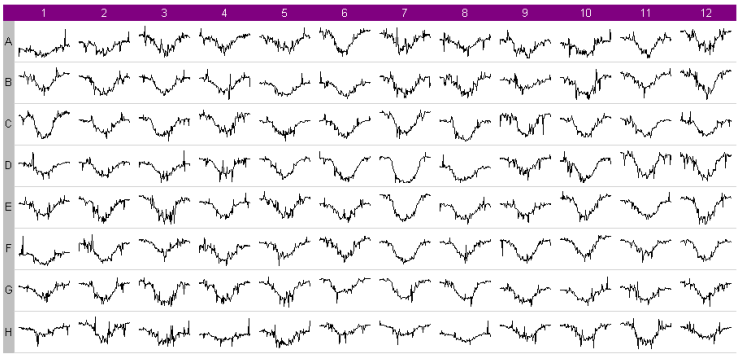

Figure 3.16. A screen shot of Kapton profiles after baking and sand blasting

The formed curvatures range from 10 µm up to 100 µm for the vertical displacement between the edges and the center point. In the baking method, the Kapton over the circular hole is pushed and likely creeps under elevated temperature overnight.

Sand blasting is performed with a protected sheet which only exposes the area over the circular hole. Using an optical profilometer, Figure 3.17 confirmed again that the Kapton substrate is curved. Also, the optical profilometer is used to see if the curvature occurrence is due to only the material removal into a dipping shape or the Kapton is being stretched. This is done by scanning the backside of the Kapton as shown in Figure 3.17. From this figure, the rough surface on the front side as a result of sand blasting, whereas the back is smooth, is shown. It is confirmed that the Kapton layer over the circular hole has been stretched through the processing. The result is the change in the test geometry that was not anticipated.

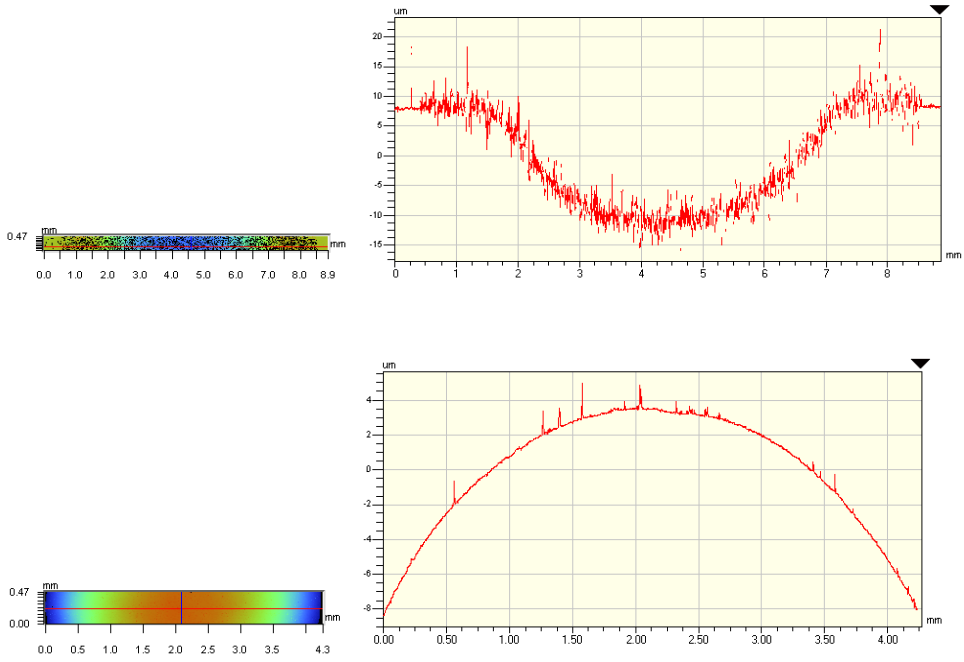

Figure 3.17. The front side of sand blasted Kapton film (top) and the back side of Kapton film (bottom)

3.2.2.2. Thickness measurement

After the polymer is deposited and cured on the pDMTA plate, the thickness of the polymer sample has to be measured and calculated. The automated laser profilometer is

specifically intended for this cause. The instrument is part of the workflow of pDMTA set-up for thickness measurement as seen in Figure 3.7. An example of polymer profiles on the pDMTA plate is shown in Figure 3.18. Originally, the data was recorded over a distance of 8 mm for each spot which means 4 mm on either side of the center point. The circular hole is approximately 5 mm. Thus, there should be enough room if the polymer solution can be dispensed to give a consistent droplet size. The problem occurs when the polymer solution spreads out beyond the 8 mm range because the Kapton bottom layer cannot be seen.

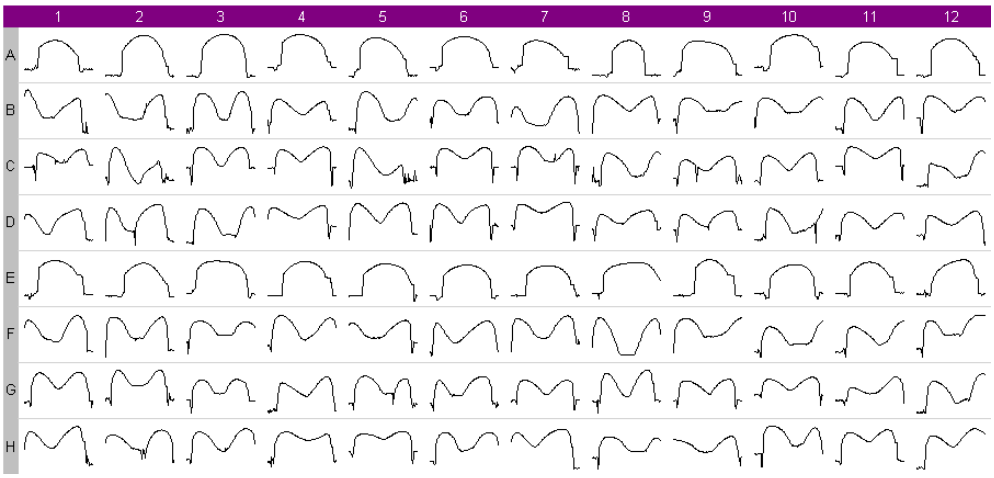

Figure 3.18. 96 droplet profile data from laser profilometer

Figure 3.18 shows that the edge showing the Kapton substrate may not appear on one or both sides of the polymer sample. This is very important because the thickness calculation depends on finding the Kapton at the edges. The measurement range was extended to 10 mm for future experiments after this finding. Figure 3.18 also shows two common shapes of these cured polymer sample. The cured droplets show either a smooth curvature or a dip at the center of the drop. The two types are clearly shown in Figure 3.19.

The 2-D profiles from the previous figures exaggerate the visualization of curvature. It should be noted that the x-scale is in millimeters and the y-scale is in micrometers, thus the droplets can be considered as relatively flat. In Figure 3.19, the blue

dots represent the data points. A fitting was performed to find an equivalent thickness/height of the droplets. An algorithm from Symyx was used to find the base on both sides, zero the data at the calculated base, adjust the height data on the polymer droplets according to the base height, and calculate a mean average of those data for the droplet profile. The deposited pDMTA plates were tested for the accuracy and precision of the thickness measurement. The thickness measurement was done six times on each plate. Six thickness values on each spot were averaged. The standard deviation and the relative error (coefficient of variation) on each spot was calculated. Figure 3.20 shows the relative errors versus average thicknesses on 96 spots on a pDMTA plate. Polymer thicknesses of 200 µm to 400 µm have less than 10% error. However, when the coatings are in a 100 µm range, the errors densely scatter around 5% to 40% and reach almost 70% error.

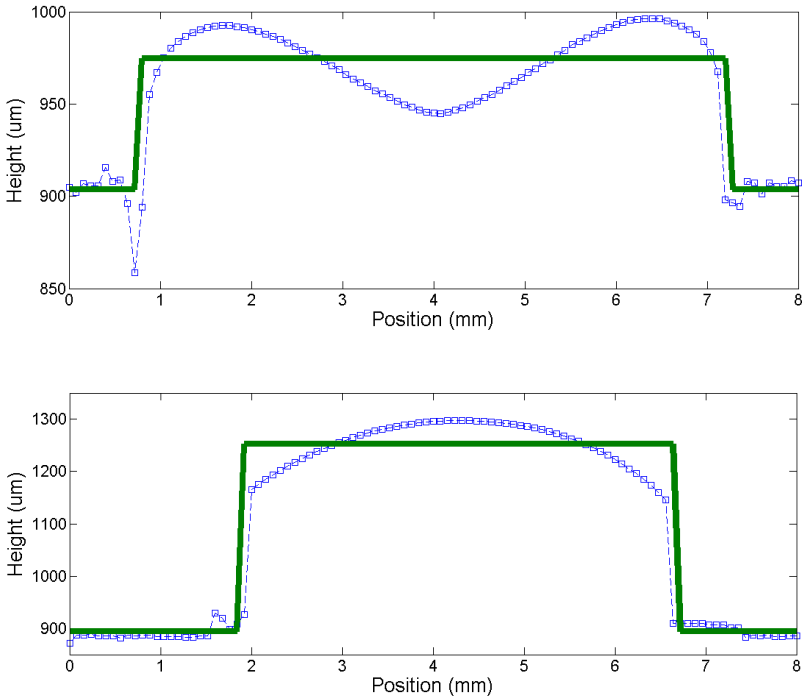

Figure 3.19. 2-D profiles of the cured polymer droplets: blue dots represent the data points and the green line represents the equivalent profile

Accurate thickness values are essential in modulus determination, thus the automated laser profilometer was tested against a contact profilometer. Figure 3.18 shows a row scan of droplet profiles using the contact profilometer (dotted line) and the laser profilometer. The results indicated that the laser profilometer is adequate in obtaining 2-D profile because, as shown in Figure 3.21, the traces match reasonably well. To improve the accuracy, the scan rate is set lower to limit the random spike effect in the averaging and for smoother operation of the stepping motor under the sample holder. This laser profilometer has a measurement range of 2-mm. It is found that the laser focus sometimes needs to be adjusted to make sure that the cut-off does not occur.

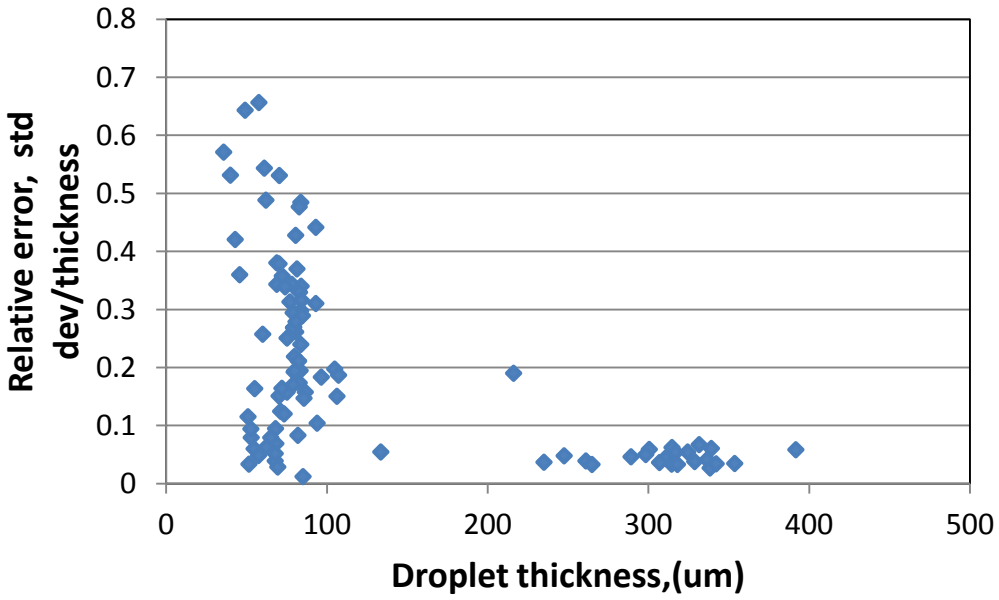

Figure 3.20. Thickness measurement

The calculated thickness is averaged without considering the size of the drop coverage. In Figure 3.19, it is shown that the drops can be slightly thicker at the edges, but if they are much farther from the 5-mm circular perforated area, they do not interfere with the testing scheme. This issue can be fixed by having the mean average done only for 5-

mm range above the 5-mm circular area. The effects of polymer drop coverage and shapes were studied further using finite element analysis.

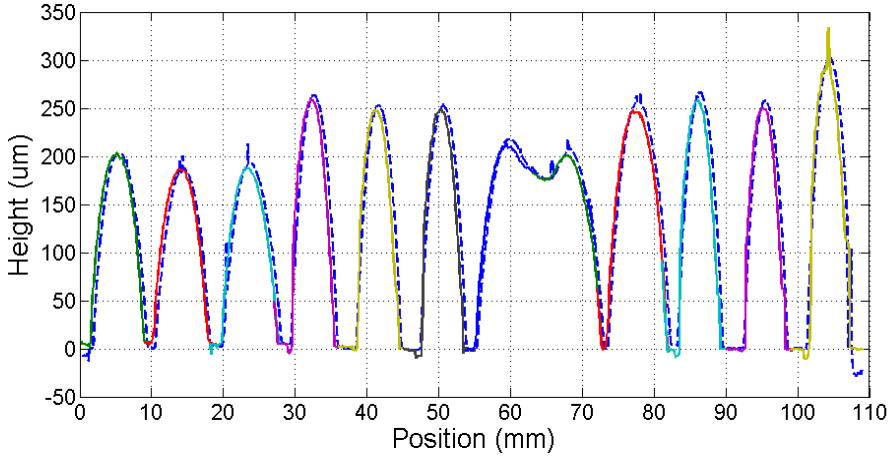

Figure 3.21. A row profiles from contact profilometer (dotted line) and laser profilometer.

3.2.2.3. Stiffness measurement

In pDMTA, the changing load is monitored with respect to a sinusoidal amplitude of 5 µm to determine the plate stiffness. Figure 3.22 shows stiffness data taken as a function of the positioning driven into the Kapton. The inner workings of pDMTA are described in the patent.[7] Two actuators are used to run the test. The first actuator is used to move the plate in and out of pin contact. The second actuator is to provide an oscillating motion. For our test, it is set at 10 Hz and a 5-µm amplitude. From Figure 3.22, the Kapton made contact with the pin from the right side (positive number positioning) and the stiffness measurement was taken as a function of the coarse positioning which is controlled by the first actuator. The first actuator is set to move at 2.5 µm per step, which is half of the oscillation amplitude. Figure 3.22 shows the Kapton data and the bilayer data. The steep slope occurs because, initially, the pin does not have a constant contact as the plate is oscillating in and out of the contact. As the first actuator moves in further, the full contact is made and there is a rapid rise in stiffness value. The instrument will look for a

predetermined threshold value (e.g. 25 N/m). Once the stiffness gets above a threshold value, the stiffness data is recorded at 2A/C+1 steps later. The 'A' represents the amplitude and 'C' is the first actuator translation distance per step. Thus, the stiffness result is used at the fifth step (2(5/2.5)+1= 5) after the threshold is reached. This is to ensure that the linear region of the stiffness is taken because the stiffness will non-linearly increase at a certain displacement as a result of a deviation from the theoretical plate deformation. This means that pDMTA records the stiffness data at approximately 10-15 μm from the point of contact.

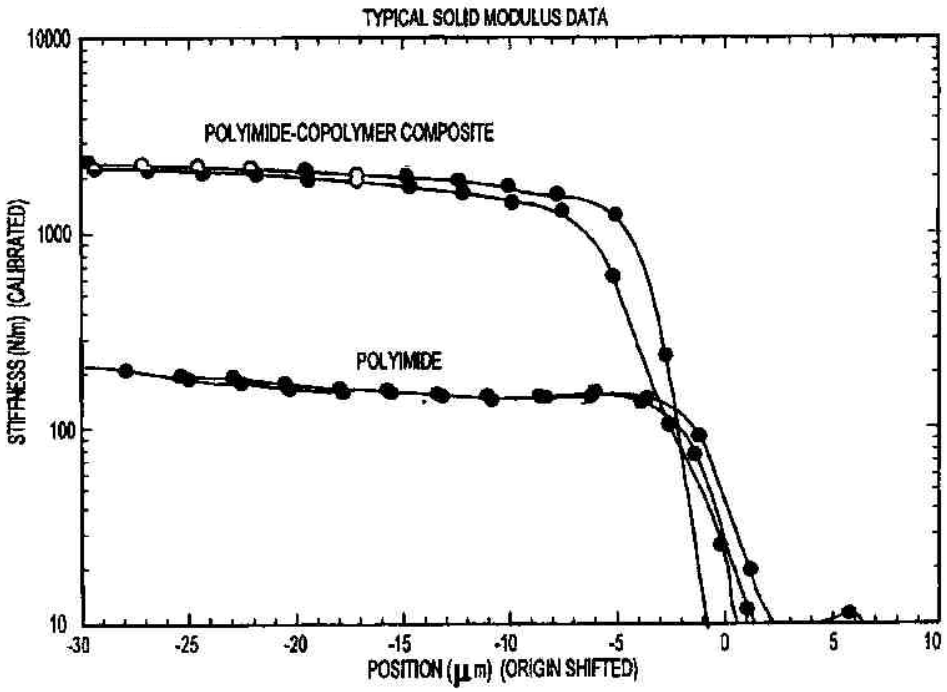

Figure 3.22. Stiffness measurement on pDMTA (reproduced from ref.[7])

The method of taking data is sound, but it is the nature of the size of the pDMTA plate with respect to the test displacement that is a major issue. The problem occurs because the contacts on all 96 pins cannot be made at the same time. From the first to last, the distance can typically be ~100 μm on the actuator displacement. The settings are

defined regarding the minimum number of pins in contact, to maximize data collection, and the maximum actuator displacement to prevent damage to the sample. Permanent deformation on the Kapton was observed where the contacts were made earlier, especially at higher than approximately 80°C, as a result of the pin pushing in. Thus, the geometry of the testing scheme changes during the experiment which is not accounted for.

3.2.2.4. Closed-form solution

The question is how accurate the closed form solution is and whether the range of moduli and polymer thicknesses can affect the approximation. The data in Figure 3.23 can explain the limitation of differentiating thick coatings from one another. In this Figure, different bilayer stiffnesses are input into the closed-form bilayer solution and the thicknesses of the top layer are varied. The elastic moduli (assuming no viscous part) are plotted as a function of thicknesses with constant bilayer stiffnesses.

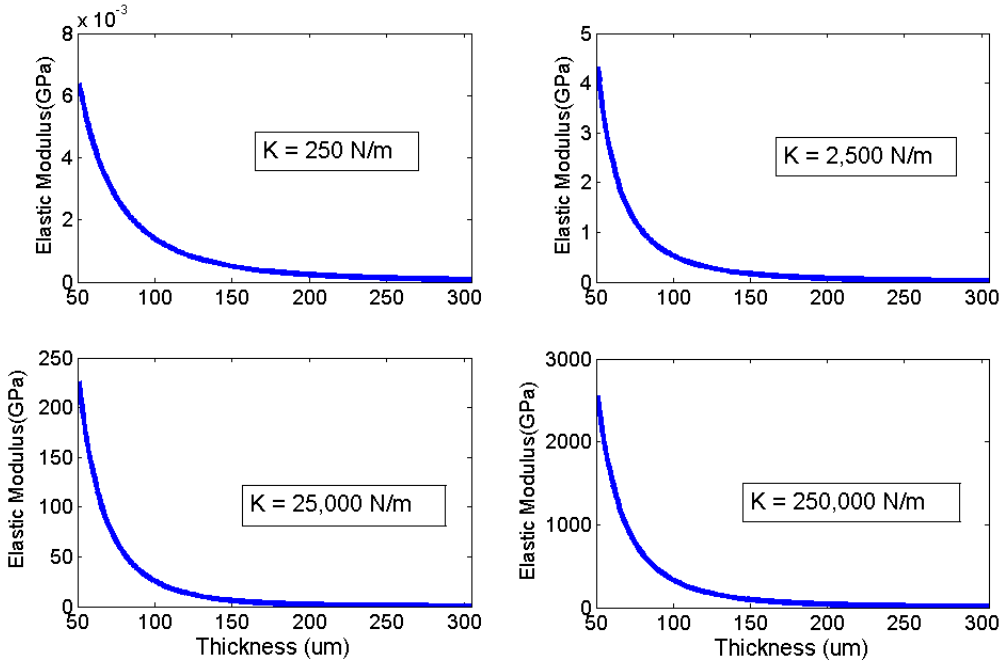

Figure 3.23. Sensitivity of closed-form solution varying with thickness of top layer

The curves in Figure 3.23 have similar shapes and they all start to display plateaus at approximately 200 μm. A steep slope in the measurement range is desirable because it would indicate the ability of the equation to separate different moduli on materials with similar thicknesses. The operating thickness range for the pDMTA instrument is quoted to be between 5 μm and 200μm. It makes sense that, intuitively, if the polymer droplets become very thick, plate bending stresses will no longer be uniform. The rigidity of the plate may transform bending into indenting on the surface of Kapton. As a result, the thicker the droplet, the more the close-form solution becomes problematic. It is necessary to look into the accuracy of the closed-form solution with respect to the thickness and other variables. Finite element analysis (FEA) offers a simple computer intensive method to study the problem without complicated analytical mathematics.

3.3. Experimental

If any material can be made to form flat droplets with similar thicknesses, the comparison would be based mainly on the accuracy of the stiffness measurement. However polymer solutions have different surface tension, viscosity, drying shrinkage and solids content and as a result the thicknesses of the polymer films can vary from 30 μm to 400 μm. It is desirable to see the effect at which point the discrepancy starts to occur based on the closed-form solution and pDMTA bilayer testing geometry. Finite element analysis software package, COMSOL 3.5a, was used to model a static axial symmetry plane stress problem with contact surfaces. In structural mechanics, there could be three main sources of nonlinearity; 1) geometric nonlinearity, 2) material nonlinearity, and 3) boundary nonlinearity.[8] The geometric nonlinearity, for example, represents large deformation and large rotation problems which do not supposedly apply to our problem according to the

design of the pDMTA testing scheme. Material nonlinearity represents time-dependent, stress/strain dependent material properties, and temperature dependent. It involves elasto-plastic, hyperelastic, viscoelastic, and creep material properties. It is assumed that the strain is small enough that the stress is below the yield point which is s valid assumption with respect to the intended design. Viscoelastic and creep are neglected as the model focuses on the static response (independent of temperature and time) which implies storage modulus calculation. The model experiments with the relationship between force and elastic properties of the top and bottom layers. Boundary nonlinearity relates to contact surfaces that are not perfectly bonded and friction. The boundary nonlinearity of contact pair is applied to our problem which better approximates the real problem than using a point load or a constant boundary load.

3.3.1. Geometry of the test

The circular area is 5 mm in diameter. The thickness of the Kapton is 50.8 µm. The thickness of the coating is a variable. An optical profilometer was used to find the pin size. The result is shown in Figure 3.24. It is the scan of the impression made in wax by the pin. The curvature fitting is done using MATLAB with optimization toolbox to a nonlinear least squares fit of an exact equation of a circle to the x-y data. The curvature was fitted into an arc of a circle to estimate the radius of the pin. Figure 3.24 shows the trace of 2D-profile (green line) and the fitted arc (blue line). The result from the selected scan line in Figure 3.24 gives a 2.11 mm radius. A 2 mm radius was used for the FEA model. This includes all the required geometric parameters.

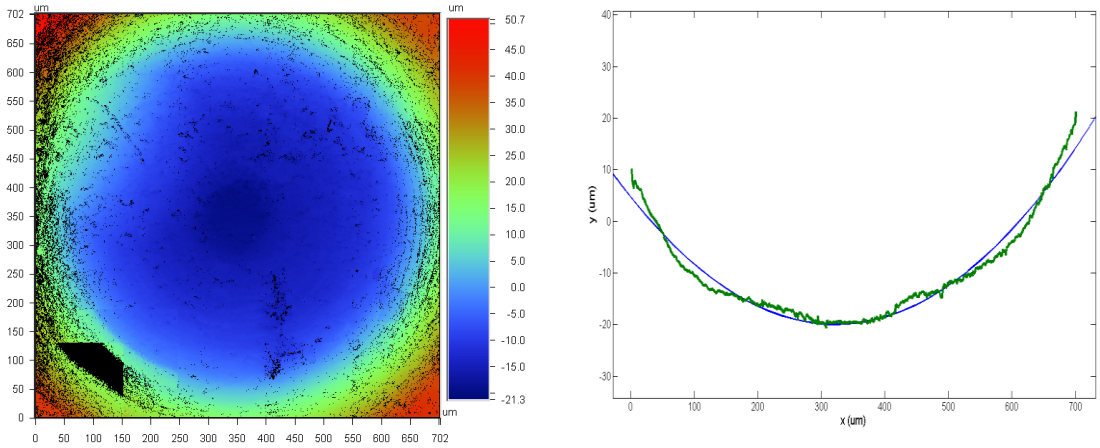

Figure 3.24. Laser profilometer: Color contour showing 3D-profile on the wax (left) and a 2D-profile with a fitted curve, blue line (right)

3.3.2. Finite element model

The model with meshing is shown in Figure 3.25. The model simulates the testing scheme as shown in Figure 3.6. The 2-D axisymmetric model reduces the computational time and complexity.

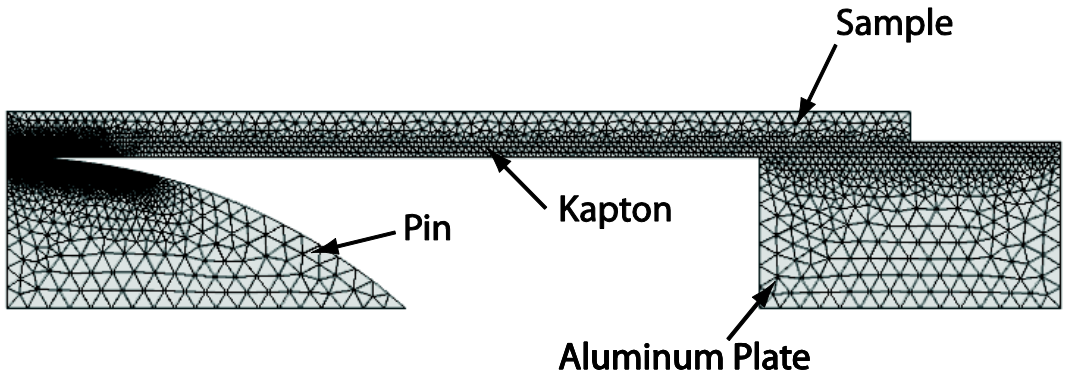

Figure 3.25. Finite element model of pDMTA

Triangular (advancing front) elements are used for all the subdomains. Material properties are isotropic and perfectly elastic. A frictionless contact pair between the indenter and the film is specified which means that the surfaces are free to slide with no friction. Also the layers between the polyimide and the coatings and between the polyimide

and the aluminum are perfectly bonded composite interfaces. These assumptions are reasonably valid within the designed range of operation of the instrument. The model allows us to conduct numerical experiments with neither a simply supported nor clamped plate problem. The model also takes into account increasing finite contact area with displacement and the effect of mismatch of Poisson's ratios on the modulus determination. However, the adhesive layer between the Kapton and the aluminum plate is neglected. Symyx did a linear fit on storage modulus curve of Kapton from conventional DMA.[9] According to the fit, at 25º C, the storage modulus of Kapton is estimated to be 2.36 GPa. The Poisson's ratio of Kapton is quoted at 0.34. In the FEA, we vary the coatings' modulus (a range of 0.5 MPa to 10 GPa), Poisson's ratio values (0.34 and 0.49), Kapton's modulus (2.36 GPa and 2.50 GPa), coating thicknesses, coating coverages relative to the hole, and Kapton's curvature due to the substrate preparation.

Firstly, since there was a slight variability in the pin size measurement from the wax impressions, the model with only Kapton layer is tested against various pin sizes. The result is shown in Figure 3.26. The force is divided by a pin displacement of 10 μm to calculate the stiffness. From 1.0 mm to 4.0 mm, the change in stiffness measurement is only 0.3%. Thus, an accuracy of the pin size is insignificant with respect to 10 μm displacement in this simulation.

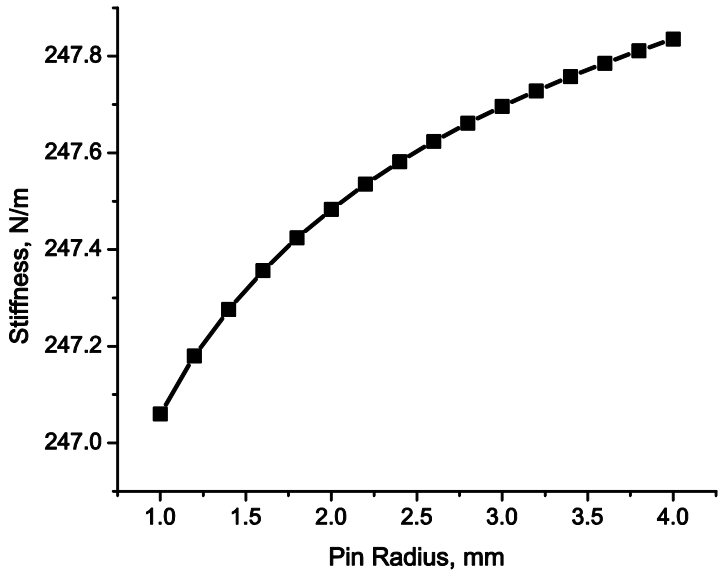

Figure 3.26. Pin size effect with stiffness for Kapton with Young's modulus of 2.5 GPa and Poisson's ratio of 0.34

3.4. Results and Discussion

Figure 3.27 shows the force versus displacement results from FEM. The solid line represents a bare plate deformation.

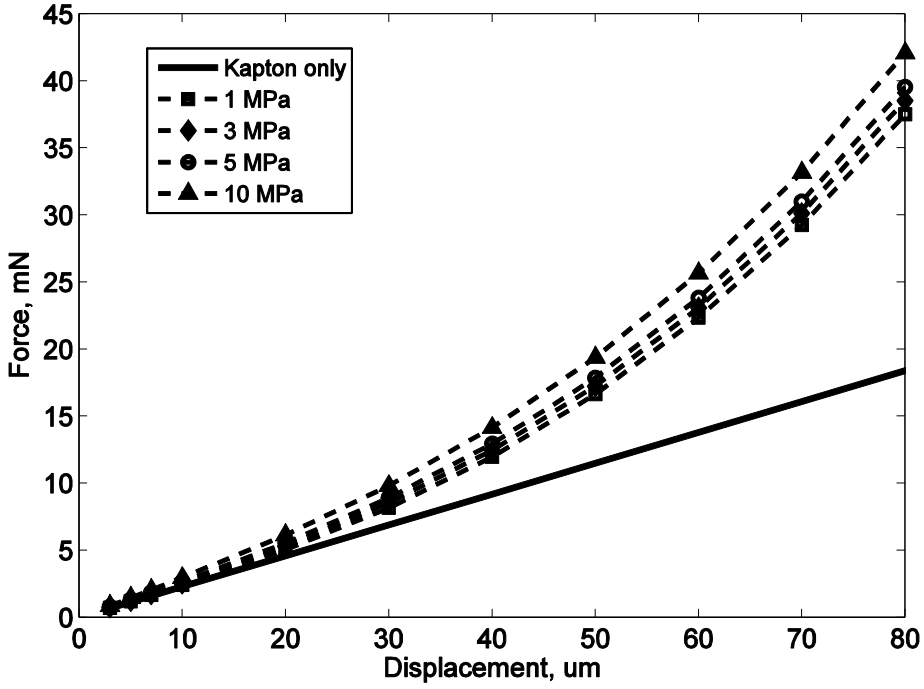

Figure 3.27. Simulated experiment with $\nu_{coating} = 0.49$

Each curve represents a different Young's modulus for the coating layer. The results show the nonlinearity of the curves as the displacement increases. The range of moduli is common for materials with rubbery behavior. At less than 20 μm displacement, the slopes, which are a measure of stiffness, are quite similar. According to the patent, the stiffness data is collected around 10-15 μm displacement with 5 μm oscillation. Observing the slope of each curve at 10-μm displacement shows the probable difficulty to distinguish each response. This shows us that there may be a problem in differentiating materials with low modulus due to the effect of a much stiffer Kapton. Figure 3.28 is similar to Figure 3.27, only at higher elastic moduli.

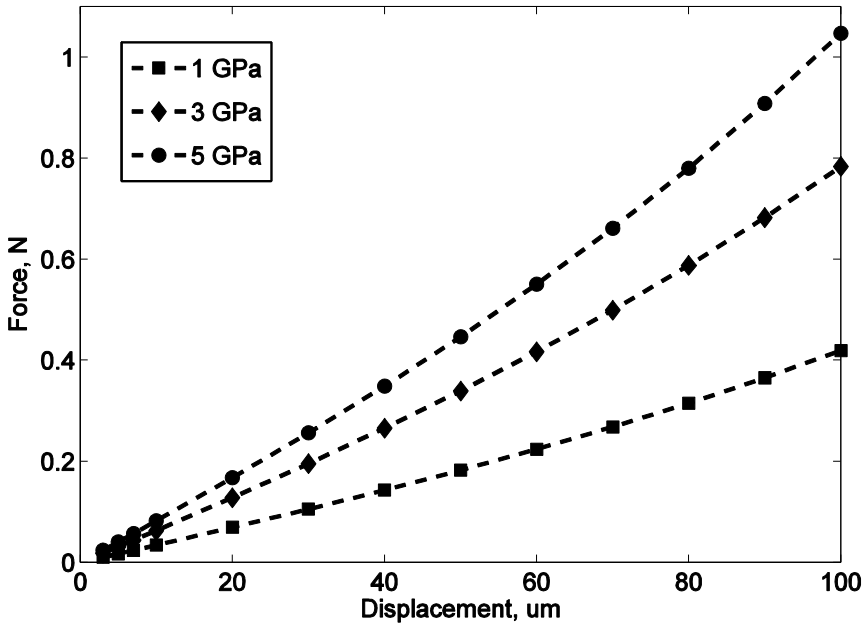

Figure 3.28. Simulated experiment with $\nu_{coating} = 0.34$

The curves in Figure 3.28 show a much higher force than those in Figure 3.27, thus each response is easily distinguished from the bare Kapton substrate and among each other. From the simulated experiments, the stiffness is calculated from the force data divided by the displacement (chosen at 10 μm). Only real numbers are used because the simulated

experiments are static with no time-dependence in material properties. The elastic modulus from the simulated experiments can be obtained by solving the closed-form equation as shown in Figure 3.13 using the simulated stiffness measurements. Thus, the model properties input versus the predicted properties from simulated experiment can be compared, or more specifically, the elastic modulus input for the coating versus the calculated elastic modulus via simulated bi-layer plate bending testing. The elastic modulus input for the coating represents the actual elastic modulus of the coating in real test and the calculated elastic modulus represented the measured modulus given by the pDMTA instrument. The correction factor can be obtained by dividing the elastic modulus input (actual) by calculated modulus (measured).

$$Correction\ factor = \frac{E\ from\ FEA\ input}{E\ calculated\ from\ simulated\ stiffness} \tag{3.13}$$

The correction factor, as shown in Equation 3.13, is based solely on FEA with its associated assumptions and the closed-form solution in Equation 3.12. In other words, the correction factor is a measure of the deviation between the actual and calculated output. It is a measured error perceived by using the closed-form solution. In the next section, coating coverage is studied to confirm our intuition that the coverage needs to be large enough to cover the entire perforated area. The correction factor will become a correcting tool, as the name implies, once the thickness effect is studied.

3.4.1. Effect of coating coverage

Next, the different coverage areas of the polymer droplets/coatings over the Kapton are modeled. The coverage has to be small enough that the laser profilometer can find the edges, but large enough for a uniform bilayer model to work. Figure 3.29 shows simple changes in the axisymmetric model to test the effect of the coverage. The size of the top

layer is varied as a ratio of the hole radius. 90%, 100% and 110% coverage areas are shown in Figure 3.29. Figure 3.30 shows coating coverage versus correction factors. The x-axis represents the ratio of coating radius and the hole radius, whereas the y-axis represents the correction factors.

Figure 3.29. Examples of FEM for testing coverage of the top layer; showing three models in coverage of 0.9, 1.0, and 1.1

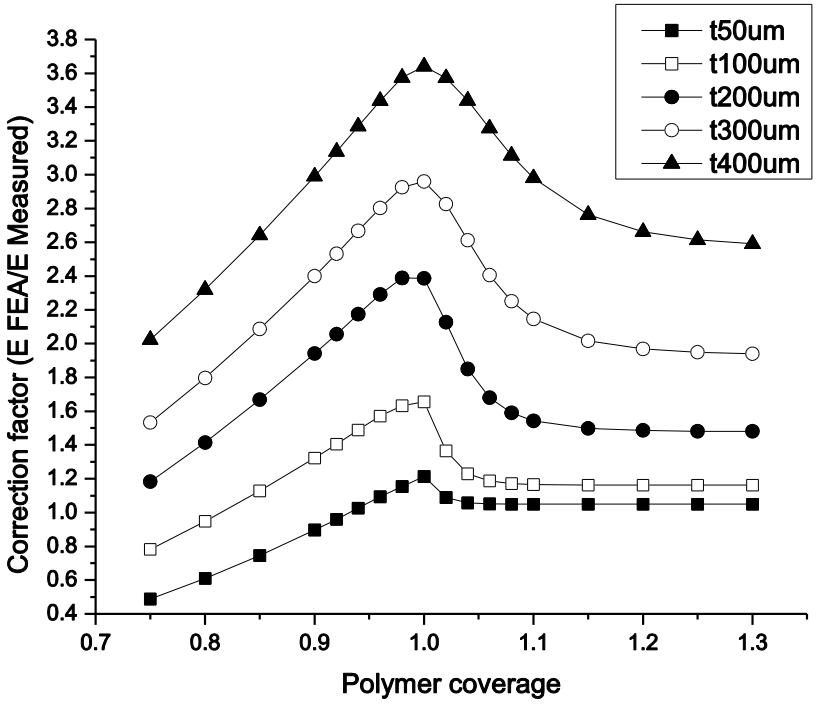

Figure 3.30. Droplet coverage effect

For the study of this effect, the modulus of coating was set to 3 GPa with a Poisson's ratio of 0.34 and the modulus of Kapton was 2.36 GPa. From Figure 3.30, it means the result is converging with higher coverage which can be seen from the plateau on the right side of each curve and the coverage of 1.2 is sufficient for up to 300 μm thick coating. Thus, it is important for the polymer droplet/coating to cover the entire circular

area and extend beyond by about 10% for coatings in the recommended 100-200 μm thickness range.

3.4.2. Effect of coating thickness

A noticeable trend in Figure 3.30 is the monotonic changes of correction factors as a function of thickness. It is desirable to be able to correct the result with respect to the thickness of the coating, so that higher accuracy can be achieved through pDMTA. The simulations were run in a 'for loop' to execute COMSOL commands for the following parameters:

Young's modulus of Kapton = [2.36, 2.5] GPa

Young's modulus of Coating =[0.5, 2, 3, 5, 7, 10, 20 ,30 ,40, 50, 60, 70, 80, 90, 100, 150, 200, 250, 300, 350, 400, 450, 500, 600, 700, 800, 900, 1000, 2000, 3000, 4000, 5000, 7000, 10000] MPa.

Poisson's ratio of Kapton = 0.34

Poisson's ratio of coating = [0.34, 0.49]

Thickness of coating = [20, 30, 40, 50, 100, 150, 200, 250, 300, 350, 400] μm

Displacement of the pin = [3, 5, 7, 10, 20, 30, 40, 50] μm

Figure 3.31, which is again based solely on FEA and the closed-form solution, gives the overview of correction factors as a function of calculated (measured) modulus for different thicknesses for the coatings with Poisson's ratio of 0.34. Each curve represents a specific thickness value with varying elastic moduli. The figure shows thicknesses range from 30 μm to 400 μm. The x-axis is elastic modulus values in log scale.

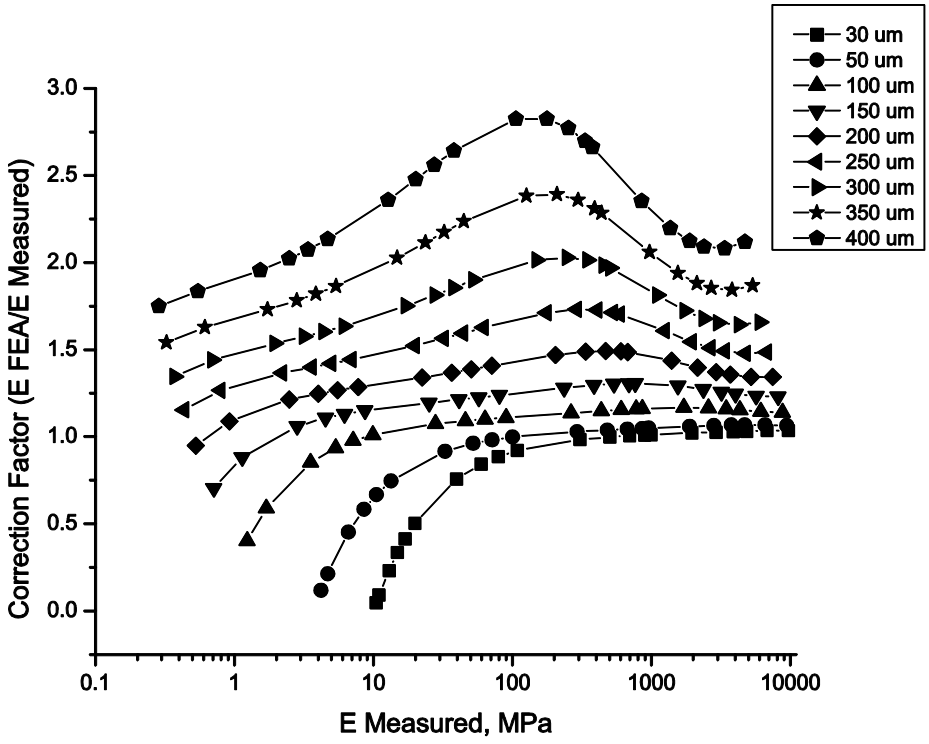

Figure 3.31. Correction factor curves with $\nu_{coating} = 0.34$ and $E_{Kapton} = 2.36$

The inherent discrepancy between the modulus input and the calculated output can be seen from the finite element analysis result. Important observations can be made from the nature of the correction factor curves. In the high modulus range, a thicker coating contributes to a larger error in the calculated result. It is postulated that with a thick coating the distributed bending stress is no longer uniform and may even be combined with the indentation mode due to high flexural rigidity. According to FEA, the closed-form solution is accurate when the correction factor is only equal to 1. When the correction factor is higher than 1.0, it means that the closed-form solution with its associated simulated stiffness results underestimates the input modulus. Unfortunately, the area is very limited to specific combinations of modulus and thickness. From modulus of 300 MPa to 10 GPa, 30 μm-, 50 μm- and 100 μm-thick films give the best results because the errors are minimal. Symyx recommends making the polymer film 100-200 μm. But for a 200 μm-thick film,

there could still be up to 35% error as seen in Figure 3.28. A thickness of 100 µm seems to be an optimum for minimal errors for a broad range of moduli. However, for 30 µm-, 50 µm- and 100 µm-thick film, the accuracy drops rapidly at the lower modulus range and the closed-form solution overestimates the input value.

3.4.3. Correction factor

One of the goals is to utilize correction factors to improve the accuracy of the measurement which deviates from the actual value. The actual value refers to the actual material property which is represented by the Young's modulus input in the FEM. The measured value from pDMTA is then represented by the calculated value from the simulated stiffness. The measured modulus from pDMTA with a known thickness can be used together to find the appropriate correction factor by interpolating the data in Figure 3.31. The three variables here are the correction factor, modulus and thickness. The surface fit can be executed to relate the three parameters using a 'nonlinear surface fit' function in OriginPro 8. The data points in Figure 3.31 are deliberately spaced. There are more data points in the magnitude of 1 GPa because that range of modulus can be easily tested for an improvement in accuracy. Equation 3.14 shows the selected surface fit equation.

$$z = z_0 + ax + by + cx^2 + dy^2 + fxy \tag{3.14}$$

where x is $\log_{10}$ of the modulus, y is the thickness, and z is the correction factor.

To avoid biasing of larger numbers on the fit, we take the logarithm of the measured moduli. Figure 3.32 shows the result of the surface fit using Equation 3.14. The colored contours represent values in Figure 3.31 whereas the contour lines represent the fitted curve. The selected equation fails to approximate the overall trend at higher thickness. Above 300 µm thickness, the fit cannot follow the changes. Thus, it would make

sense to either split results in Figure 3.31 to two parts for two independent fits or to include more terms into Equation 3.14. Table 3.1 give the fitting ranges with their corresponding fitted parameters. In the following section, the correction factor will be applied to experimental data. By separating the data into smaller segments, we make sure that the error from interpolation is minimized. Figure 3.33 shows the fit with limited range of thickness from 50 μm to 150 μm and with a limited range of modulus in GPa region. The overall fit is improved from the one in Figure 3.32.

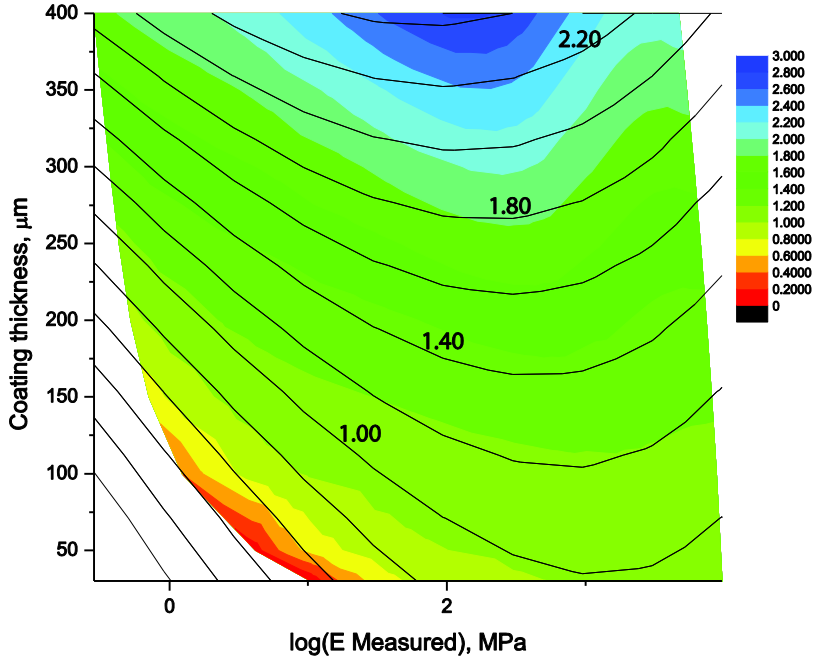

Figure 3.32. Nonlinear surface fit

Table 3.1. Coefficients for interpolation equations

Coefficient	Fitting range			
	E = 0.5 MPa to 10 GPa, *v* =0.49	**E = 0.5 MPa to 10 GPa, *v* =0.34**	**E= 0.5 MPa to 500 MPa, *v* =0.49**	**E = 500 MPa to 10 GPa, *v* =0.34**
z_0	-0.22677	-0.14837	0.07383	1.45063
a	0.65369	0.65846	0.28132	-0.42076
b	0.00459	0.00467	0.00347	0.00598
c	-0.10472	-0.10201	-0.02248	0.0842
d	2.5754E-6	2.37601E-6	2.77036E-6	5.14018E-6
f	-7.71276E-4	-7.133E-4	9.84997E-5	-0.00151

Poisson's ratio of the coating also has an effect on the results. Thus the two values are used to give estimates. Figure 3.34 shows the correction factor curves for Poisson's ratio of 0.49 with the modulus of Kapton of 2.36 MPa. Compared with Figure 3.31, the curves shift slightly lower.

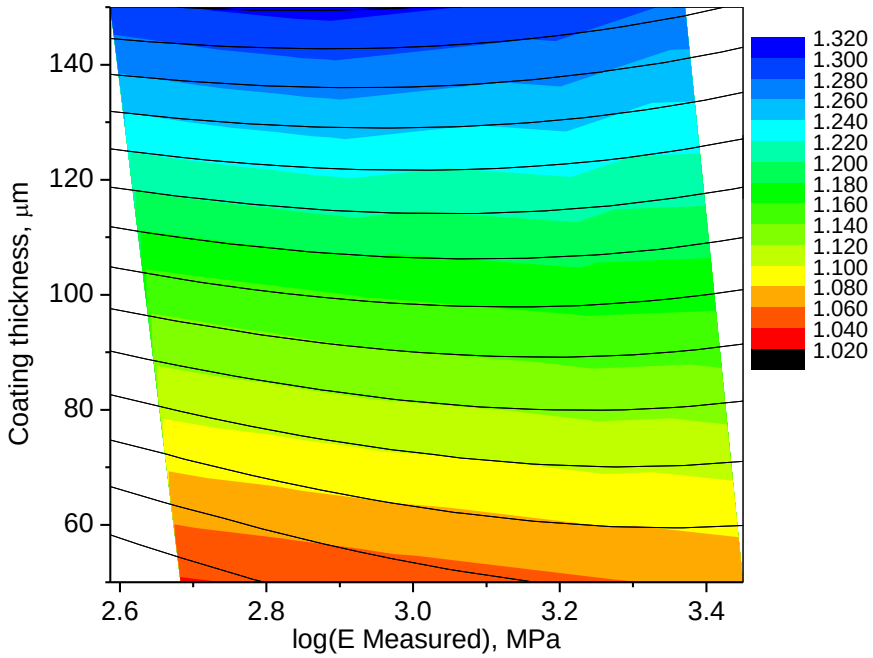

Figure 3.33. Nonlinear surface fit: $\nu_{coating} = 0.34$ and $E_{Kapton} = 2.36$

To exactly follow the assumption in closed-form solution, the Poisson's ratios of the coating and Kapton need to match which is at 0.34 in this case. Realistically, most elastomeric films have Poisson's ratio around 0.49 and hard polymers such as epoxy and polyurethane have Poisson's ratio of around 0.3-0.4.[10] Thus, it is reasonable to use equations for low modulus with a Poisson's ratio of 0.49 and for high modulus with a Poisson's ratio of 0.34.

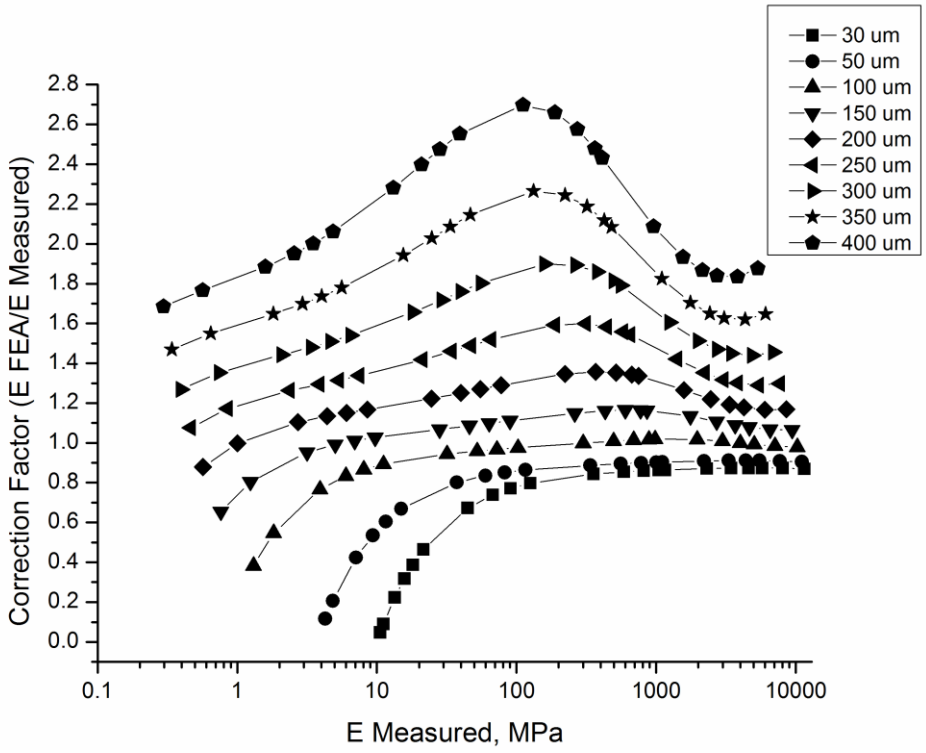

Figure 3.34. Correction factor curves with $\nu_{coating} = 0.49$ and $E_{Kapton} = 2.36$

3.4.4. Improvement of the results using correction factors

Coatings were made to identify any improvements in using the correction factor. A polyurethane clearcoat (Joncryl 901 plus polyisocyanate crosslinker, Basonat® HI 100 from BASF) was deposited at different thicknesses using a cube film applicator. The cube film applicatior has gaps of the same width and varying heights. The gap width is 16 mm. The applicator was passed through the center of a 5-mm testing area. Figure 3.35 shows cured coatings deposited on the pDMTA plate. The testing spots were reduced from 96 to 32 spots as a result of the deposition method.

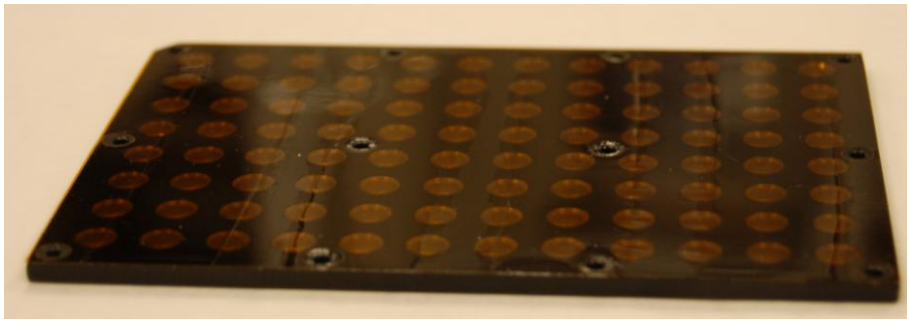

Figure 3.35. Four columns of drawdown coating at different thicknesses

The reason for selecting this deposition method is to maximize the uniformity of the coating over the testing area, whereas a droplet of polymer solution over the 5-mm hole can yield a concave or a convex dried droplet depending on the surface energy and volume of the polymer solution. Then the thicknesses were measured with the laser profilometer using a custom-made MATLAB program. The program located the edges and performed linear regression through the data points on the edges as shown in Figure 3.36 in the top graph. Then, the program performed leveling and the mean average over the 5-mm area was used.

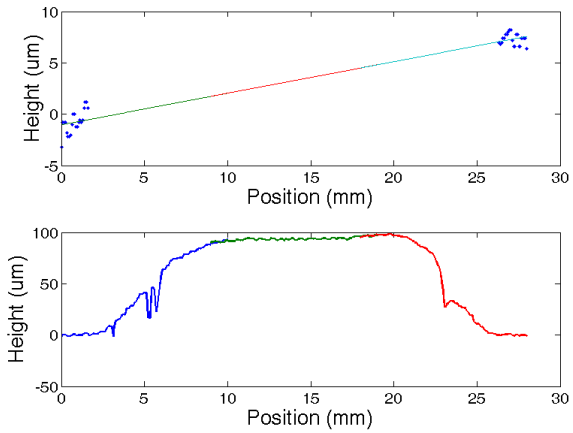

Figure 3.36. Thickness calculation for plate in Figure 3.32

The modulus is calculated using the instrument's composite stiffness output and the closed-form solution. The result of the modulus calculation at room temperature for different thicknesses and the corresponding corrections are shown in Figure 3.37.

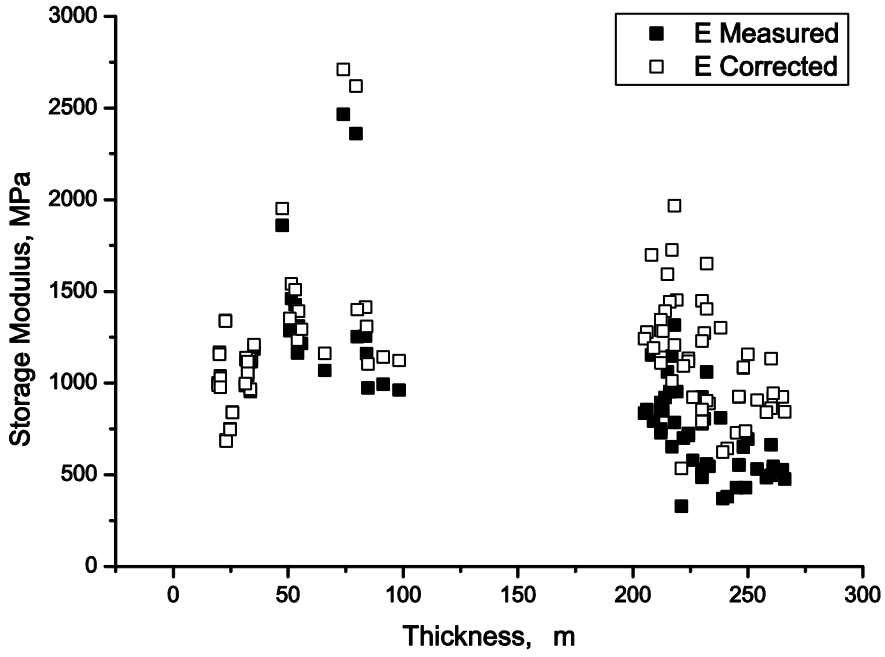

Figure 3.37. Results show scattering and improvement from using correction factors

Modulus measurements were adjusted using the correction factors. The coefficient of variation, which is standard deviation divided by an average, is used for comparison on the precision of the tests. The coefficients of variation were 42% before using correction factors and 31% with correction factors. Before the study, a roughly 200% error was observed in the modulus determination on a single plate. However, the 31% error still seemed high and lower percentages of errors were expected, especially with a well-controlled procedure in coating preparation. The errors were reduced using the correction factors by an additional 11 percentage points. From the above result, it can be concluded that a large percentage of error comes from the sample preparation procedure and the thickness measurements. Thus, a uniform film with adequate thickness measurements greatly enhances the accuracy.

It is important that the instrument is able to distinguish between similar material properties as a combinatorial characterization tool. With 31% error, the differentiation can

be obstructed. To study the effectiveness of the machine, three polyurethane formulations were tested. The Joncryl 901 formulation was compared against two additional polyurethane formulations; Joncryl 804 and 948. The polymer solutions were deposited using a 120-μm gap cube applicator on the same pDMTA plate. The mean averages and standard deviations (1σ) of the dried films were 71 ± 2 μm, 93 ± 3 μm and 94 ± 8 μm for Joncryl 804, 901, and 948, respectively. One can observe from Figure 3.28 that between 1 GPa to 10 GPa, these ranges of thicknesses require minor corrections. The mean averages of correction factors for Joncryl 804, 901 and 948 are 1.10, 1.15 and 1.15, respectively. Thus, the modulus values were adjusted by 10% to 15% for all three coatings. There were no significant changes in the coefficients of variation for all three coatings before and after corrections. The results are shown in Figure 3.38. The coefficients of variation for the corrected moduli are 9.5%, 18.7%, and 14.4%, respectively. The results show a drastic improvement in accuracy when the thicknesses are similar and the films are uniform. The storage modulus obtained from pDMTA is compared against the storage modulus from nanoDMA and from conventional DMA on the same polyurethane formulations. NanoDMA was done using Triboindenter from Hysitron Inc. with a Berkovich indenter. In Figure 3.38, from pDMTA, Joncryl 804 is distinguishable from the other two formulations, but Joncryl 901 and 948 are essentially the same. Each coating was deposited in a single column on different locations of the same plate. The results would possibly have a specific accuracy issue that will be discussed later. Nevertheless the narrow thickness distributions provide significantly lower coefficients of variation.

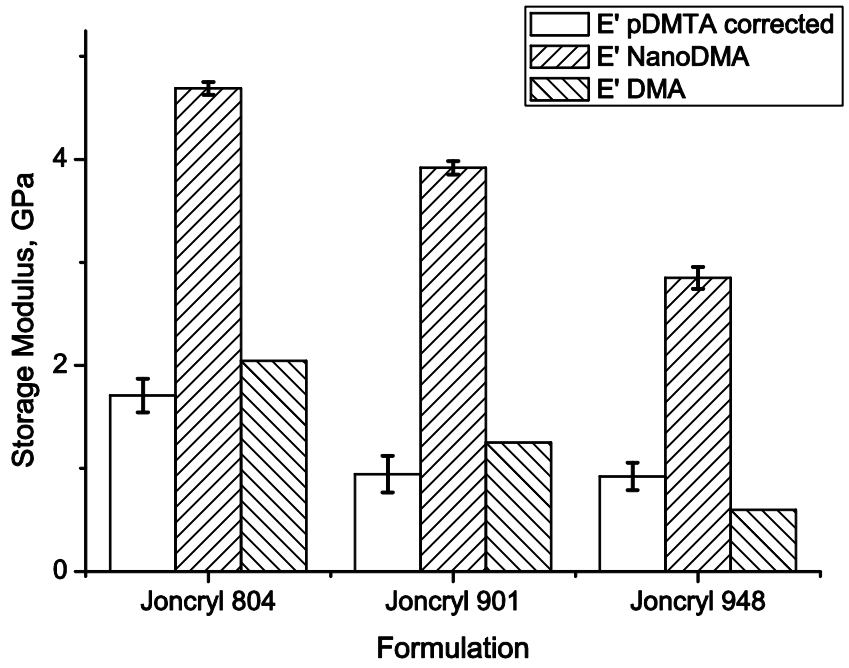

Figure 3.38. Comparison of three formulations on different tests at room temperature

In Figure 3.39, the comparison in modulus calculation is done at 110º C. This temperature is around the rubbery plateau of the samples. After the test at room temperature, the environmental chamber was heated up to 110º C and the test was initiated again. The test was not performed in a continuous mode, where the samples were subjected to stresses and measurements during a temperature ramp, because there were permanent deformations when tested at higher temperature seen as dimples on the Kapton resulting from an indenter. The permanent deformations were noticeable at higher temperature and this led to an assumption that creep occurred with the Kapton that caused a change in plate geometry, thus for the purposes of this accuracy measurement, we eliminated the changing shape factor.

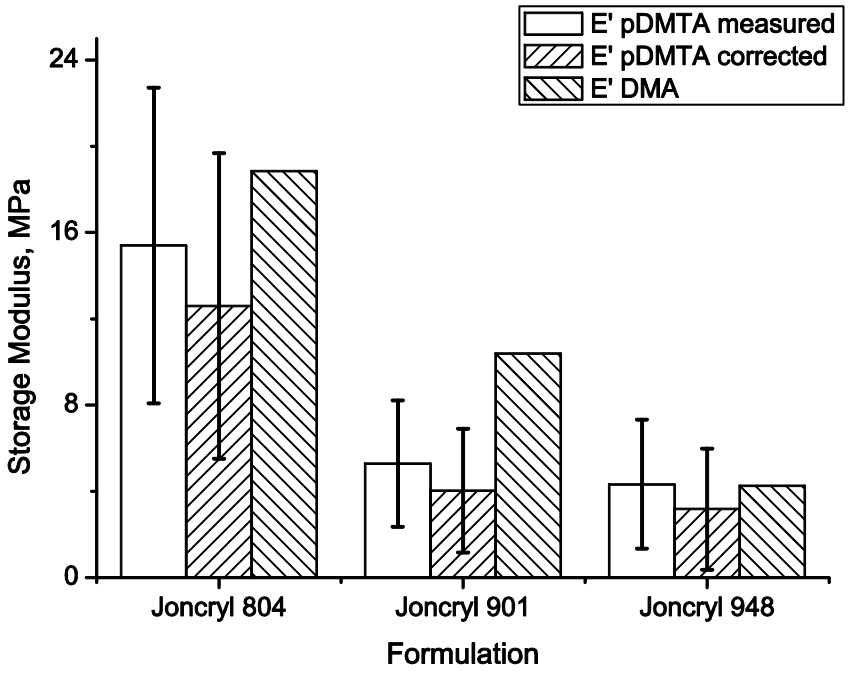

Figure 3.39. Comparison of three formulations on different tests at 110º C

From Figure 3.39, the coefficients of variations are observed to be 48%, 55% and 69%, respectively, before applying corrections. Similar to the results in Figure 3.38, improvements from the correction factors are insignificant due to the ranges and values of their thicknesses. The observed large errors imply that the instrument is unable to resolve measurements with materials in the MPa range. This is also due to the fact that Kapton has the elastic modulus of around 2 GPa at room temperature and at 110º C because of its high T_g. To accurately measure a top layer with 10^3 times softer in storage modulus than the bottom layer can be a challenge. Figure 3.40 shows the results of two pDMTA runs on a blank Kapton substrate at room temperature.

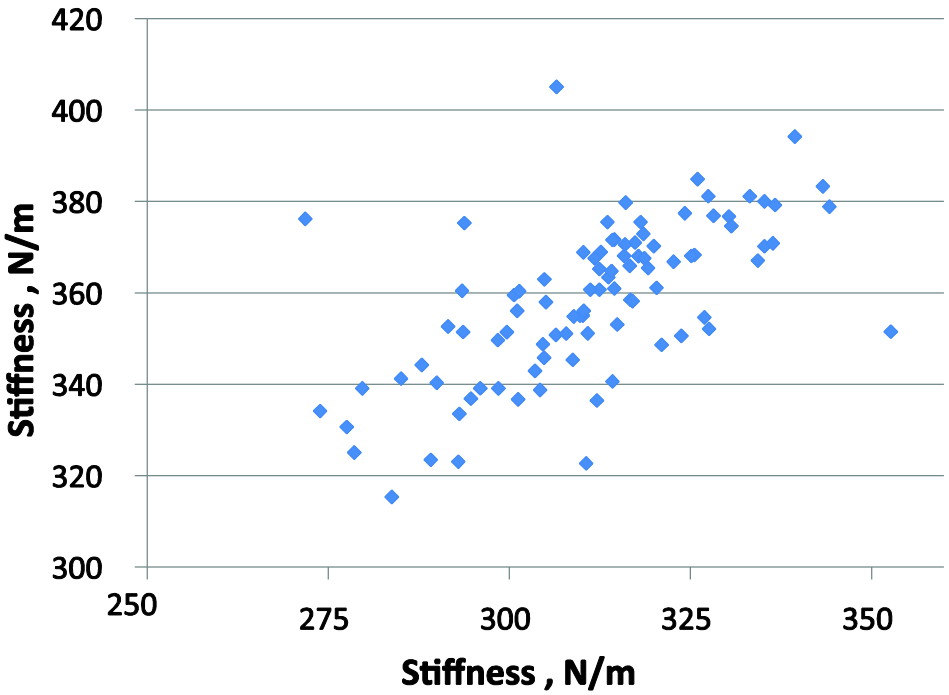

Figure 3.40. Variation due to noise and random error

The plate was tested, removed from the instrument and immediately retested again. Each data point represents a single specific location out of 96 spots with x and y values representing two separate runs. The result shows that the stiffness measurement can scatter to roughly 40 N/m due to a random error. Table 3.2 illustrates the effect of 40 N/m stiffness measurement variations on the modulus output. From Table 3.2, the assumptions are made based on an approximation to the real data. If the actual composite stiffness is 340 N/m for a 100-µm thick coating, the measurements can be in the range of 320 N/m to 360 N/m and thus a calculated modulus of 2.80 to 8.43 MPa.

Table 3.2. Hypothetical results to illustrate the effect of random error

Composite Stiffness	Film Thickness	Calculated Modulus (MPa)
320	100	2.80
340	100	5.61
360	100	8.43
340	150	2.03
340	200	0.96

Note: The assumptions are as follows; Kapton's stiffness is 300 N/m, Kapton's modulus is 2.5 GPa.

Figure 3.41 reemphasizes the argument from Figure 3.40 and Table 3.2. Figure 3.41 was generated from FEA results based on Kapton's modulus of 2.5 GPa with Poisson's ratio of 0.34. Stiffness is calculated using the force measured at 10 μm displacement (measured force divided by 10 μm). Kapton's stiffness, without a coating layer, is calculated to be 243 N/m.

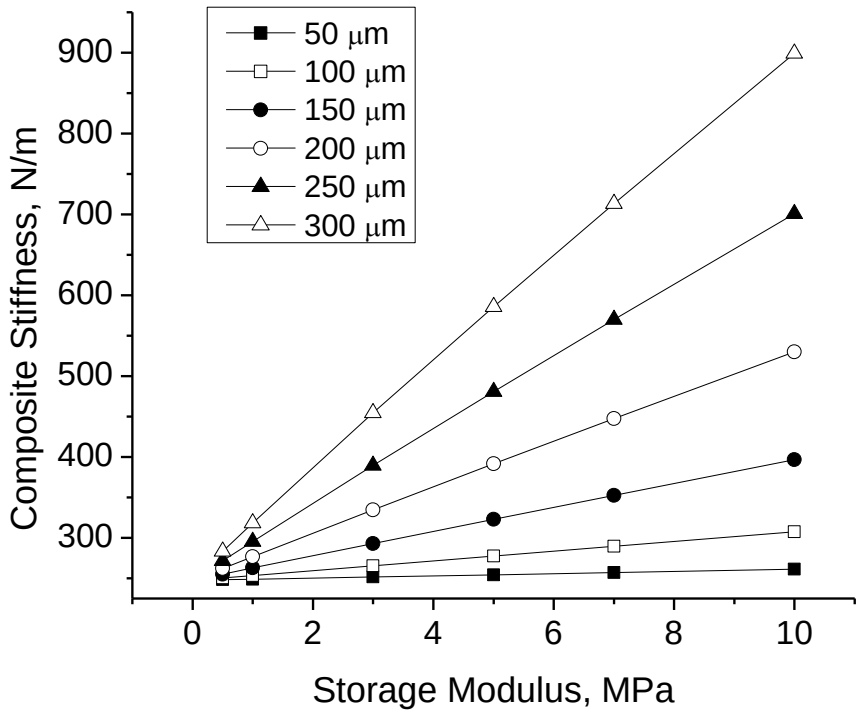

Figure 3.41. FEA results on composite stiffness versus Young's modulus of coatings at different thicknesses

The FEA results and the noise issue imply that it is extremely difficult to obtain useful modulus results for coatings with thickness less than 100 µm and with storage modulus less than 10 MPa. For modulus of 1 MPa or less, the response from the coating is not enough at any thickness to obtain useful results.

3.4.5. Other influential factors in modulus calculation

A cured droplet shape has a profound effect on the output. The droplet profiles in Figure 3.19 were used in the modeling to illustrate the differences due to the averaging of thickness. COMSOL allowed us to use the profiles to create boundaries in the models. Figure 3.42 shows the effect of two droplet shapes; one with thicker center and the other with thinner center. The differences in calculated modulus from simulated stiffness measurement are clearly significant.

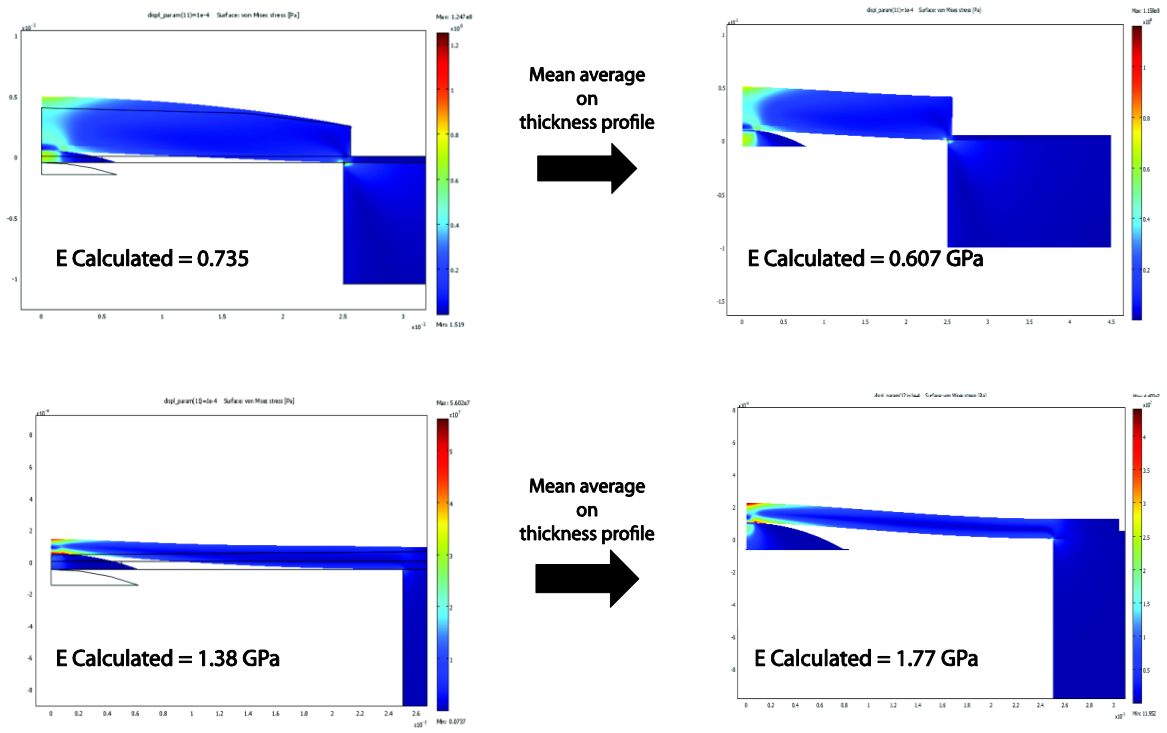

Figure 3.42. Effect of droplet shapes on modulus output: the models on the left use the actual droplet profiles whereas the ones on the right use the averages of measured heights

Kapton is also stretched and permanently deformed during plate preparation. A half section of a 2D substrate profile is shown in Figure 3.43. The center point has a total vertical displacement of 43 µm due to the stretching. Because of noise in the data from laser profilometer, the curvature was fitted using polynomial function and the fitted dipping profile was input into the model.

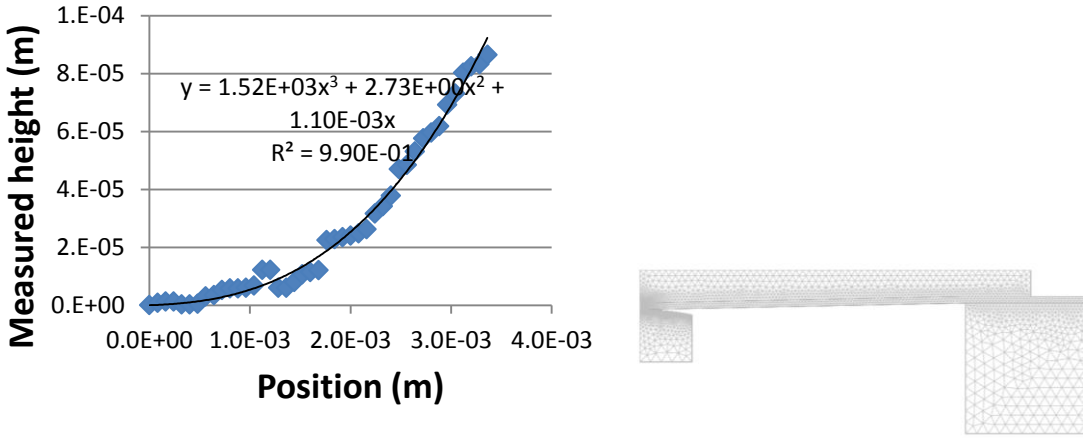

Figure 3.43. Substrate curvature: 2D profile (left) and model with substrate curvature (right)

Figure 3.44 uses FEA to compare the differences in modulus calculation between the flat Kapton substrate and the ones with curvature as in Figure 3.43. Since the thickness measurement is usually done assuming a flat substrate, the material in the dipping area of the substrate and the curvature are ignored. The results show that for a supposedly measured 100 µm thick coating layer, the impact is significant with 40% to 80% error. Substrate curvature has less impact as the coatings get thicker. As it has been stated that 100 µm is best in terms of accuracy, the curvature in tens of microns can greatly contribute to the accuracy. Thus, the coating was deposited with drawdown bar and the Kapton substrate was not sanded when we tested the correction factor and accuracy of the machine.

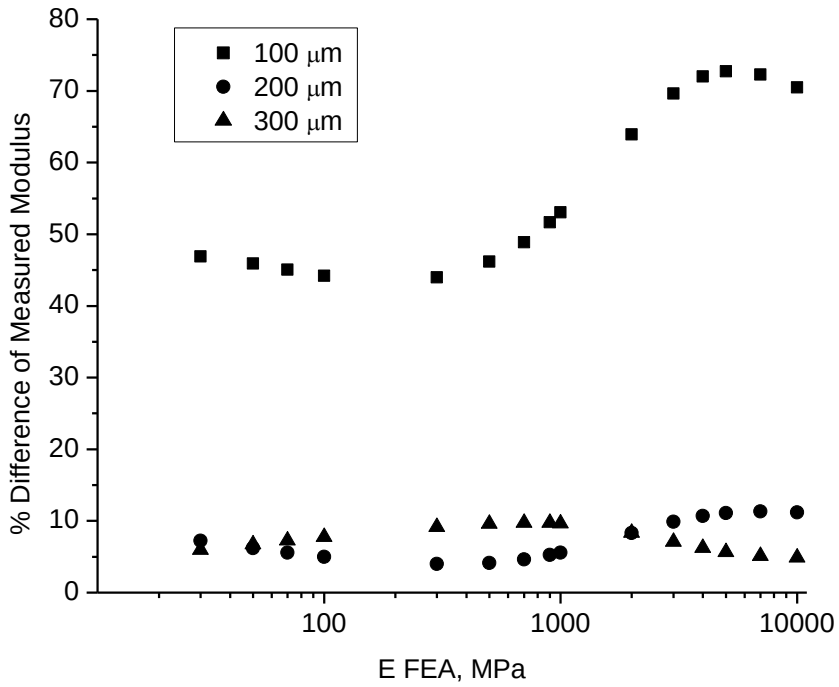

Figure 3.44. Differences of modulus calculation from flat and curved substrate from Figure 3.43

The results show that substrate preparation is critical. The substrate needs to be ensured that it is as flat as possible for the scale that we are testing. Other phenomenon that has not been studied is the curvature of the Kapton and coating due to shrinkage upon curing. A schematic of an effect of shrinkage of polymer sample on Kapton is shown in Figure 3.45.

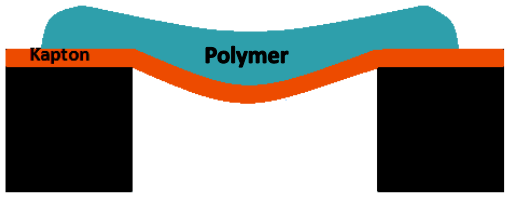

Figure 3.45. Schematic of an effect of shrinkage on Kapton

The theory of bilayer plate would not apply when these geometries occurred. Thus, sample preparation is the key to ensuring sufficient accuracy. The curvatures of the substrate can be prevented, but the droplet curvature is inherent. A future study on

correction model for droplet shape can be conducted, however, with ~10%-20% error even for drawdown coating, there have to be fundamental changes in the system for further corrections to function in order to approach an acceptable level of error.

3.4. Conclusion

The correction factor equations are generated based on the finite element models. The corrections are needed as a result of thickness variations and the limitations of the closed-form solution. A large percentage of errors comes from thickness measurement and droplet uniformity. Using a drawdown film deposition technique, the coefficient of variation is reduced to ~10% to 20% due to thickness uniformity. Table 3.3 compares the conventional DMTA to the pDMTA. Both instruments need careful sample preparation. pDMTA actually gets rid of grip length and grip pressure concerns. In DMTA, mounting the sample on to the instrument is a delicate task with a slight off-axis or uneven slack giving incorrect result.

Table 3.3. Factors that can affect the accuracy on conventional DMTA and pDMTA

DMTA	**pDMTA**
Thickness uniformity	Thickness uniformity
Homogeneity of specimen	Homogeneity of specimen
Defects	Defects
Grip length and grip pressure	Size effect
Size effect	Alignment of the probe
Alignment of specimen to the machine axis	Creep on Kapton
Slack (uniform distribution of load)	

pDMTA is a complicated test because of the bilayer structure and the test is further complicated by miniaturizing the testing area and accommodating 96 simultaneous tests. The repeatability and accuracy of the pDMTA suffer from the inability to control tolerances of testing geometries. For example, the pDMTA is 114 mm long and 78 mm wide whereas the pins need to displace only 15 μm in transverse direction to get the data on

96 spots along the length and width of the plate. This implies that a tight tolerance is required on the plate positioning relative to 96 pins. Significant creep occurs on Kapton because the plate and all of the pins cannot collide at the same time. The stiffness of Kapton also prohibits useful data when the material becomes soft such as on the rubbery plateau. Redesigning of the instrument can help, such as making the plate of 24 samples, instead of 96 samples, so that the samples are enlarged. It is crucial that the dimensions of testing geometries can be repeated and are accurate.

3.5. References

1. Brown, R., *Handbook of polymer testing: physical methods*. Marcel Dekker, Inc.: 1999.

2. Koleske, J. V., *Paint and coating testing manual: fourteenth edition of the Gardner-Sward handbook*. American Society for Testing and Materials: Ann Arbor, MI, 1995.

3. Hergenrother, P. M., The use, design, synthesis, and properties of high performance/high temperature polymers: an overview. *High Performance Polymers* **2003,** *15*, 3-45.

4. Pieper, R. J.; Ekin, A.; Webster, D. C.; Casse, F.; Callow, J. A.; Callow, M. E., Combinatorial approach to study the effect of acrylic polyol composition on the properties of crosslinked siloxane-polyurethane fouling-release coatings. *Journal of Coatings Technology and Research* **2007,** *4* (4), 453-461.

5. Uhl, F. M.; Gallagher-Lein, C. M.; Christianson, D. A.; Bahr, J. A.; Chisholm, B. J.; Gubbins, N. J.; Webster, D. C., *A combinatorial approach to rapid structure-property screening of UV-curable cycloaliphatic epoxies*. CRC Press: 2006.

6. Young, W.; Budynas, R., *Roark's formulas for stress and strain*. 7 ed.; 2002.

7. Hajduk, D. A.; Carlson, E.; Freitag, C.; Kosolov, O. Instrument for high throughput measurement of material physical properties and method of using same. US6679130, 2004.

8. MacDonald, B., *Practical stress analysis with finite elements*. Glasnevin Publishing: Dublin, 2007.

9. Kossuth, M. B.; Hajduk, D. A.; Freitag, C.; Varni, J., Parallel dynamic thermomechanical measurements of polymer libraries. *Macromolecular Rapid Communications* **2004,** *25*, 243-248.

10. McCrum, N. G.; Buckley, C. P.; Bucknall, C. B., *Principles of polymer engineering*. 2nd ed.; Oxford University Press Inc.: New York, 1997.

CHAPTER 4. FROM HIGH-THROUGHPUT METHODS TO CONVENTIONAL COATING TESTS

4.1. Introduction and Rationale

In addition to the parallel dynamic mechanical-thermal analysis instrument and the high-throughput puncture tester, the NDSU combinatorial laboratory has the capability of performing automated nanoindentation for mechanical characterization. The nanoindentation instrument can be adapted to any specific combinatorial template. The theory of nanoindentation will be briefly discussed here. An indentation experiment can give hardness values. However, hardness has different meanings in different fields and hardness can be tested in a number of different ways.[1] It could indicate wear resistance to a lubrication engineer. To a metallurgist, it could indicate resistance to penetration. A mineralogist could think of hardness as the resistance to scratching. Hardness would imply the resistance to cutting to a machinist. In coatings, the two most common hardness tests are pencil and pendulum hardness. This chapter gives our attempt at correlating results between high-throughput methods and conventional tests, including results from pDMTA.

4.2. Nanoindentation

Nanoindentation typically specifies a load and depth sensing indentation. The load and displacement are monitored continuously and the area of contact can be estimated as a function of displacement. Nanoindentation has the advantages for testing of thin films and small volumes because of a relatively small area utilized for the test. Calculated outputs, such as hardness and modulus, depend on the assumptions in the tip-area function. In the simplest case, the surface is assumed to be an elastic half-space and the variation in contact

area from pile-up due to plasticity or from adhesion due to surface energy is neglected. Some nanoindentation instruments also allow the indenter lateral movement and sensing, thus both scratch and wear experimentation can be performed. The characterization capability then expands to scratch resistance, fracture toughness and friction coefficient. It is desirable to implement an automated indentation testing protocol for coatings with a wide range of moduli. The underlying assumptions and potential inaccuracies from indentation experiments are studied.

4.2.1. Nanoindentation theory

Material properties such as modulus will govern the behavior of the deformation. Models are needed to extract those properties from the raw data. We begin with Hertz's linear elastic contact model.

4.2.1.1. Hertz's linear elastic contact

Hertz was studying Newton's interference fringes from two glass lenses as seen in Figure 4.1.[2] Hertz determined that the contact had an influence on the interference due to deformations of glass lenses. When the lenses were loaded, the center portion had no interference pattern. Interference fringes did not occur if there was no gap between the lenses or the gap was too narrow, thus it showed that there was a local elastic deformation taking place.

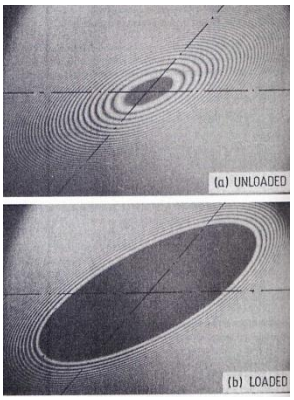

Figure 4.1. Interference fringes (Reproduced from ref.[2])

Hertz then further analyzed the stress distribution and load-displacement relationship. It was the beginning of contact mechanics. Hertz's linear elastic contact theory has the following assumptions: Surfaces are 1) continuous and non-conforming: $a \ll R$, 2) the strains are small: $a \ll R$, 3) each solid can be considered as an elastic half-space: $a \ll R$, $a \ll L$, and 4) surfaces are frictionless, so that only normal pressure is transmitted between them, where a is the contact radius and R is the effective radius of curvature. The radius of a contact circle is defined as:

$$a = \left(\frac{3PR}{4E_r}\right)^{1/3} \tag{4.1}$$

where P is the applied load and E_r is called the reduced modulus or effective modulus or combined modulus because the contact can be from two materials with different moduli.

The local deformation from the contact is resulted from both moduli. The following equation is used to separate the moduli.[2, 3] E and υ are the modulus and Poisson's ratio. The subscript, 1 and 2, describes two different materials.

$$\frac{1}{E_r} = \frac{1-\nu_1^2}{E_1} + \frac{1-\nu_2^2}{E_2} \tag{4.2}$$

Maximum contact pressure: $$p_0 = \left(\frac{3P}{2\pi a^2}\right) = \left(\frac{6PE_r^2}{\pi^3 R^2}\right)^{1/3} \tag{4.3}$$

Approach of a distant point: $$h = \frac{a^2}{R} = \left(\frac{9}{16}\frac{P^2}{RE_r^2}\right)^{1/3} \quad (4.4)$$

Figure 4.2 shows the normalized stress distribution for a flat punch (left side) and for a spherical punch (right side) that Hertz calculated. The diagram shows the stress distribution along the contact (upper portion) and stress distribution underneath the contact (lower portion). It should be noted that, for Hertzian contact, the maximum normal stresses are at the center on the contact surface, there is tensile stress component around the edge of contact, and the shear stress is at a maximum below the interface.

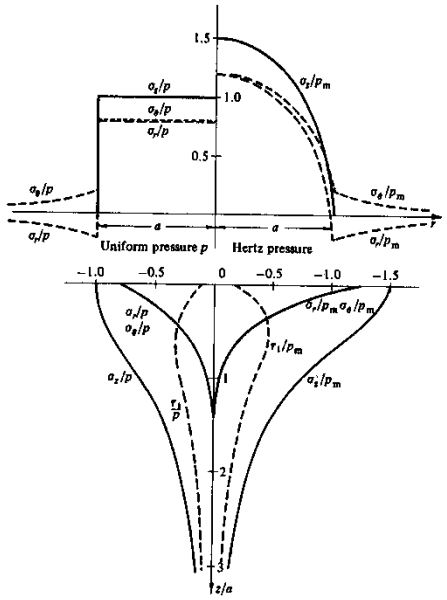

Figure 4.2. Stress distributions for flat punch and spherical punch (Reproduced from ref.[2])

Boussinesq determined the stress distribution of a rigid punch imposing a normal pressure on an elastic half-space, and, with the methods of potential theory, a solution for the case of a solid of revolution was derived.[2] Sneddon further derived a general case for arbitrary profiles.[4] Sneddon created a simple relation between load and displacement (within the linear theory of elasticity) for axisymmetric punches. From the derivation, the total load and total displacement relationship can be generated for a flat-ended cylindrical

punch, a conical punch, a paraboloid of revolution punch, a spherical punch and an ellipsoid of revolution punch. The derivations include, "the distribution of pressure under the punch" and "the shape of deformed boundary of the half space."[4] Some of the results are shown as follows.

Cylindrical flat punch; $$P = \frac{4Ga}{1-\nu}h \quad (4.5)$$

Paraboloid of revolution: $$P = \frac{8G}{3(1-\nu)}(2kh^3)^{1/2} \quad (4.6)$$

where k is the profile constant.

Conical punch; $$P = \frac{4G\cot\alpha}{\pi(1-\nu)} \quad (4.7)$$

where α is the semi-vertical angle of a cone.

The load and displacement relationships are in the form of $P = \alpha h^m$ where α and m are constant. m = 1 is for flat punch and m = 2 is for perfectly sharp cone, they are the two opposites of the indentation behavior. The relationships defined by Sneddon and Hertz form the basis for obtaining elastic modulus through nanoindentation.

4.2.1.2. Elastic-plastic material testing

Figure 4.3 shows a typical example of a load-displacement curve for an elastic-plastic material. Doerner and Nix proposed "a technique for subtracting the elastic displacement from the total displacement to obtain hardness" and a method for calculating elastic modulus.[5] The method by Doerner and Nix assumes that the contact is similar to a flat cylindrical punch during initial withdrawal which means the contact area initially remains constant.[5] Equation 4.5 can be differentiated into:

$$\frac{dP}{dh} = \frac{2}{\sqrt{\pi}}\sqrt{A}\frac{E}{(1-\nu^2)} \quad \text{or} \quad \frac{dP}{dh} = \frac{2}{\sqrt{\pi}}\sqrt{A}E_r \quad (4.8)$$

where $A = 24.5h^2$ for an ideal pyramid.

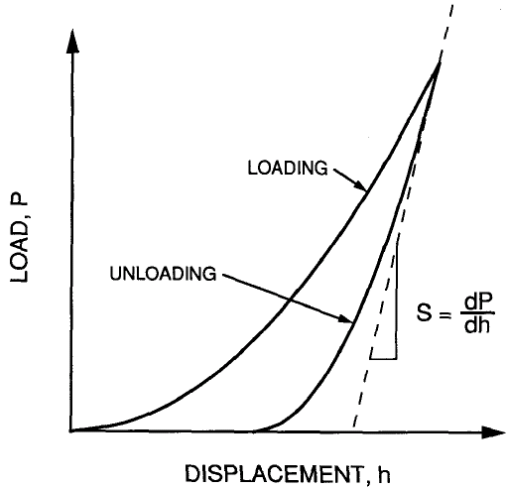

Figure 4.3. Typical load-displacement curve for elastic-plastic material (Reproduced from ref.[6])

Doerner and Nix believed that even for silicon where there was large elastic recovery, linear unloading was still observed for 1/3 of the maximum load.[5] The nonlinear unloading was believed to be a result of some loss of contact of the indenter during elastic recovery. Transmission electron microscopy (TEM) was also used to verify the contact area for tip calibration.[5] In a brass sample, the hardness decreases with increasing indentation depth. This is a result of the strain rate effect which can be written as:

$$\dot{\varepsilon} = c\left(\frac{1}{h}\frac{dh}{dt}\right) \tag{4.9}$$

where $\dot{\varepsilon}$ is the strain rate and c is an arbitrary constant. The displacement rate (speed) is held constant, thus as the indentation size increases (h increases) the strain rate decreases. This strain rate sensitivity was said to contribute to what is called the hardness size effect. Oliver and Pharr later pointed out that the results would depend on how much of the data was used in fitting for (dP/dh).[7] They observed that the unloading curve was rarely linear. Pharr et al. showed that Equation 4.8 applies for all axisymmetric indenters through the analysis from Sneddon.[6] The equation can be used during initial unloading where it is purely elastic. Based on the work of Sneddon, Oliver and Pharr used the power law

relationship to fit the elastic unloading curve, instead of the linear fit as seen from Doerner and Nix.[7] Then the derivative is calculated and evaluated at the maximum load to find the contact stiffness (*S*). It can be observed that *E* varies as a function of (1/square root of contact area). The contact area is not directly measured. The depth-sensing is used together with the area function to calculate the contact area. The total displacement can be written as $h = h_c + h_s$, where h_c is the contact depth (vertical distance along the contact) and h_s is "the displacement of the surface at the perimeter of the contact".[7] Oliver and Pharr derived <noun> the equations from Sneddon and obtained: $h_c = h_{max} - h_s = h_{max} - \omega \frac{P_{max}}{S}$, where ω depends on the tip geometry. Thus, we have,

$$E_r = \frac{\sqrt{\pi}}{2} \frac{S}{\sqrt{A(h_c)}} \tag{4.10}$$

Figure 4.4 shows the schematic of an indentation test and the load-displacement data.

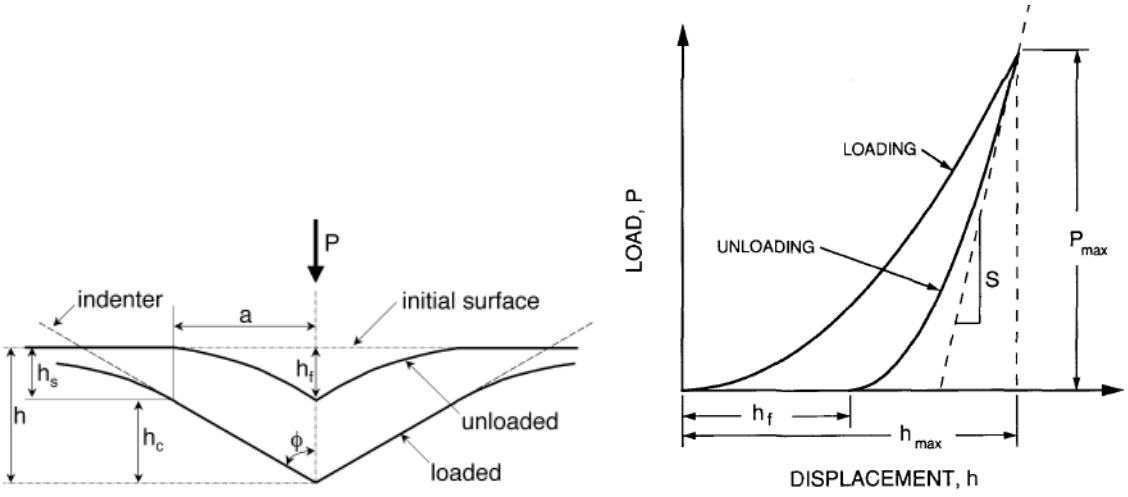

Figure 4.4. Schematic of indentation test (left) and obtained data (right) (Reproduced from ref. [7, 8])

Another method commonly used is the method of Field and Swain.[9] It is based on spherical contact from Hertz analysis to calculate the elastic modulus and hardness for elastic-plastic materials using a partial unloading technique. Oliver and Pharr have written

a review regarding the development of the methods in terms of tip area function calibration, errors due to pile-up, and correction factor for different tip profiles.[8]

4.2.1.3. Viscoelastic materials

Figure 4.5 shows a load-displacement curve for a viscoelastic material from a nanoindentation experiment. The nonlinearity of the unloading curve is apparent. This shows the difficulty in obtaining the contact stiffness for modulus determination. An unloading curve for a polymer, when fitted to the power law, may give an exponent larger than 2 which means that the unloading does not contain a purely elastic response which violates the assumption in Sneddon's solution. This is because creep and stress relaxation are apparent in polymers.

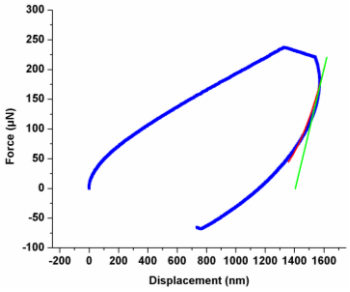

Figure 4.5. Load-displacement curve for viscoelastic material with open-looped test (Courtesy of Hysitron, Inc.)

Usually, a longer hold time is used to reduce creep rate.[10] A fast unloading rate is also used. In the early days of nanoindentation on polymers, White and Turnbull studied the effect of loading rate and hold time on a weathered unplasticized polyvinyl chloride with a 10nm radius of curvature diamond Berkovich indenter.[10] It was found that up to 200 s of hold time was required to obtain a fairly linear unloading curve. They realized that the method of Oliver and Pharr may not be applicable to their polymers due to the time-dependent unloading curve. Thus, a universal idealized hardness was used instead which is much cruder. Hardness was the force at maximum displacement divided by surface area

calculated from the maximum displacement (For example, $A = 24.5h^2_{max}$ for ideal Berkovich). It was observed that the hold time was a key variable in their results and the hardness near the surface seemed harder than the underlying material. However, the size effect on hardness results was not taken into account. Tranchida and Piccarolo strongly suggested the need for another theoretical basis by pointing out the errors in the Oliver and Pharr method.[11] The departure of polymer contact geometry from Sneddon's model and how the power law exponent in polymers can be larger than 2 were shown. Time-dependent models for nanoindentation were developed thereafter. VanLandingham and others at the National Institute of Standards and Technology (NIST) has done some work on nanoindentation of polymers.[12] It was noted that *E* normally increases as penetration depth decreases. Partly, it was due to the tip defect and low signal to noise ratio at low load and displacement. Elastic modulus measured from nanoindentation for polymers is usually higher than that from tensile test and dynamic mechanical analysis (DMA). The modulus of polymers can cover a wide range due to the "potential variations in microstruture, semicrystalline, morphology, anisotropy, molecular weight, crosslink density, etc."[12] The difficulties have been reported for polymers where there is significant displacement at the preload and the nonlinearity of unloading curve. A nonlinear power law fit usually does not converge to a solution, thus the fitting is then based on the fitting parameters at the N-th iteration. Cheng et al. derived a closed-form solution for an indentation test with a spherical tip under load relaxation and creep conditions.[13] A simple three-element model, which includes springs and a dashpot, was used. Y.T. Cheng et al. modeled linear viscoelastic behavior.[14] The conical and spherical indentation solutions were derived for linear viscoelastic materials with load-controlled and displacement-

controlled experimentation. The solutions were derived to take into account the time dependent behavior at the initial unloading.

4.2.1.4. JKR Model

Johnson, Kendall and Roberts studied the influence of surface energy on the contact between elastic solids.[15] "When a contact is formed between two smooth solid surfaces the equilibrium largely depends upon the distribution of elastic forces in the contacting bodies."[15] At low loads, contact areas are considerably larger than those predicted by Hertz and it goes toward a finite value as the load is reduced to zero. The effect of adhesive force on contact can be seen in Figure 4.6.

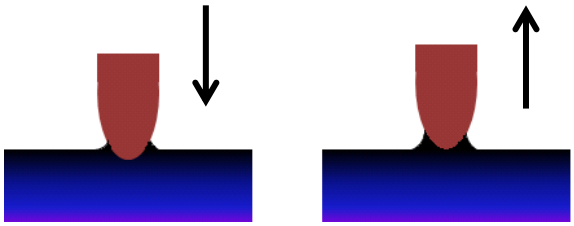

Figure 4.6. Schematic of a tip experiencing adhesion forces

At high loads, the results would follow Hertz's theory. The approximate theory comes from the thermodynamic principle of balancing energy. When the two spheres are in contact under no external load, there is a balance between "stored elastic energy and lost surface energy".[15] The exact analysis utilizes the calculation of total energy in the system with respect to contact radius. The results from the exact analysis are presented in Equation 4.11.

$$a^3 = \frac{3}{4}\frac{R}{E_r}\left(P + 3\gamma\pi R + \sqrt{6\gamma\pi RP + (3\gamma\pi R)^2}\right) \qquad (4.11)$$

The above equation is called the JKR equation (modified Hertz). When $\gamma = 0$, Equation 4.11 reverts back to Equation 4.1, the Hertz definition. Figure 4.7 shows the stress distribution at the contacting surfaces. It shows the stress distribution with lines, A, B, and

C. The other dotted line represents a contact with no adhesion force and the other solid line represents the contact with adhesion force. The arrow P shows the magnitude in compressive stress and the arrow T shows the direction of the magnitude in tensile stress. Distribution A and C comes from Hertz stress with $a = a_1$ and $a = a_0$, respectively. Distribution B is the stress distribution used in the JKR model with $a = a_1$. It shows an infinite tensile stress at the edge of contact. In reality, this is not the case, the stress falls to a finite value as the surfaces separate slightly closer to the edge. However, this should have a minimal effect on the stored elastic energy needed for the derivation.

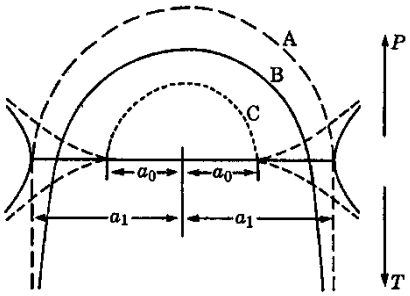

Figure 4.7. Stress distributions at the surfaces of contacting spheres (Reproduced from ref.[5])

The following equation is derived directly from the original JKR equation[16, 17]:

$$E_{JKR} = \sqrt{\frac{S^3(1-\upsilon^2)^2}{6RP}\left[\left(\frac{2}{3\sqrt{1+\frac{P}{F_{po}}}}+1\right)^3 \frac{1}{P+2F_{po}+2F_{po}\sqrt{1+\frac{P}{F_{po}}}}\right]} \tag{4.12}$$

where F_{po} is the pull-off force.

Gupta et al. applied this equation for PDMS coatings using nanoindentation in dry and aqueous environments. F_{po} is the pull-off force that has been calculated separately by contact AFM. His raw data is shown in Figure 4.8.

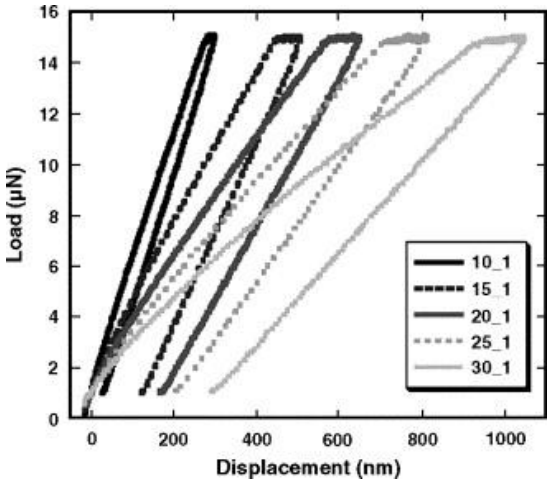

Figure 4.8. Load and displacement curves for different crosslink concentration (Reproduced from ref.[16])

Contact stiffness, maximum load and pull-off force are then used in the calculation. It has to be pointed out that the contact radius (thus contact area) is already within the theoretical model. The articles applied Hertz, JKR and Oliver and Pharr methods. Obviously JKR values will be lower than Hertz values. Notably, the method of Oliver and Pharr does not seem to apply to the data in Figure 4.8 because it would assume plastic deformation and the calculation of contact area is not correct. It is observed in Figure 4.8 that the indentations already started with some deformations. In conclusion, the trends merely present data manipulation/interpretation; however, their comparison between dry and aqueous environment is interesting. There is a decrease in the adhesion pull-off force which could be due to the weakening of electrostatic charges.

4.2.1.5. Indentation size effect

Material testing on very thin polymeric films (<200 nm) and with shallow indentations experiences the size effect where the elastic modulus or hardness can become thickness-dependent.[18-20] Figure 4.9 shows the indentation size effect on two polymers. Besides the effect from varying strain rates as shown in Equation 4.9, Han shows that the molecular structure influences the degree of size-dependence. Ultrahigh-molecular weight

polyethylene and polytetrafluoroethylene show significantly less dependence on size than epoxy and polymethymethacrylate. In Figure 4.10, Han stated the categorization of indentation hardness into three regions as a function of depth. The S region is in nanometer scale where surface roughness, tip curvature, and surface free effects have an impact on hardness. Han suggested that the *Frank* elasticity influences the second region. The M region stands for a macroscopic region hardness does not change with depth, h.

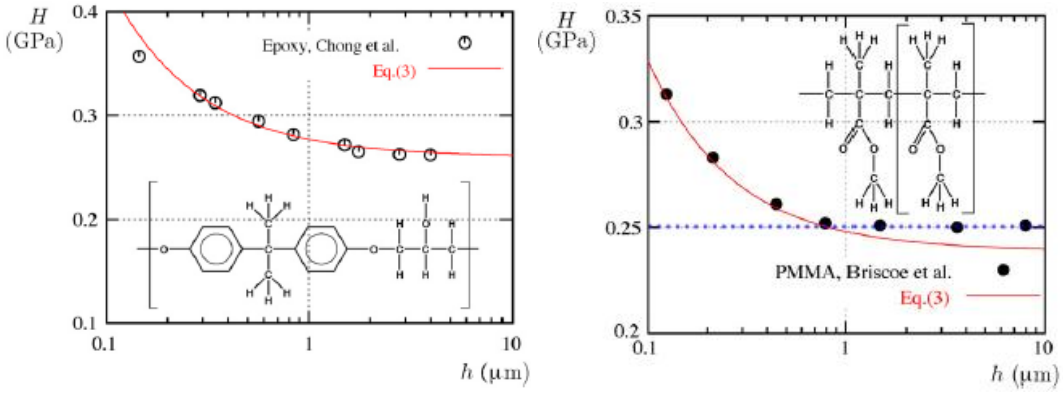

Figure 4.9. Hardness as a function of indentation depth for an epoxy (left) and PMMA (right) (Reproduced from ref.[19])

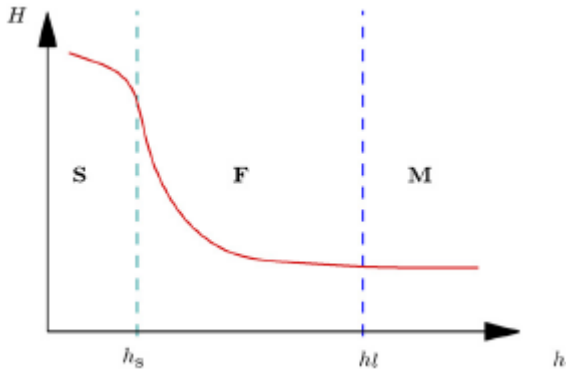

Figure 4.10. Hardness characteristic regions as a function of indentation depth (Reproduced from ref.[19])

4.2.1.6. Dynamic nanoindentation

Nanoindentation in the dynamic mode has been designed to characterize viscoelastic materials. The indenter oscillates as it indents into the material. Juliano et al. tested the mechanical properties of a gel using a cylindrical flat punch and assumed a constant contact area.[21] The use of the JKR equation was effectively avoided. The analysis from Sneddon is then applied to a dynamic problem to calculate the storage and loss modulus. Ebenstein and Wahl compare different JKR-based methods for quasi-static and dynamic indentation.[22] A dynamic nanoindentation instrument such as the Triboindenter from Hysitron, Inc. uses the Kelvin-Voigt model as seen in Figure 4.11.

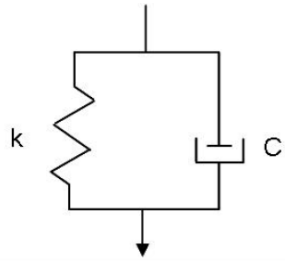

Figure 4.11. Kelvin-Voigt model

The tip-surface contact in dynamic mode can simply be modeled with the equation of motion in Equation 4.13.

$$F_0 \sin(\omega t) = m\ddot{x} + C\dot{x} + kx \tag{4.13}$$

where $x = X\sin(\omega t - \phi)$ as a displacement response.

Solutions of differential equations are rearranged and equations for k (stiffness) and C (damping) are obtained: $k = \frac{F_0}{X}\frac{1}{\sqrt{1+\tan^2\phi}} + m\omega^2$ and $C = \sqrt{\frac{\left(\frac{F_0}{X}\right)^2 \tan^2\phi}{1+\tan^2\phi}}\left(\frac{1}{\omega}\right)$.

The stiffness and damping coefficients are from the combination of the sensor and the sample. The coefficients are modeled as the sum from the sensor and sample:$k = k_{sensor} + k_s$ and $C = C_{sensor} + C_s$, where k_s and C_s are stiffness and damping values of

the sample. Both k_{sensor} and $C_{sensor}$are measured from indenting in the air. Storage modulus (E'), loss modulus (E'') and $\tan\delta$ (E'/E'') are given as:

$$E' = \frac{k_s\sqrt{\pi}}{2\sqrt{A_c}} \tag{4.14}$$

$$E'' = \frac{\omega C_s\sqrt{\pi}}{2\sqrt{A_c}} \tag{4.15}$$

$$\tan\delta = \frac{\omega C_s}{k_s} \tag{4.16}$$

The equations for storage and loss moduli can be linked back to Equation (4.8) stated by Doerner and Nix and Equation (4.10). The glass transition temperature can also be determined by coupling dynamic nanoindentation with a thermal stage.[23, 24] The glass transition temperature was found to be dependent on indentation depth, specifically on the top 10 nm of the polymer surface.

4.2.2. Nanoindentation as a high-throughput tool

The theoretical background, insights and developments in nanoindentation have been presented. Users of nanoindentation instruments need to understand the assumptions and potential error; thus the results can be presented with greater confidence. For elastic-plastic materials, the method of Oliver and Pharr and the method of Field and Swain stand the test of time. The methods are directly derived from Hertz and Boussinesq results. Viscoelastic models have not been popular due to the rigorous calculations involved in order to extract the resulting parameters. Dynamic indentation separates the in-phase and out-of-phase components, thus it eliminates further viscoelastic consideration and makes the analysis simpler. The JKR model predicts that the adhesion force depends on the surface energy and not the modulus. The JKR method is important for compliant polymers

such as silicones and gels because the adhesive force and the load applied during indentation could even be similar in magnitude.

The question arises whether nanoindentation with a single theory should be applied to coatings in a combinatorial study. Two combinatorial nanoindentation studies by mostly the same researchers at MIT used different characterizing methods. The first one from Tweedie et al. used nanoindentation to measure elastic moduli on 576 different polymer compositions in 24 h.[25] Nanoindentation was performed with a Berkovich indenter. It operated under a load control at a rate of 2 mN/s until it reached a depth of 1.5 μm. As usual, hardness was calculated by the maximum force divided by maximum contact area. The method of Oliver and Pharr was used to calculate the elastic modulus. The second one from Anderson et al. tested soft biomaterials with the majority of moduli ranging from 4 to 350 MPa.[26] This study used a spherical indenter with 500 μm radius. A load control of 5 μN/s was applied until a depth of 600 nm was reached. Elastic modulus was analyzed using the method of Field and Swain. Then, there was work done by Lin-Gibson et al. which used the continuous stiffness method with a 10 μm radius, 90° diamond cone indenter.[27] A technique called continuous stiffness method from MTS Systems Corp. utilized a continuous oscillation during loading, thus the elastic modulus could be measured continuously from the continuous stiffness measurements. Elastic modulus is calculated based on Sneddon's equation as seen in Equation 4.10. The modulus of each sample is obtained from an average of moduli between a depth range of 1000 to 4000 nm. The measured moduli in the library vary from 0.01 to 3.5 GPa. All three nanoindentation combinatorial studies differed in characterization techniques. These studies used different tips and calculations on their library. The tip was selected based on the expected material

behavior. With hard materials, either Berkovich or conical tip is sufficient. With soft materials, the small tip gives too small of a load to accurately determine the initial contact point, thus larger tip, such as spherical tip, is used. For very soft materials such as gels, a flat punch is used to avoid an unaccountable size of contact area.

4.3. Hardness Tests for Coatings

Hardness is likely a combination of other fundamental properties, such as elastic modulus, elastic limit, hardening, etc.[1] Three basic types of hardness tests for coatings are scratch hardness, indentation hardness and pendulum-rocker (damping) hardness. Previous studies showed that the pencil hardness is the most commonly used followed by the Sward-type rocker method. There is also an increasing use of indentation methods. ASTM D3363, which specifies the test method for film hardness by pencil test, is one of the methods to measure the scratch hardness of coatings. The scratch hardness is defined by the hardest pencil grade that could not mar the surface by the specified scratching procedure. The test is practical and is used extensively in the laboratory, on the production line and in the field to assess the rigidity/firmness of coatings on the substrates. The pendulum-rocker hardness tests are related to the stiffness and damping of the surface. The time or the number of oscillations for the pendulum-rocker to decay from the initial amplitude to the specific level of amplitude is a measure of hardness. Damping properties are measured on organic surfaces. The test can be very sensitive that it can follow the drying process of layers of paint. In Konig and Persoz hardness, the pendulum is supported on the test surface by two steel balls. Softer surfaces can normally damp the oscillations faster than harder surfaces. Pendulums on Konig and Persoz tests have a mass of 200 g and 500 g with ball diameters of 5 mm and 8 mm, respectively. Thus, Persoz pendulum results in a longer damping time

(~2 times longer than the Konig) which is useful for testing soft coatings because of an increase in sensitivity to small differences. However, ASTM D4366 which described the test method for Persoz and Konig hardness was withdrawn in 2003. ASTM D2134 for the Sward-Type hardness rocker was reapproved as recently as 2007. Figure 4.12 shows the Sward-Type hardness rocker and Konig pendulum hardness tester.

Figure 4.12. Sward type hardness rocker (left) and Konig pendulum hardness tester (right) (Reproduced from Ref.[28])

Each hardness method uses different properties from different mechanisms within the coating. It is stated that Sward rocker involves deformation within the elastic limit while Knoop indentation hardness involves deformation beyond the elastic limit. The pencil hardness relates to the deformation beyond the elastic limit and tearing away of material. Smith compared the Knoop hardness, Sward rocker hardness and pencil hardness on 14 organic finishes.[1] The results showed that all three tests roughly followed similar trends. Knoop hardness and pencil hardness indicated a good monotonic trend whereas the Sward and pencil hardness did not correlate as well with some scattered data points which

did not consistently give a monotonic trend. Sward hardness can be related to shear modulus and dynamic loss tangent as shown in Equation 4.17.[1]

$$G^{1/3} = NK \tan \delta \tag{4.17}$$

where G is the shear modulus, N is the Sward rocker hardness number, K is a constant, and $\tan \delta$ is the dynamic loss tangent. N is the number of complete oscillation multiplied by two.

Thus, a linear relationship is expected between the hardness number and the term, $(G^{1/3}/\tan \delta)$. It means that the loss component inversely influences the amount of damping. The higher loss component results in the lower value of hardness. The linear relationship was seen up to a Sward hardness of 60 sec which corresponds to Konig hardness of ~150 sec and Persoz hardness of ~280 sec. R. A. Cass compared the Sward rocker hardness with elastic modulus from tensile test for vinyl acetate copolymer coatings.[1] At constant film thickness, the relationship is ($E = KN^3$). For varying thickness, the equation becomes:

$$E = K_t \left(\frac{N}{t}\right)^3 \tag{4.18}$$

where E is the elastic modulus, N is the Sward hardness number, t is the coating thickness, and K_t is a coefficient function of thickness, t. However, Equation 4.18 works when the film thickness is thin and the substrate influences the damping response resulting in a thickness-dependent equation. Figure 4.13 shows the relation of Sward hardness to the modulus components and to the film thickness.

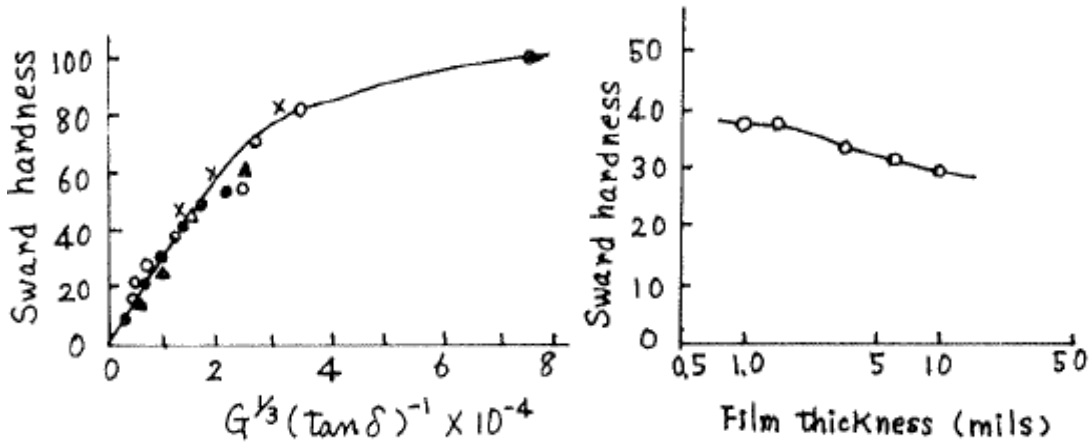

Figure 4.13. Linear relationship between hardness number and the $(G^{1/3}/\tan\delta)$ (Left) and hardness as a function of thickness (Right) (Reproduced from ref.[29])

The thickness of the coating should be thick enough so that the indenter would not be measuring the substrate. In Figure 4.14, the total depth of indentation as a function of reduced modulus is plotted based on the radius and load of the Konig pendulum hardness test using Equation 4.4. The estimation shows micro-scale penetration which is higher than the depth of typical nanoindentation. As a rule of thumb, the total depth should be less than 10% of the thickness for indentation experiment.

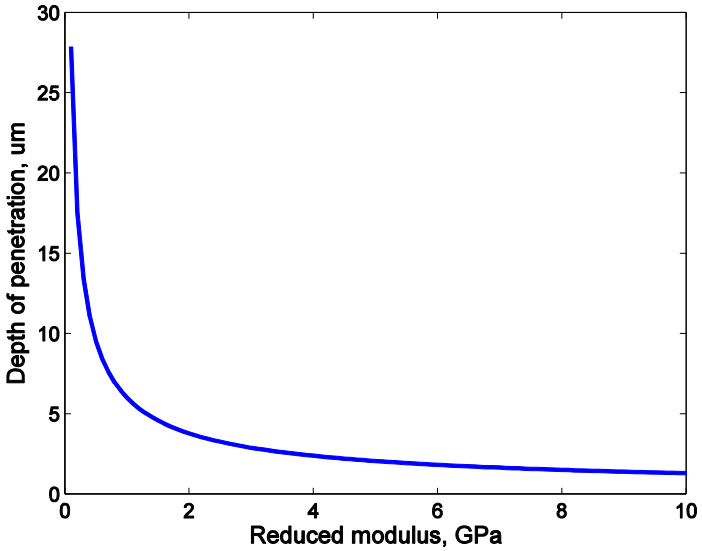

Figure 4.14. Reduced modulus versus depth of penetration of spherical indentation (R=2.5mm and 100g load) into an elastic half space (Calculated with Equation 4.4)

Figure 4.15 shows the correlation of pendulum hardness and Young's modulus. The relationship is proportional up to a point where increasing modulus does not significantly change hardness value. For those spherical indenters in Figure 4.15, this point is around 400 kg/mm^2 or 3.92 GPa in Young's modulus. The explanation is that the film becomes so stiff that the penetration of the indenter is minimal and the sensitivity to detect the loss component is significantly less or no longer available.

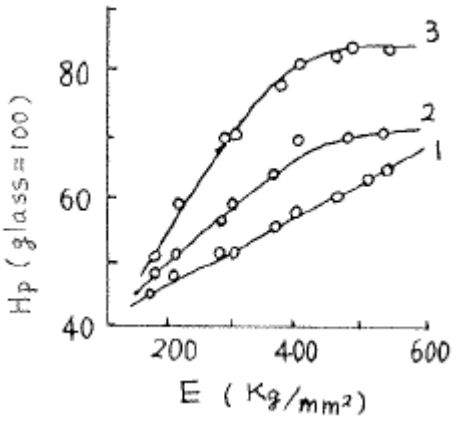

Figure 4.15. Pendulum hardness as a function of Young's modulus for cellulose nitrate coatings: with a conical indenter (data#1), a 1.56mm dia. Spherical indenter (data#2) and an 8mm dia. Spherical indenter (Data#3) (Reproduced from ref.[29])

4.4. Experimental and Results

4.4.1. Nanoindentation on soft polymers

As stated previously, nanoindentation data can be interpreted using different calculation methods. It is ideal to apply the same theory and indenter to the combinatorial library. With a single method, certain assumptions are required to calculate the outputs. Different characterization techniques using a 400-μm radius sapphire hemispherical indenter and a 500-μm radius cylindrical copper flat punch were compared. The coating system was a UV-curable, oxetane-toughened epoxy-siloxane.[30] The amounts of dioxetane were varied creating a range of elastic moduli. Figure 4.16 shows the results using the

methods of Hertz, JKR and Oliver and Pharr for the hemispherical indenter and using the contact stiffness at the unloading curve with constant contact area to calculate the elastic modulus for the flat punch.

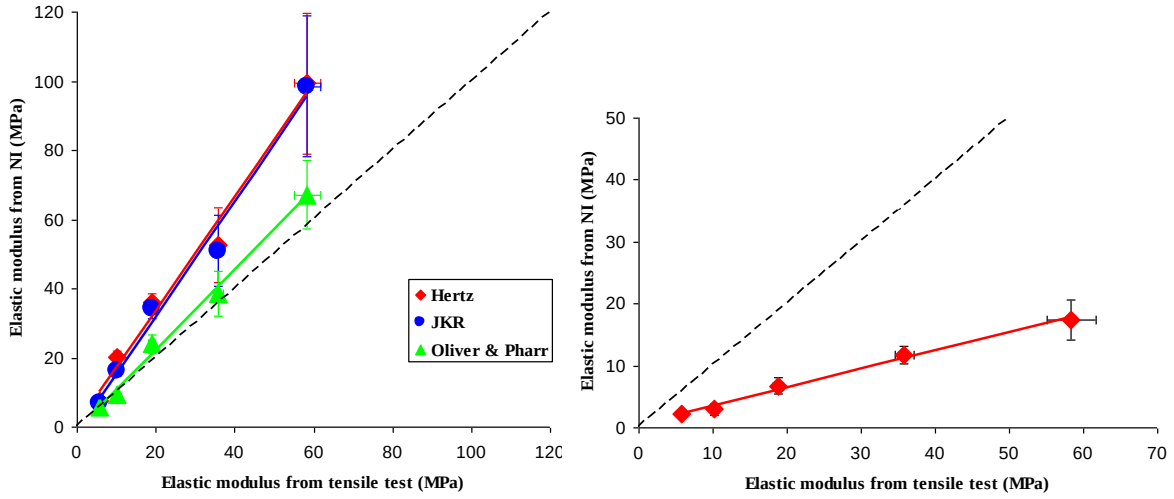

Figure 4.16. Elastic modulus results using 1) 400-µm radius spherical indenter (left) and 2) 500-µm radius cylindrical copper flat punch

In quasi-static nanoindentation, the results correlate with conventional tensile tests. All indentation calculations are based on contact stiffness with the differences being their assumptions of the contact area. Correction of the contact area with JKR has a lesser effect when the polymer gets stiffer. To run the instrument using one indenter and one theory, the penetration of the indenter should be deep enough, so that the bulk properties are measured. We would actually prefer to operate the nano-indenter in the micro-macro scale to avoid surface effect and surface imperfection for a high-throughput study. An indenter needs to be large enough to sense the force of very soft material, but small enough so that it can penetrate hard material. This depends on the indentation system. Our Triboindenter (Hysiton, Inc.) has a maximum load limit of 11 mN. Equation 4.4 can be used to approximate the total depth of indentation with respect to the size of the indenter. A 400-µm spherical tip could give too shallow indent on hard coatings. A 10-µm or 20-µm (radius

of curvature) conical tip should work well for polymer testing for a wide range of stiffness. It would be easiest to operate in the dynamic mode, such as the continuous stiffness measurement technique from MTS Systems Corp. or the nanoDMA® mode from Hysitron, Inc. With dynamic mode, the viscoelastic properties are separated and the results can be directly reported. However, the nanoDMA® can only operate in a load control mode and the optimal displacement amplitude is said to be 1-2 nm. The optimal amplitude cannot be kept within the 1-2 nm range when the elastic moduli of our combinatorial library differ by three orders of magnitude in a single automated run. For ranking between wide ranges of moduli for polymeric coatings, our current Triboindenter system (Hysitron, Inc.) would perform best using quasi-static indentation in a displacement-control mode with 10- to 100-μm (radius of curvature) conical tips. The Triboindenter senses the surface by a set pre-load, and then it holds that load to analyze for drift due to the different thermal expansions of components in the instrument. A lift height (to cause a temporary disengagement before indentation) of 1-2 μm should be used to avoid the initial deformation from drift, creep or adhesion which is caused by the pre-load in compliant coatings.

4.4.2. Correlation study

A high-throughput measurement requires an adequate sensitivity to differentiate between samples in order to provide details such as structure-property relationships. Traditional coatings characterization methods are unique, but it would be interesting to assess whether correlation with the existing high-throughput characterization methods can be identified.

BASF provided forty polyurethane formulations. Twenty are clear coatings and the other twenty are white coatings containing titanium dioxide pigments. The coatings are

different Joncryl® resins crosslinked with an aliphatic polyisocyanate, Basonat® HI 100. The results from the most common coating test results were given. These were Brookfield viscosity, potlife, dry-to-touch test, Gardner dry time, gel time, solids content, MEK rub test, impact resistance test, Konig pendulum hardness test, and pencil hardness test. Of those directly related to mechanical properties are the impact test and both of the hardness tests. Hardness tests were compared with nanoindentation. A Berkovich indenter was used for this coating set. For quasi-static nanoindentation, the load function was a 5-5-5 trapezoid displacement control to a depth of 500 nm. This implies a 5-second loading time, a 5-second hold time and a 5-second unloading time. Six indents were performed on each sample. The method of Oliver and Pharr was applied to the load-displacement data. The diamond indenter has an elastic modulus of 1140 GPa and a Poisson's ratio of 0.07. If we use Equation 4.2 and assume that the Poisson's ratio of all samples is 0.34, we have ($E_{sample} = 0.89E_{reduced} - 0.0059$) as a result of linear regression between the range of reduced moduli of 1GPa to 5 GPa. For dynamic indentation, the variable dynamic loading mode on nanoDMA® was used with the following load function parameters:

Begin Quasi Static Load: 5 uN

End Quasi Static Load: 900 uN

Frequency: 50 Hz

Dynamic Load: 2.5 uN

Number of Cycles: 100

Segment Steps: 11

Loading Rate: 30 uN/s

The result on one of the formulations is shown in Figure 4.17. Four indents were performed on each sample. The data point at the maximum depth of each dynamic indent was taken and averaged for storage modulus measurement for further analysis. The $\tan\delta$ data were noisy, thus we took the mean average of the last five data points on each indent.

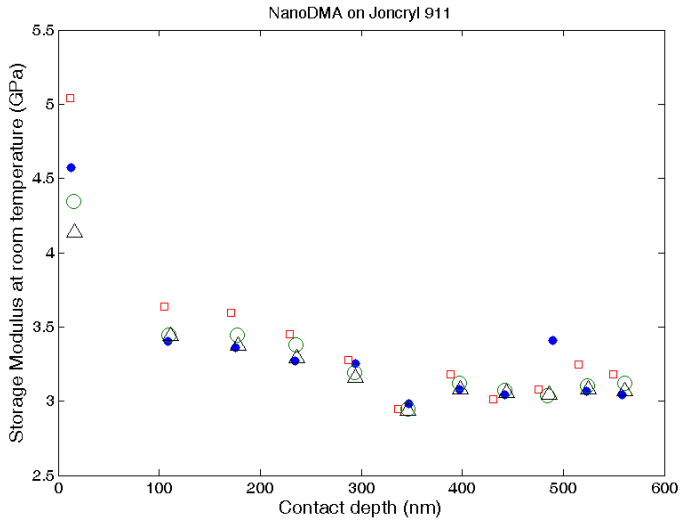

Figure 4.17. Storage modulus data from nanoindentation showing four indentations on coating with Joncryl® 911

Figure 4.18 shows the comparison of modulus data from quasi-static and dynamic indentation which means that either of the modulus measurements can be used for the correlation study.

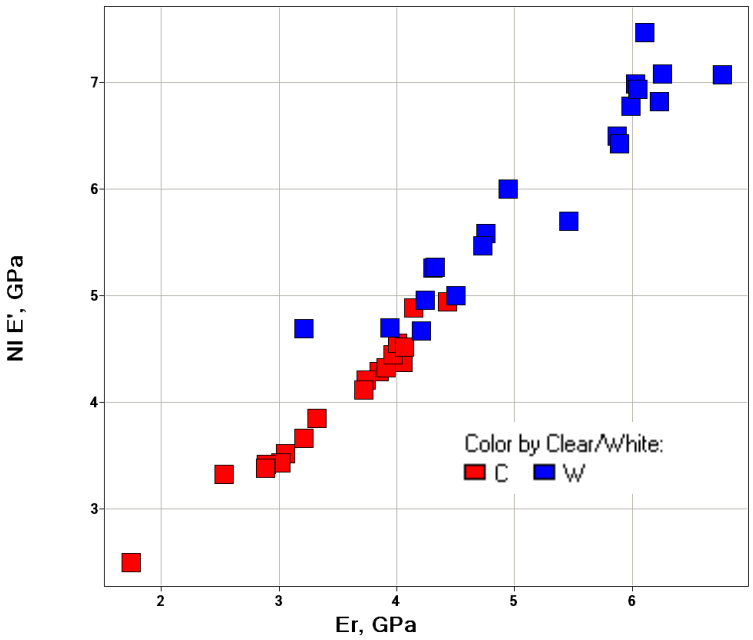

Figure 4.18. Nanoindentation results of storage modulus versus reduced modulus: Red and white symbols represent forty different clear and white coatings, respectively.

For pDMTA test, two separate plates containing 4 replicates on each plate were run.

Figure 4.19 shows a pDMTA plate with the Joncryl® clear coatings.

Figure 4.19. pDMTA sample plate with clear coatings

Figure 4.20 shows a scatter plot of the reduced moduli on the clear coatings and the T_g results from pDMTA.

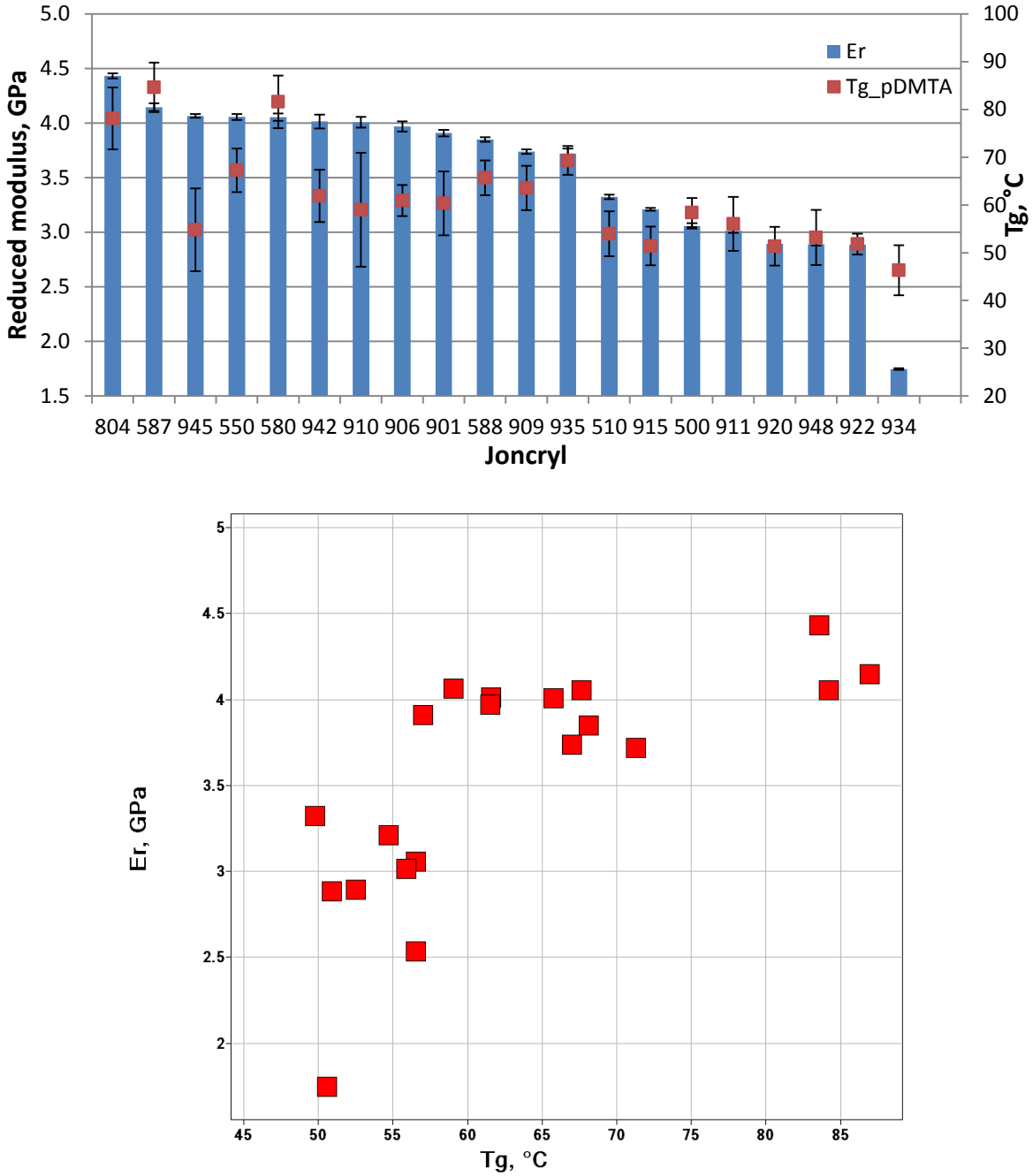

Figure 4.20. Reduced modulus from nanoindentation and T_g from pDMTA on Joncryl® clear coatings. In the top Figure, numbers underneath the columns are product number of the Joncryl® resins.

Figure 4.21 compares pendulum hardness with $(E_r{}^{1/3}/\tan\delta)$ where a linear relationship would be expected according to Equation 4.17.

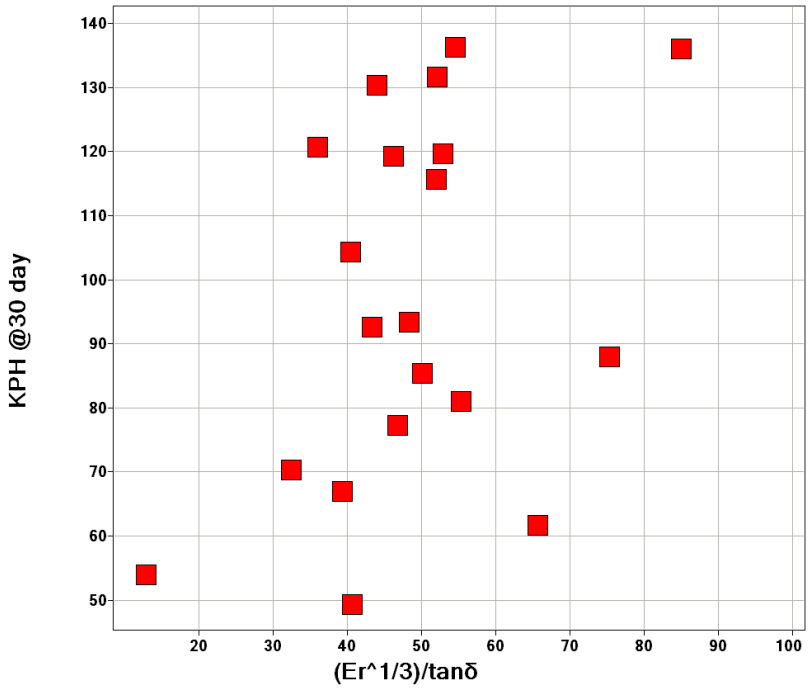

Figure 4.21. Konig pendulum hardness versus the term $(E_r{}^{1/3}/\tan\delta)$ on clear coatings

The linear trend was not observed which could be explained as follows. The nanoDMA may lack sensitivity for the loss component running at the frequency of 50 Hz. The nanoDMA should have been operated at similar frequency as that of Konig pendulum. The period of oscillation on the Konig pendulum is 1.4 sec (frequency ≈ 0.71). Also, it was possibly due to the high stiffness of the coatings causing no observable change in pendulum hardness as suggested in Figure 4.15. In addition, according to Figure 4.14 (Hertzian contact), the total depths of indentation on Konig pendulum test could be between 2-5 μm, thus the Konig pendulum measurement might be affected by the substrate effect. Figure 4.22 shows pendulum hardness as a function of storage modulus. The proportionality in Figure 4.22 was slightly better compared to Figure 4.21 but it was still scattered and the trend was not as obvious as the results in Figure 4.15. The results implied

that our experimental parameters point to a larger dependence on modulus than on $(1/\tan\delta)$ for pendulum hardness correlation.

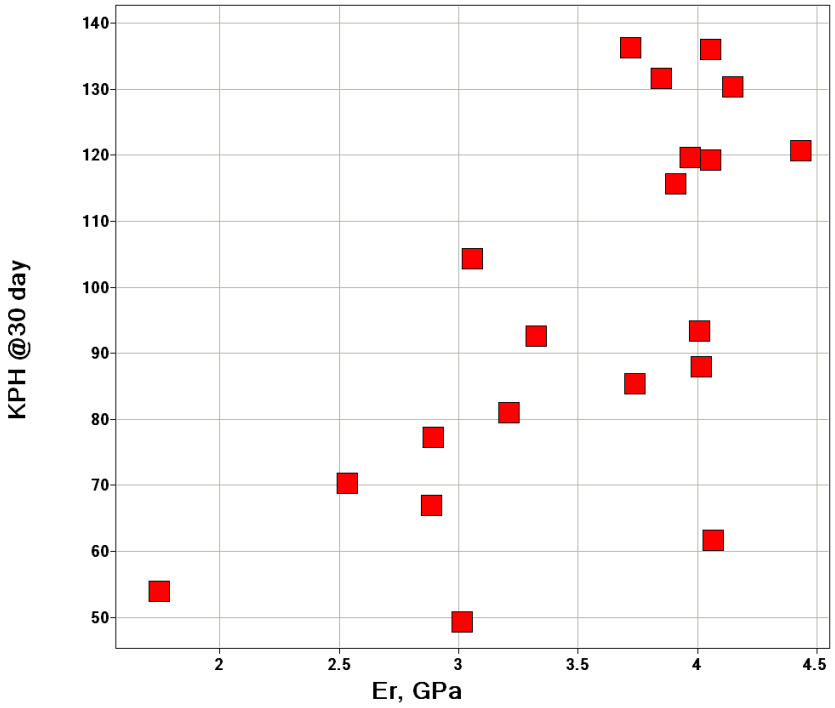

Figure 4.22. Konig pendulum hardness versus storage modulus

Figure 4.23 provides a plot of Konig pendulum hardness versus indentation hardness. There was a slight trend which was expected since they both depended on elastic response. However, they measure different properties and have merit on their own. Figure 4.24 shows Konig pendulum hardness versus T_g.

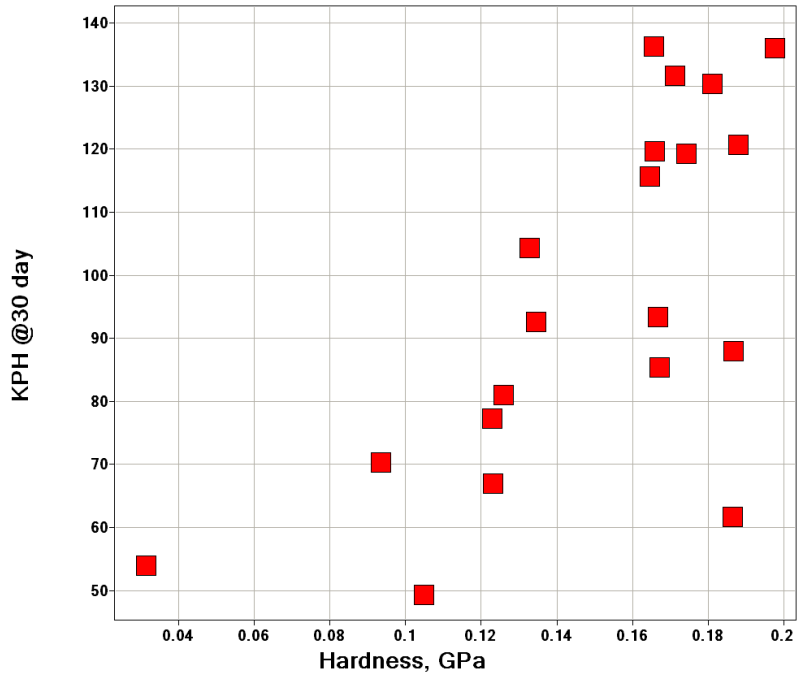

Figure 4.23. Konig pendulum hardness versus indentation hardness

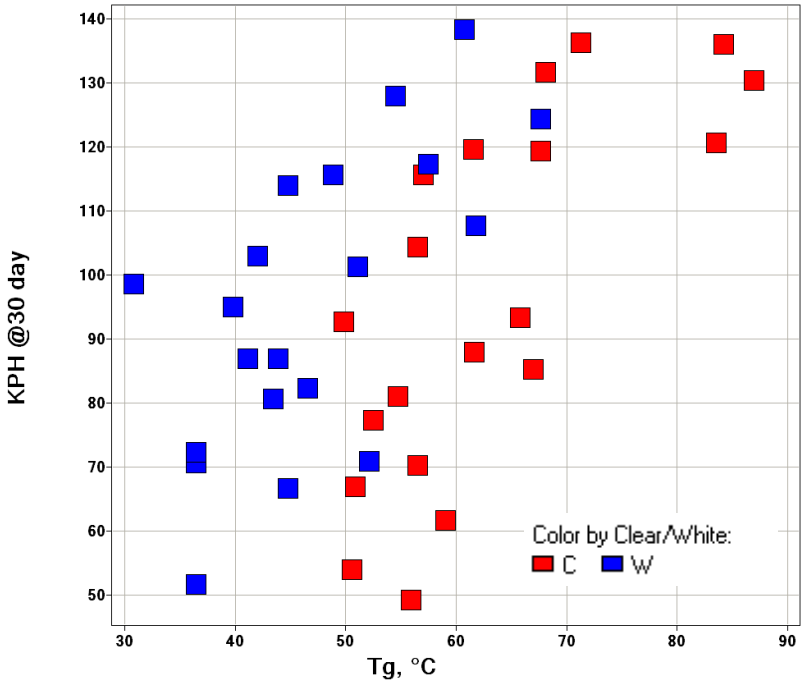

Figure 4.24. Konig pendulum hardness versus T_g: Red and white symbols represent clear and white coatings, respectively.

As shown in Figure 4.25, the pencil hardness did not correlate well with indentation hardness or modulus from nanoindentation. This library has a narrow range of modulus which could be the reason why the pencil hardness did not correlate with any of the tests. Figure 4.26 shows impact resistance with T_g.

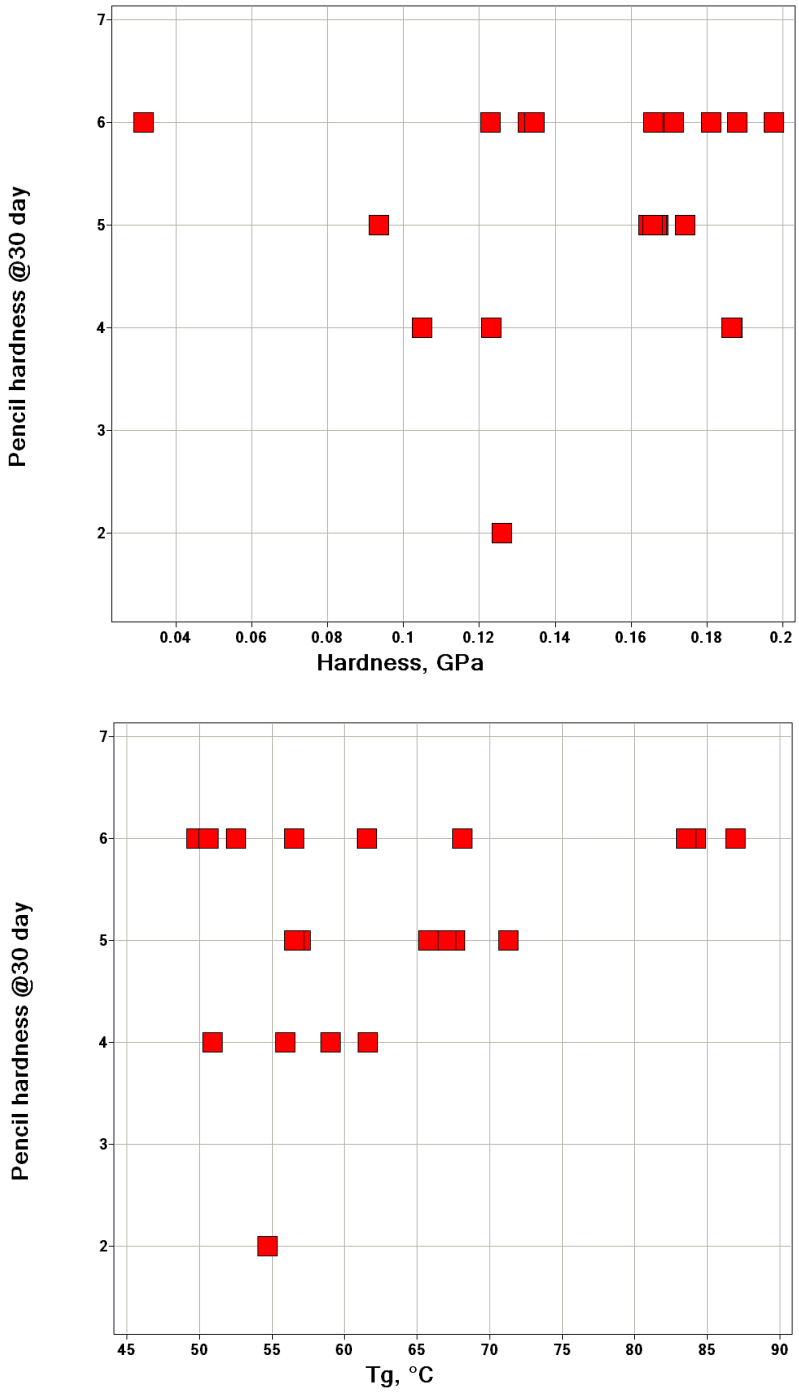

Figure 4.25. Pencil hardness versus indentation hardness (top) and T_g (bottom)

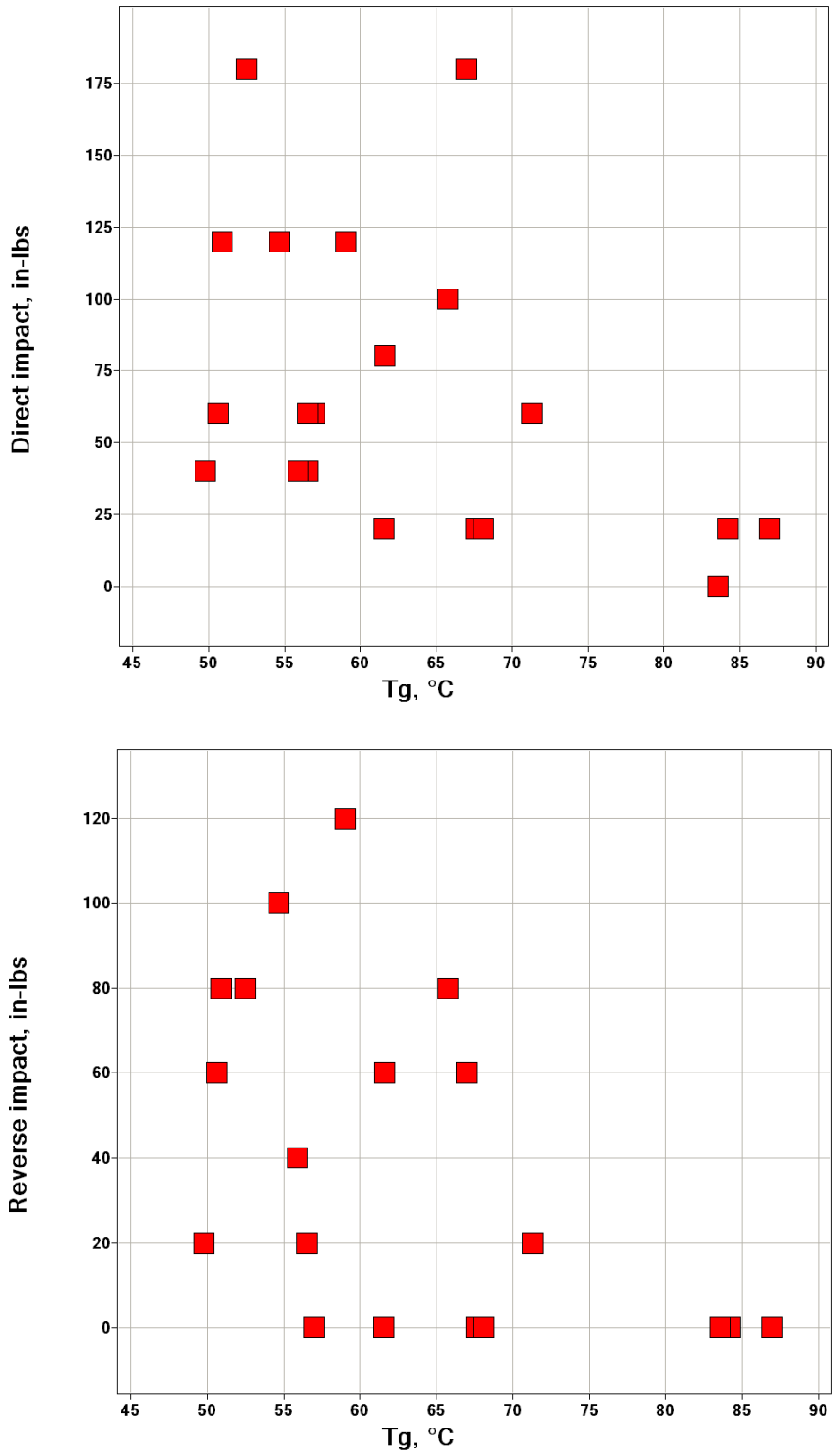

Figure 4.26. Direct impact (top) and reverse impact (bottom) versus T_g

4.5. Conclusion

Instrumented indentation was implemented in the NDSU combinatorial laboratory. The capability of automation saves time and is appropriate for a high-throughput method. The hardness and elastic properties on the near surface and bulk of the materials can be extracted. The indentation experiment also does not require the measurement of film thickness. The literature review pointed to a linear relationship between pendulum hardness and $(G^{1/3}/\tan\delta)$, even though it was not observed here which was likely due to unsuitable testing parameters. The trend between pendulum hardness and modulus was observed. There was also a trend between reduced modulus and T_g. Properties, such as pencil hardness and impact resistance, would require a comparison with tests measuring beyond the elastic limit. In the future, an automated scratch test can be performed with a current system and it could simulate the pencil scratching action. As a result, instrumented high-throughput tests can enhance and even replace some of the conventional methods making it a viable tool for a combinatorial study.

4.6. References

1. Koleske, J. V., *Paint and coating testing manual: fourteenth edition of the Gardner-Sward handbook*. American Society for Testing and Materials: Ann Arbor, MI, 1995.

2. Johnson, K. L., *Contact Mechanics*. Cambridge University Press: Cambridge, 1985.

3. Stilwell, N. A.; Tabor, D., Elastic recovery of conical indentations. *Proc. Phys. Soc.* **1961,** *78* (169-179).

4. Sneddon, I. N., The relation between load and penetration in the axisymmetric Boussinesq problem for a punch of arbitrary profile. *International Journal of Engineering Science* **1965,** *3*, 47-57.

5. Doerner, M. F.; Nix, W. D., A method for intepreting the data from depth-sensing indentation instruments. *Journal of Materials Research* **1986,** *1* (4), 601-609.

6. Pharr, G. M.; Oliver, W. C.; Brotzen, F. R., On the generality of the relationship among contact stiffness, contact area, and elastic modulus during indentation. *Journal of Materials Research* **1992,** *7* (3), 613-617.

7. Oliver, W. C.; Pharr, G. M., An improved technique for determining hardness and elastic modulus using load and displacement sensing indentation experiments. *Journal of Materials Research* **1992,** *7*, 1564-1583.

8. Oliver, W. C.; Pharr, G. M., Measurement of hardness and elastic modulus by instrumented indentation: Advances in understanding and refinements to methodology. *Journal of Materials Research* **2004,** *19* (1), 3-20.

9. Field, J. S.; Swain, M. V., *Journal of Materials Research* **1993,** *8* (2), 297.

10. Turnbull, A.; White, D., Nanoindentation and microindentation of weathered unplasticised poly-vinyl chloride. *Journal of materials science* **1996,** *31*, 4189-4198.

11. Tranchida, D.; Piccarolo, S., On the use of the nanoindentation unloading curve to measure the Young's modulus of polymers on a nanometer scale. *Macromolecular Rapid Communications* **2005,** *26*, 1800-1804.

12. VanLandingham, M. R.; Villarrubia, J. S.; Guthrie, W. F.; Meyers, G. F., Nanoindentation of polymers: An overview. **1997**.

13. Cheng, L.; Xia, X.; Scriven, L. E.; Gerberich, W. W., Spherical-tip indentation of viscoelastic material. *Mechanics of Materials* **2005,** *37*, 213-226.

14. Cheng, Y.-T.; Ni, W.; Cheng, C.-M., Determining the instantaneous modulus of viscoelastic solids using instrumented indentation measurements. *Journal of Materials Research* **2005,** *20* (11), 3061-3071.

15. Johnson, K. L.; Kendall, K.; Roberts, A. D., Surface energy and the contact of elastic solids. *Proc. R. Soc. Lond. A.* **1971,** *324*, 301-313.

16. Gupta, S.; Carrillo, F.; Li, C.; Pruitt, L.; Puttlitz, C., Adhesive forces significantly affect elastic modulus determination of soft polymeric materials in nanoindentation. *Material Letters* **2007,** *61*, 448-451.

17. Carrillo, F.; Gupta, S.; Balooch, M.; Marshall, S. J.; Marshall, G. W.; Pruitt, L.; Puttlitz, C. M., Nanoindentation of polydimethylsiloxane elastomers: Effect of crosslinking, work of adhesion, and fluid environment on elastic modulus. *Journal of Materials Research* **2005,** *20* (10), 2820-2830.

18. Ao, Z.; Li, S., Temperature- and thickness-dependent elastic moduli of polymer thin films. *Nanoscale Research Letters* **2011,** *6* (243), 1-6.

19. Han, C.-S., Influence of the molecular structure on indentation size effect in polymers. *Material Science and Engineering A* **2010,** *527*, 619-624.

20. Tatijaru, R. V. S.; Han, C.-S.; Nikolov, S., Size dependent hardness of polyamide/imide. *The Open Mechanics Journal* **2008,** *2*, 89-92.

21. Juliano, T. F.; Forster, A. M.; Drzal, P. L.; Weerasooriya, T.; Moy, P.; VanLandingham, M. R., Multiscale mechanical characterization of biomimetic physically associating gels. *Journal of Materials Research* **2006,** *21* (8), 2084-2092.

22. Ebenstein, D. M.; Wahl, K. J., A comparison of JKR-based methods to analyze quasi-static and dynamic indentation force curves. *Journal of colliod and interface science* **2006,** *298* (2), 652-662.

23. Hayes, S. A.; Goruppa, A. A.; Jones, F. R., Dynamic nanoindentation as a tool for the examination of polymeric materials. *Journal of Materials Research* **2004,** *19* (11), 3298-3306.

24. Kranenburg, J. M.; Tweedie, C. A.; Van Vliet, K. J.; Schubert, U. S., Challenges and progress in high-throughput screening of polymer mechanical properties by indentation. *Advanced Materials* **2009,** *21*, 1-11.

25. Tweedie, C. A.; Anderson, D. G.; Langer, R.; Van Vliet, K. J., Combinatorial material mechanics: high-throughput polymer synthesis and nanomechanical screening. *Advanced Materials* **2005,** *17*, 2599-2604.

26. Anderson, D. G.; Tweedie, C. A.; Hossain, N.; Navarro, S. M.; Brey, D. M.; Van Vliet, K. J.; Langer, R.; Burdick, J. A., A combinatorial library of photocrossinkable and degradable materials. *Advanced Materials* **2006,** *18*, 2614-2618.

27. Lin-Gibson, S.; Landis, F. A.; Drzal, P. L., Combinatorial investigation of the structure-properties characterization of photopolymerized dimethacrylate networks. *Biomaterials* **2006,** *27*, 1711-1717.

28. Gardco: Hardness. http://www.gardco.com/hardness.cfm (accessed 03/05/2012).

29. Sato, K., The hardness of coating films. *Progress in Organic Coatings* **1980,** *8*, 1-18.

30. Chen, Z.; Chisholm, B.; Kim, J.; Stafslien, S.; Wagner, R.; Patel, S.; Daniels, J.; Vander Wal, L.; Li, J.; Ward, K.; Callow, M.; Thompson, S.; Siripirom, C., UV-curable,

oxetane-toughened epoxy-siloxane coatings for marine fouling-release coating applications *Polymer International* **2008,** *57* (6), 879-886.

CHAPTER 5. SURFACE CHARACTERIZATION OF SILOXANE-POLYURETHANE COATINGS

5.1. Introduction and Rationale

Nontoxic marine coatings have gained much attention in the paint and coatings industry. Antifouling paints have been effective, but they mainly contain copper or organotins which cause environmental concerns as the released chemicals can enter the food chain.[1] Fouling-release coatings represent an alternative. The coatings are based on fluoropolymers and silicones and are nontoxic. Fouling-release coatings are designed to have low adhesion to marine fouling organisms. The organisms would not adhere or only weakly adhere which can be easily removed as the ships travel through the water and during routine cleaning. However, as Brady pointed out, the marine environment is complex with over 4,000 marine organisms and 12 different ocean zones with different temperature and salinity, etc.[1] Many design parameters are involved. Fouling-release coatings need to have hydrolytic stability, low adhesion to marine organisms, and durability.

The surface properties of the coatings clearly play an important role in the adhesion of marine organisms. A qualitative relationship between surface free energy and relative bioadhesion has been established through the "Baier curve" as shown in Figure 5.1.[1-3] The curve illustrates a 'V' shape with a minimum relative adhesion at a surface energy of ~24 mN/m.

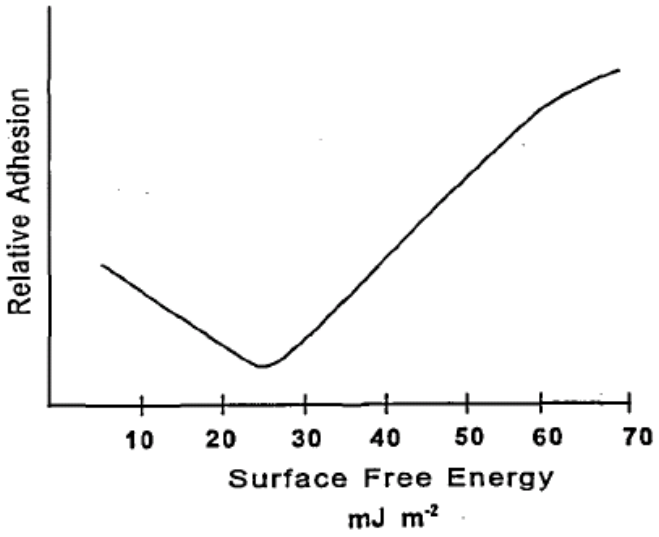

Figure 5.1. Empirical relationship in the Baier curve (reproduced from ref.[3])

Brady and Singer also observed that the relative adhesion is proportional to $(E\gamma_c)^{1/2}$, as seen in Figure 5.2, where E is the elastic modulus and γ_c is the critical surface free energy.[3]

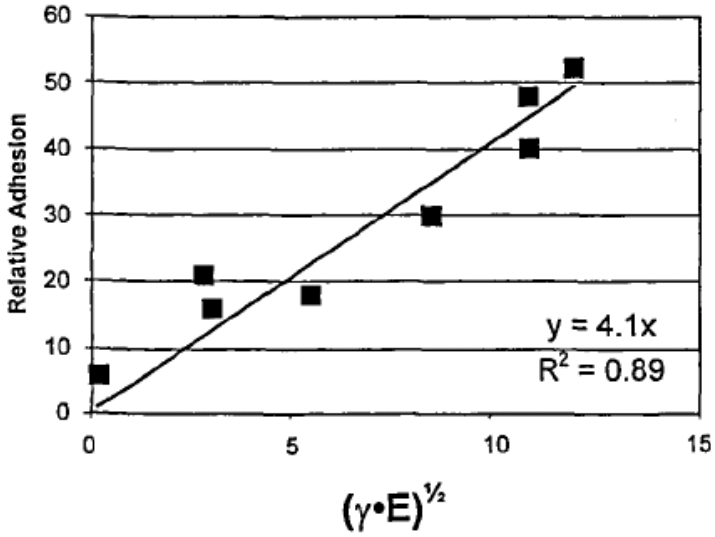

Figure 5.2. Relative adhesion versus a function of critical surface energy and the elastic modulus (Reproduced from ref.[3])

For the above reasons, silicone elastomeric coatings have received a lot of attention due to both the optimum surface energy and low elastic modulus. The studies imply that relatively soft and low surface energy coatings can give the best overall fouling-release

performance. Brady concludes the design criteria for silicone fouling-release coatings as follows:

1) Smooth surface at molecular level to avoid mechanical interlocking with fouling organisms
2) "Absence of heteroatoms, ions and dipoles" [1] on the coating surface to avoid ionic and dipolar interactions with adhesives from marine organisms
3) Stability in marine environment both chemically and physically
4) Flexible linear silicone backbone
5) Low surface energy from sufficient molecular weight and chain mobility
6) Low elastic modulus
7) Hydrolytic stability to prevent surface roughening
8) Thicker coatings offer better release than thinner coatings.

Silicones must be tailored to satisfy the above criteria, but there are apparent drawbacks that are inherent to silicone elastomers. Firstly, they can exhibit poor adhesion to the underlying metal or primer and, secondly, they have lower toughness than hard coatings in a sense that it normally takes much lower energy to propagate a crack to failure.[4, 5] The low toughness then implies a durability issue in service. This means a shorter lifetime of the coating. Fillers can be added to silicones to improve mechanical properties with a trade-off in an increase of elastic modulus. Griffith developed a duplex coating, which is a two-layer system with a silicone topcoat and silicone blended with copolymers as a stiffer bond coat. A bond coat is specifically used to improve the toughness and to improve the overall bond strength of the topcoat, the bond coat and the epoxy basecoat.[4] Distinct layers of topcoat, bond coat, and basecoat can be observed with

an optical microscope where the thickness of each layer is controlled via the application method and the percent solid content.

At NDSU, a new type of fouling release coating is being explored which is based on a self-stratified siloxane-polyurethane system which attempts to combine the benefits of the low surface energy of silicone and the excellent toughness of the polyurethane.[6-8] The siloxane-polyurethane coating, as the name implies, contains the polyurethane and siloxane components in which they are covalently bonded into a crosslinked system. The components are mixed together and two interlocking layers are created in a single application. Due to the differences in surface energies, the siloxane component migrates, during a liquid phase, towards the air-coating interface before they are cured and locked in place.[9] The phenomenon is called a self-stratifying process. The schematic of the self-stratifying siloxane-polyurethane is shown in Figure 5.3.

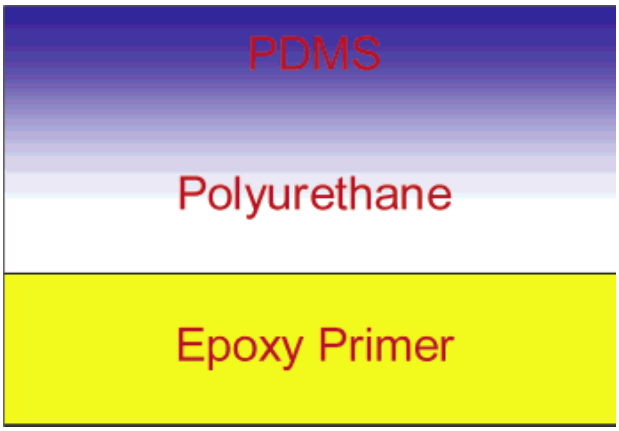

Figure 5.3. Schematic of a siloxane-polyurethane coating (Reproduced from ref.[6])

In Figure 5.3, the PDMS and polyurethane are distinctly separated to the top and bottom regions with a gradient of concentration in the middle region. The postulated scheme is used to illustrate the migration, but the detailed and actual distribution of PDMS as a function of formulation parameters had not been characterized for our coatings until

the experiments presented in this chapter. The assumption of a top silicone layer is supported by observing hydrophobic surfaces from contact angle measurements and measuring their low force of adhesion compared with the polyurethane control.[6, 8, 9]

A thorough surface characterization can be accomplished using methods such as x-ray photoelectron spectroscopy (XPS), transmission electron microscopy (TEM), and time-of-flight secondary ion mass spectroscopy (TOF-SIMS).[9-14] XPS can be used to conduct elemental analysis at the surface. Kim et al. used XPS to demonstrate the surface segregation of polydimethylsiloxane in a polycarbonate system with polycarbonate-polydimethylsiloxane block copolymers as an additive to improve surface and wear properties.[12] Angle-dependent XPS is used as a non-destructive depth-profiling method to observe the stratifying element composition.[15] Surface morphology can be observed with TEM as shown in Figure 5.4.[14] In the figure, the amount of PDMS soft segment is varied in organosiloxane modified segmented polyether polyurethanes. At 15%, dark domains representing PDMS are about 0.1 μm in diameter and, at 55 wt% PDMS, the surface becomes more continuous.

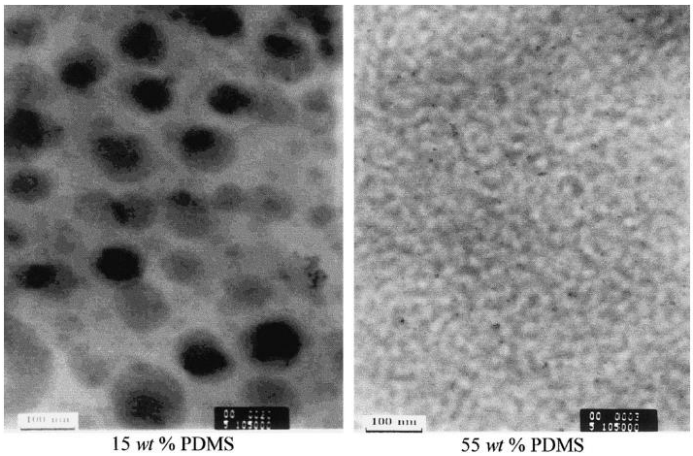

Figure 5.4. TEM images showing a surface morphology of PDMS containing segmented thermoplastic polyurethanes (Reproduced from ref.[14])

In a copolymer, the extent of segregation depends on a number of factors such as the bulk composition, block length, processing conditions (annealing, solvent casting, etc.) and the block sequence distribution.[12] Gardella and Mahoney used TOF-SIMS to determine the molecular weight distribution of PDMS on the surface and it was apparent that longer PDMS chains prefer to segregate toward the surface.[10] TOF-SIMS showed a shift to higher mass distribution on the surface as compared with the bulk. Other driving forces for segregation include the solvent-polymer solubility parameter and the evaporation rate of solvent.[9, 12] Self-stratifying surfaces of polystyrene/polydimethyl siloxane (PS/PDMS) block copolymers were tested. The polymers were dissolved in two main groups of solvents differed by their range of solubility parameters and vapor pressures. The solvent group with smaller difference in solubility parameter to polystyrene gave a thicker overlayer of PDMS. Thus, the incompatibility between the solvent and the siloxane can assist in driving the siloxane away from the bulk. Kim et al. studied the solubility parameter difference of the copolymer itself with the solvent which is an extension of the above observation.[12] It was found that smaller solubility parameter difference yields higher segregation of PDMS near the surface. If the solubility parameter differences were similar, the higher concentration of PDMS was found on slower evaporation rate solvent. Thus, a longer time to equilibrate favors segregation than a shorter evaporation time.

To gain a better understanding of the surface composition of siloxane-polyurethane coatings, surface characterization was performed. Information such as the surface elemental composition and the thickness of the concentrated PDMS layer, were measured. Siloxane-polyurethane coatings were characterized with x-ray photoelectron spectroscopy

(XPS), transmission electron microscopy (TEM), Rutherford backscattering spectroscopy (RBS), and nanoindentation.

Previous work on how the siloxane-polyurethane coatings were synthesized and tested for fouling-release marine coating application are in the references [6-8, 16, 17]. In this study, siloxane-polyurethane coatings were differed in PDMS content, PDMS molecular weight, PDMS functionality and polyol type. The characterizations are carried out to observe the fundamental differences in surface properties between formulations.

5.2. Experimental

5.2.1. Formulations

There are ten formulations with the following acronyms shown in Table 5.1.

Table 5.1. Siloxane-polyurethane formulations

Sample name	**Polyol**	**PDMS functionality**	**PDMS MW (**g mol^{-1})	**PDMS weight % of solid**
ACR-M-20%	ACR	1	30,000	20
ACR-D-20%	ACR	2	30,000	20
ACR-M-10%	ACR	1	30,000	10
ACR-D-10%	ACR	2	30,000	10
PCL-M-20%	PCL	1	30,000	20
PCL-D-20%	PCL	2	30,000	20
PCL-M-10%	PCL	1	30,000	10
PCL-D-10%	PCL	2	30,000	10
A4	ACR	2	20,000	20
D3	PCL	2	20,000	20

ACR stands for an acrylic polyol copolymer composed of 80% butyl acrylate and 20% hydroxyethyl acrylate with the average molecular weight of 10,000 g mol^{-1}. The equivalent weight of ACR is 581 g mol^{-1}. PCL represents a commercial polycaprolactone polyol TONE 0305 from Dow Chemical. It is a tri-functional polyol with an average molecular weight of 540 g mol^{-1}. PDMS macromers have the average molecular weight of 30,000 g

mol^{-1}, except for A4 and D3 samples where it is 20,000 g mol^{-1}. PDMS in D3 is diluted in ethyl ethoxy propionate (EEP), but PDMS in A4 is not. The chemical structures are shown in Figure 5.5.

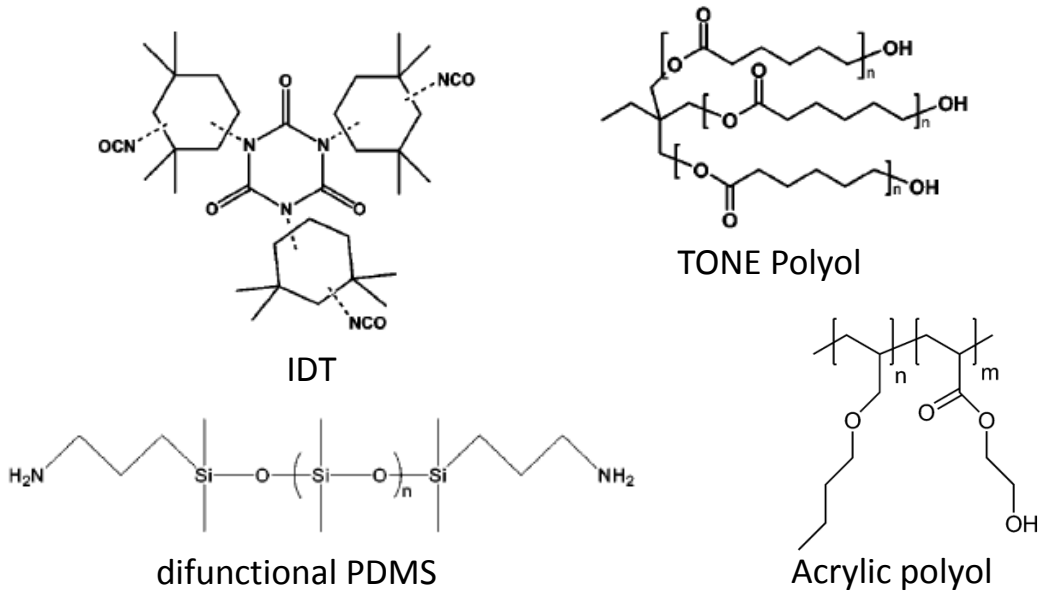

Figure 5.5. Chemical structures (Reproduced from ref.[6])

Monofunctional aminopropyl terminated PDMS was synthesized by Stacy Sommer (refer to ref. [8] for details). Rajan Bodkhe supplied the difunctional PDMS. The isocyanate to hydroxyl and amine ratio was 1.1:1. The difunctional PDMS and the polyol were mixed overnight, followed by the additions of Tolonate IDT 70B (IDT) and dibutyltin diacetate (DBTDAc) as an isocyanate crosslinker and a catalyst, respectively, the next morning. In contrast, monofunctional PDMS and IDT were firstly mixed overnight. Polyol and catalyst were added the next day. The polymer solutions were applied on cleaned aluminum Q-panels® with an 8-mil gap drawdown bar. The ACR and PCL polyurethane controls without PDMS were also made. All siloxane-polyurethane and polyurethane control coatings were cured in ambient conditions overnight and oven cured at 80°C for 45

minutes the following day. Dow Corning® 3140 (DC3140), a moisture-cured silicone elastomer, was used as a PDMS control for RBS analysis.

5.2.2. Characterization

Siloxane-polyurethane coatings were characterized with x-ray photoelectron spectroscopy (XPS), Rutherford backscattering spectroscopy (RBS), transmission electron microscopy (TEM), scanning electron microscopy (SEM) and nanoindentation.

5.2.2.1. X-ray photoelectron spectroscopy (written by Dr. Bing Luo, XPS specialist)

The XPS measurements were performed at the University of Minnesota on an SSX-100 system (Surface Science Laboratories, Inc.) equipped with a monochromated Al K_α X-ray source, a hemispherical sector analyzer (HSA) and a resistive anode detector. The base pressure of the XPS system was 4.0 x 10^{-10} Torr. During the data collection, the pressure was *ca.* 1 x 10^{-8} Torr. For the angle-dependence measurements, the samples (size 22 x 22 mm^2 or 10 x 15 mm^2) were mounted on a rotation sample stage. All of the samples were not sufficiently conductive and a low-energy electron beam (5 – 16 eV) was used for charge neutralization. The X-ray spot size was 1x1 mm^2, which corresponded to an X-ray power of 200 W. Each survey spectrum was collected with 8-14 scans at 150 eV pass energy and 1 eV/step. The atomic percentages were calculated from the survey spectra using the ESCA 2005 software provided with the XPS system. In most of the angle-dependence measurements, a six-degree aperture was used on the entrance of the electron analyzer (the collection angle was 30 degree if the aperture was not used). The estimated errors in the angles were plus minus 5 degrees.

5.2.2.2. Rutherford backscattering spectroscopy (RBS)

RBS is a non-destructive and multielemental analysis technique. The technique gives elemental depth profiles with a depth resolution of 5-50 nm and a maximum depth of 2-20 μm. A MAS 1700 pelletron tandem ion accelerator (5SDH) equipped with charge exchange RF plasma source by National Electrostatics Corporation (NEC) was used along with an Analytical endstation (RBS 400) by Charles Evans & Associates. A fixed ion detector at 165º is used for RBS. A common way to analyze RBS data is to create a simulation in order to compare with the experimental result. QUARK – version 1.3 is used for simulation. QUARK stands for Quantitative Analysis of Rutherford Kinematics and is made by Prof. William N. Lennard at The University of Western Ontario and Christopher P. McNorgan. Table 5.2 lists the experimental parameters for the simulations.

Table 5.2. Experimental parameters for Quark simulation

Experimental Parameters			
Beam		**Geometry**	
Ion	4He+	Detector Angle	165º
Energy	2.3 MeV	Target Angle	0º
Q	20 μC	Ω	3.6 msr
Detector Resolution			
dE/E	18.5 keV		
Dispersion (determined from spectra)			
Slope	3.22 keV/channel		
Intercept	70 keV (at channel 0)		

5.2.2.3. Transmission electron microscopy (TEM)

The prepared free films were embedded in an epoxy and cross-sectioned with a Leica UC6 ultramicrotome at 70 nm thickness. A JEOL 1200-EX II TEM was used. In bright field imaging mode, the darker regions specify a thicker region of the sample or a region of higher atomic number element. It was expected to observe a siloxane layer or domains from a distinctly darker region in TEM images due to higher electron density of Si

from other elements (C, H, N, and O) in the coatings. Majumdar and Webster were able to observe micron-size PDMS domains on the surface and bulk with TEM.[16]

5.2.2.4. Scanning electron microscopy (SEM)

The prepared free films were freeze fractured in liquid nitrogen and coated with carbon on an aluminum mount. A field-emission SEM, JEOL JSM-7600F, was used.

5.2.2.5. Nanoindentation

Quasi-static nanoindentation is performed using a Triboindenter (Hysitron, Inc.). A 400-μm radius hemispherical sapphire indenter was used. The load function is a 25-5-25 trapezoidal load function with a closed-loop displacement control mode. The 25-5-25 means loading for 25 seconds, holding for 5 seconds and unloading to zero displacement for another 25 seconds. The indenter displaces at a rate of 12 nm/s to a depth of 300 nm, holds for 5 seconds and unloads at 12 nm/s. The Oliver-and-Pharr calculation from the instrument's default is used, which implies a power law fit at the unloading curve and cylindrical flat punch formula from Sneddon.[18, 19]

5.3. Results and Discussion

5.3.1. XPS characterization of siloxane-polyurethane coatings

XPS, also known as ESCA (Electron Spectroscopy for Chemical Analysis), operates by irradiating the samples with X-rays which resulted in photoemitted electrons.[20] An energy analysis of these electrons then differentiates each element. An ultra-high vacuum is required to reduce the contaminant from residual gas molecules on the surface and to allow the photoemitted electrons to reach the analyzer without being scattered. The kinetic energy of the emitted electron and the electron count are measured by the electron

energy analyzer and the detector, respectively. Figure 5.6 describes the XPS instrumentation.

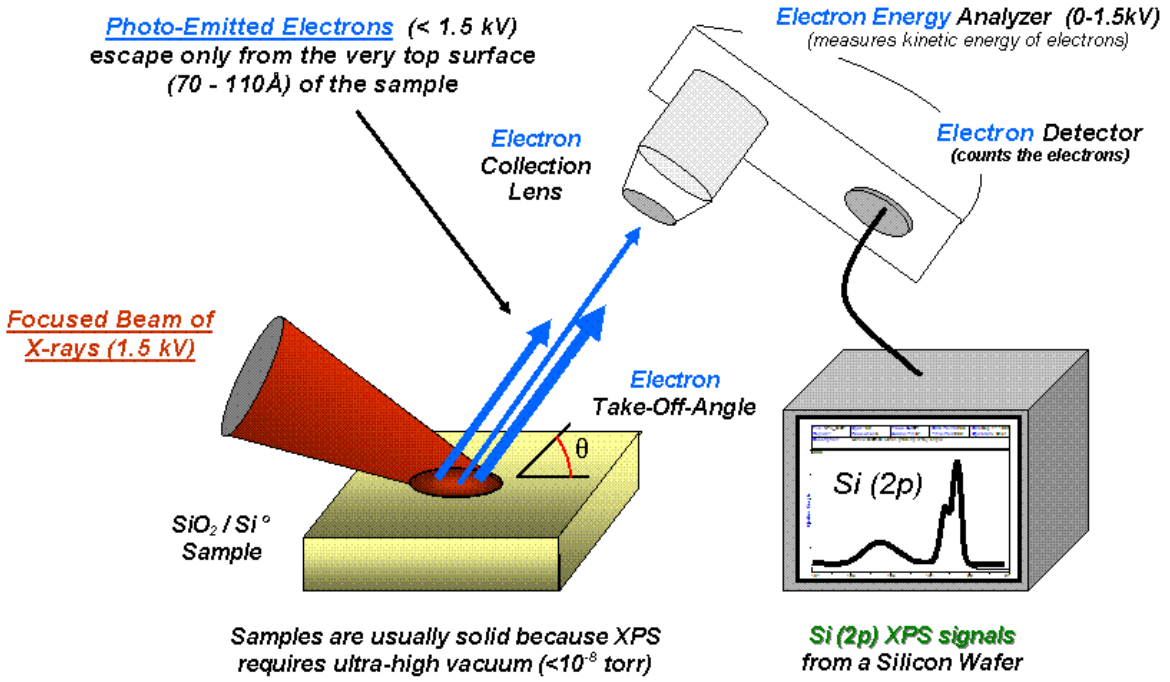

Figure 5.6. Schematic of XPS

The measured kinetic energy can be used to calculate the binding energy of each electron with the following equation.

$$E_K = h\nu - E_B - \Phi_{sp} \tag{5.1}$$

where E_K is the measured kinetic energy, $h\nu$ is the energy of the X-ray photon, E_B is the electron binding energy and Φ_{sp} is the spectrometer work function (~5 eV).

Depth-profiling can be achieved with either ion sputtering which is a destructive method or a non-destructive angle-dependent (ADXPS)/angle-resolved (ARXPS) method. In ADXPS, the collection angle is varied to allow collection of electrons at different take-off angles to the surface. However, sampling depth with ADXPS will be limited to roughly 10 nm from the sample surface. Two extreme take-off- angles of 10° and 90° are normally used to gain

qualitative insights. A series of data from different take-off angles can be used to construct a concentration depth-profile.

Figure 5.8 shows the XPS survey scans of ACR-D-10% at different take-off angles. XPS does not detect hydrogen. The first peak from the right at ~100 eV is the Si 2p peak. The second peak is the Si 2s peak. Si 2p peak is used for calculation along with C 1s, N 1s and O 1s peaks which are seen roughly at 285, 400 and 534 eV, respectively. The scans in Figure 5.7 are shifted to where the carbon peaks (C 1s) are 285 eV. It is difficult to compare these peaks because the counts are not normalized. At the take-off angle of 10 degrees, there are fewer counts (less electrons striking the collection lens) than at 35 and 80 degrees. There is a higher percentage of Si at 10 degrees, but the comparisons are not obvious due to the differences in "counts".

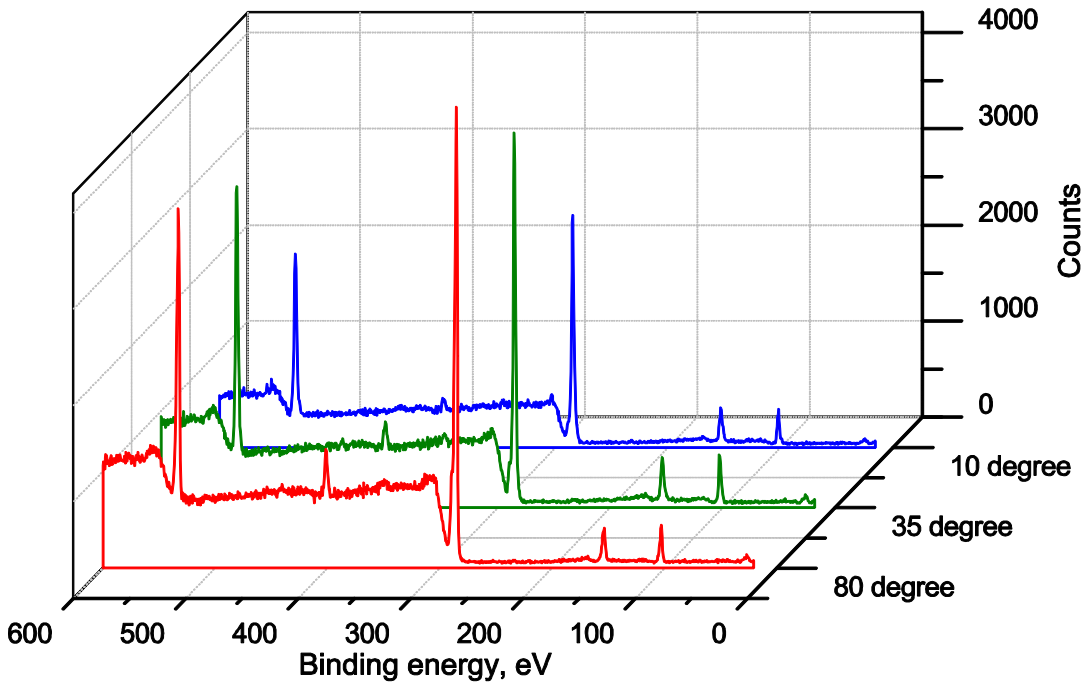

Figure 5.7. ACR-D-10% survey scans at three different angles

The area under the curve with a sensitivity factor for each element is calculated and compared to give the percentages of each element. It is of interest to conduct depth

profiling analysis with XPS. There are two depth profiling options; one is to use the ion beam sputtering and another is the angle-dependent method. An angle-dependent XPS is chosen based on availability and cost. The drawback is that the depth at a fixed X-ray energy can be only as deep as the length of the inelastic mean free path (IMFP) of the electrons. Elemental analysis from XPS is shown in Table 5.3. Elemental percentages on each siloxane-polyurethane coatings are presented at 10°, 35° and 80° collection angles. As expected, silicon content from PDMS is found at the highest concentration at the lowest angle. Nitrogen, which is a part of polyurethane network, then increases as the sampling depth increases. There is noticeably more silicon content in coatings made using the mono-functional PDMS comparing with the di-functional PDMS. Within the same type of PDMS, the differences of Si content in 10% and 20% PDMS are subtle. There is a higher amount of nitrogen in PCL PU compared with ACR PU, because the PCL PU has a higher weight percent of isocyanate due to lower equivalent weight of PCL polyol.

Table 5.3. Elemental analysis from XPS for the siloxane-polyurethane coatings.

Sample		10º	35º	80º	Sample		10º	35º	80º
ACR-M-20	**Si**	24.57	21.24	18.01	**PCL-M-20**	**Si**	21.05	21.27	17.11
	C	50.71	55.16	57.72		**C**	53.20	54.68	57.50
	N			1.73		**N**	0.56	0.72	2.73
	O	24.72	23.60	22.54		**O**	25.18	23.33	22.65
		10º	**35º**	**80º**			**10º**	**35º**	**80º**
ACR-D-20	**Si**	9.39	6.37	4.22	**PCL-D-20**	**Si**	7.06	6.66	4.61
	C	66.90	69.76	71.41		**C**	69.94	70.08	72.74
	N	3.76	3.88	5.14		**N**	7.10	7.18	7.53
	O	19.95	19.99	19.23		**O**	15.89	16.07	15.11
		10º	**35º**	**80º**			**10º**	**35º**	**80º**
ACR-M-10	**Si**	21.68	17.86	14.69	**PCL-M-10**	**Si**	20.43	18.75	17.42
	C	53.45	58.51	60.61		**C**	54.17	56.47	57.03
	N	0.71	1.23	2.39		**N**	2.51	2.13	2.05
	O	24.15	22.40	22.31		**O**	22.90	22.65	23.51
		10º	**35º**	**80º**			**10º**	**35º**	**80º**
ACR-D-10	**Si**	9.74	8.68	5.71	**PCL-D-10**	**Si**	7.39	5.47	6.72
	C	68.22	69.97	71.33		**C**	71.19	71.80	70.30
	N	2.37	2.64	4.46		**N**	4.74	6.48	6.66
	O	19.66	18.71	18.50		**O**	16.67	16.25	16.31
		10º	**35º**	**80º**			**10º**	**35º**	**70º**
D3	**Si**	23.01	19.79	13.35	**PCL PU**	**Si**			
	C	52.01	54.35	60.81		**C**		77.72	77.40
	N	1.28	2.02	3.96		**N**		9.79	10.00
	O	23.70	23.85	21.88		**O**		12.49	12.61
		10º	**35º**	**80º**			**10º**	**35º**	**70º**
A4	**Si**	11.34	9.17	5.53	**ACR PU**	**S**		0.34	
	C	63.59	66.58	69.80		**C**		79.71	
	N	5.30	5.44	6.54		**N**		3.09	
	O	19.77	18.81	18.14		**O**		16.86	

IMFP's for PDMS and PU at 1000 eV are estimated to be 4.2 and 3.0 nm, respectively using the calculation in Cumpson's paper.[21] For electrons at different energies, the IMFP (λ_i) is expressed as the power-law dependence proposed by Wagner [21]:

$$\lambda_i = \lambda_i^{1\ keV}(E, keV)^{0.79} \tag{5.2}$$

where $\lambda_i^{1\ keV}$ is the IMFP at 1000 eV and '*E, keV*' is the kinetic energy in 'keV' units which can be calculated from Al K_α X-ray energy of 1486.6 eV subtracted by binding energies. Figure 5.8 shows that a length of 1λ represents 63% of the measured signal. A length of 3λ is commonly used for a sampling depth which corresponds to 95% of the signal.[20] This means that 63% of the measured electrons come from within 1λ and 95% of the measured electrons come from within 3λ. The electron collection aperture is at an angle from a plane parallel to the sample, then we apply trigonometry to estimate the vertical sampling depths.

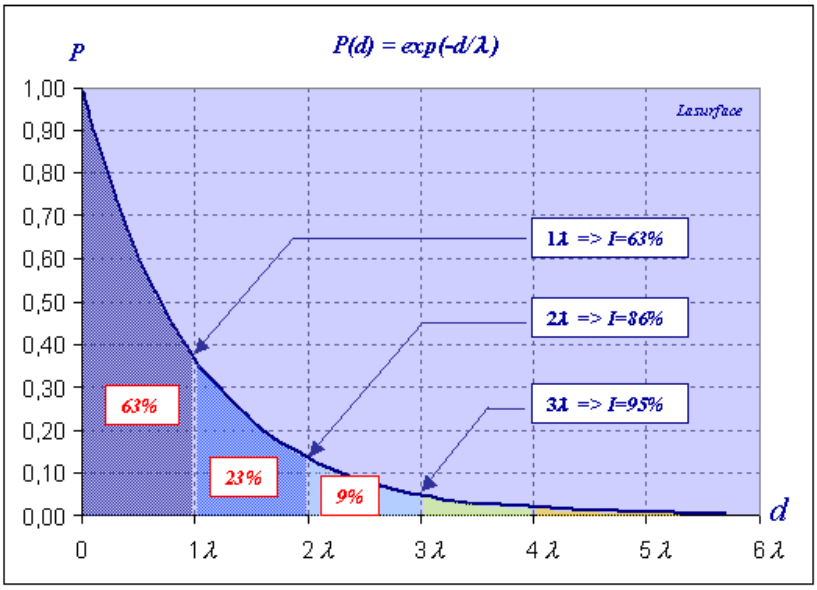

Figure 5.8. Percentage of detection with respect to IMFP **(**Reproduced from ref.[22])

Table 5.4 shows the calculated sampling depth at different take-off angle using the power-law dependence and the IMFP values from Cumpson.[21] The sampling depth increases with increasing collection angle and changes with each element due to differences in binding energies.

Table 5.4. XPS sampling depths as a function of binding energy and take-off angle

Element	Binding energy (eV)	Kinetic energy (eV)	λ_i^{PDMS} (nm)	λ_i^{PU} (nm)	$3\lambda\sin(10^o)$ (nm)		$3\lambda\sin(35^o)$ (nm)		$3\lambda\sin(80^o)$ (nm)	
					PDMS	PU	PDMS	PU	PDMS	PU
Si	~100	1387	5.44	3.89	2.8	2.0	9.4	6.7	16	12
C	~285	1202	4.86	3.47	2.5	1.8	8.4	6.0	14	10
N	~400	1087	4.49	3.20	2.3	1.7	7.7	5.5	13	9.5
O	~534	953	4.04	2.89	2.1	1.5	7.0	5.0	12	8.5

Note: Binding energies are obtained from Ref. [20].

In order to effectively illustrate the migration of PDMS to the surface, the wt% of PDMS can be estimated based on the known stoichiometric ratio of each component and the elemental percentages from XPS results. The stoichiometric ratio is given in Table 5.5.

Table 5.5. Calculated stoichiometry

Material	Stoichiometry				
	C	H	O	N	Si
PDMS	2	6	1	-	1
Acrylic polyol	8.40	14.24	1.56	-	-
PCL polyol	13.11	25.85	5.37	-	-
IDT	33	54	6	6	-

Table 5.6 shows the estimated wt% of PDMS at different collection angles on all siloxane-polyurethane coatings. The stoichiometric ratio for PDMS is needed to calculate the weight of PDMS from the elemental analysis based on the amount of silicon. Because the amount of hydrogen is not measured, the overall percentage weight cannot be directly calculated with the atomic mass. The stoichiometric ratios of acrylic polyol, PCL polyol, and IDT are needed. IDT has a finite structure and molecular weight whereas acrylic polyol and PCL polyol are based on a molecular weight distribution. Acrylic polyol, in particular, is a high molecular weight random copolymer. The weight of IDT is calculated with respect to the measured amount of nitrogen. The left-over percentage of carbon is then used

to calculate the amount of hydrogen using the stoichiometry of the polyol, thus this procedure give an estimation of the overall weight ratio and the resulting data in Table 5.6.

Table 5.6. Estimated wt% of PDMS at different collection angle

Sample	wt% PDMS			Sample	wt% PDMS		
	10°	**35°**	**80°**		**10°**	**35°**	**80°**
ACR-M-20	98.7	88.2	77.2	PCL-M-20	87.2	88.2	73.9
ACR-D-20	44.2	31.0	21.0	PCL-D-20	34.2	32.4	22.9
ACR-M-10	89.6	76.7	65.1	PCL-M-10	85.5	79.7	74.9
ACR-D-10	45.7	41.2	28.0	PCL-D-10	35.5	26.9	32.6
A4	52.3	43.3	27.2	D3	93.9	83.2	59.9

From Table 5.6, it is confirmed that PDMS is stratified to the surface. The mono-functional PDMS is more present at the surface, whereas the di-functional PDMS is distributed deeper into the bulk. The use of the acrylic polyol also results in more PDMS being present on the surface than the PCL polyol, except for the case of D3. The difference of D3 is likely from a different formulating procedure than the others which shows the sensitivity of the self-stratifying process at the molecular level. Figure 5.9 shows the result of Table 5.3 for silicon content with the estimated sampling depth from Table 5.4.

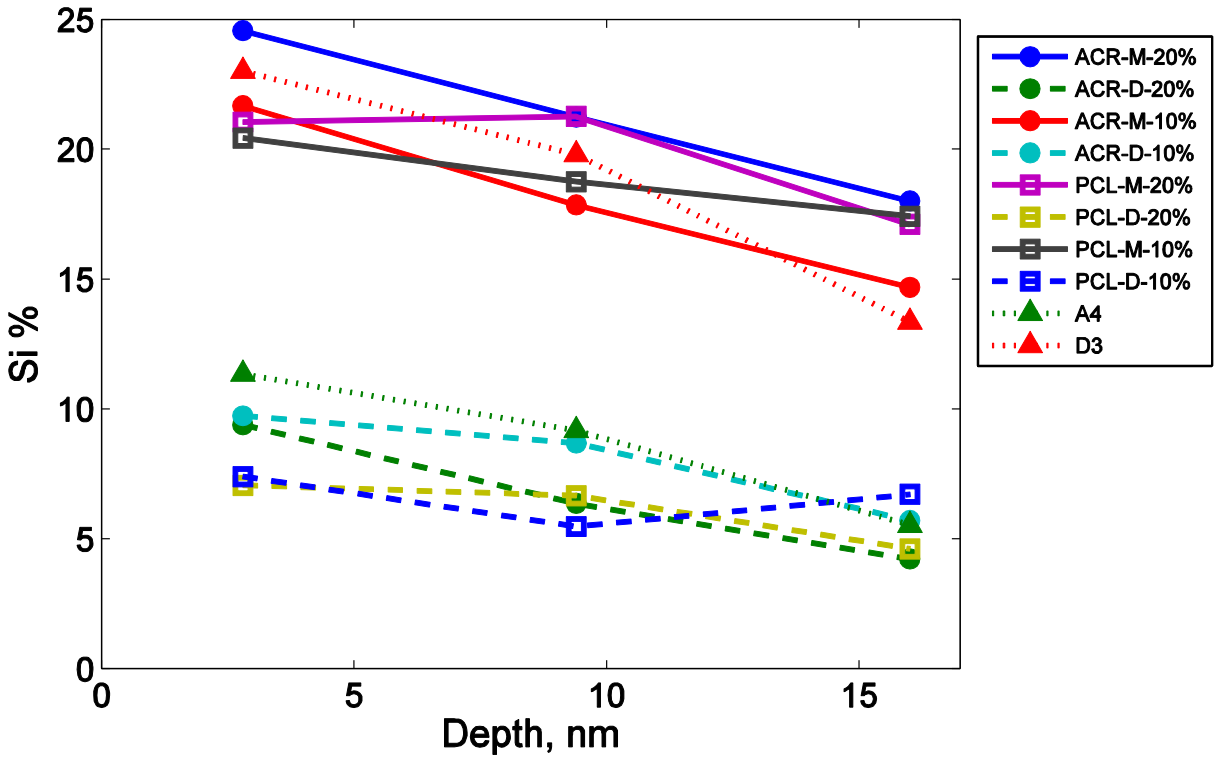

Figure 5.9. Si% versus estimated sampling depth, $3\lambda sin(\theta)$

The sampling depth is roughly calculated, but it gives a sense of depth, rather than plotting it with a detector angle. Except for D3, there are two distinct regions between mono-functional PDMS-PU coatings and di-functional PDMS-PU coatings. D3 is different from others in the way it is formulated and the result from D3 is quite unusual from the rest. The Si content of A4, as shown in Table 5.6, is in the range within other di-functional PDMS-PU coatings and also shows the higher Si concentration due to the acrylic polyol as compared with those coatings made with the PCL polyol. The Si% composition of PDMS would be 25%, disregarding the hydrogen content which is not measured with XPS. At 10º detector angle, ACR-M-20% has a Si content of 24.6% which is the highest of all the coatings, whereas PCL-M-20% has 21.1 Si%. The result implies a nearly complete self-stratified layer of PDMS on mono-functional PDMS-PU coatings, especially the ACR-M-

20%. PCL-M-20% and ACR-M-10% has similar Si contents at a low angle of 10º, but Si content of ACR-M-10% drops off much faster. Thus, the amount of PDMS, the functionality of the PDMS, and the type of polyol play a role in the extent of self-stratification in terms of near-surface concentration and thickness.

Figure 5.10 shows the nitrogen content as a function of depth. From Table 5.5, we can see that IDT contains nitrogen and there is nitrogen at the aminopropyl end group of the PDMS which are not accounted for. All of the coatings, except PCL-D-10%, show increases in nitrogen as the depth increases. Most of them show steeper increase between 35° and 80° take-off angles than from 10° to 35° take-off angle. This effect implies that the nitrogen as part of a polyurethane component being pushed back underneath by the stratified PDMS. In case of ACR-M-20%, nitrogen was not detected at both 10° and 35° take-off angles. As stated previously, ACR polyol seems to bring more PDMS to the surface than PCL polyol. Similarly, if we compare the amounts of nitrogen of these coatings by keeping PDMS content and PDMS type as constants, we will notice a trend that coatings with PCL polyol have more nitrogen near the surface than the coatings with ACR polyol. From Table 5.6 and Figure 5.9, the differences between polyol with respect to nitrogen become clear. An example is with ACR-M-10% and PCL-M-10% at 35° take-off angle. PCL-M-10% actually contains more PDMS according to Table 5.6 than ACR-M-10%, thus we would expect more nitrogen at 35° in ACR-M-10% than in PCL-M-10%, but that is not the case. Coatings with PCL polyol do have a higher amount of IDT in the formulations because of their lower equivalent weight. Also, the ACR and PCL polyol have lower surface energy than IDT. Thus, they likely stratify toward the surface, but they also react with IDT to form a network. The nitrogen content results in ACR and PCL are

then postulated to be a function of molecular weight of the polyol, IDT loading, and surface energy difference.

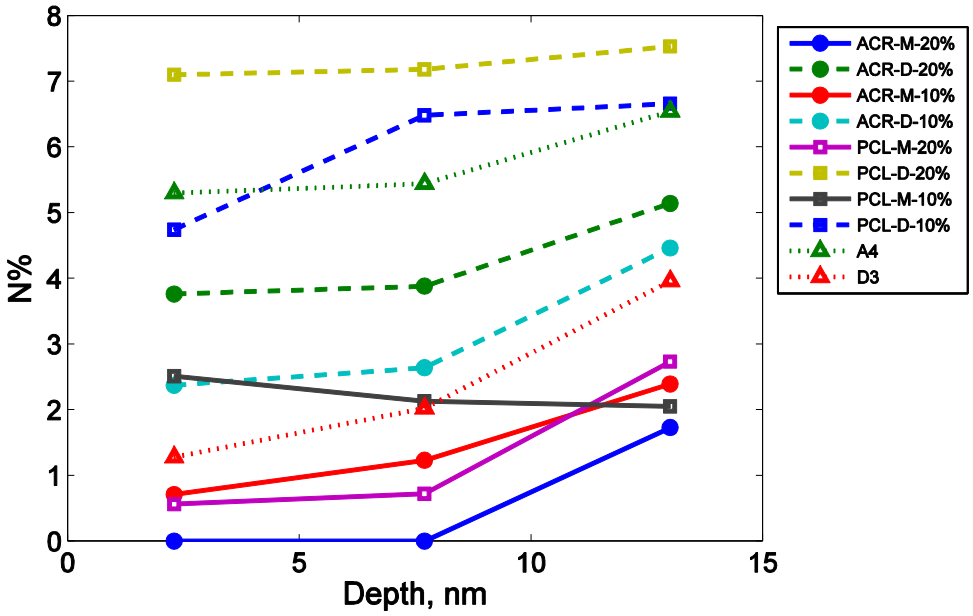

Figure 5.10. N% versus estimated depth, $3\lambda sin(\theta)$

Figure 5.11 shows the carbon and oxygen contents as a function of depth. From the stoichiometry in Table 5.5, a lower amount of carbon is present in PDMS than in either of the polyols and IDT. Thus, the amount of carbon corresponds to the silicon content in an opposite manner with two main groups divided based on the type of PDMS. Oxygen content appears to have one distinct group coming from monofunctional PDMS and D3. This is in relation to oxygen content in PDMS, which is a 1:1 for oxygen and silicon. The group of coatings based difunctional PDMS seems to be scattered but it is only within 5% range. It should be noted that the sampling depth of oxygen is significantly lower (~25% lower in magnitude) than for silicon with respect to each take-off angle. The differences in sampling depth can contribute to a slight dissimilarity between silicon and oxygen overall results.

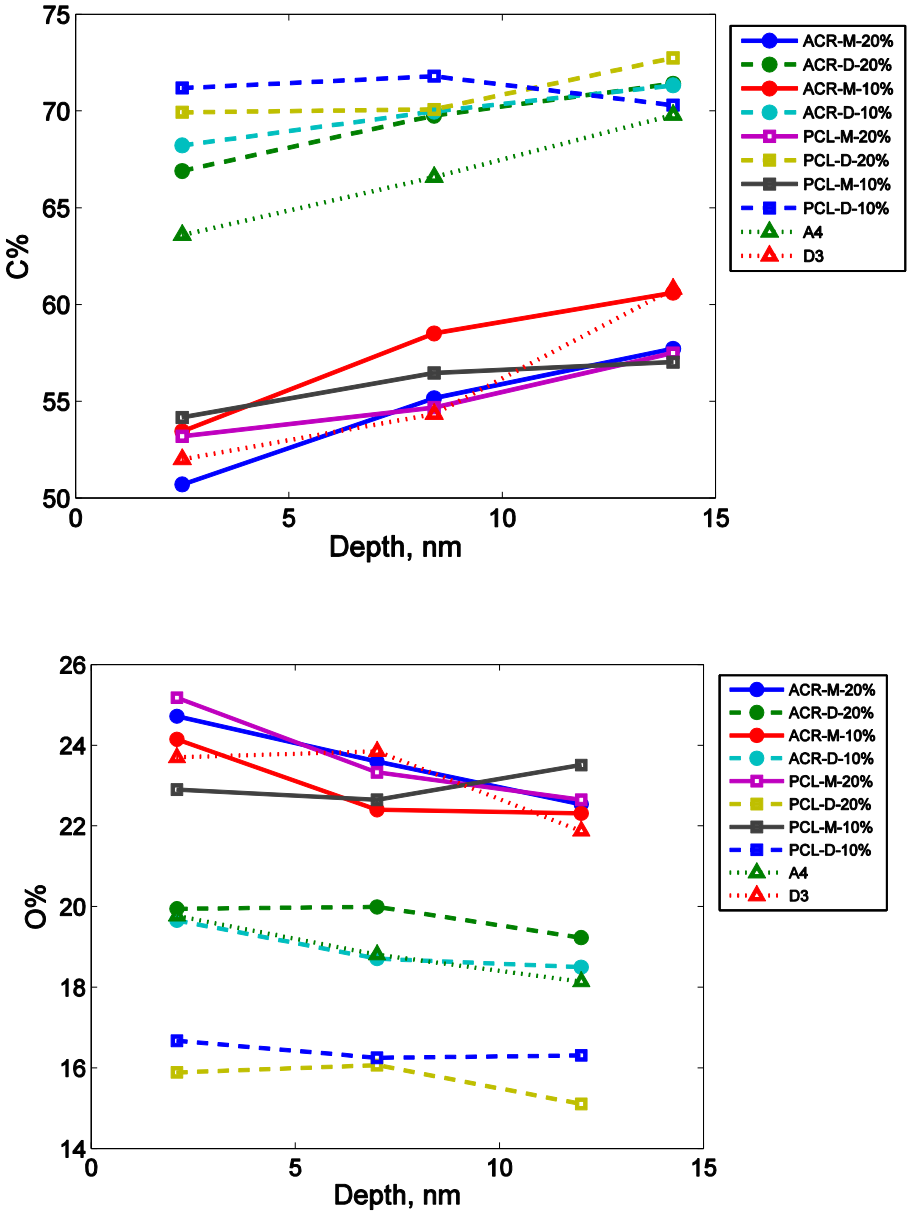

Figure 5.11. C% and O% versus estimated depth, *3λsin(θ)* are shown in top and bottom graphs, respectively.

5.3.2. Rutherford backscattering spectroscopy result

When high-energy ions bombard a surface, there are three possible resulting interactions.[23] The first case occurs when an incident atom collides with the target atom (for example, when ^{4}He strikes ^{12}C). An elastic collision occurs and the incident atom

bounces backward. In Rutherford backscattering spectroscopy (RBS), the energy of backscattered atoms is measured and the elemental composition can then be calculated. A second scenario occurs when an incident atom is heavier than the target atom. This happens when ^{4}He collides with ^{1}H. ^{4}He would not be backscattered and ^{1}H would experience an elastic recoiled phenomenon. Figure 5.12 shows different ion beam analysis techniques, which include RBS, elastic recoil detection analysis (ERDA), and nuclear reaction analysis (NRA).

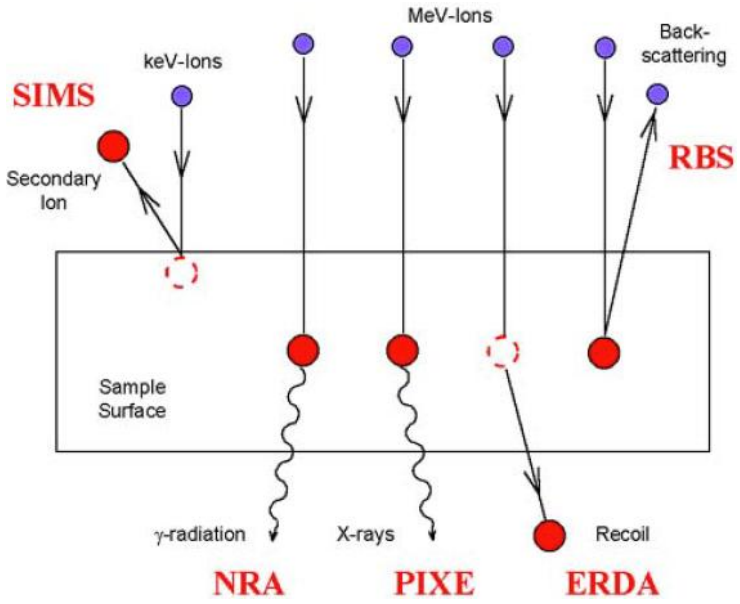

Figure 5.12. Ion beam analysis techniques (Reproduced from ref.[24])

ERDA measures the elastic recoil hydrogen and deuterium as occurred in the second scenario. It is the most widely method used for polymeric materials.[25] The third scenario, which results in a depth profiling capability of the ion beam analysis, occurs when the incident atoms lose energy due to collision with electrons along the depth of the sample. The atoms penetrate the surface and eventually collide with larger atoms and are backscattered. They again lose some energy via impact with electrons on the way back.

In our case, silicon is a heavier element than carbon, nitrogen and oxygen, thus RBS can be very useful in characterizing the Si distribution along the coating's depth. An example of this is from Hwang et al. which they used RBS to characterize surface segregation of siloxane in a block copolymer.[26] Figure 5.13 shows the experimental data on four coatings. DC 3140 silicone elastomer was used as a silicone standard. ACR-PU is an acrylic polyol polyurethane coating without PDMS. The other two coatings are ACR-M-20% and ACR-D-20%.

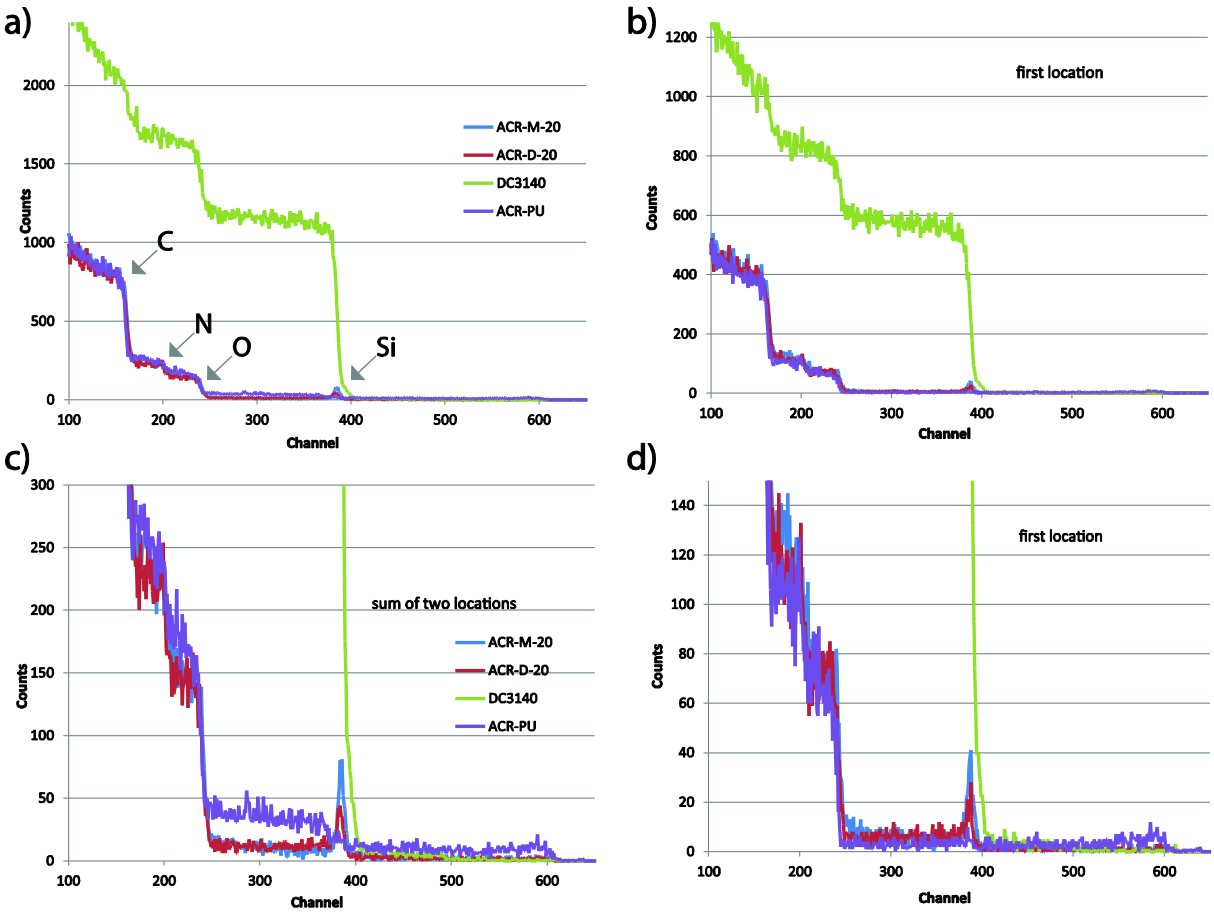

Figure 5.13. RBS results on DC3140, ACR-PU, ACR-M-20% and ACR-D-20%: a) and b) represent the sum of two test locations being measured and a single first location being measured with their corresponding enlarged images in c) and d), respectively.

The x-axis is reported as 'Channel' which has a linear relationship with backscattered energy. To convert to energy, the slope and intercept are found in the

parameter table (Table 5.2). The x-axis then represents low energy to high energy from left to right. A heavy element would show up on the right side because the elastic collision with the incident atom provides greater backscattered energy than a smaller element. As shown in Figure 5.13 a), the Si peak can still be observed as it moves lower in energy. This happens because of an inelastic process of energy loss as a function of depth. Oxygen, nitrogen and carbon appear as the energy gets lower, respectively. The counts at a particular energy become a cumulative of backscattered atoms from different target atoms and depths. Figure 5.13 c) and d) actually show a very small bump at 600 'Channel' for ACR-PU coating. This appears to be a contamination of a heavy element. Tin is suspected as it is in the catalyst used, but there is no further investigation. The silicon signal appears weak and surface localized for ACR-M-20% and ACR-D-20%. The small Si peaks are found and they did not sustain which imply low concentration and very shallow in Si distribution. It indicates a stratification of PDMS to the surface. Due to the sizes of Si peaks, it also demonstrated that the coating with mono-functional PDMS contains more PDMS near the surface than the coating with di-functional PDMS.

Next, the experimental data is matched with the simulation data. In Table 5.2, the calculated stoichiometries for each component and the overall formulation are shown. These material parameters are needed for the simulation along with parameters from Table 5.1. The stoichiometry of each layer, the thickness and the density are the required parameters in the simulation. The values in Table 5.7 are used as a starting point to adjust the fit. Table 5.8 shows the examples of simulation parameters. From the XPS results, we can assume that the top layer is predominantly PDMS. The thickness of PDMS layer

affects the size of the signal peak. Thicknesses and compositions of the subsequent layers are adjusted to fit the simulated signal to the experimental data.

Table 5.7. Calculated stoichiometry

Material	**Stoichiometry**				
	C	**H**	**O**	**N**	**Si**
PDMS	0.539	1.62	0.270		0.270
Acrylic polyol	2.90	4.92	0.539		
IDT	1.16	1.89	0.210	0.210	
Formulated PDMS-PU	4.60	8.43	1.02	0.210	0.270

Table 5.8. Simulations

Sim #	**Layer**	**Stoichiometry**					**Thickness (Å)**	**Figure # shown**
		C	**H**	**O**	**N**	**Si**		
18	1	4.6	8.43	1.02	0.21	0.27	40,000	5.12
3,6,7,8	1	2	6	1		1	50,30,35,70	5.13, 5.14
	2	25	42	7	1	3	10	
	3	25.8	43.1	5.46	1		30,000	
21	1	2	6	1		1	35	5.15
	2	4.6	8.4	0.7	0.45	0.014	30,000	

Note: Densities of 1 g/cm^3 are assumed for all layers simulated.

Figure 5.14 shows the simulation results along with the two PDMS-PU coatings. Here, the simulation is as if the PDMS and PU were to homogeneously mix, based solely on formulation calculation.

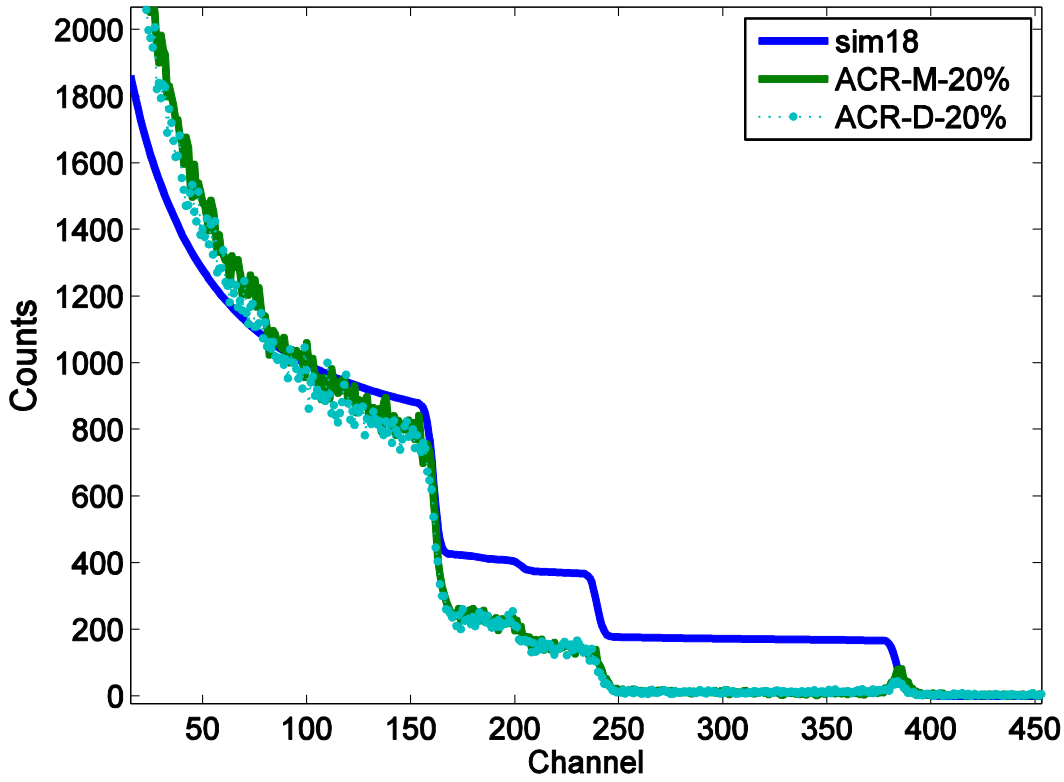

Figure 5.14. Results and simulations of RBS

The silicon signal is present throughout the measurement depth whereas the experimental data shows silicon peaks. These peaks can be simulated using PDMS as the first layer as shown in Table 5.8. Figure 5.15 shows simulations with different thicknesses of PDMS layer to estimate the silicon signal. Thus, we can estimate that ACR-D-20% and ACR-M-20% has a PDMS concentrated layer of 35 Å and 70 Å, respectively, as shown in Figure 5.15 and 5.16.

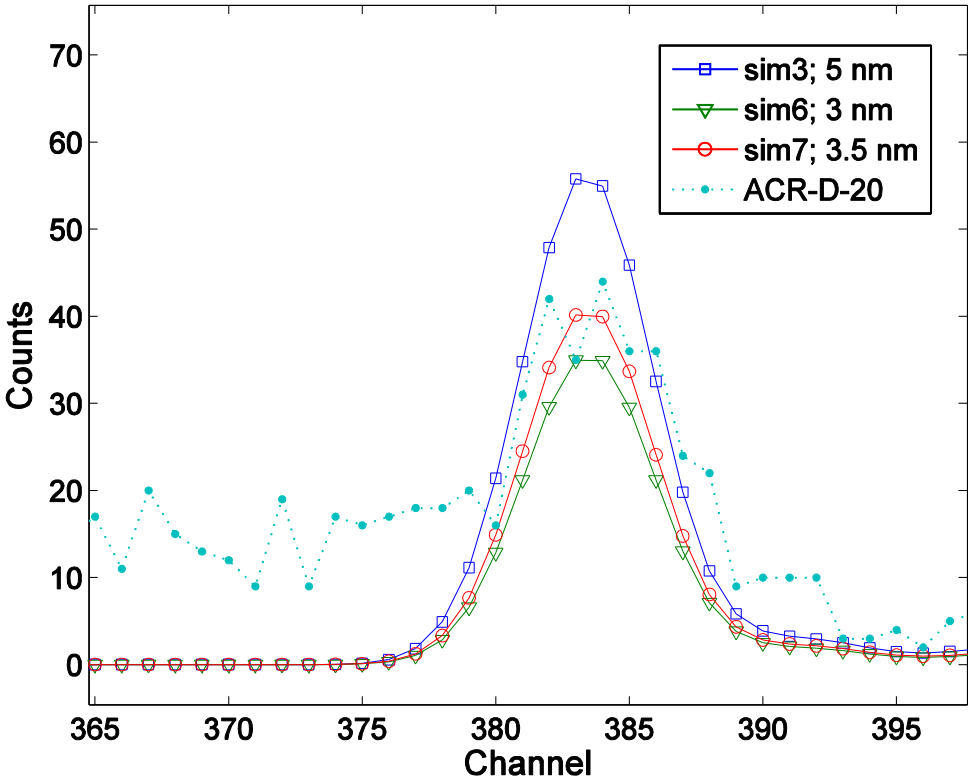

Figure 5.15. ACR-D-20% result compared with simulation

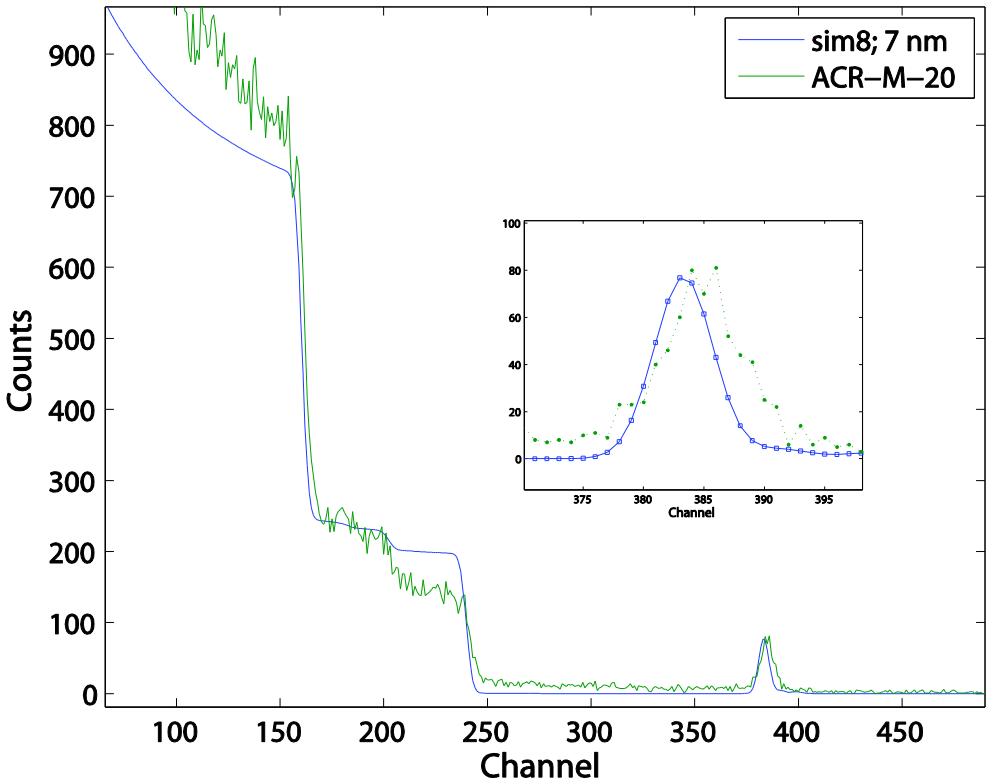

Figure 5.16. ACR-M-20% result compared with simulation

An interesting observation can be made that the signal from the experimental data did not return to zero. There is scattering from silicon towards lower energy until a nitrogen response. Thus, a reasonable assumption is that PDMS is present throughout the measurement depth, but at a much smaller amount. In PDMS, silicon is estimated at ~10% of total stoichiometry, excluding hydrogen. The fit yields the silicon of ~0.1% of the total stoichiometry in the second layer which implies a hundredfold less in elemental concentration compared with the first layer. In an attempt to get the best overall fit, the second layer in the simulation was initially estimated based on the XPS result of the acrylic polyol formulation without the PDMS and the overall calculated PDMS-PU formulation, but neither fits well. The reason for the initial guess is because a homogeneous polyurethane dominated layer is expected at some depth below. However, the simulated curves need to be adjusted until a seemingly optimum fit is obtained as shown in Figure 5.17.

Because of the lower surface energy of the acrylic polyol compared to the polyisocyanate, it is assumed that there would be an effect on the amounts of nitrogen and oxygen with respect to all the elements. There is more nitrogen than in the calculated formulation in the simulation in Figure 5.17. We may expect more carbon if we believe the polyol would rise toward the surface over the isocyanate counterpart. However, for analytical programs, it is not possible to fit the low energy data, thus a poor fit on the left side of the graph.[27] More sophisticated programs such as simNRA (shareware) can account for some multiple scattering events that contribute to the background, but not everything. Another solution is to utilize Monte Carlo simulations which can be adequate in simulating the low energy region.[27]

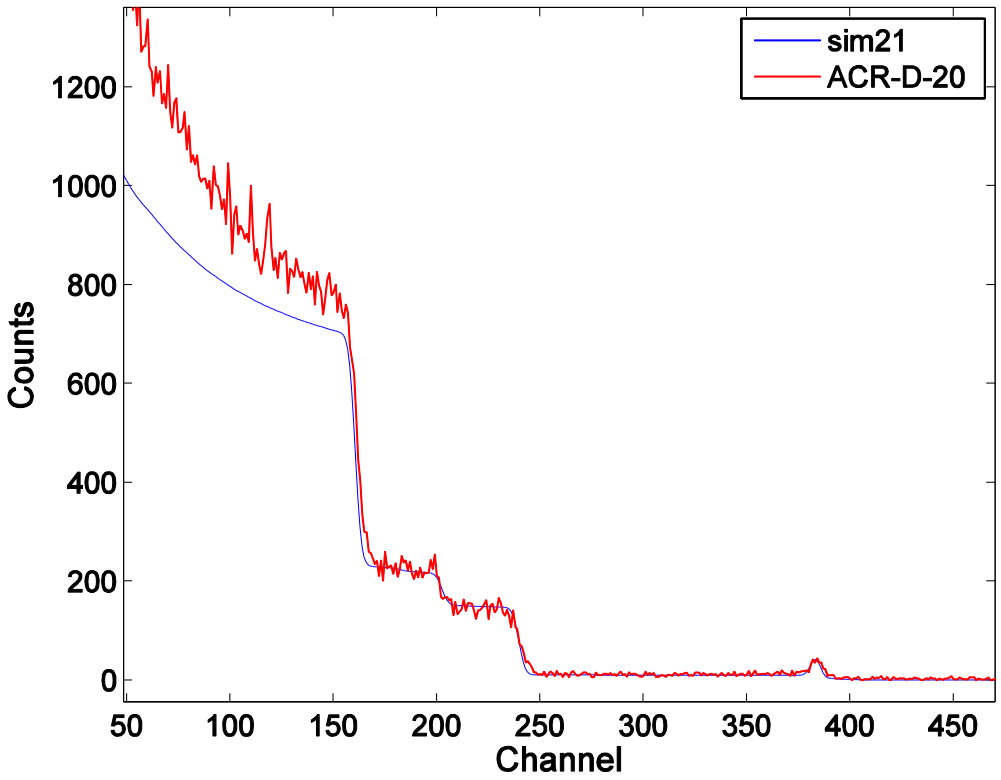

Figure 5.17. ACR-D-20 versus simulation data

The RBS results show a 7 nm layer of concentrated PDMS in the mono-functional PDMS coatings compared with a 3.5 nm layer for the di-functional PDMS coatings. Interestingly, the concentrated PDMS layer thickness of the di-functional PDMS coatings actually reduced by half compared with the mono-functional PDMS coatings. Both of the functional PDMSs have similar average molecular weights. These chains will coil in their normal state. From the results, there can potentially be a monolayer of PDMS at the surface, but that would need a further study into the radius of gyration of the PDMS chains to test the hypothesis.

5.3.3. Electron microscopy results

Figures 5.18, 5.19 and 5.20 show cross-section images of ACR-D-20% using TEM at different magnifications. The air-coating interface and epoxy matrix (embedding medium for microtoming) become separated during cutting by the microtome. The

substrate-coating interface can be seen adhering to the embedded epoxy. From the image contrast, darker regions lead us to believe that those regions have a higher concentration of PDMS. A distinct layer within 100 nm from the air-coating interface was expected, but we were not able to clearly focus at the required resolution using this TEM instrument and settings. However, the distribution of darker regions is seen at the micron scale. The PDMS content is deep inside the coating, but higher concentration is seen toward the air-coating interface. Interestingly, Figure 5.20 shows a lighter area about half a micron from the surface whereas, on a different spot in Figure 5.19, it clearly shows a darker region towards air-coating interface.

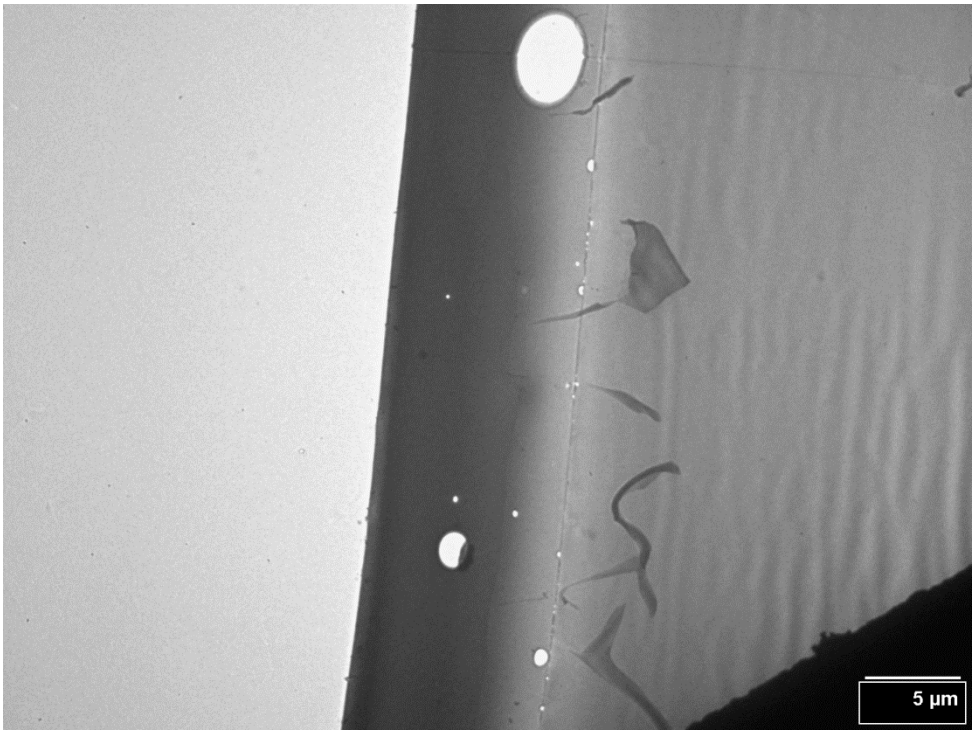

Figure 5.18. TEM image of ADR-D-20% magnification of 2500x

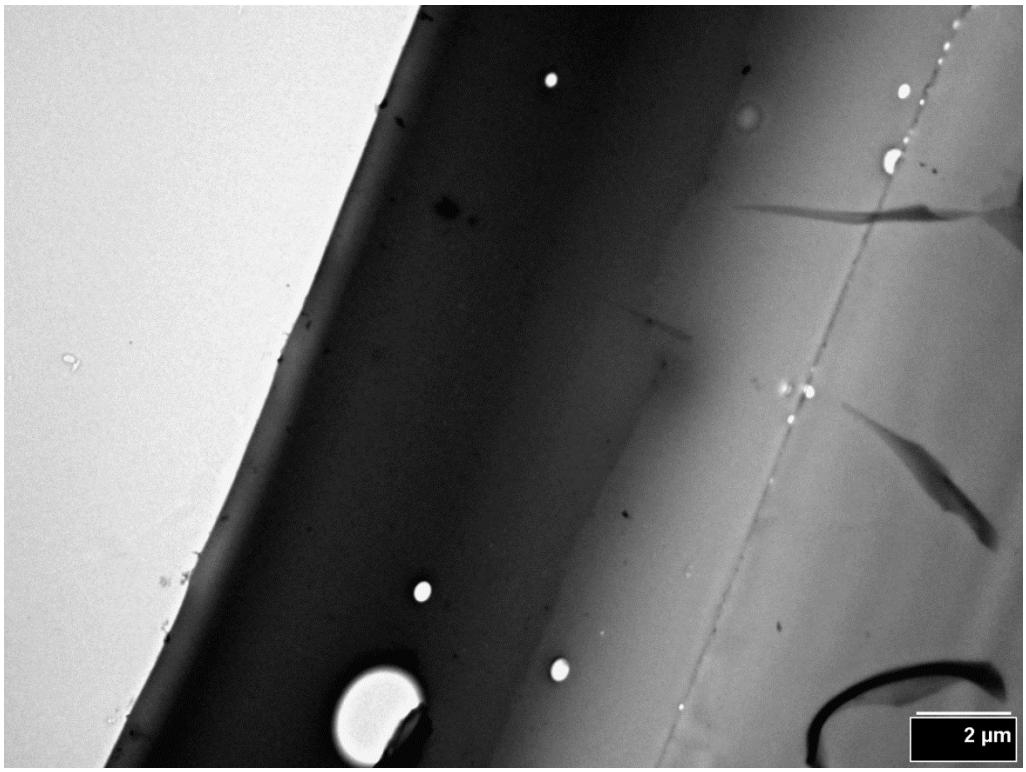

Figure 5.19. TEM image of ACR-D-20% at 6000x magnification

The results suggest that PDMS remains in the bulk along the cross-section for the difunctional-PDMS. The near surface regions also can have different concentration of PDMS. The self-stratification still occurs to an extent because we can observe a much lighter region towards the coating-substrate interface.

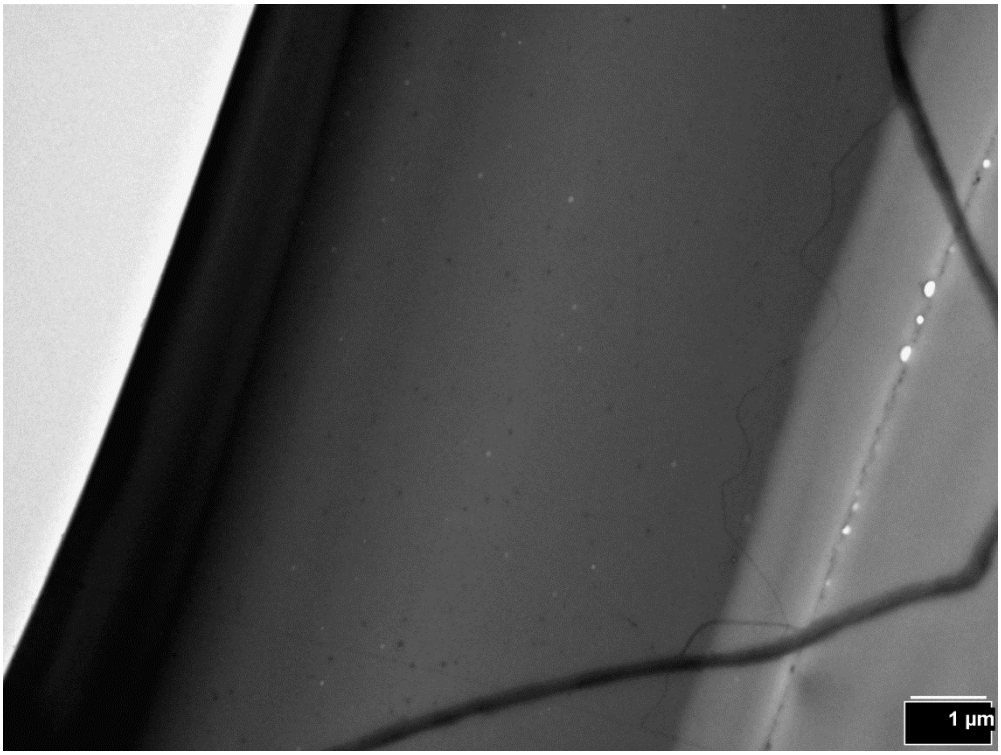

Figure 5.20. TEM image of ACR-D-20% at 7500x magnification

Noticeably, there are pinholes along the cross-section. The holes can be either domain regions or air bubbles. There are fewer pinholes in ACR-D-20%, but ACR-M-10% and PCL-M-20% have much higher numbers of pinholes as can be seen in their TEM images below. It has to be noted that the images do not represent the overall distributions of the pinholes and the distributions of size, surface area, and number were not quantified. Figures 5.21, 5.22, 5.23 and 5.24 show images of ACR-M-10% at different magnifications. For this sample, air-coating interfaces are on the right side of the images. ACR-M-10% shows a different cross-section morphology than ACR-D-20%. In ACR-M-10% there is no distinct layer (from the difference in contrast) at a magnification of 2,500 along the depth of the coating. Figure 5.21 and 5.22 show streaks of darker regions arising from the pinholes. There could be two hypotheses for this phenomenon. One is that it is due to cutting with the microtome because the streaks go in the same direction as the knife mark

as can been seen in Figure 5.22. The cutting may take the material out and fold it across or the pinholes are actually liquid domains which are broken and smeared the sample in the knife cutting direction. However, the first assumption can be easily argued that there is no sign of material protruding out from the air-coating interface if the material has actually been folded over as shown in Figure 5.23. Also, if the pinholes are liquid domains that have been smeared, there should be no reason for a larger smear to stop moving toward the interface the way it does.

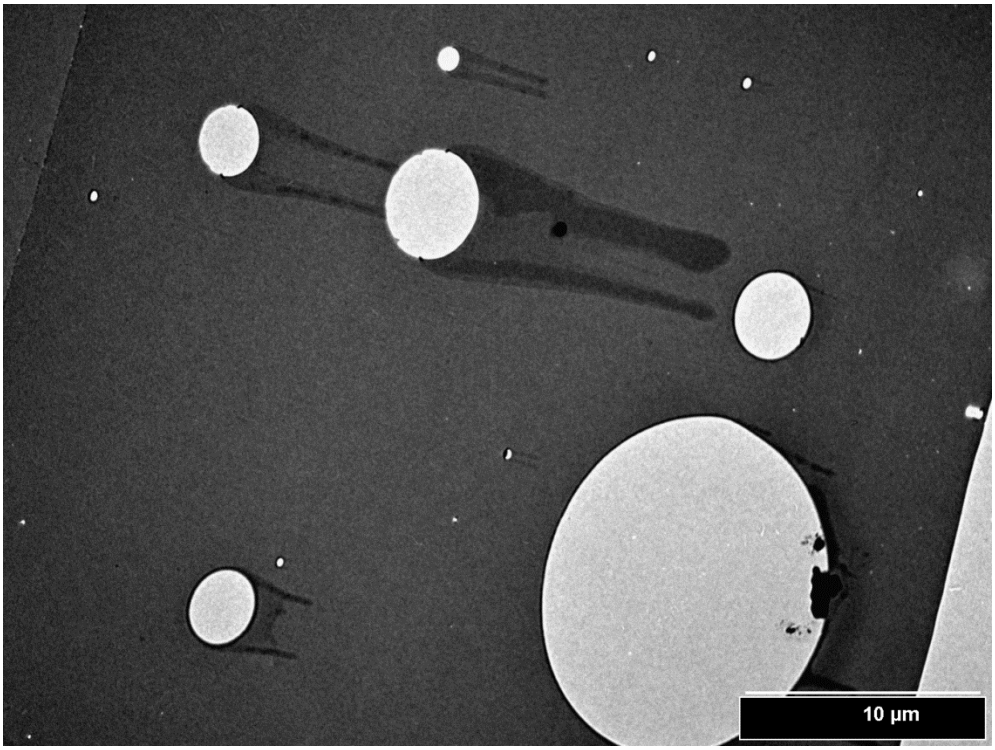

Figure 5.21. TEM image of ACR-M-10% at 2500x magnification

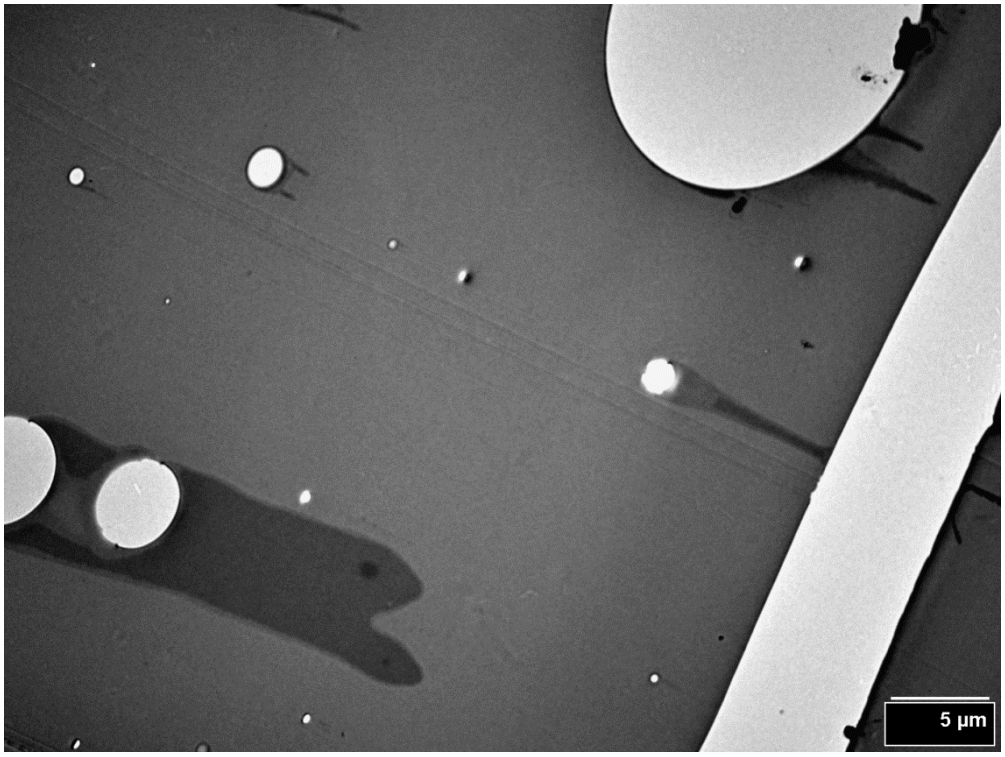

Figure 5.22. TEM image of ACR-M-10% at 2500x magnification

The second assumption is that the PDMS component is moving toward the air-coating interface. Figure 5.23 shows that the streak comes all the way to the surface. However, since it is believed that self-stratification occurs as soon as the coating formulations were applied, this stratifying process may not be due to thermodynamic-driven surface energy differences. The more likely explanation is that these domains are PDMS-rich domains and they slowly move toward the surface due to the density differences, perhaps during curing. As seen in Figure 5.24, the silicone layer comparable to XPS and RBS results cannot be observed based on this TEM experiment.

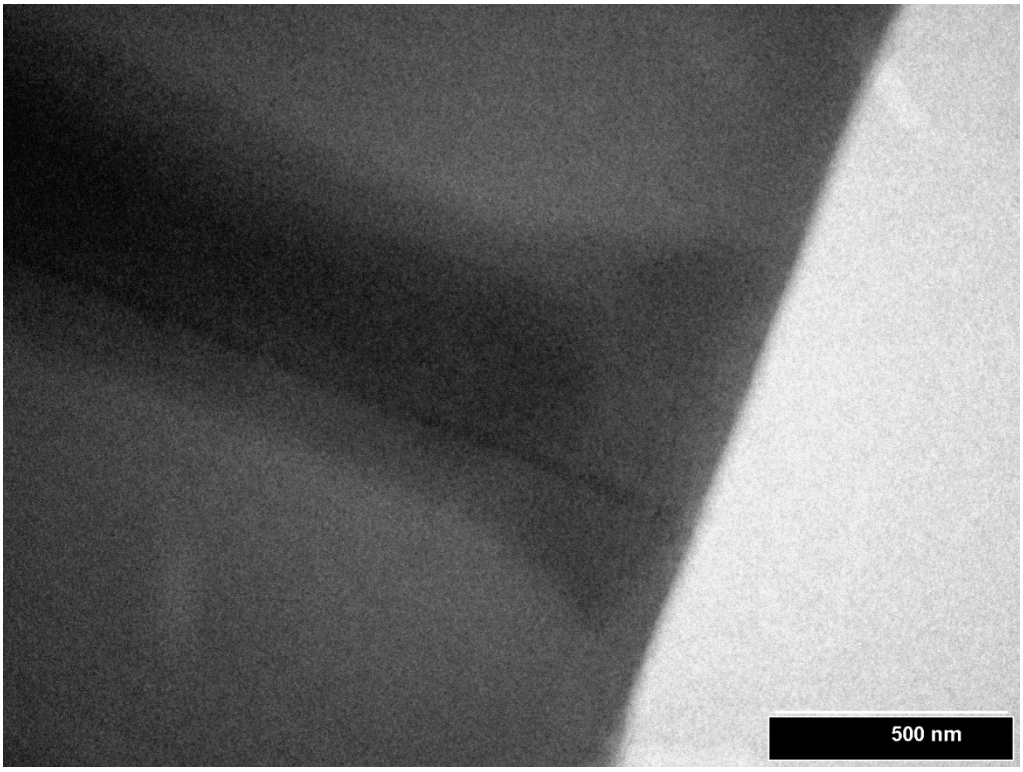

Figure 5.23. TEM image of ACR-M-10% at 60,000x magnification

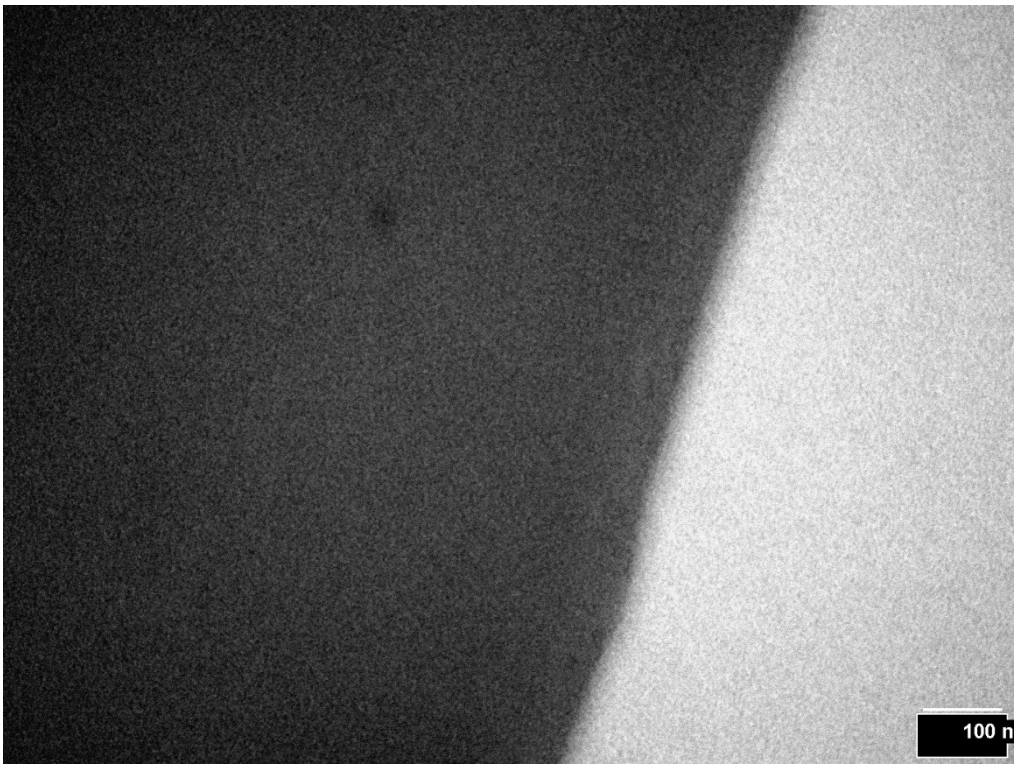

Figure 5.24. TEM image of ACR-M-10% at 100,000x magnification

Figures 5.25, 5.26, and 5.27 show images of PCL-M-20% at different magnifications with the air-coating interface on the left side. PCL-M-20% and ACR-M-10% look quite similar, but PCL-M-20% does have more pinhole presence on average. This is probably due to a higher PDMS content. Figure 5.27 shows PDMS migrating towards the surface. Figure 5.28 is a freeze fracture sample of ACR-M-20% under SEM. It shows domains/pinholes with different sizes distributed throughout the cross-section. The use of SEM was initially done in order to use the energy dispersive X-ray spectroscopy with SEM, so that the elemental distribution along the cross-section could be observed.

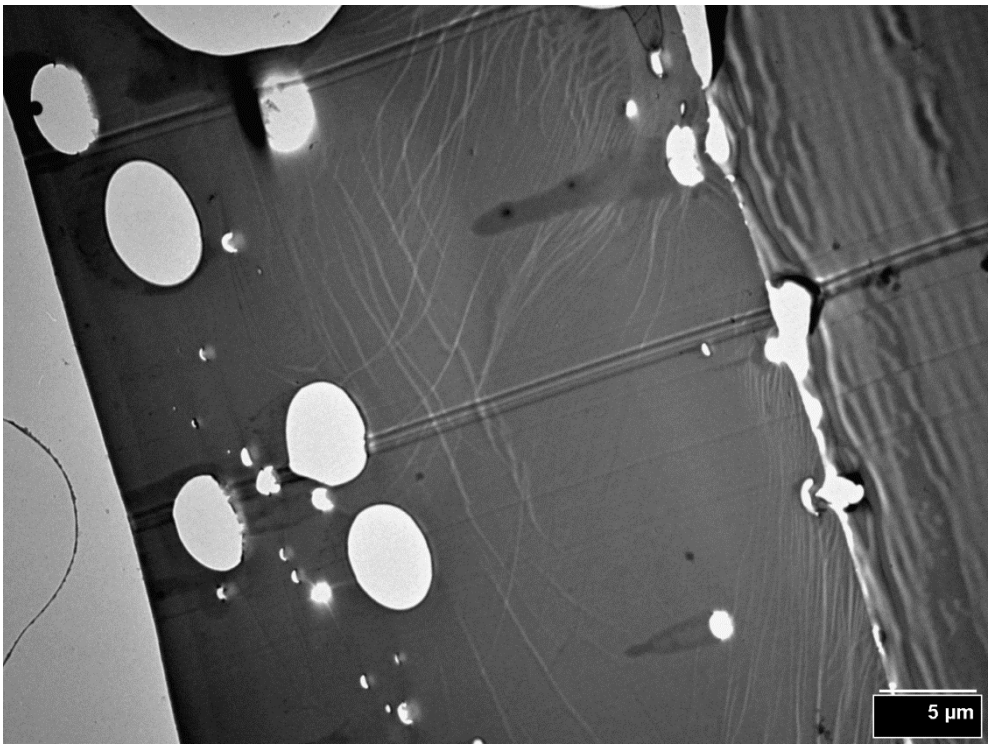

Figure 5.25. TEM image of PCL-M-20% at 2500x magnification

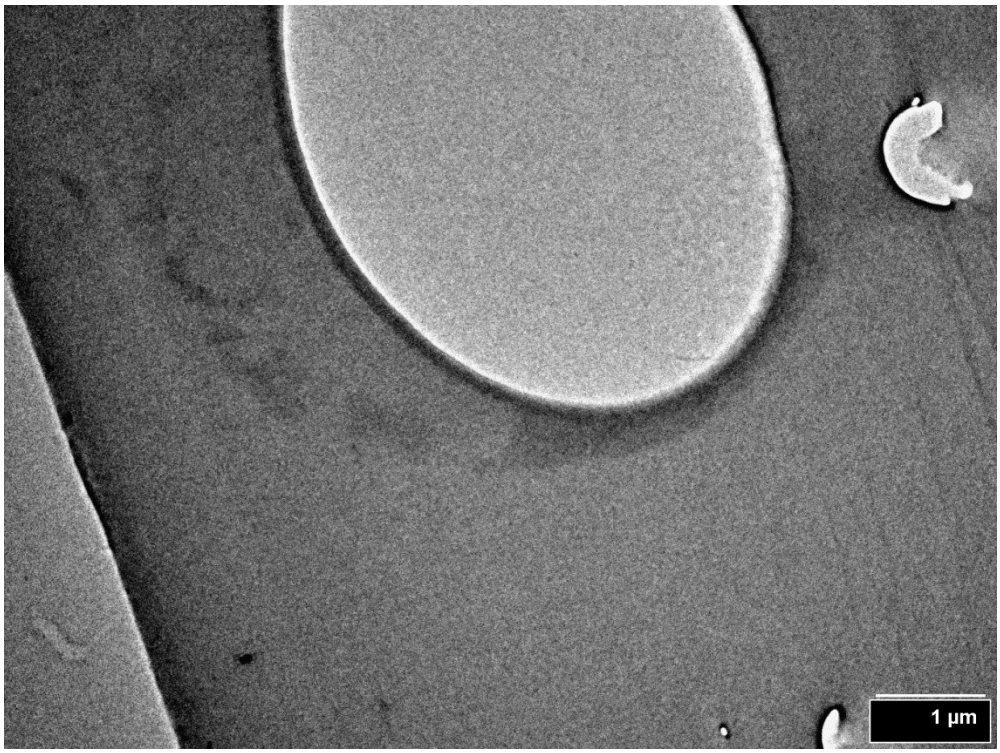

Figure 5.26. TEM image of PCL-M-20% at 15,000x magnification

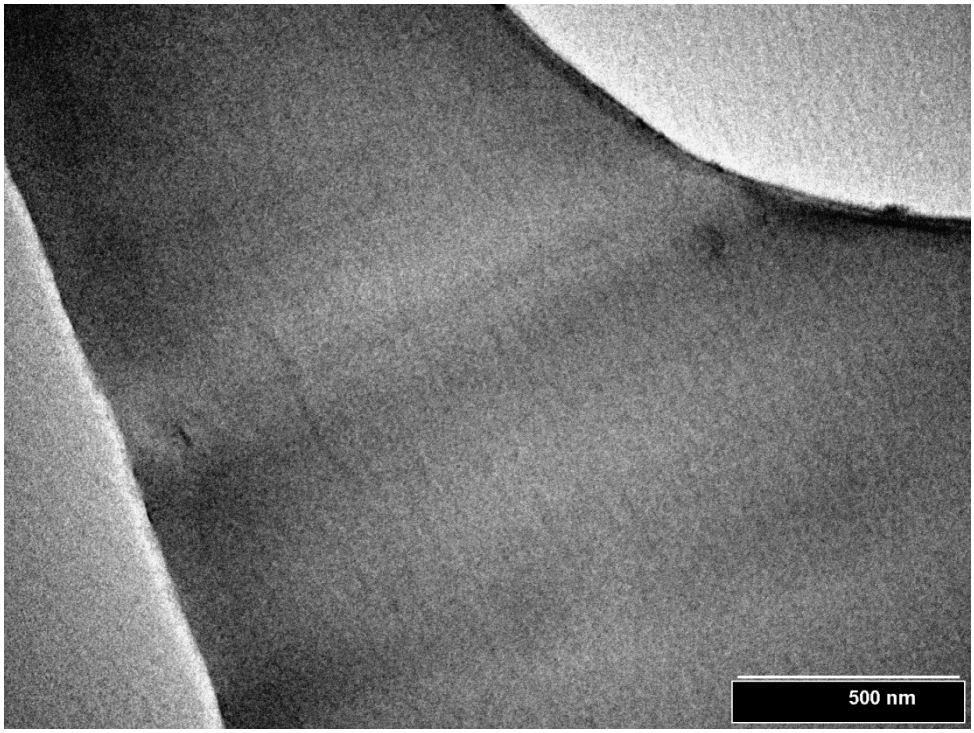

Figure 5.27. TEM image of PCL-M-20% at 60,000x magnification

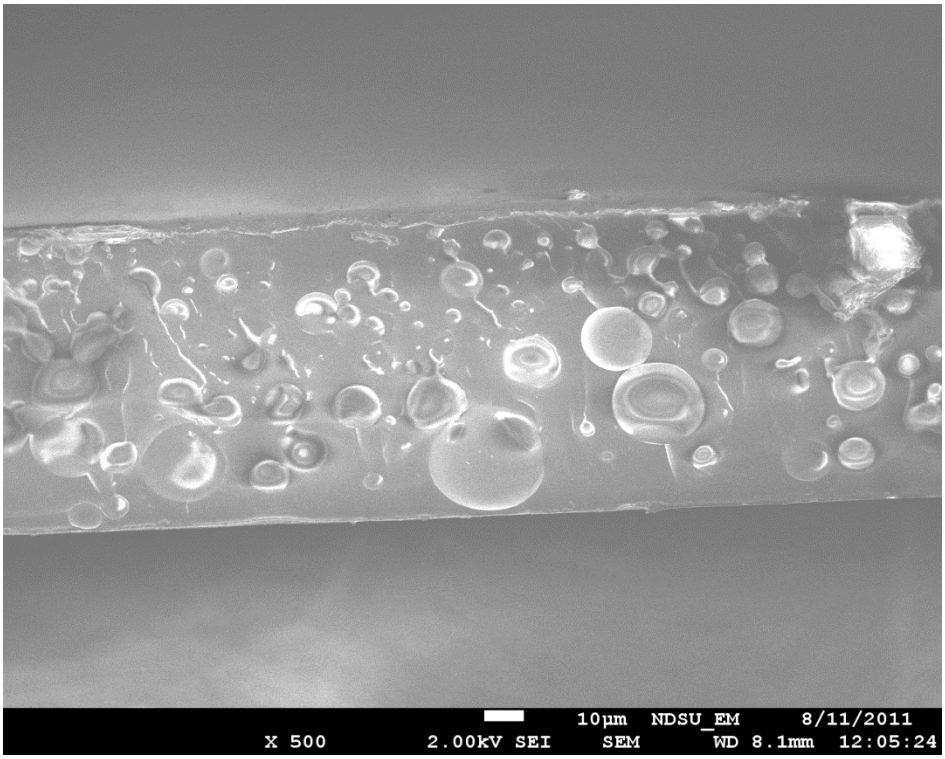

Figure 5.28. SEM image of ACR-M-20%

From the TEM experiment, a very thin PDMS layer near the surface as shown in XPS and RBS tests cannot be observed with our experimental parameters. But the images show an overall distribution of PDMS along the cross-section. In the di-functional PDMS, the higher concentrated layer of PDMS is seen deep inside the coating. Pinholes can be observed on coatings with mono-functional PDMS. These pinholes likely come from heterogeneity of the mixture. The trace of PDMS droplets remains in the coating as the coating solidifies.

5.3.4. Nanoindentation results

Nanoindentation is used to measure the modulus near the surface of our coatings. It is a load and depth sensing instrument. The contact area of the indentation is estimated based on the calibration with a quartz standard. The reduced modulus results are shown in

Table 5.9 and Figure 5.29. The reduced modulus is the measured modulus that consists of the elastic deformations from both the sapphire indenter and the samples.

Table 5.9. Nanoindentation results

Sample	Reduced modulus (GPa)	Minimum measured load (µN)
AM20	1.40 (+/- 0.24)	-43.81 (+/- 12.76)
AD20	1.23 (+/-0.26)	-44.72 (+/- 17.78)
AM10	1.63 (+/- 0.12)	-11.40 (+/- 0.98)
AD10	1.54 (+/- 0.08)	-31.47 (+/- 16.49)
PU	1.87 (+/- 0.23)	-18.24 (+/- 5.93)
A4	2.27 (+/- 0.09)	-20.18 (+/- 4.48)
D3	1.74 (+/- 0.35)	-37.10 (+/- 34.23)

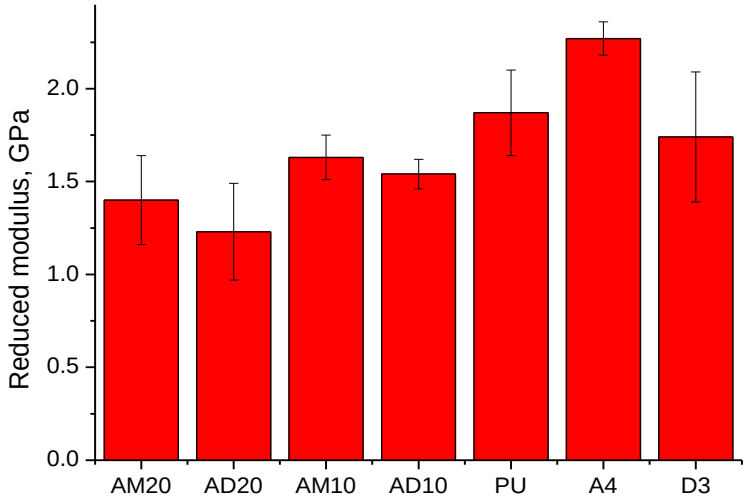

Figure 5.29. Reduced modulus results

The XPS and RBS results point to a very thin layer of concentrated PDMS. The release mechanism of siloxane-polyurethane coatings is of interest, specifically, whether the elasticity of the coatings near the surface can be measured by mechanical technique. The elasticity of the coating will impact the fracture energy on the interface.[28] The reduced modulus of PDMS using 400µm diameter spherical indentation has been quoted at around

3 MPa.[29] From Figure 5.29, it can be observed that the reduced modulus calculation using the Oliver and Pharr method[18] of siloxane-polyurethane coatings are relatively similar to the acrylic-polyurethane coating. This result can be explained from the previous RBS results which showed a highly surface localized PDMS layer of 3-8 nm and mostly polyurethane underneath up to the measurement range of ~3 μm from the surface. There are two indentation options for practical purposes; one is to use a small radius of curvature probe such as Berkovich or cube corner indenter to conduct nanoindentation at an extremely shallow depth and the other is to use a large indenter to be able to detect the small load very near the surface. The nanoindentation probe with AFM is not available and the current Triboindenter system is not capable of discriminating such a low force at less than 10 nm deep. A flat punch can be used to obtain a large measurable load, but the parallelism of the test apparatus and samples cannot be ensured. A problem with using a large probe also deals with the surface roughness of the samples. A surface roughness measurement done by Rajan Bodkhe with optical profilometer shows an average roughness of ~100-200 nm in a 200-μm by 300-μm scan size. Due to the surface roughness and load resolution, it is not possible to use large indenters to detect elastic properties below 100 nm with confidence. Thus, 300-nm displacement in our indentation test is used to lessen the impact of the surface roughness in modulus determination.

Another motivation for the quasi-static nanoindentation is to observe the pull-off force resulting from the sapphire indenter and sample interface. Figure 5.30 shows the minimum load we can measure during unloading. ACR-M-20 and ACR-D-20 are essentially similar. ACR-M-10 distinctly has smallest pull-off force than the rest.

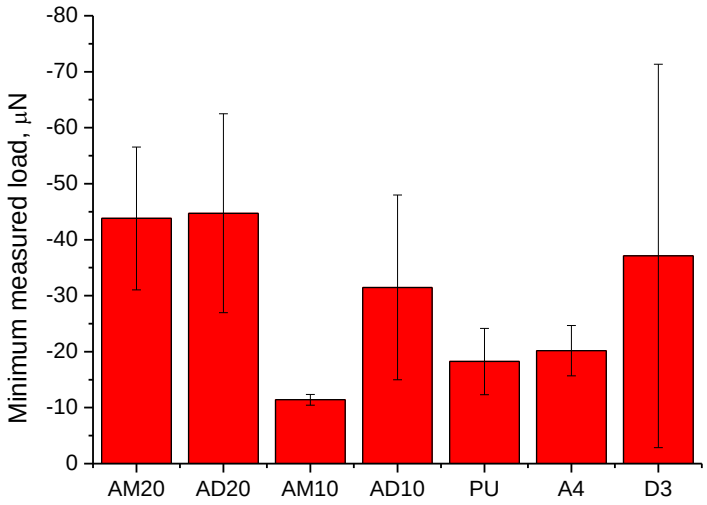

Figure 5.30. Minimum measured load results

To give a brief overview of elastic contact with a large radius indenter, the Johnson-Kendall-Roberts (JKR) model can be used.[30] The JKR adhesion model can be applied to indentation experiment to account for the adhesion force and the increase in contact area. A non-dimensional Tabor parameter (μ) can be calculated to see whether the JKR model is expectedly valid:[29]

$$\mu = \left(\frac{R\Delta\gamma^2}{E_r^2 z_0^3}\right)^{1/3} \tag{5.3}$$

where R is the indenter's radius of curvature, $\Delta\gamma$ is the work of adhesion, E_r is reduced modulus, z_0 is the equilibrium separation of surfaces (usually taken as between 0.3 and 0.5 nm). The JKR theory may be applied when μ>5. When JKR can be applied, we have:

$$P_{adh} = -\frac{3}{2}\pi\Delta\gamma R \tag{5.4}$$

where P_{adh} is the pull-off force. It is assumed that the minimum measured loads are the pull-off forces or close to them. The work of adhesion can then be calculated. The work of adhesion between the coating and the sapphire indenter can be written as:

$$\Delta\gamma = \gamma_{sapphire} + \gamma_{coating} - \gamma_{sapphire/coating} \quad (5.5)$$

Since the interfacial energy ($\gamma_{sapphire/coating}$) was not measured, it was not possible to make a definitive conclusion from this nanoindentation experiment whether the flexibility of siloxane-polyurethane coatings can be recognized. It could be postulated that the higher pull-off forces from siloxane-polyurethane coatings compared to acrylic polyurethane are due to higher critical contact areas which are the contact areas right before separation. Since the critical contact area has an inverse relationship with the elastic modulus, the higher pull-off force may point to the near-surface flexibility of siloxane-polyurethane coatings. A future additional study using more appropriate tools would give a better insight into the near-surface deformation and adhesion for this novel stratified coating system.

From Sommer et al., the pull-off adhesion test with epoxy glue can be viewed as a mechanical test but its main purpose is to measure the release load.[17] From Figure 5.31, ACR-D-20% distinctly has the highest removal force with the rest of the PU-PDMS coatings at around 7-10 N.

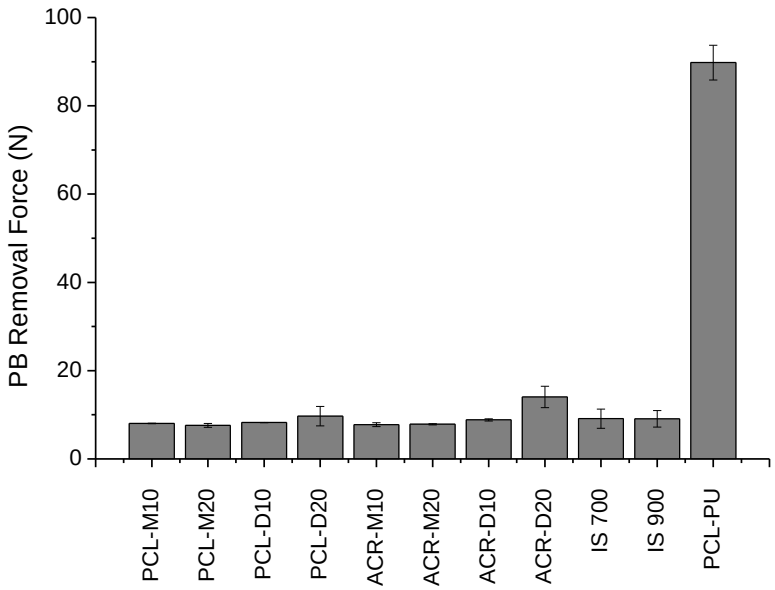

Figure 5.31. Pseudo-barnacle removal force on coatings (Reproduced from ref.[17])

The automated high-throughput pseudobarnacle pull-off test cannot effectively differentiate among the siloxane-polyurethane coatings which could be due to the fact that the adhesion to epoxy glue is effectively equal or the resolution of the load cell coupled with the small gluing area prohibits differentiation. Thus, for future testing, combining both appropriate indentation technique and pull-off test will provide the differentiation of mechanical properties near the surface on the coatings.

5.3.5. Surface energy measurement

Figure 5.32 shows the measurements of surface energy using Owen-Wendt method using water and methylene iodide as test liquids.[31]

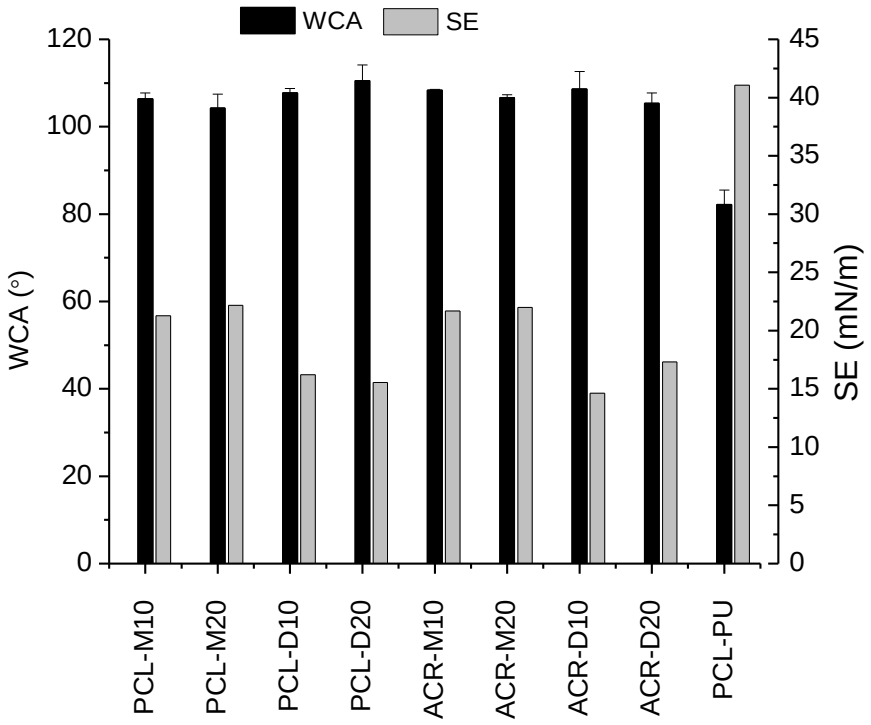

Figure 5.32. Contact angle and surface energy measurements (Reproduced from ref.[17])

The PDMS content near the surface is high, such that the surfaces consistently have high water contact angle. The coatings with mono-functional PDMS clearly have higher surface energies than coatings with di-functional PDMS. This may seem counterintuitive

from the observed PDMS contents found in other characterization techniques. XPS results cannot explain why lower surface energy is found in di-functional PDMS since we would expect the trend to follow the PDMS content. The attempt was made to measure surface energy with the Zisman plot.[32] Water, methylene iodide, hexadecane, ethylene glycol, dimethylformamide, and glycerol were used, but the Zisman plots were quite scattered and did not give a good fit. The only currently available method to check the surface energies in our laboratory is the pendant drop method which is prone to errors if the optics are not calibrated properly. The coatings were characterized again with the Owen-Wendt method using water and methylene iodide. This is on a different set of coatings formulations and the result is shown in Figure 5.33.

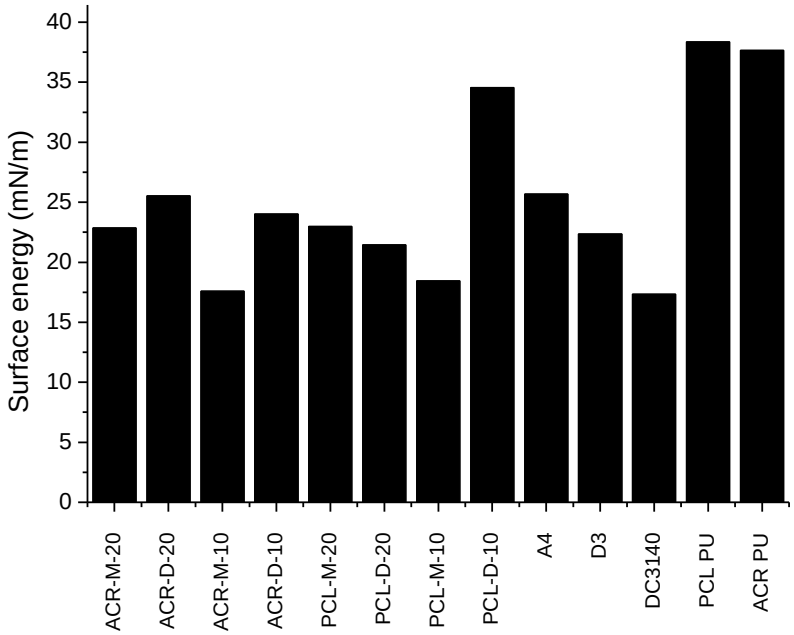

Figure 5.33. Surface energy measurement using Owen-Wendt method

From Figure 5.33, there is no longer an observable trend as seen previously in Figure 5.32. This shows a sensitivity of the test on surfaces, thus the surface energy measurement is inconclusive and needs further experimentation.

5.4. Correlation between Surface Characterization Results and Fouling-release Performance

The surface characterization performed in this study is compared with previous fouling-release laboratory analysis and field test. Previously, Sommer et al. compared laboratory analysis with field test and found that good field test performance can generally be predicted by results in laboratory assays.[17] Field tests are performed at sites in Florida, California, and Singapore as a result of collaborations with Florida Institute of Technology, California Polytechnic State University and National University of Singapore. Figure 5.34 shows fouling-release laboratory assays using bacteria *Cellulophaga lytica (C. lytica)*, *Halomonas pacifica (H. pacifica)*, algae *Navicula incerta (N. incerta)*, *Ulva linza (U. linza)*, and barnacle reattachments.

From Figure 5.34 A, B, and E, the laboratory assays results for *C. lytica* and *U. linza* show that mono-functional PDMS-PU coatings perform better than the di-functional PDMS-PU coatings. Thus, from previous surface characterization results, the PDMS content has a direct relationship to the percent removal and an inverse relationship with biofilm surface coverage for *C. lytica*. It implies that PDMS content or, in other words the surface coverage of PDMS on the surface has significant impact on *C. lytica* and *U. linza* due to their low affinity for silicone surfaces.

In Figure 5.34 C, for *N. incerta*, PCL-PU coating provides the greatest water jet removal. Elastomeric coatings actually perform worse in this case. Then, PDMS-PU coatings appropriately have the % removal in the range between that of PCL-PU coating and elastomeric coatings. The di-functional-PDMS PU coatings are expected to have greater removal due to lesser PDMS content than mono-functional counterparts, but the

water jet removal result shows the opposite. Other parameters, such as surface roughness, may be a factor, however these parameters have not yet been accounted for in this study.

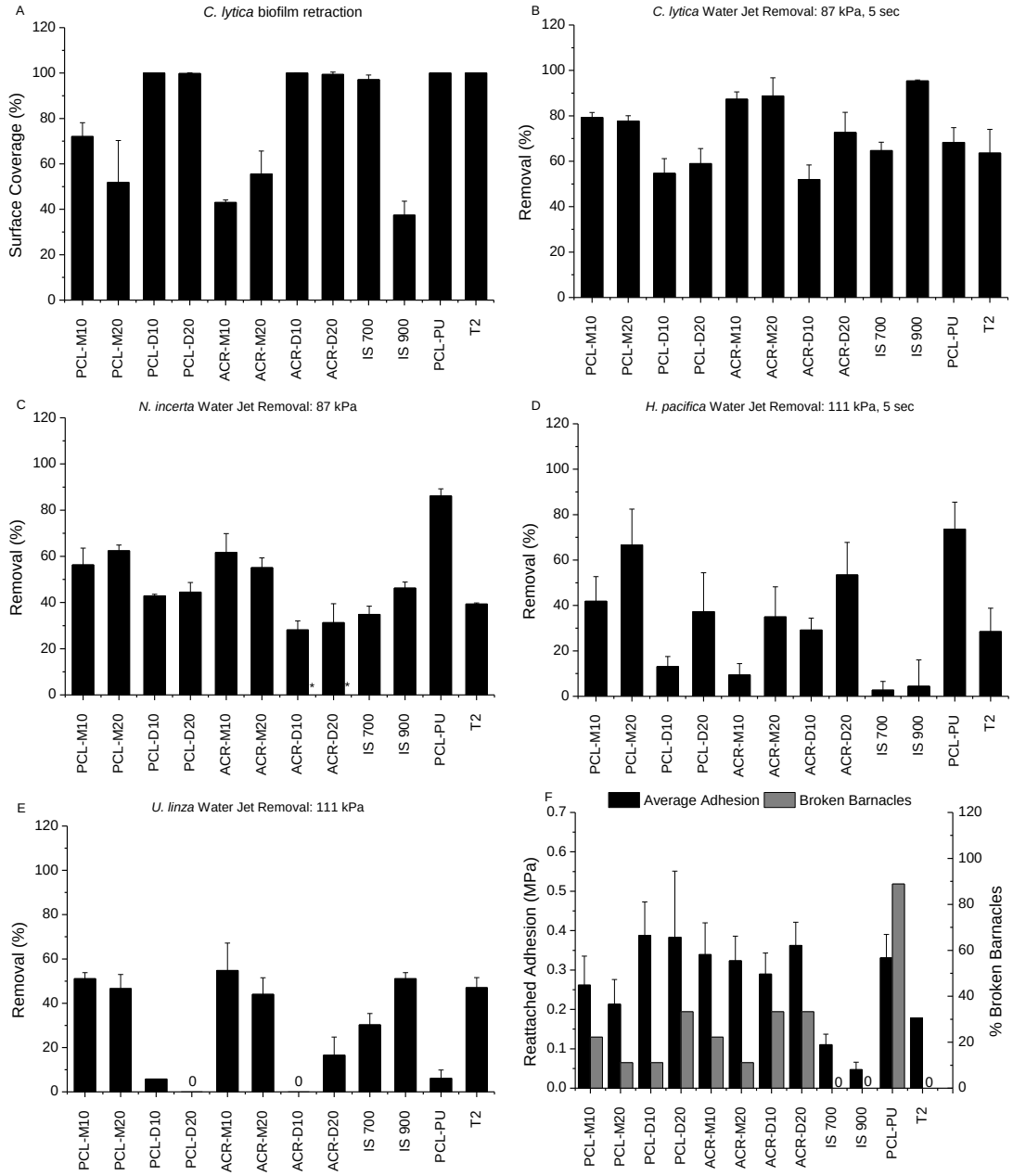

Figure 5.34. Results from laboratory assays (Reproduced from ref.[17])

In Figure 5.34 D, the removal *of H. pacifica* does not show a trend that separates mono- and di-functional PDMS. The commercial elastomeric coatings perform poorly with *H. pacifica* where PCL-PU coating has the highest removal. Again, PDMS-PU coatings fall

in between the two standards, but the PCL-M coatings distinctly outperform the rest. Barnacle reattachment adhesion on many of PDMS-PU coatings is shown to be similar to PU coating, as shown in Figure 5.34 F. Only PCL polyol based coatings with mono-functional PDMS are significantly different from PU coating. PCL-M-20% performs the best in this experiment.

From Figure 5.35, field test results at CalPoly shows that coatings with mono-functional PDMS have greater slime removal at 1 month than those with di-functional PDMS, but there is no similar trend at 3 months and 6 months. Soft and hard fouling are easier to remove for coatings with mono-functional PDMS. Furthermore, mono-functional PDMS with PCL polyol coatings have the lowest water jet pressure for hard fouling removal and the best barnacle release property. Lateral push-off test of barnacle shows that PCL-M-20 and ACR-M-20 yield comparable removal force to IS700 and IS900.

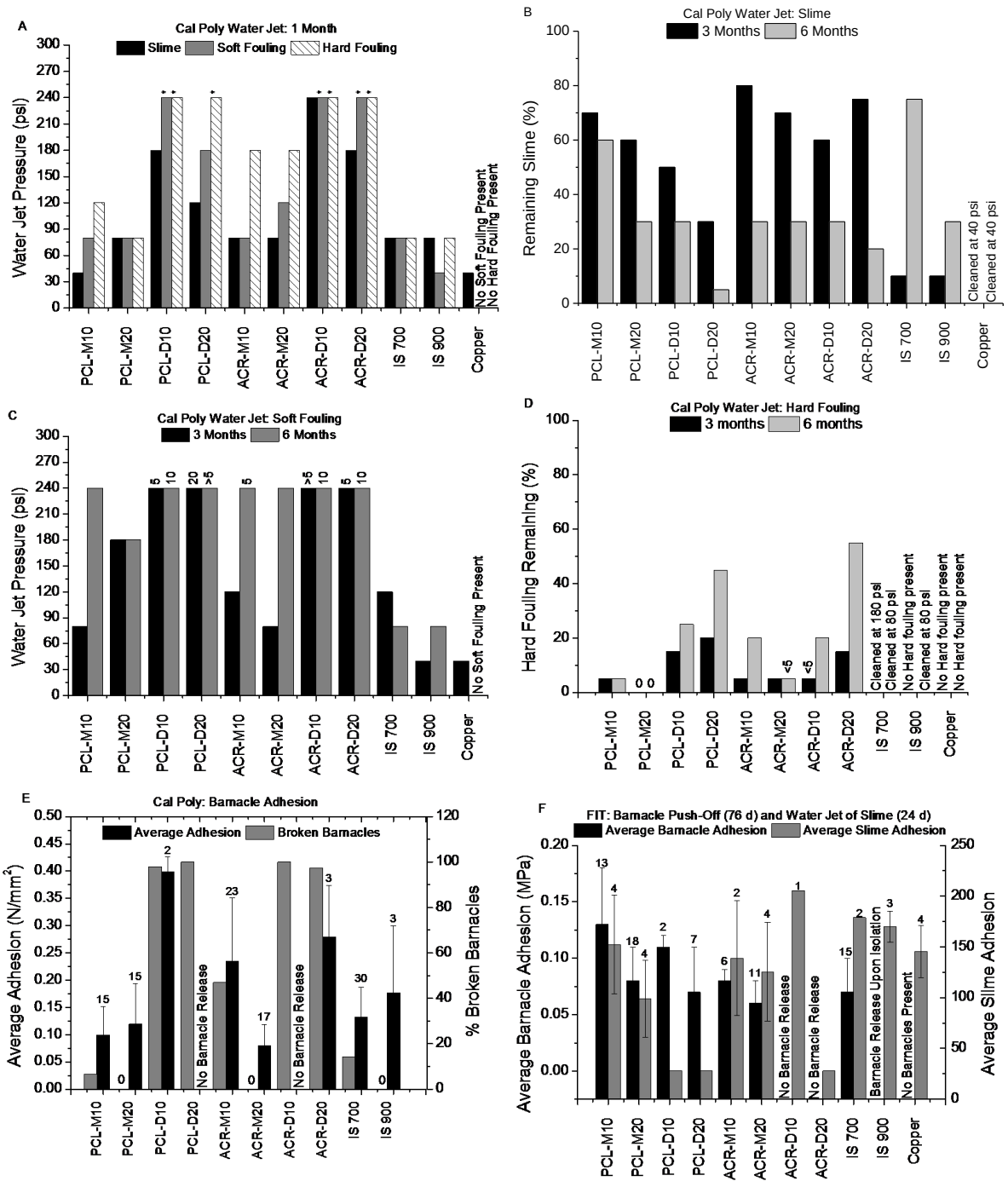

Figure 5.35. Field test data from CalPoly and FIT (Reproduced from ref.[17])

At FIT, coatings with mono-functional PDMS perform well and are comparable to IS700 and IS900 for slime adhesion at 24 days. However, barnacle push-off results are

relatively similar for most PDMS-PU coatings with perhaps the exception of PCL-M-10 that shows slightly higher adhesion.

Results from Singapore are shown at 3-month and 6-month of immersion in Figure 5.36 and Figure 5.37, respectively.

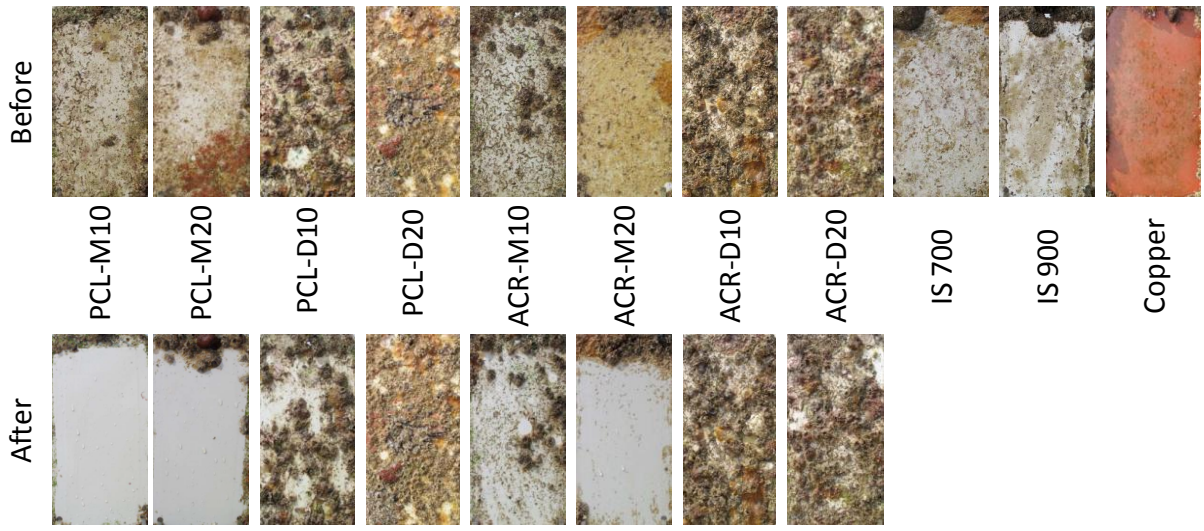

Figure 5.36. Before and after soft sponging after 3-month immersion in Singapore (Reproduced from ref.[17])

As observed in Figure 5.36, coatings with mono-functional PDMS outperform those with di-functional PDMS. ACR-M-10% is the worst among the mono-functional PDMS coatings. Figure 5.37 show the soft sponging result after 6 months of immersion. The PCL-M coatings give better performance than the ACR-M-20% with PCL-M-20% being the best performer among PDMS-PU coatings.

Interestingly, at Singapore, PCL-M-10% and PCL-M-20% outperform ACR-M-20%, even though ACR-M-20% has the largest PDMS content near the surface according to the XPS result. Thus other factors, such surface roughness, definitely play a role in the fouling-release property.

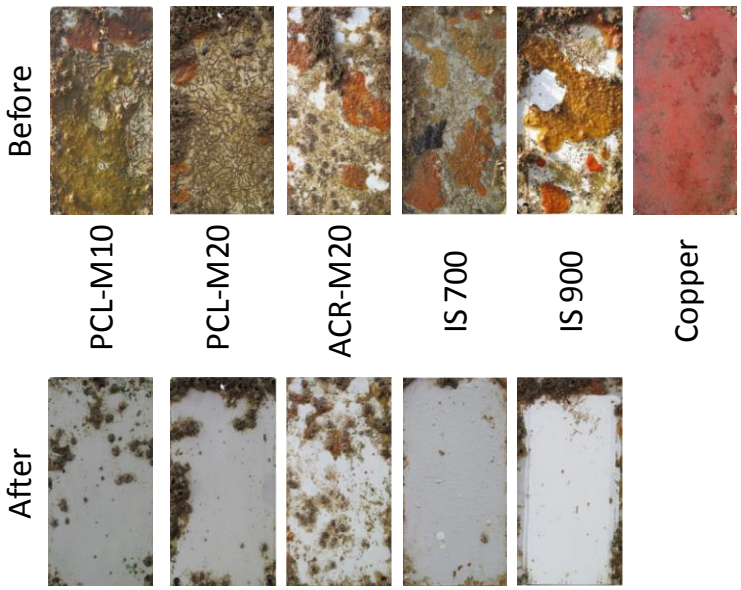

Figure 5.37. Before and after soft sponging after 6-month immersion (Reproduced from ref.[17])

5.5. Further Discussion

The field test results point to some comparable performances between PDMS-PU coatings and commercial silicone marine coatings. One specific example is the barnacle adhesion test at CalPoly. From fracture mechanics theory, it can be shown that the critical stress at debonding is inversely proportional to the strain energy-release rate. The influence of thickness and elastic modulus on the release property in fouling-release coating has been discussed by Brady and Singer.[3] We can look into Kendall's equations. For thin elastomeric films, the critical pull-off force, P_c, and critical stress, $\sigma_{c,}$, are written as:[3]

$$P_c = \pi a^2 \left(\frac{2G_c K}{t}\right)^{1/2} \tag{5.6}$$

$$\sigma_{c=} \left(\frac{2G_c K}{t}\right)^{1/2} \tag{5.7}$$

where G_c is the critical strain energy-release rate, K is the bulk modulus, t is the film thickness and a is the contact radius.

Thus, release is easier with softer and thicker films. G_c is also represented by Dupre's work of adhesion between the two contacting surfaces. The strain energy-release rate is observed by Han et al. using finite element analysis to model the pull-off test on elastomeric coatings.[28] A small crack is assumed at the edge of the interface. The virtual crack closure technique is used in the model. The simulation result shows that the strain energy-release rate decreases as the elastic modulus increases. The strain energy-release rate also increases as the thickness increases and also increases as the crack length increases. Figure 5.38 illustrates the FEA results.

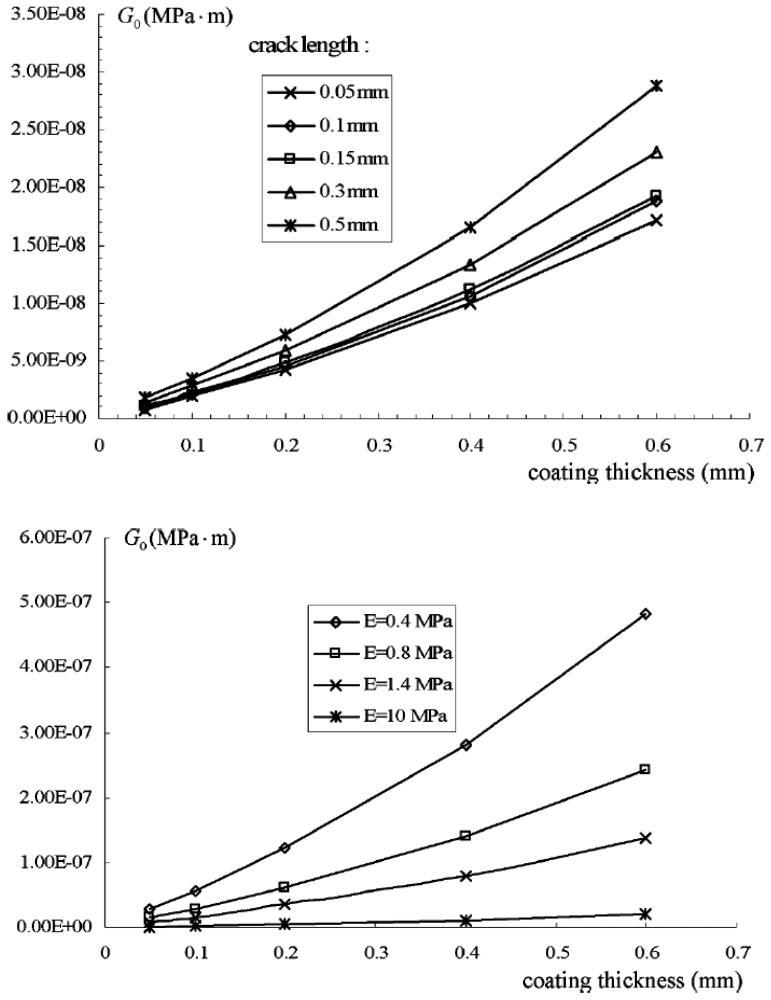

Figure 5.38. Strain energy-release rate is shown as a function of crack length and thickness (top), and as a function of elastic modulus and thickness (bottom). (Reproduced from ref.[28])

Critical stress, σ_c, is derived to following relation:

$$\sigma_c(t) = \sigma_0\sqrt{\frac{G_c}{cG_0(t)}} \tag{5.8}$$

The critical stress directly translates from the applied load. We can see that σ_c is inversely proportional to the strain energy-release rate (as a function of thickness), $G_0(t)$. Intuitively, in elastomeric coatings, the strain-field during pull-off test or shear test would be larger in magnitude and area than in the PU coating based on their stress-strain behaviors. The PU coating experiences much more localized stress due to its much stiffer behavior and an energy loss from viscoelastic behavior. The elastic strain energy in elastomeric coatings can be stored easier with a larger deformation and wider area that is not necessarily in the measurable direction vector of the transducer. Thicker elastomeric coatings would then have lower barnacle adhesion than thinner ones. The mono-functional PDMS-PU coatings should then have lower adhesion based on the above concept because the surface characterization results point to a thicker PDMS layer on the surface. Because of the overall modulus and thickness, it is then not surprising that most PDMS-PU coatings perform similarly in barnacle adhesion, as shown in Figure 5.34, which is likely influenced by the macro-scale mechanical properties. However, the question can be raised regarding just how the PCL-M coatings can perform better than the rest of the PDMS-PU coatings. It is an intriguing thought that a PDMS concentrated layer of 75 nm can have an impact on release forces following Kendall's equation. From Figure 5.34, Barnacle adhesions in PCL-M-10% and PCL-M-20% are only slightly higher than in the T2 commercial silicone elastomer and are also comparable to commercial silicone fouling-release coatings at CalPoly. It would imply that the mono-functional PDMS layer has an extremely low elastic modulus which could be the case at the free surface. It would also mean that ACR-M-10%

and ACR-M-20% should perform similarly to the coatings PCL-M-10% and PCL-M-20%. We can revisit the duplex coating research where Kendall's model has been modified to take into account both top coat and bond coat.[4]

$$P_c = \pi a^2 \left(\frac{2G_c K_t}{t^*}\right)^{1/2} \tag{5.9}$$

$$t^* = t_t\left(1+\frac{\alpha}{\beta}\right), \alpha = \frac{t_b}{t_t}, \beta = \frac{K_b}{K_t}$$

where t^* is the equivalent thickness, t_t and t_b are the top coat and bond coat thicknesses, K_t and K_b are the bulk moduli of top coat and bond coat. Kohl et al. had focused on studying ways to improve the durability of silicone-base coatings, particularly with duplex coating.[4, 5, 33] Duplex coating shows better performance in scratch test than a single coat. A bond coat improves the durability and adhesion, but the thickness of each layer should be in the region of a few hundred micrometers for optimum release. The derivation of the modified Kendall's model for duplex coating is based on the energy balance between surface energy, strain energy and work. Only the volume directly underneath the contact area is assumed to deform. From the equation, it is stated that the equation will reverted back Kendall's model for three cases: 1) no bond coat ($t_b = 0$), 2) they have the same bulk modulus ($\beta = 1$), and 3) bond coat is much stiffer than the top coat (bond coat deformation is insignificant, $\beta \gg \alpha$ *and* $t = t_t$). The relationship between bulk modulus (K) and Young's modulus (E) is

$$K = \frac{E}{3(1-2\nu)} \tag{5.10}$$

where ν is the Poisson's ratio. For the siloxane-polyurethane coating system, if we imagine the top layer is stratified PDMS and polyurethane as a second layer, we may attempt to use the above equations. The problem is that the Poisson's ratio can be quite different between PDMS and PU, with ν closer to 0.5 for PDMS elastomer. Thus, K_t cannot be calculated

from a known *E*. However, from the material's point of view, polyurethane would likely be three orders of magnitude stiffer than the siloxane. This means that

$$\beta \sim 10^3 \quad \text{and} \quad \alpha \sim (10^{-9}/10^{-5}) \approx 10^{-4},\ t = t_t$$

and, here, the third case is applicable where only the top layer needs to be under consideration according to the energy balance of the system due to surface energy, strain energy and work. Therefore, based on Kendall's model, the siloxane-polyurethane should have an incredibly low modulus at the top layer as the release properties have pointed to comparable performance to silicone coating. It is known that the surface properties, such as molecular structure, density, electrical conductivity and elastic modulus, can be different from the bulk.[34] It is found that the surface layer of a polymer has larger mobility and lesser density. This is known as a size dependent property which has been studied using thin film. The property of thin film is dominated by the surface property as the surface to volume ratio dramatically increases. Stafford et al. found that the moduli of ~5 nm-thick polystyrene and poly (methyl methacrylate) films are about an order of magnitude less than their bulk moduli.[35] Further investigation is needed whether the monofunctional PDMS on the surface of siloxane-polyurethane coating has a significantly lower elastic modulus than the bulk due to its mobility with only one reactive end on each chain. Other factors are likely involved which have not been investigated. Surface roughness, from pits and valleys on the surface, can result in microvoids around the adhesion surfaces. These microvoids behave as crack propagation sites and allow for easier release.[4] The low surface energy, low elastic modulus and the surface roughness can contribute to good field test performance in the siloxane-polyurethane coating with its superior durability compared to other silicone elastomeric coating.

5.6. Conclusions

Surface characterization of a set of siloxane-polyurethane coatings using XPS, RBS, TEM, and nanoindentation have been performed. According to XPS results, ACR polyol brings more PDMS to the surface than the PCL-polyol under the same PDMS type and loading. But the PDMS concentration drops faster with depth in ACR polyol than in PCL polyol. More PDMS is present at the surface with 20% loading than with 10% loading. From RBS, ACR-M-20% has a 7 nm of PDMS concentrated layer at the surface, whereas ACR-D-20% has a 3.5 nm PDMS concentrated layer. TEM also shows the distribution of PDMS into the bulk of the coatings with di-functional PDMS.

5.7. References

1. Brady Jr, R. F., Clean hulls without poisons: devising and testing nontoxic marine coatings. *Journal of Coatings Technology* **2000,** *72* (900), 45-56.

2. Brady Jr, R. F., Properties which influence marine fouling resistance in polymers containing silicon and fluorine. *Progress in Organic Coatings* **1999,** *35* (1-4), 31-35.

3. Brady Jr, R. F.; Singer, I. L., Mechanical factors favoring release from fouling release coatings. *Biofouling* **2000,** *15* (1-3), 73-81.

4. Kohl, J. G.; Singer, I. L., Pull-off- behavior of epoxy bonded to silicone duplex coatings. *Progress in Organic Coatings* **1999,** *36*, 15-20.

5. Kohl, J. G.; Singer, I. L.; Schwarzer, N.; Yu, V. Y., Effect of bond coat modulus on the durability of silicone duplex coatings. *Progress in Organic Coatings* **2006,** *56*, 220-226.

6. Ekin, A.; Webster, D. C., Combinatorial and high-throughput screening of the effect of siloxane composition on the surface properties of crosslinked siloxane-polyurethane coatings. *Journal of Combinatorial Chemistry* **2007,** *9*, 178-188.

7. Majumdar, P.; Ekin, A.; Webster, D. C., Thermoset siloxane-urethane fouling release coatings. *ACS Symposium Series 957 (Smart Coatings)* **2007**, 178-188.

8. Sommer, S.; Ekin, A.; Webster, D. C.; Stafslien, S. J.; Daniels, J.; VanderWal, L. J.; Thompson, S. E. M.; Callow, M. E.; Callow, J. A., A preliminary study on the properties and fouling-release performance of siloxane-polyurethane coatings prepared from poly(dimethylsiloxane) (PDMS) macromers. *Biofouling* **2010,** *26* (8), 961-972.

9. Dwight, D. W.; McGrath, J. E.; Riffle, J. S.; Smith, S. D.; York, G. A., ADXPS/STEM studies of surface and bulk microphase behavior in block- and graft-copolymers and their blends. *Journal of Electron Spectroscopy and Related Phenomena* **1990,** *52*, 457-473.

10. Gardella, J. A., Jr.; Mahoney, C. M., Determination of oligomeric chain length distributions at surfaces using ToF-SIMS: segregation effects and polymer properties. *Applied Surface Science* **2004,** *231-232*, 283-288.

11. Hook, D. J.; Valint, P. L., Jr.; Chen, L.; Gardella, J. A., Jr., Quantitative and high mass ToF-SIMS studies of siloxane segregation in hydrogel polymers using cryogenic sample handling techniques. *Applied Surface Science* **2006,** *252*, 6679-6682.

12. Kim, Y. S.; Yang, J.; Wang, S.; Banthia, A. K.; McGrath, J. E., Surface and wear behavior of bis-(4-hydroxyphenyl) cyclohexane (bis-Z) polycarbonate/polycarbonate-polydimethylsiloxane block copolymer alloys. *Polymer* **2002,** *43*, 7207-7217.

13. Lee, J.-W.; Jeong, E. D.; Cho, E. J.; Gardella, J. A., Jr.; Hicks, W., Jr.; Hard, R.; Bright, F. V., Surface-phase separation of PEO-containing biodegradable PLLA blends and block copolymers. *Applied Surface Science* **2008,** *255,* 2360-2364.

14. Wang, L. F.; Ji, Q.; Glass, T. E.; Ward, T. C.; McGrath, J. E.; Muggli, M.; Burns, G.; Sorathia, U., Synthesis and characterization of organosiloxane modified segmented polyether polyurethanes. *Polymer* **2000,** *41,* 5083-5093.

15. Ha, C.-S.; Gardella, J. A., Jr., X-ray photoelectron spectroscopy studies on the surface segregation in poly(dimethylsiloxane) containing block copolymers. *Journal of Macromolecular Science Part C - Polymer Reviews* **2005,** *45* (1-18).

16. Majumdar, P.; Webster, D. C., Influence of solvent composition and degree of reaction on the formation of surface microtopography in a thermoset siloxane-urethane system. *Polymer* **2006,** *47,* 4172-4181.

17. Sommer, S.; Stafslien, S. J.; Webster, D. C.; Bodkhe, R.; Pieper, R.; Daniels, J.; VanderWal, L. J.; David, R.; Callow, M. E.; Callow, J. A.; Ralston, E.; Swain, G.; Brewer, L.; Wendt, D.; Dickinson, G.; Teo, S., Comparison of laboratory analysis with field testing of siloxane-polyurethane fouling-release coatings. **2011**.

18. Oliver, W. C.; Pharr, G. M., An improved technique for determining hardness and elastic modulus using load and displacement sensing indentation experiments. *Journal of Materials Research* **1992,** *7,* 1564-1583.

19. Sneddon, I. N., The relation between load and penetration in the axisymmetric Boussinesq problem for a punch of arbitrary profile. *International Journal of Engineering Science* **1965,** *3,* 47-57.

20. Briggs, D., *Surface analysis of polymers by XPS and static SIMS*. Cambridge University Press: New York, 1998.

21. Cumpson, P. J., Estimation of inelastic mean free paths for polymers and other organic materials: use of quantitative structure-property relationships. *Surface and Interface Analysis* **2001,** *31*, 23-34.

22. Benoit, R. IMFP: Inelastic mean free path. http://www.lasurface.com/xps/imfp.php# (accessed 8/16).

23. Composto, R. J.; Walters, R. M.; Genzer, J., Application of ion scattering techniques to characterize polymer surfaces and interfaces. *Materials Science and Engineering: R: Reports* **2002,** *38* (3-4), 107-180.

24. Lennard, W. N. Rutherford backscattering (RBS), Channeling, Heavy Ion RBS, ERD, MEIS, PIXE, NRA. http://publish.uwo.ca/~wlennard/ (accessed 6/22/2011).

25. Sperling, L. H., *Introduction to Physical Polymer Science*. Forth ed.; John Wiley & Sons, Inc.: Hoboken, New Jersey, 2006.

26. Hwang, S. S.; Ober, C. K.; Perutz, S.; Iyengar, D. R.; Schneggenburger, L. A.; Kramer, E. J., Block copolymers with low surface energy segments: siloxane- and perfluoroalkane-modified blocks. *Polymer* **1995,** *36* (6), 1321-1325.

27. Ignatova, V.; Karpuzov, D.; Chakarov, I.; Katardjiev, I., Computer simulations of surface analysis using ion beams. *Progress in Surface Science* **2006,** *81*, 247-335.

28. Han, C.-S.; Zhang, C.; Wang, J.; Kim, J.; Choi, S.-B., Finite element analysis of thickness dependent debonding forces of elastomer coatings. *The Journal of Adhesion* **2007,** *83*, 535-551.

29. Ebenstein, D. M.; Wahl, K. J., A comparison of JKR-based methods to analyze quasi-static and dynamic indentation force curves. *Journal of Colloid and Interface Science* **2006,** *298*, 652-662.

30. Johnson, K. L., *Contact mechanics*. Cambridge University Press: 1987.

31. Owens, D. K.; Wendt, R. C., Estimation of the surface free energy of polymers. *Journal of Applied Polymer Science* **1969,** *13* (8), 1741-1747.

32. Zisman, W. A., Relation of the equilibrium contact angle to liquid and solid constitution. In *Contact Angle, Wettability, and Adhesion*, Fowkes, F. M., Ed. American Chemical Society: 1964; Vol. 43, pp 1-51.

33. Kohl, J. G.; Singer, I. L.; Simonson, D. L., Determining the viscoelastic parameters of thin elastomer based materials using continuous microindentation. *Polymer testing* **2008,** *27*, 679-682.

34. Ao, Z.; Li, S., Temperature- and thickness-dependent elastic moduli of polymer thin films. *Nanoscale Research Letters* **2011,** *6:243*.

35. Stafford, C. M.; Vogt, B. D.; Harrison, C.; Julthongpiput, D.; Huang, R., Elastic moduli of ultrathin amorphous polymer films. *Macromolecules* **2006,** *39*, 5095-5099.

CHAPTER 6. CONCLUSIONS

An automated puncture tester was built and analyzed. One of the most important design criteria for coatings is the toughness. The coatings need to have the ability to withstand impact and to resist wear and tear. The total energy to break divided by the thickness of the sample was used for comparison of toughness between samples. For elastomeric coatings, there were linear relationships between puncture energy with toughness from tensile test and with tear strength. The instrument significantly reduces the time required by a worker. The stiffness of coatings, which is another important mechanical property of the material, can also be extracted from the measurement.

The Symyx parallel dynamic mechanical-thermal analysis (pDMTA) instrument was analyzed for potential sources of error in the modulus measurement. The test plates were run repeatedly with the same polymer control. One of the sources determined was the thickness measurement using the laser profilometer. Adjustments were made to the algorithm of the thickness calculation. The results from finite element analysis show the limitations of the closed-form solution. The optimum thickness of the sample is at 100 μm. A 200-μm thick sample would already yield an error of more than 25%. With careful sample preparation, the errors were reduces to be within 30% from the previous errors of more than 100%. The correction factor equations were generated to account for the variation of thickness. The droplet shape of polymer samples and the curvature of the substrates are also the sources of errors which should be minimized.

The automated nanoindentation instrument provides high-throughput characterization of hardness and elastic modulus measurement of coatings. For quasi-static indentation, the displacement control mode should be used because the strain rate varies

with the depth of indentation. The dynamic indentation mode eliminated the complications of analyzing viscoelastic materials. The different analytical methods of calculation have their assumptions which may result in the inaccuracy of the result. Nevertheless, these methods are adequate for the purpose of ranking within the polymer library. The loss tangent result from dynamic indentation should also be inversely proportional to the pendulum hardness. However, the polyurethane coatings in the study showed dependence on storage modulus whereas the dependence on the loss tangent was insignificant. It is believed that with a lower rate of applied oscillation, both dependencies would be observed.

The chemical analysis techniques, such as RBS and angle-dependent XPS, provide not only the confirmation of self-stratification, but also the distribution of siloxane component as a function of depth. The coatings with mono-functional PDMS have better performance in field testing than the coatings with di-functional PDMS. It can be explained by the higher concentration of PDMS near the surface for coatings with mono-functional PDMS than those with the di-functional counterparts.

CHAPTER 7. FUTURE WORK

Significant improvements can be made to the automated puncture tester. Currently, the lubricant is automatically applied only at the beginning of the first puncture. This can be easily fixed by re-programing the logic. The machine compliance will be calculated to yield higher accuracy of the measured displacement. The centering of the indenter to the free film area is the most crucial factor in achieving repeatability. A self-aligning mechanism should be investigated. The secant modulus can be calculated readily from the stress-strain curve. However, it will be interesting to apply an algorithm that uses repeated numerical simulations to scan through possible combinations of pre-strain and elastic modulus that can match the experimental data. The problem here lies with the accuracy of the instrument, the accuracy of the thickness measurement and the film uniformity. Also, the fixed sampling rate should be higher than the current rate of 10 Hz.

In the pDMTA system, finite element analysis or other means can be performed to account for the shapes of droplets whether it is a dimple or a convex shape. But the current analysis already shows significant errors with flat samples. The miniaturization of the test geometry causes variations because the tolerances cannot be limited. We have experimented with using a customized drawdown bar which has 12 gaps to cast 12 samples onto the existing pDMTA plate. This results in 12 different samples, each with 8 replicates on a single plate. As long as the polymer solutions in each column do not merge due to flow, the test provides better accuracy than analyzing with droplets. The pDMTA can be improved tremendously with redesigning of the apparatus. The sample plate can be reduced in the numbers of testing sites from 96 to 48 or 24. Then, it would be easier to handle the samples. But if we want to keep a 96-sample template, there needs to be a redesign on the

measuring pin. The major problem is that not all the pins make contact at the same time, but the pins connected to the load sensors are relatively rigid. This causes significant indentations on many of the testing spots because the certain amounts of pins need to be in contact. As a result, bending plate regime no longer applies. The pin mounting should be redesigned so that they are load with soft springs or any mechanism that can ensure similar contact loads on all the testing spots. Kapton is relatively stiff, especially for polymers at their rubbery plateau. We should look for a substitute which has lower modulus than the modulus of Kapton. It should also be thermally stable and does not have a T_g near testing temperatures.

Further experiments can be performed to correlate pendulum hardness with the dynamic indentation. It was recommended not to run the Triboindenter (Hysitron Inc.) lower than 10 Hz. This is still an order of magnitude different from the pendulum test. The scratch test using Triboindenter can be performed to correlate results with pencil hardness test. A sharp conical tip is used in the scratch experiment. A load is ramped up until there is a fracture of polymers. The instrument needs to allow enough displacement and load to scratch the polymer surface.

APPENDIX A. PROGRAMMING IN CHAPTER 2

A.1. Effective Gauge Length Calculation

Effective gauge length is used because we do not have the tool to monitor the change in length on the narrow section of the dumbbell specimen. The effective gauge length calculation is based on small strain using Hook's law. The larger section of the dumbbell will give a total elongation that is equivalent to the narrow section width at some equivalent length. This equivalent length for the whole specimen is then defined as effective gauge length. Thus, the effective gauge length is always shorter than the grip length because of the dumbbell geometry.

w_n is the width of the narrow section.

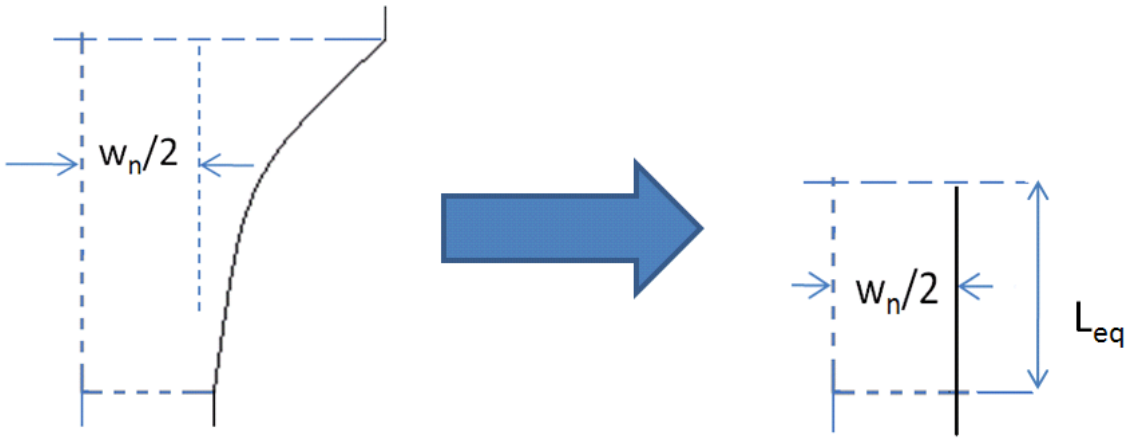

Figure A.1. Schematic of an equivalent gauge length

A change in length from actual specimen is the same as the change in length from specimen having equivalent length.

$$\Delta L_{actual} = \Delta L_{equivalent} \tag{A.1}$$

Strain is define as:

$$\varepsilon = \frac{\Delta L}{L} \tag{A.2}$$

According to Hooke's law,

$$\sigma = \frac{F}{A} = \varepsilon E \tag{A.3}$$

Thus, we have,

$$\Delta L = \frac{\sigma L}{E} = \frac{F}{A}\frac{L}{E} \tag{A.4}$$

$$\Delta L_{actual} = \frac{F}{E}\frac{\Delta x_1}{A_1} + \frac{F}{E}\frac{\Delta x_2}{A_2} + ... + \frac{F}{E}\frac{\Delta x_n}{A_n} \tag{A.5}$$

$$= \frac{F}{E}\sum_{n=a}^{b}\frac{\Delta x_n}{A_n} = \frac{F}{E}\int_a^b \frac{1}{A(x)}dx \tag{A.6}$$

From previous statement,

$$\Delta L_{actual} = \Delta L_{equivalent} \tag{A.7}$$

Therefore,

$$\frac{F}{E}\int_a^b \frac{1}{A(x)}dx = \frac{F}{E}\frac{L_{eq}}{A} \tag{A.8}$$

y(x) represents the shape of the dumbbell. y is measured from the center axis of symmetry along the length.

$$A(x) = 2t\ y(x) \tag{A.9}$$

A(x) = 2*t*y(x); a factor of 2 is included because we want to take into account both sides across the axis of symmetry.

$$\frac{F}{E2t}\int_a^b \frac{1}{y(x)}dx = \frac{F}{E}\frac{L_{eq}}{(w_n t)} \tag{A.10}$$

Depending on the range of a through b, the factor of 2 will be cancelled out if the axis of symmetry along the width is used.

$$L_{eq} = w_n \int_a^b \frac{1}{y(x)} dx \tag{A.11}$$

The shape of a dumbbell is obtained by tracing the actual geometry of a cut specimen. We obtain the profile (y(x)) directly from the cut specimen. A variable x represents a value on a symmetrical axis along the length on the specimen. A variable y represents height of the profile along the x-axis. The specimen picture file is obtained with a scanner and MATLAB program (grapit.m, available to download on MATLAB Central) is used to manually obtain data points (y as a function of x). Then, the effective gauge length is calculated from the code below. The data points were integrated using trapezoidal integration to the center axis of symmetry along the length.

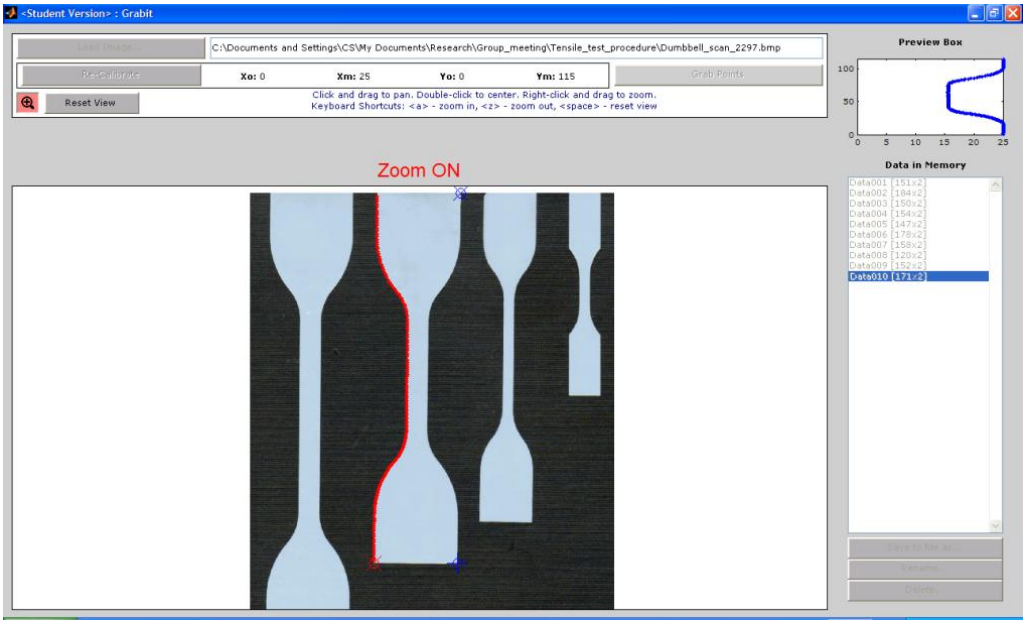

Figure A.2. Tracing a shape profile of a dumbbell specimen

$$L_{eq} = \frac{w_n}{2} \int_0^{grip\ length} \frac{1}{y(x)} dx \qquad \text{(A.12)}$$

The integration is done on the data points within the grip separation length. Grip length is not constricted to supposedly the end of the curve section because there is no assumption and complexity of the calculation and measurement involved.

For D412 Die D with grip length 67.4 mm, the effective gauge lengths are 47.80 and 48.0 on the left side (arbitrary chosen) and 44.13 and 43.86 on the right side. The average is 45.95 mm.

For D412 Die C with grip length 90.0 mm, the effective gauge lengths are 57.73 and 57.28 on the left side (arbitrary chosen) and 56.81 and 56.47 on the right side. The average is 56.98 mm.

The reasons for discrepancy could be that the origin of x and y, the x-y axes and the data points (shape profile) were selected manually, thus due to some errors. Also the specimen may not actually be perfectly symmetry which could be due to the uneven cut which may cause movement of the specimen during cut, or in case of Die D, the die gets dull on some areas from abuse and the die shape slightly changes in some parts of the die, this could be the reason for large difference between the two opposite sides.

```
% To calculate gauge length with profile data
% November 17, 2009
% Author: Chavanin S.
clc;
%D412 Die D
%spL=100;% specimen length
%grL=67.4;% Grip length
%we=16; % end width, width of large section
%wn=3; % Width of narrow section
% D412 Die C
spL=115;% specimen length
grL=90;% Grip length
we=25; % end width, width of large section
```

```
wn=6; % Width of narrow section
Ingrip=spL-grL; % In the grip area
Ingrip_each=Ingrip/2; % In the grip on each side
%x=D412D(:,2); % dumbbell profile, just switch the columns
%y=D412D(:,1);
x=D412C(:,2); % dumbbell profile, just switch the columns
y=D412C(:,1);
% Thus the profile should starts where to grip ends, which is
x0=Ingrip_each;
xend=Ingrip_each+grL;
y0 = interp1q(x,y,x0);
yend = interp1q(x,y,xend);

xf(1)=x0;
yf(1)=y0;
p=2;
for n=1:size(x);
    if x(n)>x0 && x(n)<xend
        xf(p)=x(n);
        yf(p)=y(n);
            p=p+1;
    end
end
p;
xf(p)=xend;
yf(p)=yend;
yf=yf-(we/2);
plot(xf,yf),axis equal
one_y=1./yf;
inY=trapz(xf,one_y);  % Trapezoidal integration
Effective_gauge_length=inY*wn/2
```

A.2. Data Analysis

The automated puncture instrument will only give the maximum force accurately because the instrument's software has no algorithm to determine the contact point and the puncturing point of the film. A simple MATLAB code was written to calculate the interested parameters (extension, area under the curve, estimated slope) on all 12 wells with one execution. MATLAB code sequences are shown as follow.

1. *Split into 12 separate data sets.* The raw data output is given into 3 columns; the well number, displacement in inches, and loads in pounds.
2. *Find contact point on each well.* Use 'if' statement to check for increasing force trend. Check if '2^{nd} data point > 1^{st} data point' and $3^{rd} > 1^{st}$ and $4^{th} > 1^{st}$ and $5^{th} > 2^{nd}$

and $6^{th} > 3^{rd}$ and $7^{th} > 3^{th}$ and $8^{th} > 4^{th}$ and $9^{th} > 5^{th}$ and $10^{th} > 3^{rd}$. If the conditions do not satisfy, move to the next data point. In rare cases, it doesn't work because the indenting-in-the-air load stepped up, then we can apply additional 'if' conditions to the loop.

3. *Find the end point on each well.* Use 'if' statement to check the next data point that has a drop in magnitude of 20% or more.
4. *Change to SI units and calculate extension at break, maximum load, area under the curve.* Before calculation, the measured load before contact has to be subtracted from the load after contact is made. Since the output load has a stepwise nature due to signal conditioning from software programmer, the mode average is used to get the baseline for subtraction.
5. *Calculate modulus.* Three different simple procedures are executed. First one is to find a data point at half way and select the next six and the previous six data points in stress-strain data. Stress-strain is calculated based on Meredith's simplified calculation. Then linear fit is used to find the slope. Second procedure is to use a third- or fourth-order polynomial fit to the stress-strain curve. Then Symbolic math toolbox in MATLAB is used to differentiate the polynomial functions and do the evaluation at a specific strain. In the current code, 4^{th} order polynomial and 5% strain are chosen, but they can be readily changed if the results are not satisfactory. The third procedure uses secant modulus as described in Meredith's paper, but a specific strain was not selected. I select a half-way data point and divide the force by the displacement at the mid-point data. This is because at low strains, the differences in slope are not obvious.

**********Start of Main Program**********

Separate the data set, make plots and find contact points

```
% Plot raw data from automated puncture station
% data array is the output from the instrument.
n1=1;n2=1;n3=1;n4=1;n5=1;n6=1;
n7=1;n8=1;n9=1;n10=1;n11=1;n12=1;
for k=1:max(size(data));

if data(k,1)==1
    data1(n1,1)=data(k,2);
    data1(n1,2)=data(k,3);
    n1=n1+1;
elseif data(k,1)==2
    data2(n2,1)=data(k,2);
    data2(n2,2)=data(k,3);
    n2=n2+1;
elseif data(k,1)==3
    data3(n3,1)=data(k,2);
    data3(n3,2)=data(k,3);
    n3=n3+1;
                        .                       .
                        .                       .
                         Continue through well#12
                        .                       .
                        .                       .
end
end
diff_well_1=max(data1(:,1))-max(data2(:,1)); % Well#1 has longer
travel,...
% range because it started higher than other spots.
data1Adj=data1-diff_well_1;
data1Adj(:,2)=data1(:,2);  % This won't be used anyway.

plot(data1Adj(:,1),data1(:,2),data2(:,1),data2(:,2),data3(:,1),data3(:,2)
,...
    data4(:,1),data4(:,2),data5(:,1),data5(:,2),data6(:,1),data6(:,2),...
    data7(:,1),data7(:,2),data8(:,1),data8(:,2),data9(:,1),data9(:,2),...
data10(:,1),data10(:,2),data11(:,1),data11(:,2),data12(:,1),data12(:,2)),
...
    xlabel('Displacement, inch'),ylabel('Force, lb'),...
    legend('1','2','3','4','5','6','7','8','9','10','11','12')

figure(2) % plot with Newton and mm
plot(data1Adj(:,1).*25.4,data1(:,2).*4.4482,'.',...
    data2(:,1).*25.4,data2(:,2).*4.4482,'.',...
    data3(:,1).*25.4,data3(:,2).*4.4482,'.',...
    data4(:,1).*25.4,data4(:,2).*4.4482,'.',...
    data5(:,1).*25.4,data5(:,2).*4.4482,'.',...
    data6(:,1).*25.4,data6(:,2).*4.4482,'.',...
    data7(:,1).*25.4,data7(:,2).*4.4482,'.',...
    data8(:,1).*25.4,data8(:,2).*4.4482,'*',...
    data9(:,1).*25.4,data9(:,2).*4.4482,'*',...
    data10(:,1).*25.4,data10(:,2).*4.4482,'*',...
```

```
    data11(:,1).*25.4,data11(:,2).*4.4482,'*',...
    data12(:,1).*25.4,data12(:,2).*4.4482,'*')
    xlabel('Displacement, mm'),ylabel('Force, Newton'),...
    legend('1','2','3','4','5','6','7','8','9','10','11','12')
%% Find start position on each well
% This can be shorten if I use function and eval and loop the variable
name.

for n=1:(max(size(data1))-4)
if (data1(n+1,2)> data1(n,2)) && (data1(n+2,2)> data1(n,2)) &&...
        (data1(n+3,2)> data1(n,2)) && (data1(n+4,2)> data1(n+1,2)) &&...
        (data1(n+5,2)> data1(n+2,2)) && (data1(n+6,2)> data1(n+2,2))&&...
        (data1(n+7,2)> data1(n+3,2)) &&(data1(n+8,2)> data1(n+4,2)) &&...
        (data1(n+9,2)> data1(n+2,2))
   n1=n;
    disp('n1 =');disp(n1); break
end
end

for n=1:(max(size(data2))-4)
if (data2(n+1,2)> data2(n,2))&&(data2(n+2,2)> data2(n,2))&&...
        (data2(n+3,2)> data2(n,2))&&(data2(n+4,2)> data2(n+1,2)) &&...
        (data2(n+5,2)> data2(n+2,2))&&(data2(n+6,2)> data2(n+2,2)) &&...
        (data2(n+7,2)> data2(n+3,2))&&(data2(n+8,2)> data2(n+4,2)) &&...
        (data2(n+9,2)> data2(n+2,2))
    n2=n;
   disp('n2 =');disp(n2); break
end
end
```

```
                        .                       .
                        .                       .
                         Continue through well#12
                        .                       .
                        .                       .
```

Use a user-defined function (named 'anaPuncDat') to locate breaking point and calculate max force and max displacement

```
% if the point adjacent after contact point drops sharper than a set ...
% percentage, then a data point before is the breaking point.
% per=0.20; % 20 percent default
% Calculate the max force, max displacement, area under the curve.
% change data to mm and Newton
per=0.20; % percent drop off criteria
[n1f,Exten1,Max1,baseline1,areaBase1,areaAll1,areaF1,dataf1]=anaPuncDat(d
ata1,per,n1);
disp('Max extension, well#1');disp(Exten1)
disp('Max force, well#1');disp(Max1)
disp('Energy, well#1');disp(areaF1)
clear a nf ns
[n2f,Exten2,Max2,baseline2,areaBase2,areaAll2,areaF2,dataf2]=anaPuncDat(d
ata2,per,n2);
disp('Max extension, well#2');disp(Exten2)
disp('Max force, well#2');disp(Max2)
disp('Energy, well#2');disp(areaF2)
clear a nf ns
```

```
                        .                       .
                        .                       .
                         Continue through well#12
                        .                       .
                        .                       .
figure(3)
plot(dataf1(:,1),dataf1(:,2),'.-',dataf2(:,1),dataf2(:,2),'.-',...
     dataf3(:,1),dataf3(:,2),'.-',dataf4(:,1),dataf4(:,2),'.-',...
     dataf5(:,1),dataf5(:,2),'.-',dataf6(:,1),dataf6(:,2),'.-',...
     dataf7(:,1),dataf7(:,2),'.-',dataf8(:,1),dataf8(:,2),'s-',...
     dataf9(:,1),dataf9(:,2),'s-',dataf10(:,1),dataf10(:,2),'s-',...
     dataf11(:,1),dataf11(:,2),'s-',dataf12(:,1),dataf12(:,2),'s-')
     xlabel('Displacement, mm'),ylabel('Force, Newton'),...
     legend('1','2','3','4','5','6','7','8','9','10','11','12')

Output results into rows and columns
% Create table for output; Cut and paste to Excel spreadsheet
output_table_horizontal=[1,2,3,4,5,6,7,8,9,10,11,12;...
    Exten1,Exten2,Exten3,Exten4,Exten5,Exten6,Exten7,Exten8,Exten9,...
    Exten10,Exten11,Exten12;...
    Max1,Max2,Max3,Max4,Max5,Max6,Max7,Max8,Max9,...
    Max10,Max11,Max12;...
    areaF1,areaF2,areaF3,areaF4,areaF5,areaF6,areaF7,areaF8,areaF9,...
    areaF10,areaF11,areaF12];
output_table_vertical=[1,Exten1,Max1,areaF1;2,Exten2,Max2,areaF2;...
    3,Exten3,Max3,areaF3;4,Exten4,Max4,areaF4;...
    5,Exten5,Max5,areaF5;6,Exten6,Max6,areaF6;...
    7,Exten7,Max7,areaF7;8,Exten8,Max8,areaF8;...
    9,Exten9,Max9,areaF9;10,Exten10,Max10,areaF10;...
    11,Exten11,Max11,areaF11;12,Exten12,Max12,areaF12];

Use a user-defined function (named 'CalModulus') to calculate the
modulus(slope) at half-way or at selected %strain

% Calculate slopes
% We can do fit between half way or select at 5% strain.
[E_half_1,E_5percent_1,E_Meredith_1,Stress_1,Strain_1]=CalModulus(dataf1,
h(1));
disp('Modulus half way, well#1');disp(E_half_1)
disp('Modulus 5% Strain, well#1');disp(E_5percent_1)

[E_half_2,E_5percent_2,E_Meredith_2,Stress_2,Strain_2]=CalModulus(dataf2,
h(2));
disp('Modulus half way, well#2');disp(E_half_2)
disp('Modulus 5% Strain, well#2');disp(E_5percent_2)
                        .                       .
                        .                       .
                         Continue through well#12
                        .                       .
                        .                       .


output_Modulus_vertical=[1,E_half_1,E_5percent_1,E_Meredith_1;...
    2,E_half_2,E_5percent_2,E_Meredith_2;...
    3,E_half_3,E_5percent_3,E_Meredith_3;...
    4,E_half_4,E_5percent_4,E_Meredith_4;...
```

```
    5,E_half_5,E_5percent_5,E_Meredith_5;...
    6,E_half_6,E_5percent_6,E_Meredith_6;...
    7,E_half_7,E_5percent_7,E_Meredith_7;...
    8,E_half_8,E_5percent_8,E_Meredith_8;...
    9,E_half_9,E_5percent_9,E_Meredith_9;...
    10,E_half_10,E_5percent_10,E_Meredith_10;...
    11,E_half_11,E_5percent_11,E_Meredith_11;...
    12,E_half_12,E_5percent_12,E_Meredith_12];
%     11,E_half_11,E_5percent_11,E_Meredith_11;...
% 2,E_half_2,E_5percent_2,E_Meredith_2;...
%    9,E_half_9,E_5percent_9,E_Meredith_9;...

figure(4)
plot(Strain_1,Stress_1,'.-',Strain_2,Stress_2,'s-',...
     Strain_3,Stress_3,'.-',Strain_4,Stress_4,'.-',...
     Strain_5,Stress_5,'.-',Strain_6,Stress_6,'.-',...
     Strain_7,Stress_7,'.-',Strain_8,Stress_8,'s-',...
     Strain_9,Stress_9,'s-',Strain_10,Stress_10,'s-',...
     Strain_11,Stress_11,'s-',Strain_12,Stress_12,'s-')
     xlabel('Strain, m/m'),ylabel('Stress, Pa'),...
     legend('1','2','3','4','5','6','7','8','9','10','11','12')
```

********** End of Main Program**********

**********Subroutine function*********

```
function[nf,Exten,Max,baseline,areaBase,areaAll,areaF,dataf]=anaPuncDat(d
at,per,ns)
a=[];
per=1-per; % I have to subtract from one because it is a percent drop
% off not a percent of the other point. This way it represents % drop off
% the previous data point.
 for a=ns:(max(size(dat))-4)
 if dat(a,2)*per> abs(dat(a+1,2)) % If the load drop more than specified
percentage
    nf=a;
     disp('nf =');disp(nf);
     break
end
end
% clear a
% for a=ns:(max(size(dat))-4)
% if dat(a+1,2) < dat(a,2)*per  % If the load drop more than specified
percentage
%    nf=a;
%     disp('nf =');disp(nf);
%     break
% else nf=1;
% end
% end
% Calculate area under baseline first
baseline=mode(dat(1:ns,2)).*4.4482;
% Instead of calculate area under the base I can zero the y force by
% subtracting from mode(beginning data)
% Or I can use this method but zero the y force at the end
% or use mean average, baseline=mean(dat(1:ns,2));
% Calculate area under the curve, Extension at break, Max force
% Cut data to only between ns and nf and change to mm and Newton.
```

```
b=1;
for c=ns:nf
dataf(b,1)=(dat(c,1)-dat(ns,1))*25.4; % Zero the x data and convert unit
dataf(b,2)=dat(c,2)*4.4482; % Shift and cut y data and convert unit
b=b+1;
end
% It is observed that there are repeated y force values occurring along
% the measurement.
% We make an assumption that the y force data is collected twice
% occasionally. So I will remove the y-data point and shift the x-axis
% data. Even though data spacing appear to be fixed, I want to write a
code that step through each data point and not just shift the whole
% array.
%
% Simple way is to just cut the y data and assume equal spacing on x.
n=2; y(1)=dataf(1,2);
for m=2:max(size(dataf))
    if dataf(m,2)==dataf(m-1,2)
       % n=n;
    else y(n)=dataf(m,2);
        n=n+1;
    end
end
for p=1:n-1
    dataff(p,1)=dataf(p,1);
    dataff(p,2)=y(p);
end

dataf=dataff; % for output the conditioned data
%Exten=dat(nf,1)-dat(ns,1);
Exten=max(dataf(:,1));
Max=max(dataf(:,2));

% for area I need to calculate area under the force baseline.
% Use Mode average because the raw load data is quite stepwise.
% Calculate area under baseline first
areaBase=baseline*Exten;
areaAll=trapz(dataf(:,1),dataf(:,2));
areaF=areaAll-areaBase;
for c=1:max(size(dataf));
dataf(c,2)=dataf(c,2)-baseline;
end
```

**********End of subroutine*********

**********Subroutine function*********

```
function[E_half,E_5percent,E_Meredith,Stress2,Strain2]=
CalModulus(dataf,h)

a=6.35*10^-3; % radius =6.35 mm
% Change a and h to meter unit
% Change dataf to m unit.
dataf(:,1)=dataf(:,1).*10^-3;
Stress=(dataf(:,2)./(2*pi*a*h)).*(sqrt((dataf(:,1).^2)+a.^2)./dataf(:,1))
;
Strain=(sqrt((dataf(:,1).^2)+a.^2)-a)./a;
```

```
Length_data=max(length(dataf));
Middle=round(Length_data./2);

x=[Strain(Middle-6),Strain(Middle-5),Strain(Middle-4),Strain(Middle-
3),...
    Strain(Middle-2),Strain(Middle-1),Strain(Middle),Strain(Middle+1),...

Strain(Middle+2),Strain(Middle+3),Strain(Middle+4),Strain(Middle+5),...
    Strain(Middle+6)];
y=[Stress(Middle-6),Stress(Middle-5),Stress(Middle-4),Stress(Middle-
3),...
    Stress(Middle-2),Stress(Middle-1),Stress(Middle),Stress(Middle+1),...

Stress(Middle+2),Stress(Middle+3),Stress(Middle+4),Stress(Middle+5),...
    Stress(Middle+6)];

p1=polyfit(x,y,1);
E_half=p1(1);

% Use Symbolic Math Toolbox to differentiate a fitted polynomial
syms k;

% polyfit will not work if I did not cut a set of initial stress data,..
% because the curve is abnormal due to division close to zero.

% Thus start from strain of 0.5% or 0.005, this is the 16th element in an
% array.
% Some data still rising after 0.5%, thus I change to start at 24th
element
Stress2=Stress(24:end);
Strain2=Strain(24:end);
p2=polyfit(Strain2,Stress2,4)

diff_Stress_Strain=diff((p2(1)*k^4)+(p2(2)*k^3)+(p2(3)*k^2)+(p2(4)*k));
E_5percent=subs(diff_Stress_Strain,k,0.05);
Force=dataf(Middle,2);
displ=dataf(Middle,1);
E_Meredith=Force./(2*pi*h*displ);
```

**********End of subroutine*********

A.3. Numerical Simulation

The code below was last updated on May 31, 2011. Three inputs are required to execute; 1) Span ratio (h/a), 2) Poisson's ratio (ν), and 3) Pre-strain (eps0). The outputs are (w/a) from numerical simulation, plate solution and membrane solution. Notice that all the inputs and output are dimensionless. Also, elastic modulus is not required, because the imposed load is normalized (called pload in the code). The stress function F and the slope β

are calculated at each increment of pload. From β, (w/a) is calculated for each pload iteration and stored. The code does not store β since it is unnecessary at this point. Lastly, plate and membrane closed form solutions are used and plotted with the numerical simulation result.

The relaxation ('solvde') solvers are called by the main program in FORTRAN. The 'solvde', 'pinv', 'red' and 'bksub' solvers are available from Numerical Recipes in FORTRAN: The Art of Scientific Computing, 2nd Edition. 'difeq' is where the finite difference algebraic equations for this problem are written. MATLAB was first written in the same manner. But in FORTRAN, when c and s matrices are called, the matrices are manipulated accordingly. In MATLAB, the c and s matrices are redefined every time they leave the functions, thus erasing the previous numbers. The attempt to define c and s as 'global' variables was not successful. Thus I eliminated the use of call functions by putting all the codes in sequence as it would be run. The code can be cleaned up and shorten if need arises. Traces of FORTRAN code are left for comparison.

```
% Code translated to Matlab from FORTRAN(Komaragiri)
% Chavanin S.,  Nov. 2008
%INTEGER NE,M,NB,NCI,NCJ,NCK,NSI,NSJ,NYJ,NYK
clear;clc;
%global x h lambda v hb eps0
%COMMON /BLOCK1/ x,h,lambda,v,hb,eps0
%global it
%COMMON /BLOCK3/ it
%PARAMETER(NE=4,M=1751,NB=2,NCI=NE,NCJ=NE-NB+1,NCK=M+1,NSI=NE,...
%NSJ=2*NE+1,NYK=M)
ne=4;M=1751;nb=2;nci=ne;ncj=ne-
nb+1;nck=M+1;nsi=ne;nsj=2*ne+1;nyj=ne;nyk=M;
%CHARACTER(80) :: outputfile
%INTEGER itmax,k,indexv(NE),LCASE,it,pos
%REAL conv,h,slowc,c(NCI,NCJ,NCK),s(NSI,NSJ),pload
%REAL v,hb,eps0,Eb,hstrain(18000),max_strain,max_strain_position
%REAL max_rstrain,max_rstrain_position,rstrain(18000)
%REAL scalv(NE),x(M),y(NE,M),lambda,SOLUTION(4,500000),lamb
%REAL avg_angle,z,dr,plsol,memsol,pi,temp1,Q,load,disp,alpha
%REAL ss_hstrain,ss_rstrain,ss_beta,ss_f,ra,gap
```

```
pi=3.141592;
itmax=5000;
conv=5.e-6;
slowc=1.;

indexv(1)=1;
indexv(2)=2;
indexv(3)=3;
indexv(4)=4;

for i=1:18000
  hstrain(i)=0.0;
  rstrain(i)=0.0;
end

%!  ***PROGRAM INPUT***  !

hb=input('Thickness/Span(h/a) Ratio =  ');
%write(*,'(1x,2A)',ADVANCE = "NO") "Thickness/Span(h/a) Ratio="
%read*,hb

v=input('Poisson Ratio (v)  =  ');
%write(*,'(1x,3A)',ADVANCE = "NO") "Poisson's Ratio (v)="
%read*,v

eps0=input('Pre-Strain(eps)  =  ');
%write(*,'(1x,2A)',ADVANCE = "NO") "Pre-Strain(eps) ="
%read*,eps0
% Chavanin : Time it takes to run the codes.
tic;

Eb = (1./(12.*(1.-v^2)));

pload = 1.0e-8;  %!*************pload = 12P(1-v^2)/(Ea^2)********** !

lambda = (pload^2.)/((hb^8.)*Eb);  %!******Defined in Eqn. (3.1)*****!

%! **************CREATING A MESH************** !

x(1) = 0.000001;

for k = 2:301
 x(k)= x(k-1)+(0.00001-0.000001)/(300);
end

for k =302:601
 x(k)= x(k-1) + (0.0001-0.00001)/(300);
end

for k = 602:901
 x(k)= x(k-1) + (0.001-0.0001)/(300);
end

for k = 902:1201
```

```
 x(k)= x(k-1) + (0.01-0.001)/300;
end

for k = 1202:1501
 x(k)= x(k-1) + (0.1-0.01)/300;
end

for k = 1502:M
 x(k)= x(k-1) + (1.-0.1)/(M-1501);
end

%!****************INITIALISING VARIABLES********** !

%!   Normalized Rotation Function, V=B(Eah/P)^(1/3)

%!   Normalized Stress Function, G = (f/P)(P/Eah)^(1/3)
%!
%!   Y(1)= V_PRIME (Normalized Rotation derivative)
%!   Y(2)= V      (Normalized Rotation)
%!   Y(3)= G_PRIME (Normalized Stress Function Derivative)
%!   Y(4)= G       (Normalized Stress Function)
y=zeros(4,1751);
for k=1:M-1

  y(1,k)= -(lambda^(1./3))*(1./(4.*pi))*(1.0+log(x(k)));
  y(2,k)= -(lambda^(1./3))*(1./(4.*pi))*(x(k)*log(x(k)));
  y(3,k)= 0.1e-3;
  y(4,k)= 0.1e-3;

end

x(M) =1.;

%!***BOUNDARY CONDITION***!

y(1,M)=-(1./(4.*pi))*(lambda^(1./3.));
y(2,M)=1.e-9;
y(3,M)=1.e-9;
y(4,M)=1.e-9;

scalv(1)=10.0;
scalv(2)=1.0;
scalv(3)=1.0;
scalv(4)=1.0;

%!***START OF ITERATIONS***!
it=1;
for LCASE=1:605  % Koma uses LCASE=1,100000; But pload reaches 1e-3 at
LCASE =605

    if pload > 1.e-3
       %disp ( ' pload is more than dotZeroZeroOne ');
        break
       %error('what pload>1e-3')
       %goto 9990
```

```
    end

    if pload < 3.0e-6
        pload = pload + 1.e-8;

    elseif pload >= 3.e-6 && pload < 3.e-4
        pload = pload +1.e-6;
    elseif pload >= 3.e-4
        pload = pload +1.e-4;
    end

    if it>itmax-1
       disp('what it>itmax-1?');
       break
        %error('it>itmax-1')
       %goto 9990
    end

    lambda = (pload^2.)/((hb^8.)*Eb);

    %call
solvde(itmax,conv,slowc,scalv,indexv,NE,NB,M,y,NYJ,NYK,c,NCI,NCJ,NCK,s,NS
I,NSJ)
    %y=solvde(M,ne,nb,itmax,conv,slowc,h,scalv,indexv,y);
%%
%function y2=solvde(M,ne,nb,itmax,conv,slowc,h,scalv,indexv,y2)

% SUBROUTINE solvde(itax,conv,slowc,scalv,indexv,ne,nb,m,y,nyj,nyk,
%*c,nci,ncj,nck,s,nsi,nsj)
%INTEGER itmax,m,nb,nci,ncj,nck,ne,nsi,nsj,nyj,nyk,indexv(nyj),NMAX
%REAL conv,slowc,c(nci,ncj,nck),s(nsi,nsj),scalv(nyj),y(nyj,nyk)
%PARAMETER (NMAX=10)
NMAX=10;
%CU    USES bksub,difeq,pinvs,red
%INTEGER ic1,ic2,ic3,ic4,it,j,j1,j2,j3,j4,j5,j6,j7,j8,j9,jc1,jcf,
%*jv,k,k1,k2,km,kp,nvars,kmax(NMAX)
%REAL err,errj,fac,vmax,vz,ermax(NMAX)
k1=1;
k2=M;                % Change to Capital M. This is no. of mesh points.
nvars=ne*M;          % Change to Capital M.
j1=1;
j2=nb;
j3=nb+1;
j4=ne;
j5=j4+j1;
j6=j4+j2;
j7=j4+j3;
j8=j4+j4;
j9=j8+j1;
ic1=1;
ic2=ne-nb;
ic3=ic2+1;
ic4=ne;
jc1=1;
jcf=ic3;
%global s c
```

```
%s=zeros(nsi,nsj);c=zeros(nci,ncj,nck);
s=zeros(4,9);c=zeros(4,3,1752);

% Change from looping solvde with for loop to while loop, so it stops
once
% it gets the error is less than conv.
err=1;
while err>conv && it<itmax;
    %for it=1:itmax;

    k=k1;
        %s=difeq(k,j9,indexv,y2,[s]);
%%
        %function s=difeq(k,jsf,indexv,y)
jsf=j9;
%SUBROUTINE difeq(k,k1,k2,jsf,is1,isf,indexv,ne,s,nsi,nsj,y,nyj,nyk)
% global x h lambda v hb eps0
% global k1 k2
%COMMON/BLOCK1/x,h,lambda,v,hb,eps0
%INTEGER k,k1,k2,jsf,is1,isf,ne,nsi,nsj,nyj,nyk,indexv(nyj)
%REAL s(nsi,nsj),y(nyj,nyk)
%REAL alpha,v,temp1,temp2,hb
%PARAMETER (M=1751)
M=1751;
%REAL h,x(M),lambda,pi,eps0

pi=3.141592;

%! Poisson's ratio is shared) !

alpha = (lambda)^(1./3.);

temp1=alpha*(hb^2)/(12.*(1.-v^2));
temp2=((lambda)^(1./6.))*hb*((1./(12.*(1.-v^2)))^(0.5));

if k==k1            %!********LEFT BOUNDARY CONDITION*******!
  s(3,4+indexv(1))=1.e-9;
  s(3,4+indexv(2))=1;
  s(3,4+indexv(3))=1.e-9;
  s(3,4+indexv(4))=1.e-9;

  s(3,jsf)=y(2,1);

  s(4,4+indexv(1))=1.e-9;
  s(4,4+indexv(2))=1.e-9;
  s(4,4+indexv(3))=1.e-9;
  s(4,4+indexv(4))=1;

  s(4,jsf)=y(4,1);

end
  %return
  %END
 %%
 %      [s,c]=pinvs(ic3,ic4,j5,j9,jc1,k1,[s],[c]);
 %function [s,c]=pinvs(ie1,ie2,je1,jsf,jc1,k,s,c)
```

```
% PINVS subroutine
% Need to define K
%SUBROUTINE pinvs(ie1,ie2,je1,jsf,jc1,k,c,nci,ncj,nck,s,nsi,nsj)
%INTEGER ie1,ie2,jc1,je1,jsf,k,nci,ncj,nck,nsi,nsj,NMAX
%REAL c(nci,ncj,nck),s(nsi,nsj)
%PARAMETER (NMAX=10)
%INTEGER i,icoff,id,ipiv,irow,j,jcoff,je2,jp,jpiv,js1,indxr(NMAX)
%REAL big,dum,piv,pivinv,pscl(NMAX)

%global s c
k1=1;
k2=M;                % Change to Capital M. This is no. of mesh points.
nvars=ne*M;          % Change to Capital M.
j1=1;
j2=nb;
j3=nb+1;
j4=ne;
j5=j4+j1;
j6=j4+j2;
j7=j4+j3;
j8=j4+j4;
j9=j8+j1;
ic1=1;
ic2=ne-nb;
ic3=ic2+1;
ic4=ne;
jc1=1;
jcf=ic3;
% important keep track of coefficient!!!!!!!!!!!!!!!
ie1=ic3;ie2=ic4;je1=j5;jsf=j9;jc1=jc1;k=k1;

Zero=0; One=1; Nmax=10;

je2=je1+ie2-ie1;
js1=je2+1;

for i=ie1:ie2;
big=Zero;
        for j=je1:je2;
            if abs(s(i,j))>big
               big=abs(s(i,j));
            end
        end
        if big==0;
            disp('Singular matrix, row all 0 in pinvs')
        return
        % break
        end
    pscl(i)=One./big;
    indxr(i)=0;
end


for id=ie1:ie2;
    piv=0;
        for i=ie1:ie2;
```

```
                if indxr(i)==0
                   big=Zero;
                        for j=je1:je2;
                                if abs(s(i,j))>big
                                    jp=j;
                                    big=abs(s(i,j));
                                end
                        end
                        if big*pscl(i)>piv
                            ipiv=i;
                            jpiv=jp;
                            piv=big*pscl(i);
                        end
                end
        end

        if s(ipiv,jpiv)==Zero
        disp('Singular matrix in pinvs')
        break
        end
        indxr(ipiv)=jpiv;
        pivinv=One./s(ipiv,jpiv);

        for j=je1:jsf;
            s(ipiv,j)=s(ipiv,j)*pivinv;
        end
        s(ipiv,jpiv)=One;
        for i=ie1:ie2;          % No. 17
            if indxr(i)~=jpiv && s(i,jpiv)~=Zero;
               dum=s(i,jpiv);
                for j=je1:jsf;
                    s(i,j)=s(i,j)-dum*s(ipiv,j);
                end
               s(i,jpiv)=Zero;
            end
         end
end

jcoff=jc1-js1;
icoff=ie1-je1;
for i=ie1:ie2;
    irow=indxr(i)+icoff;
        for j=js1:jsf;
            c(irow,j+jcoff,k)=s(i,j);
        end
end
 %c_k1=c;
        %c_all(:,:,k1)=c;
        %call difeq(k,k1,k2,j9,ic3,ic4,indexv,ne,s,nsi,nsj,y,nyj,nyk)
        %call pinvs(ic3,ic4,j5,j9,jc1,k1,c,nci,ncj,nck,s,nsi,nsj)
    for k=k1+1:k2;
        kp=k-1;
       % s=difeq(k,j9,indexv,y2,[s]);
%%
        %function s=difeq(k,jsf,indexv,y)
k1=1;
```

```
k2=M;                % Change to Capital M. This is no. of mesh points.
nvars=ne*M;          % Change to Capital M.
j1=1;
j2=nb;
j3=nb+1;
j4=ne;
j5=j4+j1;
j6=j4+j2;
j7=j4+j3;
j8=j4+j4;
j9=j8+j1;
ic1=1;
ic2=ne-nb;
ic3=ic2+1;
ic4=ne;
jc1=1;
jcf=ic3;
% keep track of coefficient !!!!!!!!!!!!!!
jsf=j9;
M=1751;

pi=3.141592;

%! Poisson's ratio is shared) !

alpha = (lambda)^(1./3.);

temp1=alpha*(hb^2)/(12.*(1.-v^2));
temp2=((lambda)^(1./6.))*hb*((1./(12.*(1.-v^2)))^(0.5));


if k>k2 %!******RIGHT BOUNDARY CONDITION*****!
  s(1,4+indexv(1))=1.e-9;
  s(1,4+indexv(2))=1.e-9;
  s(1,4+indexv(3))=1.*temp1;
  s(1,4+indexv(4))=-v*temp1;

  s(1,jsf)=temp1*(y(3,M)-v*y(4,M))-eps0;

  s(2,4+indexv(1))=1.e-9;
  s(2,4+indexv(2))=1.*temp2;
  s(2,4+indexv(3))=1.e-9;
  s(2,4+indexv(4))=1.e-9;

  s(2,jsf)=y(2,M)*temp2;
  %s(3,3)=1.e-9;  % I add this to try
  %s(4,3)=1.e-9;  % I add this to try

else            %!******IN BETWEEN BOUNDARIES*********!

  s(1,indexv(1))=       -1.+(x(k)-x(k-1))/(x(k)+x(k-1));
  s(1,indexv(2))=       -(x(k)-x(k-1))*(alpha*(y(4,k)+y(4,k-1))/...
      (2.*(x(k)+x(k-1)))+2./(x(k)+x(k-1))^2.);
  s(1,indexv(3))=       1.0e-9;
  s(1,indexv(4))=       -(x(k)-x(k-1))*(alpha*(y(2,k)+y(2,k-1))/...
      (2.*(x(k)+x(k-1))));
```

```
  s(1,4+indexv(1)) =    1.+(x(k)-x(k-1))/(x(k)+x(k-1));
  s(1,4+indexv(2)) =    s(1,indexv(2));
  s(1,4+indexv(3)) =    1.0e-9;
  s(1,4+indexv(4)) =    s(1,indexv(4));

  s(2,indexv(1))=       -(x(k)-x(k-1))/2.;
  s(2,indexv(2))=       -1.0;
  s(2,indexv(3))=       1.e-9;
  s(2,indexv(4))=       1.e-9;
  s(2,4+indexv(1))=     s(2,indexv(1));
  s(2,4+indexv(2))=     1.0;
  s(2,4+indexv(3))=     1.e-9;
  s(2,4+indexv(4))=     1.e-9;

  s(3,indexv(1))=       1.e-9;
  s(3,indexv(2))=       -(x(k)-x(k-1))*(-1./2.)*((y(2,k)+y(2,k-1))/...
      (x(k)+x(k-1)));
  s(3,indexv(3))=       -1.+(x(k)-x(k-1))/(x(k)+x(k-1));
  s(3,indexv(4))=       -2.*(x(k)-x(k-1))/(x(k)+x(k-1))^2;
  s(3,4+indexv(1))=     1.e-9;
  s(3,4+indexv(2))=     s(3,indexv(2));
  s(3,4+indexv(3))=     1.+(x(k)-x(k-1))/(x(k)+x(k-1));
  s(3,4+indexv(4))=     s(3,indexv(4));

  s(4,indexv(1))=       1.e-9;
  s(4,indexv(2))=       1.e-9;
  s(4,indexv(3))=       -(x(k)-x(k-1))/2.;
  s(4,indexv(4))=       -1;
  s(4,4+indexv(1))=     1.e-9;
  s(4,4+indexv(2))=     1.e-9;
  s(4,4+indexv(3))=     s(4,indexv(3));
  s(4,4+indexv(4))=     1.;

  s(1,jsf)= (y(1,k)-y(1,k-1))-(x(k)-x(k-1))*(alpha*(y(2,k)+y(2,k-1))*...
      (y(4,k)+y(4,k-1))/(2.*(x(k)+x(k-1)))-alpha/(pi*(x(k)+x(k-1)))-...
      (y(1,k)+y(1,k-1))/(x(k)+x(k-1))+2.*(y(2,k)+y(2,k-1))/...
      ((x(k)+x(k-1))^2.));

  s(2,jsf)= (y(2,k)-y(2,k-1))-(x(k)-x(k-1))*(y(1,k)+y(1,k-1))/2.;

  s(3,jsf)= (y(3,k)-y(3,k-1))-(x(k)-x(k-1))*(2.*(y(4,k)+y(4,k-1))/...
      ((x(k)+x(k-1))^2.)-(y(3,k)+y(3,k-1))/(x(k)+x(k-1))-(1./4.)*...
      (((y(2,k)+y(2,k-1))^2.)/(x(k)+x(k-1))));

  s(4,jsf)= (y(4,k)-y(4,k-1))-(x(k)-x(k-1))*(y(3,k)+y(3,k-1))/2;
end
  %return
  %END
 %%
 %       s=red(ic1,ic4,j1,j2,j3,j4,j9,ic3,jc1,jcf,kp,[c],[s]);
 % function s=red(iz1,iz2,jz1,jz2,jm1,jm2,jmf,ic1,jc1,jcf,kc,c,s)
k1=1;
k2=M;                % Change to Capital M. This is no. of mesh points.
nvars=ne*M;          % Change to Capital M.
j1=1;
j2=nb;
```

```
j3=nb+1;
j4=ne;
j5=j4+j1;
j6=j4+j2;
j7=j4+j3;
j8=j4+j4;
j9=j8+j1;
ic1=1;
ic2=ne-nb;
ic3=ic2+1;
ic4=ne;
jc1=1;
jcf=ic3;
% keep track of Coefficient !!!!!!!!!!!!1
iz1=ic1;iz2=ic4;jz1=j1;jz2=j2;jm1=j3;jm2=j4;jmf=j9;ic1=ic3;jc1=jc1;jcf=jc
f;kc=kp;
%In solvde, kp and k2 represent kc here.

%      SUBROUTINE red(iz1,iz2,jz1,jz2,jm1,jm2,jmf,ic1,jc1,jcf,kc,c,nci,
%     *ncj,nck,s,nsi,nsj)
%      INTEGER ic1,iz1,iz2,jc1,jcf,jm1,jm2,jmf,jz1,jz2,kc,nci,ncj,nck,
%     *nsi,nsj
%      REAL c(nci,ncj,nck),s(nsi,nsj)
%      INTEGER i,ic,j,l,loff
%      REAL vx

%global s c
loff=jc1-jm1;
ic=ic1;
for j=jz1:jz2;
        for l=jm1:jm2;
        vx=c(ic,l+loff,kc);
                for i=iz1:iz2;
                s(i,l)=s(i,l)-s(i,j)*vx;
                end
        end
vx=c(ic,jcf,kc);
        for i=iz1:iz2;
        s(i,jmf)=s(i,jmf)-s(i,j)*vx;
        end
ic=ic+1;
end
 %%   [s,c]=pinvs(ic1,ic4,j3,j9,jc1,k,s,c);
 % function [s,c]=pinvs(ie1,ie2,je1,jsf,jc1,k,s,c)
k1=1;
k2=M;               % Change to Capital M. This is no. of mesh points.
nvars=ne*M;         % Change to Capital M.
j1=1;
j2=nb;
j3=nb+1;
j4=ne;
j5=j4+j1;
j6=j4+j2;
j7=j4+j3;
j8=j4+j4;
j9=j8+j1;
ic1=1;
```

```
ic2=ne-nb;
ic3=ic2+1;
ic4=ne;
jc1=1;
jcf=ic3;
ie1=ic1;ie2=ic4;je1=j3;jsf=j9;jc1=jc1;
% PINVS subroutine
% Need to define K
%global s c

Zero=0; One=1; Nmax=10;

je2=je1+ie2-ie1;
js1=je2+1;

for i=ie1:ie2;
big=Zero;
        for j=je1:je2;
            if abs(s(i,j))>big
               big=abs(s(i,j));
            end
        end
        if big==0;
            disp('Singular matrix, row all 0 in pinvs');
        return
        % break
        end
    pscl(i)=One./big;
    indxr(i)=0;
end

for id=ie1:ie2;
    piv=0;
        for i=ie1:ie2;
                if indxr(i)==0
                   big=Zero;
                        for j=je1:je2;
                                if abs(s(i,j))>big
                                    jp=j;
                                    big=abs(s(i,j));
                                end
                        end
                        if big*pscl(i)>piv
                            ipiv=i;
                            jpiv=jp;
                            piv=big*pscl(i);
                        end
                end
        end

        if s(ipiv,jpiv)==Zero
        disp('Singular matrix in pinvs');
        break
        end
        indxr(ipiv)=jpiv;
        pivinv=One./s(ipiv,jpiv);
```

```
        for j=je1:jsf;
            s(ipiv,j)=s(ipiv,j)*pivinv;
        end
        s(ipiv,jpiv)=One;
        for i=ie1:ie2;        % No. 17
            if indxr(i)~=jpiv && s(i,jpiv)~=Zero;
               dum=s(i,jpiv);
                for j=je1:jsf;
                    s(i,j)=s(i,j)-dum*s(ipiv,j);
                end
               s(i,jpiv)=Zero;
            end
         end
end

jcoff=jc1-js1;
icoff=ie1-je1;
for i=ie1:ie2;
    irow=indxr(i)+icoff;
        for j=js1:jsf;
            c(irow,j+jcoff,k)=s(i,j);
        end
end

end

    k=k2+1;
%%        s=difeq(k,j9,indexv,y2,s);
   %call difeq(k,k1,k2,j9,ic1,ic2,indexv,ne,s,nsi,nsj,y,nyj,nyk)
%function s=difeq(k,jsf,indexv,y)
k1=1;
k2=M;               % Change to Capital M. This is no. of mesh points.
nvars=ne*M;         % Change to Capital M.
j1=1;
j2=nb;
j3=nb+1;
j4=ne;
j5=j4+j1;
j6=j4+j2;
j7=j4+j3;
j8=j4+j4;
j9=j8+j1;
ic1=1;
ic2=ne-nb;
ic3=ic2+1;
ic4=ne;
jc1=1;
jcf=ic3;
jsf=j9;

M=1751;

pi=3.141592;

%! Poisson's ratio is shared) !
```

```
alpha = (lambda)^(1./3.);

temp1=alpha*(hb^2)/(12.*(1.-v^2));
temp2=((lambda)^(1./6.))*hb*((1./(12.*(1.-v^2)))^(0.5));


  s(1,4+indexv(1))=1.e-9;
  s(1,4+indexv(2))=1.e-9;
  s(1,4+indexv(3))=1.*temp1;
  s(1,4+indexv(4))=-v*temp1;

  s(1,jsf)=temp1*(y(3,M)-v*y(4,M))-eps0;

  s(2,4+indexv(1))=1.e-9;
  s(2,4+indexv(2))=1.*temp2;
  s(2,4+indexv(3))=1.e-9;
  s(2,4+indexv(4))=1.e-9;

  s(2,jsf)=y(2,M)*temp2;
  %s(3,3)=1.e-9;  % I add this to try
  %s(4,3)=1.e-9;  % I add this to try

  %return
  %END
%%
% s=red(ic1,ic2,j5,j6,j7,j8,j9,ic3,jc1,jcf,k2,c,s);
% function s=red(iz1,iz2,jz1,jz2,jm1,jm2,jmf,ic1,jc1,jcf,kc,c,s)
k1=1;
k2=M;               % Change to Capital M. This is no. of mesh points.
nvars=ne*M;         % Change to Capital M.
j1=1;
j2=nb;
j3=nb+1;
j4=ne;
j5=j4+j1;
j6=j4+j2;
j7=j4+j3;
j8=j4+j4;
j9=j8+j1;
ic1=1;
ic2=ne-nb;
ic3=ic2+1;
ic4=ne;
jc1=1;
jcf=ic3;
iz1=ic1;iz2=ic2;jz1=j5;jz2=j6;jm1=j7;jm2=j8;jmf=j9;ic1=ic3;jc1=jc1;jcf=jc
f;kc=k2;

%In solvde, kp and k2 represent kc here.

%global s c

loff=jc1-jm1;
ic=ic1;
for j=jz1:jz2;
```

```
        for l=jm1:jm2;
        vx=c(ic,l+loff,kc);
                for i=iz1:iz2;
                s(i,l)=s(i,l)-s(i,j)*vx;
                end
        end
vx=c(ic,jcf,kc);
        for i=iz1:iz2;
        s(i,jmf)=s(i,jmf)-s(i,j)*vx;
        end
ic=ic+1;
end
%%
%[s,c]=pinvs(ic1,ic2,j7,j9,jcf,k2+1,s);
%function [s,c]=pinvs(ie1,ie2,je1,jsf,jc1,k,s,c)
k1=1;
k2=M;               % Change to Capital M. This is no. of mesh points.
nvars=ne*M;         % Change to Capital M.
j1=1;
j2=nb;
j3=nb+1;
j4=ne;
j5=j4+j1;
j6=j4+j2;
j7=j4+j3;
j8=j4+j4;
j9=j8+j1;
ic1=1;
ic2=ne-nb;
ic3=ic2+1;
ic4=ne;
jc1=1;
jcf=ic3;
ie1=ic1;ie2=ic2;je1=j7;jsf=j9;jc1=jcf;
% PINVS subroutine
% Need to define K
%global s c

Zero=0; One=1; Nmax=10;

je2=je1+ie2-ie1;
js1=je2+1;

for i=ie1:ie2;
big=Zero;
        for j=je1:je2;
            if abs(s(i,j))>big
               big=abs(s(i,j));
            end
        end
        if big==0;
            disp('Singular matrix, row all 0 in pinvs');
        return
        % break
        end
    pscl(i)=One./big;
```

```
    indxr(i)=0;
end


for id=ie1:ie2;
    piv=0;
        for i=ie1:ie2;
                if indxr(i)==0
                   big=Zero;
                        for j=je1:je2;
                                if abs(s(i,j))>big
                                    jp=j;
                                    big=abs(s(i,j));
                                end
                        end
                        if big*pscl(i)>piv
                            ipiv=i;
                            jpiv=jp;
                            piv=big*pscl(i);
                        end
                end
        end

        if s(ipiv,jpiv)==Zero
        disp('Singular matrix in pinvs');
        break
        end
        indxr(ipiv)=jpiv;
        pivinv=One./s(ipiv,jpiv);

        for j=je1:jsf;
            s(ipiv,j)=s(ipiv,j)*pivinv;
        end
        s(ipiv,jpiv)=One;
        for i=ie1:ie2;        % No. 17
            if indxr(i)~=jpiv && s(i,jpiv)~=Zero;
               dum=s(i,jpiv);
                for j=je1:jsf;
                    s(i,j)=s(i,j)-dum*s(ipiv,j);
                end
               s(i,jpiv)=Zero;
            end
         end
end

jcoff=jc1-js1;
icoff=ie1-je1;
for i=ie1:ie2;
    irow=indxr(i)+icoff;
        for j=js1:jsf;
            c(irow,j+jcoff,k)=s(i,j);
        end
end
%%
       %call difeq(k,k1,k2,j9,ic1,ic2,indexv,ne,s,nsi,nsj,y,nyj,nyk)
        %call red(ic1,ic2,j5,j6,j7,j8,j9,ic3,jc1,jcf,k2,c,nci,ncj,nck,s,
```

```
        %*nsi,nsj)
        %call pinvs(ic1,ic2,j7,j9,jcf,k2+1,c,nci,ncj,nck,s,nsi,nsj)
        %call bksub(ne,nb,jcf,k1,k2,c,nci,ncj,nck)

%SUBROUTINE bksub(ne,nb,jf,k1,k2,c,nci,ncj,nck)
%INTEGER jf,k1,k2,nb,nci,ncj,nck,ne
%REAL c(nci,ncj,nck)
%INTEGER i,im,j,k,kp,nbf
%REAL xx
% global ne nb
% %global nci ncj nck
% global k1 k2
% % In solvde, jcf was used instead of jf in this bksub.
% global jcf
k1=1;
k2=M;               % Change to Capital M. This is no. of mesh points.
nvars=ne*M;         % Change to Capital M.
j1=1;
j2=nb;
j3=nb+1;
j4=ne;
j5=j4+j1;
j6=j4+j2;
j7=j4+j3;
j8=j4+j4;
j9=j8+j1;
ic1=1;
ic2=ne-nb;
ic3=ic2+1;
ic4=ne;
jc1=1;
jcf=ic3;

jf=jcf;

nbf=ne-nb;
im=1;
for k=k2:-1:k1;
    if k==k1;
       im=nbf+1;
       %kp=k+1;
    end
    kp=k+1;                  % this line within if or not??
    for j=1:nbf;
        xx=c(j,jf,kp);
        for i=im:ne;
            c(i,jf,k)=c(i,jf,k)-c(i,j,k)*xx;
        end
    end
end
for k=k1:k2;
    kp=k+1;
    for i=1:nb;
          c(i,1,k)=c(i+nbf,jf,k);
    end
    for i=1:nbf;
```

```
        c(i+nb,1,k)=c(i,jf,kp);
    end
end
% RETURN
% END
%C  (C) Copr. 1986-92 Numerical Recipes Software _35.
%% Continue Solvde
err=0.;
    for j=1:ne;
        jv=indexv(j);
        errj=0.;
        km=0;
        vmax=0.;
        for k=k1:k2;
            vz=abs(c(jv,1,k));
            if vz>vmax
               vmax=vz;
               km=k;
            end
            errj=errj+vz;
        end
        err=err+errj/scalv(j);
        ermax(j)=c(jv,1,km)/scalv(j);
        kmax(j)=km;
    end
    err=err/nvars;
    fac=slowc/max(slowc,err);
    for j=1:ne;
        jv=indexv(j);
        for k=k1:k2;
            %y2(j,k)=y2(j,k)-fac*c(jv,1,k);
            y(j,k)=y(j,k)-fac*c(jv,1,k);
        end
    end

   it=it+1;
end
    % pause 'itmax exceeded in solvde'
%!  ****CALCULATION OF MID_POINT DEFLECTION**** !
   %z=0;
  z = 0.0d0;

    for k=1:M

        if k>1
           avg_angle = 0.5*(y(2,k)+y(2,k-1));
            dr = x(k)-x(k-1);
            z = z +avg_angle*dr;
        end
    end

    load = (hb^4)*((Eb*lambda)^(0.5));
    disp = z*hb*(Eb^(0.5))*(lambda^(1./6.));

    SOLUTION(1,LCASE)=load;
    SOLUTION(2,LCASE)=disp;
```

```
end
%END DO

%!***END OF ITERATIONS***!

pload
it
%9990 pause

%!****WRITING SOLUTION INTO FILE****!

%open(unit=99,file=outputfile,status='unknow')
%write(99,'(18(A,2x))')"","PLoad(P/E*a^2)","Disp(w/a)","Plate","membrane"

%write(*,'(a)')'LOAD DEPTH PLSOL MEMSOL'

for k=1:LCASE-1
  Q = (1./hb^2).*SOLUTION(1,k);%! Q = p/E*h^2
  plsol(k) = (1./(16.*pi))*(Q)*(1./hb);
  memsol(k)= (1.0491-0.1462*v-0.15827*v*v)*((Q*Eb*hb)^(1./3.));

  if k==1
    gap = SOLUTION(2,k)/plsol(1);
  end

  %write(99,'(18(e12.6,2x))')SOLUTION(1,k),SOLUTION(2,k),gap*plsol,memsol
end
%END DO
%END
%dlmwrite('trial_1.txt',SOLUTION);
TimeSpent=toc;


%!**********************END OF MAIN PROGRAM**********************!
% plot data for my use.
%
% With gap and without gap
% plot(SOLUTION(2,:),SOLUTION(1,:),plsol,SOLUTION(1,:),...
%     gap*plsol,SOLUTION(1,:),memsol,SOLUTION(1,:)),...
%     legend('Num Sim','plsol','gap*plsol','memsol'),...
plot(SOLUTION(2,:),SOLUTION(1,:),...
    gap*plsol,SOLUTION(1,:),memsol,SOLUTION(1,:)),...
    legend('Num Sim','gap*plsol','memsol'),...
    xlabel('w/a'),ylabel('pload')
```

APPENDIX B. SYMYX CALCULATION IN CHAPTER 3

The example of modulus calculation from plate stiffness measurement is provided by Symyx as follow:

1) Bare plate stiffness

Firstly, we measure the stiffness of the bare Kapton on the prepared pDMTA array,

$t_b = 50.8 \times 10^{-6}\ m$

$k_b = 341.01 + 29.762i\ \frac{N}{m}$; (the number is arbitrary taken at -25.6° C from experiment as example)

2) Plate stiffness correction

Symyx's procedure require the bare Kapton to be measured at a single temperature (here, it is taken at 20°C). The empirical correction applies to both the magnitude and phase of the bare plate stiffness.

Temperature

T= 20° C; $ReE_{Kapton} = 2423 - 4.23(20) = 2338\ MPa$ (B.1)

T= -25.6° C; $dR = \frac{2423-4.23(-25.6)}{2338} = 1.083$ (B.2)

Frequency

Freq =10 Hz; $dTheta = 0.006283Freq\left(\frac{2.56}{Freq} + 0.624\right) = 0.055$ (B.3)

Adjust the magnitude in real and imaginary parts with the corrections,

$k_bReal\_Corrected = dR((k_b)^2 + Im(k_b)^2)^{0.5}\cos(dTheta) = 370.039$ (B.4)

$k_bIm\_Corrected = dR((k_b)^2 + Im(k_b)^2)^{0.5}\sin(dTheta) = 20.48$ (B.5)

Thus, the corrected bare plate stiffness is

$$k_b = 370.039 + 20.48i\ \frac{N}{m}$$

3) Composite stiffness measurement

Polymer sample thickness is measured, and then the composite stiffness (Kapton with polymer sample) is measured as a function of temperature.

Polymer thickness: $t_c = 234.74 \times 10^{-6}$

Measured composite stiffness: $k_c = 11837.99 + 5134.3i \ \frac{N}{m}$

4) Solving quadratic equation

The non-dimensional parameters are calculated.

$$\tau = \frac{t_c}{t_b} = 4.621 \tag{B.6}$$

$$K = \frac{k_c}{k_b} = 32.659 + 12.067i \tag{B.7}$$

Solve for μ,

$$\mu = \frac{\left(-4\tau^2-6\tau-4+K\right)+\left[\left(4\tau^2+6\tau+4-K\right)^2-4\tau^2(1-f\right]^{0.5}}{2\tau^2} \tag{B.8}$$

$$\mu = 0.331 + 0.163i$$

5) Modulus calculation

$$\varepsilon = \frac{\mu}{\tau} = \frac{0.331+163i}{4.621} = 0.0716 + 0.0353i \tag{B.9}$$

$$\varepsilon = \frac{E_{coating}}{E_{Kapton}} \tag{B.10}$$

Thus, we need the Kapton modulus.

Using the fixed edge circular plate equation from Figure 3.2,

$$k_b = \frac{4\pi E_{Kapton} t_b^3}{3R^2(1-\nu_b^2)} \tag{B.11}$$

$$E_{Kapton} = \frac{k_b 3R^2(1-\nu_b^2)}{4\pi t_b^3} \tag{B.12}$$

$$E_{Kapton} = 3.49 \times 10^9 + 1.932i \times 10^8 \ Pa$$

Modulus of the sample can then be calculated.

$$E_{coating} = \varepsilon E_{Kapton} = (0.716 + 0.0353i)(3.49 \times 10^9 + 1.932i \times 10^8)$$

$$E_{coating} = 2.429 \times 10^8 + 1.368i \times 10^8 \text{ Pa}$$